

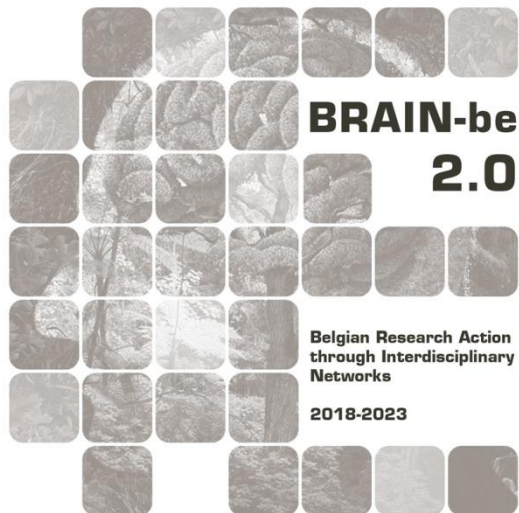
LASUGEO

**monitoring LAnd SUbsidence caused by Groundwater exploitation
through gEOdetic measurements**

Xavier Devleeschouwer – Pierre-Yves Declercq – Atefe Choopani - Geological Survey of Belgium (GSB), Royal Belgian Institute of Natural Sciences (RBINS)

Marc Van Camp – Kristine Walraevens - Universiteit Gent (UGent)

Aline Moreau – Alain Dassargues – Philippe Orban – Université de Liège (ULiège)



NETWORK PROJECT

LASUGEO

monitoring LAnd SUbsidence caused by Groundwater exploitation
through gEOdetic measurements

Contract - B2/191/P1/LASUGEO

FINAL REPORT

PROMOTORS: Xavier DEVLEESCHOUWER – GSB, RBINS
Michel VAN CAMP – RBINS
Kevin GOBRON – ROB – (left ROB)
Pierre-Yves DECLERCQ - GSB, RBINS
Atefe CHOOPANI - GSB, RBINS and ULiège
Marc VAN CAMP – UGent – (retired)

- Kristine WALRAEVENS - UGent – (retired)
- Alain DASSARGUES – ULiège – (retired)
- Philippe ORBAN – ULiège
- Aline MOREAU– ULiège – (left, contract stopped)

AUTHORS: Xavier Devleeschouwer – Pierre-Yves Declercq – Atefe Choopani - GSB,
RBINS
Marc Van Camp – Kristine Walraevens - UGent
Aline Moreau – Alain Dassargues – Philippe Orban – ULiège



Published in 2025 by the Belgian Science Policy Office

WTCIII

Simon Bolivarlaan 30 bus 7

Boulevard Simon Bolivar 30 bte 7

B-1000 Brussels

Belgium

Tel: +32 (0)2 238 34 11

<http://www.belspo.be>

<http://www.belspo.be/brain-be>

Contact person: Koen Lefever

Tel: +32 (0)2 238 35 51

Neither the Belgian Science Policy Office nor any person acting on behalf of the Belgian Science Policy Office is responsible for the use which might be made of the following information. The authors are responsible for the content.

No part of this publication may be reproduced, stored in a retrieval system, or transmitted in any form or by any means, electronic, mechanical, photocopying, recording, or otherwise, without indicating the reference:

X. Devleeschouwer, P.-Y. Declercq, A. Choopani, M. Van Camp, K. Walraevens, A. Moreau, A. Dassargues, Ph. Orban. ***monitoring LAnd SUBsidence caused by Groundwater exploitation through gEOdetic measurements***. Final Report. Brussels: Belgian Science Policy Office 2025 – 147 p. (BRAIN-be 2.0 - (Belgian Research Action through Interdisciplinary Networks))

TABLE OF CONTENTS

1. EXECUTIVE SUMMARY OF THE REPORT	5
2. ACHIEVED WORK	7
3. FINAL RESULTS	138
4. CONCLUSIONS AND RECOMMANDATIONS	140
5. VALORISATION ACTIVITIES	144
5.1 PUBLICATIONS	144
5.2 PARTICIPATION/ORGANISATION OF SEMINARS (NATIONAL/INTERNATIONAL)	144
5.3 SUPPORT TO DECISION MAKING (IF APPLICABLE)	145
6. ENCOUNTERED PROBLEMS AND SOLUTIONS	148

1. EXECUTIVE SUMMARY OF THE REPORT

The LASUGEO project started after the confirmed signatures of all the contracts in the different partner institutions around end March/April 2020. This time frame coincided with the beginning of the pandemic due to the Covid19 crisis, the lockdown, and the beginning of the homeworking activities. Several colleagues were facing a difficult time due to IT issues, developing in urgency the follow-up of the teaching activities and developing new ones for the end of the academic year in 2020. The preliminary kick off meeting was postponed, and the different partners have delayed their work activities till the beginning of the 2020 end summer. The PhD work and related contracts of Aline Moreau were delayed as well to the end of summer period and the beginning of the Academic Year. Despite the difficulties encountered by the partners with the Covid19 pandemic, the main works were started by the different teams and were followed even if some aspects have been largely delayed. The tasks and deliverables were almost all processed according to the original workplan. Some new tasks and deliverables were added to the original plan and some planned at the end of the project were purely abandoned due to the chaotic aspects and change of the teams in the partners during the project with cascading effects on the way the project was originally organized. Even if some of the tasks were delayed and one main task/deliverable was cancelled due to fragile conclusions sometimes going into different conclusions and views.

The coordination activities were engaged with multiple bilateral discussions during the second semester of 2020 till the beginning of 2023 to properly define the different tasks and the case studies with the different teams according to their respective expertise. Following, extensive radar interferometry processing made by the SAR team of the GSB to update all the historical and recent ground deformations across Belgium. Some of the case studies in the WP2 have been modified according to the SAR data and will be detailed further in this report. New sites were chosen for hydrogeological and geomechanical models where ground deformations were and are still observed from the SAR imagery.

The hydrogeological models and the SAR data comparison that have been ongoing in the WP2 both for the Deep Aquifer System (DAS) and Tertiary Aquifer System (TAS) in Flanders.

The new study areas (Leuven and Antwerp) where hydrogeological modelling approaches were part of the ongoing WP2 have been processed as much as the data allowed to progress. A fifth and new case study was initiated by the Liège team under this project on the Brussels case area. A sixth case study area was also initiated but without real hydrogeological model due to a very limited availability of data and will be reported in the WP4 and was a second case study area belonging to the PhD work of Atefe Choopani.

WP3 concerns geodetic investigations with gravimetry data and models. Only 2 stations out of the 8 stations planned were measured during 2020-2022 period. The other areas/stations were not collected due to the covid crisis and the difficulties organizing fieldwork activities during that period. The work on the gravity time series was foreseen later. Detailed investigations on the GNSS time series were done and processed by Kevin Gobron before leaving ROB and the project itself. This work was dedicated to cover the whole Belgium area and surrounding neighboring countries alone in a first step to derive the ground movements recorded at all the GNSS stations under study. After statistical analyses and filtering technique to optimize the signal, the GNSS time series were compared to the SAR historical data collected and processed by the SAR team at GSB inside the WP4. From the historical data, ERS, ENVISAT are processed for the entire country. Those of Sentinel-1A and 1B were processed till the end of the Sentinel-1B that stopped working. The treatments were ongoing with different SAR processing chains to optimize the results and minimize the border problems between tracks/images. New SAR scenes from the Sentinel-1 constellation are downloaded and processed to regularly update the SAR data across the entire country. Inside WP4, the SAR team started a procedure to select the best option combining different geodetic techniques to buy and install new artificial corner reflectors and professional GPS stations called IGR stations with another partner (i.e. the National Geographic Institute). These geodetic ground control solutions were installed in two places where ground deformations were already observed (i.e. Doel and Houthaalen). To do so and to install those structures for the long-term (8-10 years), a partnership has been established with NGI. The GSB and NGI are joining their forces to find the 4 next most suitable

places and NGI has acquired two additional GPS stations (with a budget of 24 000 €) to install them on the GSB artificial corner reflectors.

The milestones planned in the WP5 (future land subsidence vs groundwater exploitation: models and scenarii), dropped out at the end of the project due to limited exchanges between the partners and very different results while some areas have presented quite good and conclusive comparisons and models between the different geodetic techniques while other areas have given a very negative comparison and clearly not in the same order of magnitude. The LASUGEO partners cannot overcome those inconsistencies between the different case study areas to progress on a very broad and largely accepted model combining different thematics to link the geohazards observed using SAR data. The main discussion is the amount of data necessary to depict the deep vs the shallow causes affecting the surface deformations observed by SAR, and GNSS/IGR data sets.

2. ACHIEVED WORK

WP1 Management, communication and dissemination activities

Task 1.1 Project Management:

A Teams workspace was set up by the GSB/RBINS as a communication and data exchange platform.

Task 1.2 Website

The preliminary website was not used by the teams nor the social medias to largely disseminate the results while the personal accounts of some of the different partners were used instead.

Task 1.3 Dissemination activities

Most of the results were published during conferences and through papers in peer reviewed journals, some are still in review processing phase and others are still planned (i.e. ongoing work on the IGR data and results validation including the installation of the last foreseen 4 IGR stations planned)

The publications dealing with the LASUGEO project are listed in the output and published results chapters.

WP2 Groundwater exploitation targeted sites and hydrogeological modelling

Target site 1. Deep Aquifer System (DAS) under the western part of Flanders - (Deliverables: D.2.1./D.2.1.1./D.4.4./D.4.4.1.)

Introduction

During the last three decades, land subsidence has been affecting several towns in the Belgian provinces (Declercq et al., 2021; Devleeschouwer et al., 2021). However, in recent years, both the rate of subsidence and the surface area being affected are decreasing. Except for groundwater exploitation, other human activities and natural phenomena have not been noted in the area in the specified subsidence period. Detailed analysis and mapping of the land subsidence and its evolution from 1992 to 2020 were done using remote sensing images of ERS 1-2, ENVISAT, Terra SAR-X, and Sentinel 1A satellite SAR scenes (Declercq, 2020). The observed land subsidence phenomena have been related to historical groundwater exploitation. The major early subsidence in southern West-Flanders was thought to be related to the 20th century industrial period water exploitation boom of the deep aquifer system. However, a detailed analysis of the compaction of different lithological layers was missing.

In the western part of Flanders, long and intensive exploitation of the deep aquifer system in the Paleozoic basement, the Cretaceous and the Landenian aquifers has led to very low piezometric levels and the development of regional-scale deep depression cones (De Breuck et al., 1986a, 1986b, 1988). Exploitation started more than a century ago and the economic boom of the 1960s has increased the downward trend even more. Restrictions on pumping rates have been implied by the administration starting from around 2006 and groundwater levels are now slowly recovering (Melger, 2018). But recharge rates of these deep aquifers are very low, as they are covered by thick tertiary clay layers and full recovery will take a very long time. Besides the depletion of the groundwater storage in these deep layers, another concern has risen about the possible impact on ground levels as lowering the piezometric levels by more than 100 m may have caused compaction of the pumped layers and the covering aquitards. The combined effect of the compaction in all the affected layers is expected to result in land subsidence on a regional scale, considering the spatial extension of the enormous depression cones. In this study, the land subsidence is quantified using a groundwater flow model of the deep aquifer system (DAS) and a module for simulating aquifer layer compaction and land subsidence. A simplified one-dimensional MODFLOW model was also developed to estimate potential subsidence caused by the compaction of the overlying Ypresian aquitard. This model is also used for sensitivity analysis and to test specific scenarios, such as varying vertical conductivity and storage coefficients, as well as elastic and inelastic deformation conditions.

Methodology

A transient 3D groundwater flow model for the deep aquifer system (DAS), that was developed to simulate the piezometric evolution of 1920 to 2000, has been used as a basis that was updated to calculate the compaction of aquifer layers and thus, the subsidence of the ground surface. Furthermore, a 1D vertical flow model is developed to specifically calculate the compaction of the thick Ypresian clay overlying the DAS aquifers. The data for the aquifer geometry (aquifer thickness, and top and bottom elevations) are taken from the DOV portal. Water level observations are taken from the VMM water level monitoring network.

Geological and hydrogeological setup

The three-dimensional modeling and calculation of the subsidence on the deep aquifer system are applied to the Landenian, the Chalk and the Paleozoic Basement aquifers, while the land subsidence due to the compaction in the

overlying aquitard is calculated with a 1-dimensional model for the Ypresian clay. Thus, a summarized geological and hydrogeological characterization of these hydrogeological units is presented as follows, and shown in 4 profiles, shown on the map in fig. 1.

Ypresian Clay

The Ypresian clay predominantly consists of soft, marine clays rich in organic matter, often interbedded with silty and sandy layers. This formation reflects a marine environment from the Early Eocene epoch (Bucur et al., 2016). The Ypresian clays lie above the Paleozoic, Cretaceous and Landenian deposits and below the Lutetian formations, indicating a transgressive marine sedimentation pattern (De Paepe et al., 1995).

The Ypresian clay acts as a confining layer due to its low permeability, affecting the groundwater dynamics of underlying aquifers, such as the Landenian sands (Van Houtte et al., 2017).

Landenian aquifer

The Landenian aquifer belongs to the Paleocene epoch, specifically the Landenian stage, which is part of the Tertiary period in the geological timescale. The Landenian deposits are composed mainly of sandy and clayey layers. The sand layers typically make up the aquifer, while the clay layers act as confining units or aquitard (Maréchal et al., 2004). The Landenian aquifer is considered a semi-confined to confined aquifer, depending on the presence and thickness of overlying confining layers (De Smedt & Batelaan, 2001). According to Van Camp and Walraevens (2009), the transmissivity of the Landenian aquifer is a few tens of m²/d. The Cretaceous and Landenian aquifers are more homogeneous and spatial correlation scales are larger than in the Basement Aquifer.

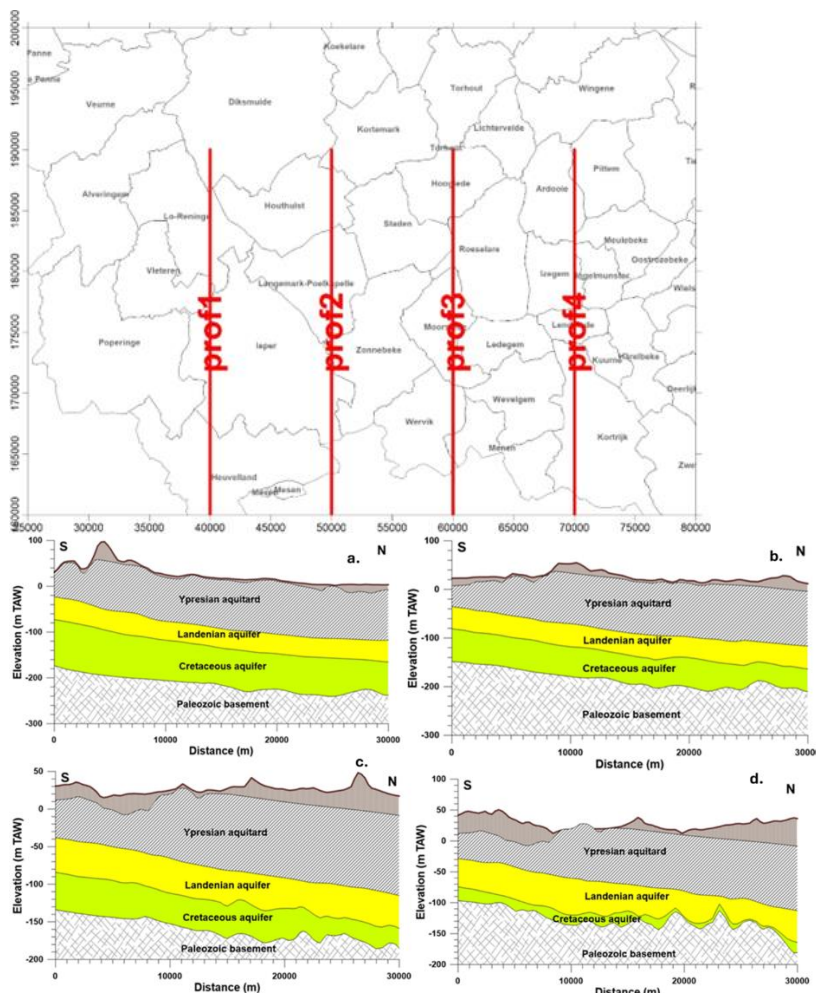


Figure 1. Hydrogeological profiles: profile 1 (a), profile 2 (b), profile 3 (c), and profile 4 (d)
Cretaceous aquifer or Chalk aquifer

The Cretaceous aquifer in Western Flanders dates to the Late Cretaceous period, approximately 100 to 66 million years ago. The aquifer is primarily composed of the formations from the Campanian and Maastrichtian stages. The Cretaceous deposits in this region are predominantly composed of chalk and marl, which are typical of marine environments. The

chalk is often soft and has a high porosity due to its microporous structure (Gogu, 2000). The Cretaceous formations underlie the Tertiary deposits and are often overlain by Paleogene sediments in the region. They are missing in some parts of the model area

The Cretaceous aquifer is characterized by high porosity and permeability, particularly in the chalk formations, which allow for significant groundwater storage and flow. Hydraulic conductivity values typically range from 1×10^{-4} to 1×10^{-2} m/s, depending on the degree of fracturing and the presence of marl interbeds (Gogu, 2000).

Paleozoic aquifer

The Paleozoic aquifer in Western Flanders dates back to the Paleozoic era, which spans from approximately 541 to 252 million years ago. The lithology of the Paleozoic aquifer comprises a variety of rock types, including sandstones, limestones, and shales. The Paleozoic aquifer in Western Flanders is referring to the Brabant Massif, consisting of hard rocks of Cambro-Silurian age. The rocks consist of consolidated to slightly metamorphic sediments, such as sandstone, quartzite, schists and phyllites, and of magmatic rocks at the South rim of the Brabant Massif. To the South of the Brabant Massif, the Namur Basin is found, consisting of rocks of Devonian-Carboniferous age, which are present only in a very small part of the model area, around Moeskroen.

The transmissivity of the Brabant Massif, derived from measurements of the specific capacity of wells in the study by Walraevens et al. (2000) is presented in Figure 2. The transmissivity values are spatially variable, higher along two perpendicular zones: WNW-ESE (corresponding to longitudinal fractures formed by an overthrust shear zone) and NNE-SSW (transversal fractures) had been noted. The very high transmissivity values near Moeskroen (Figure 2) are associated with the Kolenkalk (Carboniferous limestone aquifer) of the Namur Basin rather than the Cambro-Silurian rocks of the Brabant Massif. High values (100–200 m²/d) in certain zones (excluding Moeskroen) represent the highest transmissivity within the Cambro-Silurian rocks of the Brabant Massif, mainly corresponding to the perpendicular shear and fractured zones. Moderate values (10–50 m²/d) are typical of fractured Cambro-Silurian rocks. Low values (1–10 m²/d) suggest areas with less fracturing. The Basement Aquifer consists of fractured rocks, differing from the overlying porous sediments. Fracturing is most prominent in the upper 50 m, decreasing with depth, though sporadic fractures occur deeper (Van Camp and Walraevens, 2009). Transmissivity is highly heterogeneous, with spatial correlation often below 1 km, making reliable mapping challenging. Average transmissivity is around 10 m²/day, ranging from <1 to several hundreds of m²/day.

Transmissiviteit (m²/d) van de Sokkel (Massief van Brabant - Kolenkalk)

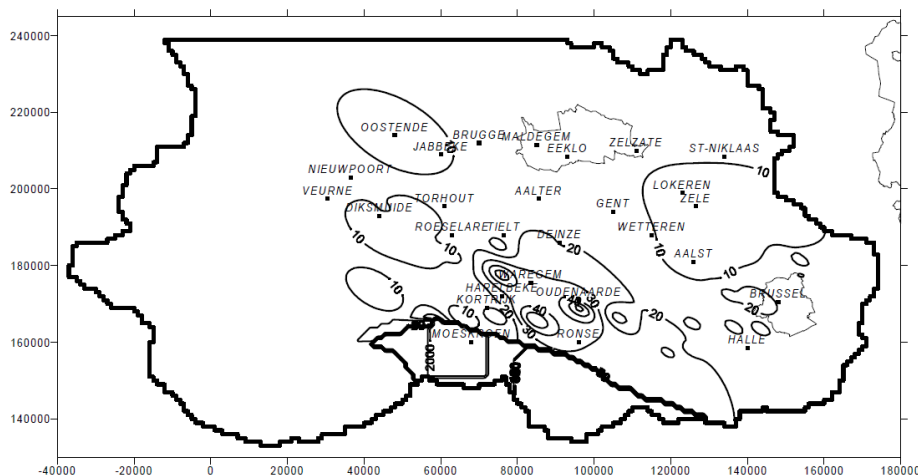


Figure 2. Transmissivity values are derived from the specific capacity (Walraevens, Van Camp & Martens, 2000).

Groundwater flow model of the DAS

The groundwater flow model, and calculation of subsidence on the deep aquifer layers is based on a MODFLOW model of the DAS (Walraevens & Van Camp, 2004), which includes the three deep aquifer layers: the Landenian, the Cretaceous and Paleozoic aquifers. It is a large-scale model including the whole Belgian provinces of West- and East-Flanders, the western part of Flemish Brabant province and parts of Zeeland in the Netherlands and North of France. It has been constructed as a tool for supporting management strategies of the deep layers and developing remediation timeframes for recovering the overexploited aquifer systems. It uses a spatial discretization of 1 km. In the framework of the LASUGEO project, this model has been updated, integrating the new geological 3D model G3DV3.1, and refining the layer discretization, introducing the Ypresian clay as an explicit layer. Model layers are set into five layers (Figure 2): all layers above Ypresian aquitard (Layer 1), Ypresian clay layer (Layer 2), Landenian aquifer (Layer 3), Cretaceous aquifer (Layer 4), and Paleozoic basement aquifer (Layer 5).

With the model, 130 years spanning simulation was done in the current study, including an 80 years reconstruction of the increasing exploitation in the period 1920-2000, followed by a 20 years period during which pumping rates were decreased, with 80% in the basement aquifer and with 50% in the Landenian aquifer, and a last period of 30 years during which the restricted pumping rates were continued (2020-2050). The time evolution is somewhat simplified and schematized compared to the real situation. From the model runs, the evolution of the depression cones could be obtained. Besides the depletion of the groundwater storage in these deep layers, another concern has risen about possible impact on ground levels, as lowering the piezometric levels by more than 100 m may have caused compaction of the pumped layers and possibly also the overlying aquitard. The combined effect of the compaction in all the affected layers results in a land subsidence on a regional scale, considering the spatial extension of the enormous depression cones. The land subsidence has been quantified using the updated groundwater flow model of the DAS and a module for simulating layer compaction and land subsidence for the aquifers.

2.2.1. 3D Model layers thicknesses

The model layers' top and bottom elevations and thickness are taken from the Geological buildup 3D model G3D V3.1. The geological buildup has been carefully assessed for top, bottom, and thickness of the Ypresian clay (Formation of Kortrijk) and top, bottom, and thickness of the Landenian aquifer, as these deposits are expected to be more susceptible to compaction. The top of the Paleozoic basement has been assessed in detail as well. The thickness of the layers is presented in Figure 3 and discussed in the following paragraph.

The Landenian aquifer thickness varies significantly across the region (Figure 3a). The thicker areas are predominantly located in the western part, especially around Alveringem and Veurne, with thicknesses reaching up to 60 m. Thinner sections are present in the central and southeastern areas, with values dropping to around 10-20 m. The Cretaceous aquifer shows a different pattern, with its thickness generally increasing as you move toward the northern and eastern parts (Figure 3b). The thicker regions, with values of up to 80 m, are in the western part near Veurne and Diksmuide. Thinner zones are found toward the southern regions, particularly in the area surrounding Poperinge and Ieper, where the thickness drops to 10-20 m.

The Ypresian clay displays a distinct pattern with the thickest sections concentrated in the southern and southeastern areas, particularly around Wevelgem and Mesen, where the thickness exceeds 100 m (Figure 3c). In contrast, the northern regions exhibit significantly thinner clay layers, particularly in areas like Veurne and Lo-Reninge, where the thickness decreases to 50-60 m.

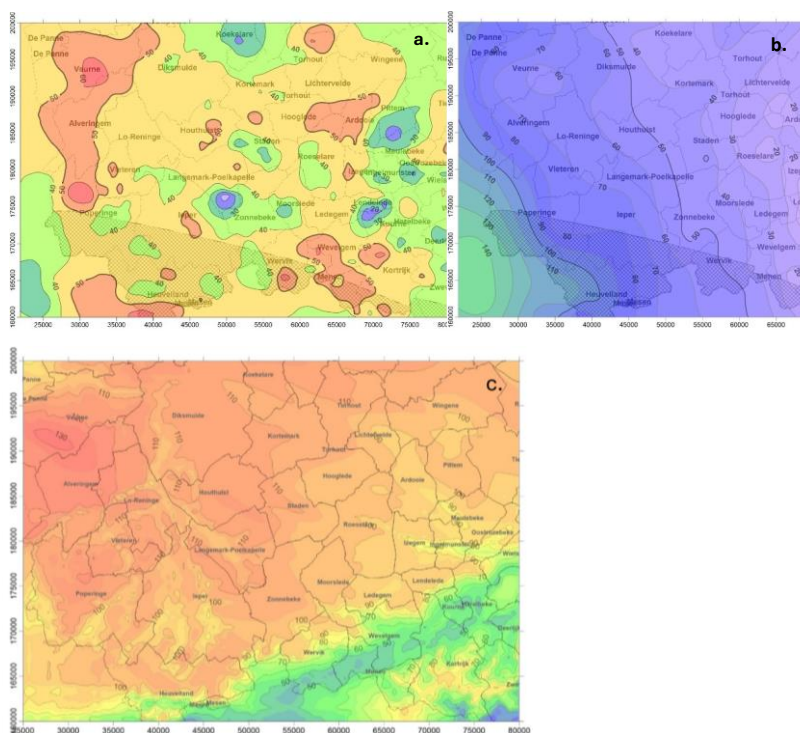


Figure 3. a) Thickness of Landenian aquifer (m); b) thickness of Cretaceous aquifer (m); c) thickness of the Ypresian clay adopted from the new geological 3D model G3DV3.1 of the DOV

2.2.2. Subsidence module parameters

The compaction of aquifers and aquitards is computed as a function of drawdown, aquifer thickness, and specific storage.

$$\text{compaction (m)} = \text{drawdown (m)} * \text{thickness (m)} * S_a \text{ (1/m)} \quad (1)$$

Where S_a is a specific storage

Deeper subsurface materials tend to be more compacted due to the total stress of overburden, thereby decreasing porosity and compressibility leading to lower S_a (Chowdhury et al., 2022). In this study, the S_a is calculated by the empirical formula developed by Van der Gun (1979), as cited by Boonstra and de Ridder (1981), that calculates S_a as a function of depth. The equation has been used to calculate the storage coefficient S and then the specific storage S_a (S is equal to S_a multiplied by saturated aquifer thickness) for confined and semi-confined aquifers.

$$"S" = 1.8 * 10^{(-6)} * ((d_2 - d_1) + 8.6 * 10^{(-4)}(d_2^{0.3} - d_1^{0.3})) \quad (2)$$

Where d_1 = depth of top (m), and d_2 = depth of bottom (m)

For example, for the Landenian aquifer in the center depression cone in Langemark, $d_1 = 112.4$ m and $d_2 = 155.7$ m (and thus aquifer thickness = 43.3 m). With equation (2), a storage coefficient of $4.392 \cdot 10^{-4}$ is deduced. With the thickness of 43.3 m, this results in $S_a = 1.014 \cdot 10^{-5}$.

MODFLOW 1D column model

This is a simplified model to simulate subsidence for a single vertical column, focusing on localized processes. It is often used for sensitivity analysis and specific scenarios (e.g., different vertical hydraulic conductivity k_v and storage coefficients) at a given location in detail unlike the 3D MODFLOW model used to evaluate regional subsidence patterns across the study area. The 3D model is used to correlate subsidence with observed piezometric depressions and INSAR maps and predict the effect of regional pumping on subsidence. With the 1D model, compaction of the Ypresian aquitard has been simulated, by applying a fine discretisation for this clay layer. The geological build-up was conceptualized in the 1D model as shown in Figure 4. Both models use the subsidence module for estimating the land subsidence due to groundwater exploitation. A 1D column model was constructed with MODFLOW, using 15 layers, 1 column, 1 row, and a cell size of 100 m x 100 m. The MODFLOW modules used are: LPF (Layer Property Flow), GHB (General Head Boundary), SUB (Subsidence), and PCG (Preconditioned Conjugate Gradient). The Ypresian aquitard was subdivided into 10 layers, to calculate compaction as a function of depth within the aquitard. The DAS is subdivided into its four-constituting aquifer/aquitard layers. This model was based on Well 3-0521b, located to the west of Langemark-Poelkapelle (Figure 3a).

When modeling subsidence due to groundwater extraction, elastic and inelastic storage can be distinguished. This was also tested with the 1D model. The sensitivity of the k_v and elastic/inelastic storage behaviour were tested by the developed 1D model. Thus, six scenarios have been considered, in which different storage type percentages and possible vertical hydraulic conductivity values were assumed. The scenarios are 100% elastic storage, 100% inelastic storage, and 50% elastic storage, and with two possible values of the vertical hydraulic conductivity of the Ypresian clay (Table 1).

Shallow aquifer (Quaternary, Tertiary)	L1
sublayer 1	L2
Ypresian aquitard	
sublayer 9	L10
sublayer 10	L11
Landenian aquifer	L12
Landenian aquitard	L13
Cretaceous aquifer	L14
Paleozoic aquifer	L15

Figure 4. The 1D model layers

Scenario	k_v Ypresian (m/d)	S_a Ypresian	storage type
A	10-5	10-5	100% elastic
B	10-6	10-5	100% elastic
C	10-5	10-5	100% inelastic
D	10-6	10-5	100% inelastic
E	10-5	10-5	50% elastic
F	10-6	10-5	50% elastic

Table 1. Scenarios and module parameters for the 1-D model

2.4. Correlation between InSAR-derived land subsidence and piezometric trends

The piezometric evolution of all 3 aquifers composing the Deep Aquifer System (DAS), namely the Landenian aquifer, the Cretaceous aquifer and the Paleozoic basement aquifer (mainly Brabant Massif aquifer, also Carboniferous aquifer), has been compared to the InSAR subsidence maps.

3. Results and discussion

3.1. Piezometry

The piezometric time series of the Landenian aquifer has been compiled (Figure 5). All piezometers show an initial drop of hydraulic head, followed by a rise. The timing differs according to the location. Also, the shorter time series for the other piezometers were studied.

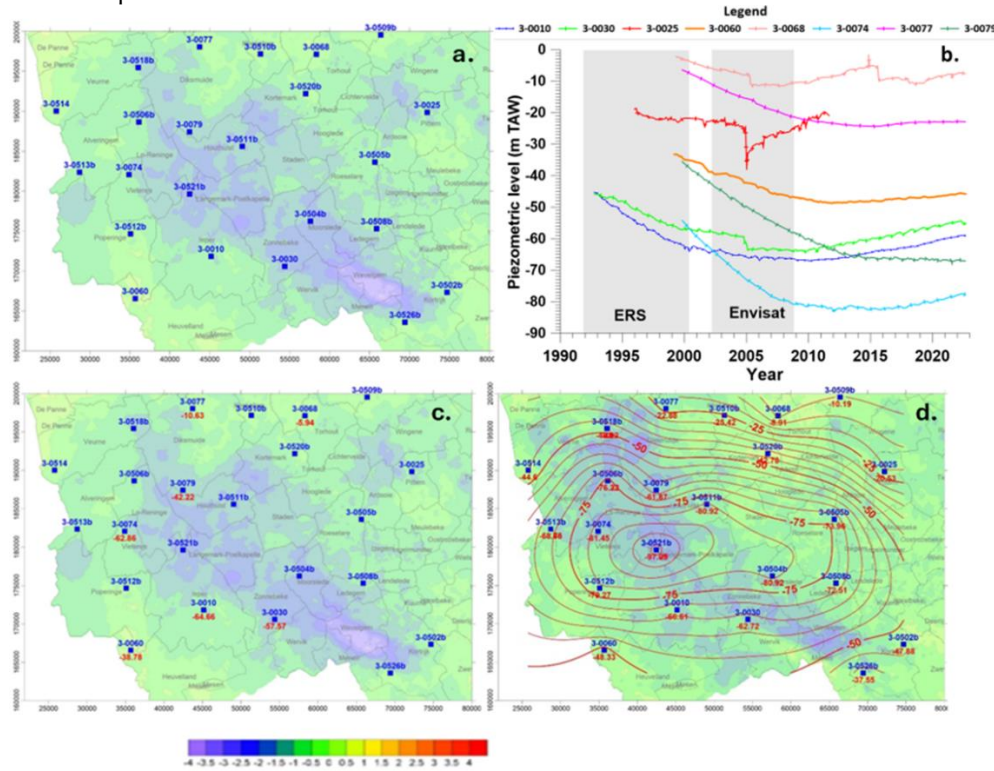


Figure 5. Monitoring network (VMM) for Landenian aquifer: a) location of VMM wells; b) long piezometric time series; c) piezometric levels in January 2002; and d) piezometric levels in January 2011. The shaded time windows in figure b show the subsidence information for ERS 1992-2001 and for Envisat 2003-2010. The background subsidence map is in units of mm/year.

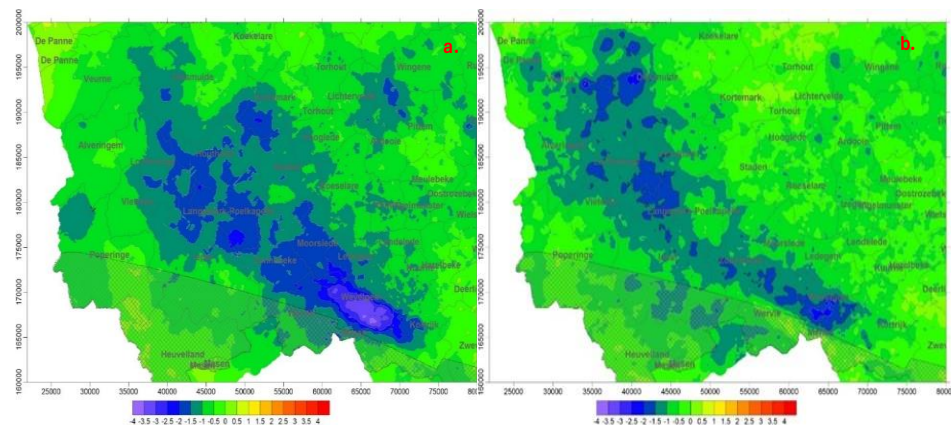


Figure 6. a) Land subsidence (mm/year) using ERS from 1992-2001, b) and Envisat from 2003-2010.

The piezometric maps were compiled for the end of the ERS data period (January 2002, Figure 5c) and the end of the Envisat data period (January 2011, Figure 5d). For January 2002, no contours were plotted because of a lack of sufficient data. The corresponding InSAR-derived subsidence data are plotted as a background on each map and shown in Figure 6. It is observed that the depression cone of the Landenian Aquifer corresponds with the western part of the InSAR-derived area with high subsidence (several mm/year, in blue), but not with the eastern part. A comparison of both maps shows that piezometric levels have continued dropping in between, as also confirmed by Figure 5b.

For the Cretaceous Aquifer, only two (remote) monitoring wells existed in January 2002 (Figure 7a), while in January 2012, a deep depression cone was revealed by unexpectedly low heads (Figure 7b). Although data are insufficient, the depression cone seems to align with the one in the Paleozoic Basement (Figure 8b) (although an exceptionally low head was found in Kortemark, well 3-0520a unlike the Paleozoic basement). For sure, these both depression cones do not correspond with the south-eastern zone of maximal compaction deduced from InSAR, which is even larger than in the western part (Figure 6a). The maximal compaction was found in Wevelgem (Figure 6a), which is situated at the south border of the center of the depression cone in the Paleozoic Basement Aquifer.

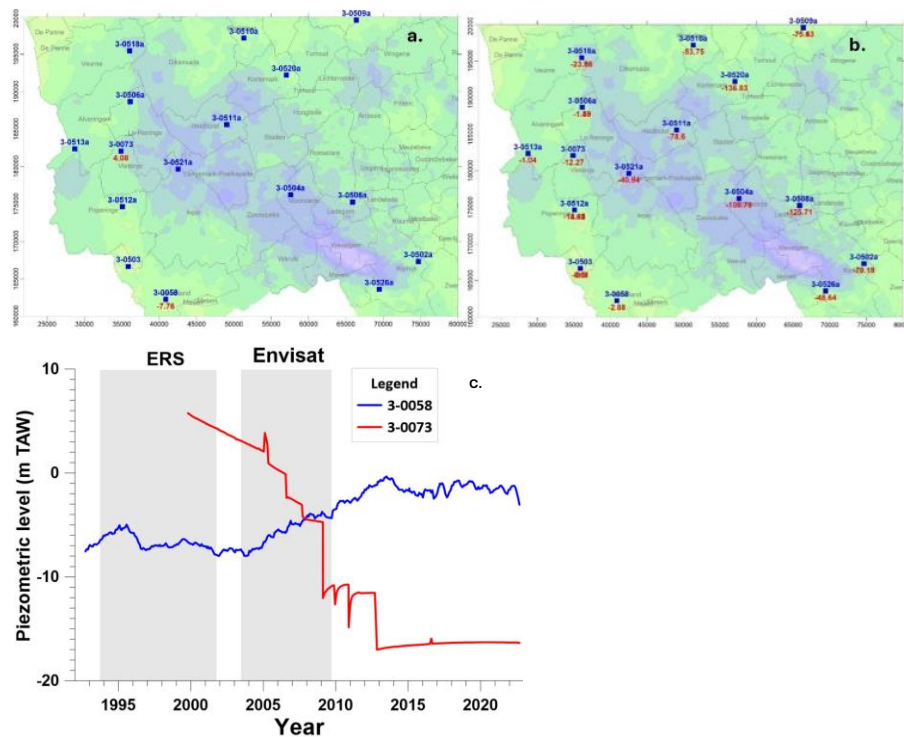
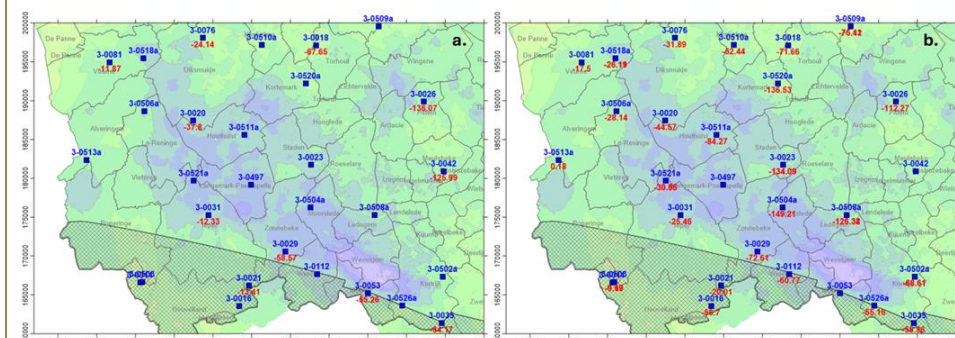


Figure 7. a) Observed hydraulic heads in the Cretaceous Aquifer in January 2002; b) in January 2012; c) long-term piezometric time series.



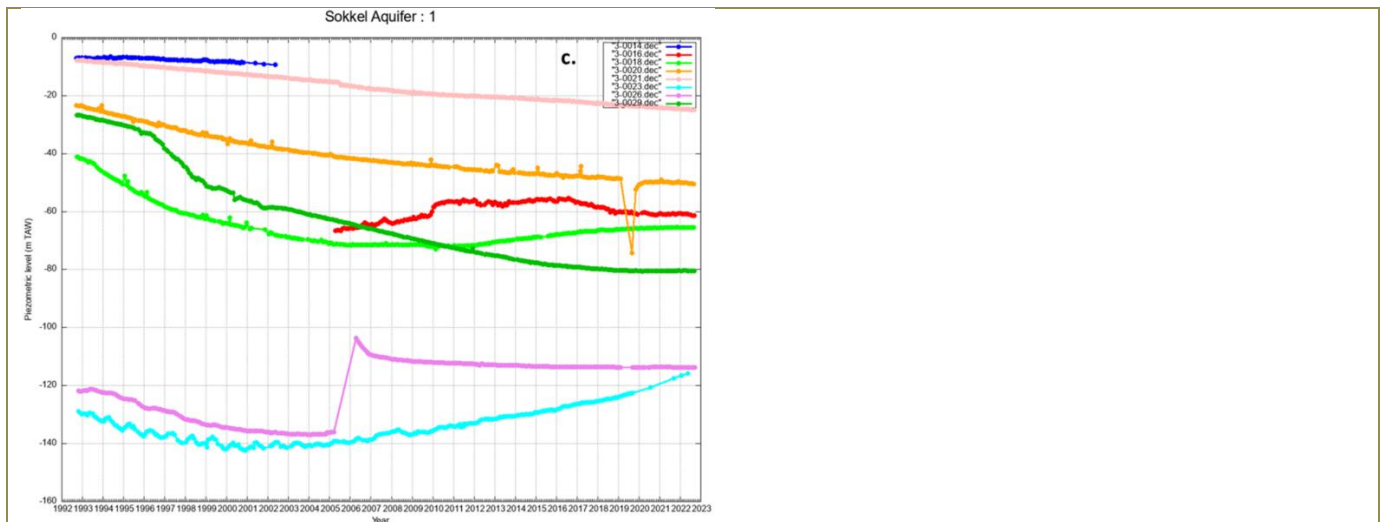


Figure 8. Observed hydraulic heads in the Brabant Massif (Paleozoic basement aquifer) in January 2002 (a) and January 2012 (b), and examples of long piezometric time series (c). The hatching shows the Carboniferous aquifer.

An extensive monitoring network has been set up for the Brabant Massif, as part of the Paleozoic Basement (Figure 8a). Some examples of long-time series have been represented in Figure 8c. They show decreasing groundwater levels with time. However, some monitoring wells start showing a recovery, starting in around 2006. That is due to the new government policy of restricting pumping from the aquifer (the target is 75% reduction). This has caused a rise in the center of the depression cone, while, at its periphery, water levels continue to decrease, due to the lateral flow of water towards the center of the cone. A rise of about 1 m/year has been observed in the center of the large depression cone in the Brabant Massif in the last 15 years. The hatched area in Figure 8a, b and Figure 9a indicates the region where the Carboniferous Aquifer is overlying the Brabant Massif. In Figure 9a, the location of the monitoring wells in the Carboniferous Aquifer is represented, and in Figure 9b, the time series for the piezometers in the Carboniferous Aquifer have been shown.

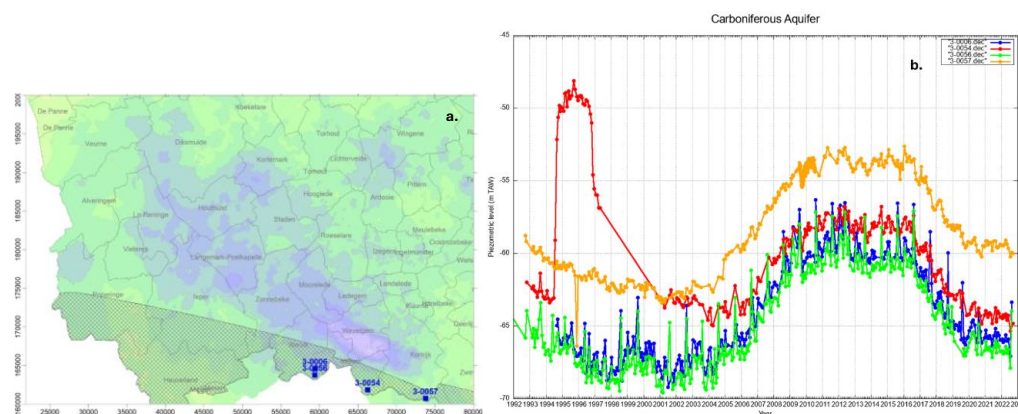


Figure 9. Monitoring network (VMM) for Carboniferous Aquifer (part of Paleozoic Basement Aquifer) (a) and piezometric time series (b).

The hydraulic head in the Carboniferous Aquifer is strongly affected by groundwater exploitation, predominantly in France. The occurrence of the aquifer being outside the area of InSAR deduced strong compaction, it cannot be responsible for the phenomenon.

Maps with the calculated drawdowns in the Paleozoic basement aquifer and the Landenian aquifer in the year 2000, when water levels were at their lowest, are presented in Figures 10a and b. It should be noticed on the maps that the centers of the depression cones in the heavily pumped Paleozoic and Landenian aquifers are not on the same place. The Paleozoic aquifer was mainly used by industry while the Landenian aquifer was tapped by agriculture. The latter depression cone is located more to the west.

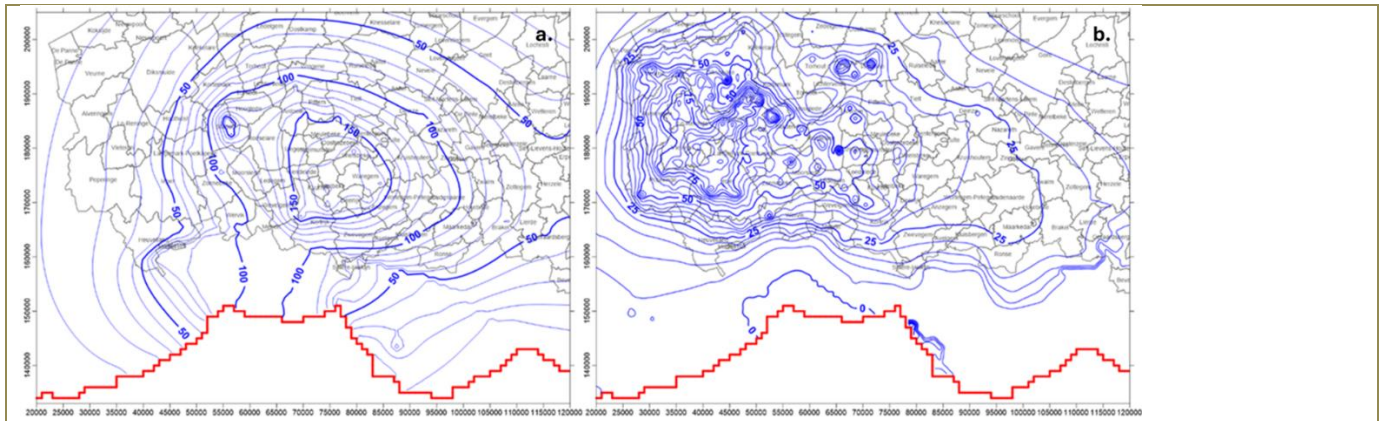


Figure 10. a) Calculated drawdowns in the depression cone in the Paleozoic basement aquifer in the year 2000, and b) Calculated drawdowns in the depression cone in the Landenian aquifer in the year 2000.

3.2. Calculation of compaction of aquifers based on the DAS MODFLOW model

The simulated drawdown with the MODFLOW model of the DAS in the Landenian Aquifer is shown in Figure 11a. The calculated subsidence with the SUB module of the MODFLOW model, accounting for an average thickness for the Landenian Aquifer of 43.4 m based on the 3D Geological model G3DV3.1 and a specific elastic storage coefficient $S_a = 10^{-5} \text{ m}^{-1}$, is represented in Figure 12a.

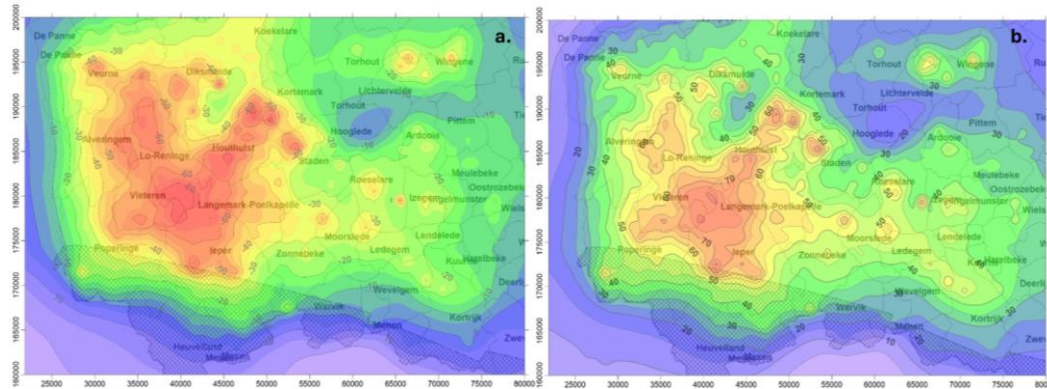


Figure 11. MODFLOW model of the DAS: simulated piezometric levels (in m) in Landenian Aquifer in 2000 (a); simulated drawdown (in m) Landenian Aquifer in 2000 (b).

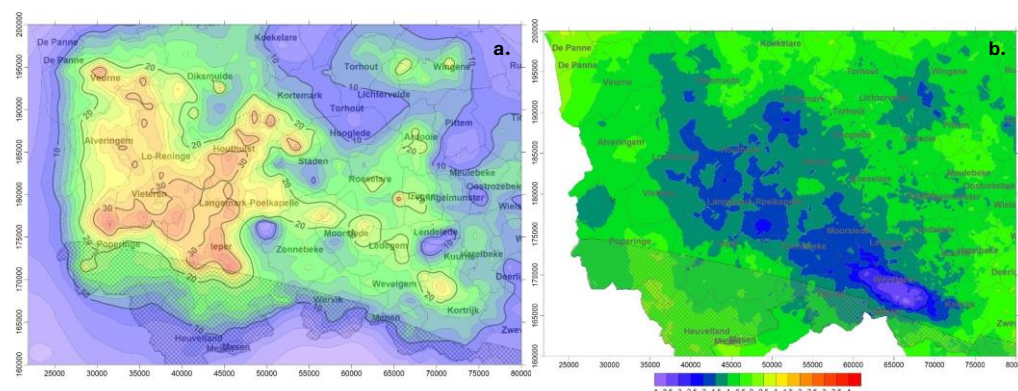


Figure 12. Simulated compaction (in mm) of Landenian Aquifer in 2000 (a); subsidence calculated from ERS images in the years 1992-2001 (mm/year) (b).

Simulated compaction of the Landenian aquifer using the DAS model well captures the subsidence of the central parts of the study area (leper to Langemark-Poelkapelle), exhibiting both high compaction (up to 40 mm) (Figure 12a) and high subsidence (Figure 12b), indicating a strong correlation between the two. This suggests that the model's predictions align well with observed ground subsidence in these regions. In contrast, the southeastern areas show discrepancies between compaction and subsidence. For example, the compaction around the Wevelgem area is moderate (20-30 mm), however, significant subsidence (light blue areas) by the ERS shows that this region experiences more substantial

ground surface subsidence than what the simulated compaction alone might suggest. These regions may require further investigation to understand the underlying causes of the observed subsidence, as it could be influenced by factors not fully captured by the compaction model.

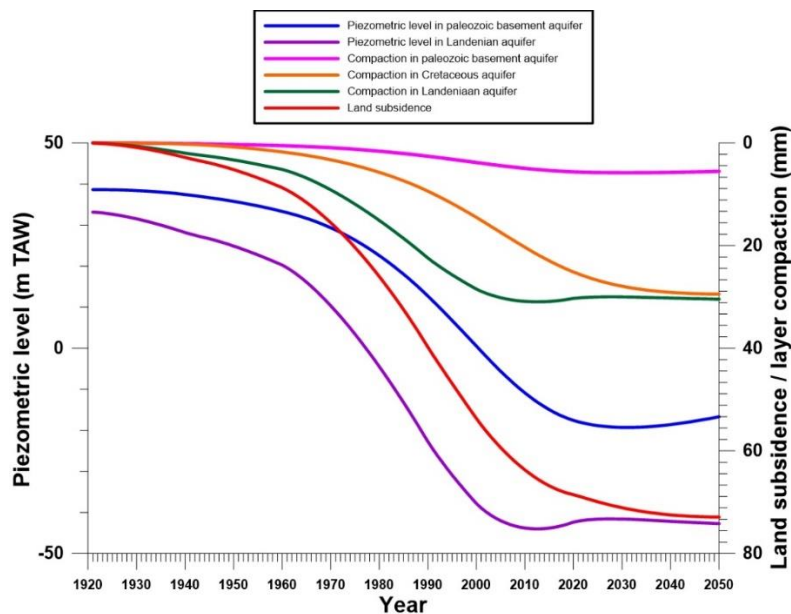


Figure 13. Evolution of the simulated piezometric levels, compaction and land subsidence in the DAS aquifers, in the center of depression cone of the Landenian aquifer.

Simulated piezometric levels, compaction, and land subsidence in the center of the depression cone of the Landenian aquifer are presented in Figure 13.

The simulated piezometric level in the Paleozoic basement aquifer remains relatively stable from 1920-1940, indicating low extraction rates. It is the period with minimal compaction, correlating with the stable or slowly declining piezometric levels. From 1940-1960, a gradual piezometric decline began, suggesting that higher extraction rates were starting. The steeper decline was from about 1960 to 1990, probably due to the 1950s industrial boom and increased groundwater use. Generally, compaction in the Paleozoic basement aquifer is relatively small compared to the compaction in the Cretaceous and Landenian aquifers. This is because compaction in fractured aquifers is low as the rock matrix is almost incompressible compared to unconsolidated formations (Fitts, 2013). Compaction begins to increase more significantly, which aligns with the steeper drop in piezometric levels, indicating that the removal of water from the aquifer is causing the layers to compress. From 1990-2050, the rate of decline slows down slightly but continues, indicating ongoing stress on the aquifer. In this period, compaction continues but at a slower rate, in response to the reduced groundwater withdrawal, leading to a stabilization in the compaction rate.

Like the Paleozoic, the piezometric levels in the Landenian aquifer from 1920-1950 are relatively stable, and from about 1950-1980, a sharp decline starts to reach extremely steep from 1980-2000, probably showing that the aquifer is under severe stress and might be approaching critical levels. The Landenian aquifer shows the most significant compaction, reflecting high groundwater extraction rates and higher compressibility compared to the hard rock aquifer. From 1920-1980, compaction in the Landenian aquifer remained low, even as the piezometric level started to drop significantly. From 1980-2000, a noticeable increase in compaction occurred, correlating with the period of rapid piezometric decline. From 2000-2050, the decline continues but at a slightly reduced pace, suggesting that extraction has moderated. During this period, the compaction rate stabilizes, similar to the other aquifers, in response to reduced exploitation, reducing the stress on the aquifer. The Cretaceous aquifer shows notable compaction, starting later than the Paleozoic and Landenian aquifers, indicating delayed effects of the groundwater extraction. From 1920-1950, the Cretaceous aquifer also shows minimal compaction during the early years, like the Paleozoic aquifer. On the other hand, from 1950 to 1980, a significant increase in compaction occurred, suggesting that groundwater extraction was affecting this aquifer more seriously during this period. However, from 1980-2050, the compaction rate stabilizes and then gradually decreases, in response to limitation of groundwater extraction, thus reducing further compaction. Fig. 14 shows compaction as a function of aquifer thickness and drawdown.

The land subsidence trend closely follows the compaction trends, particularly that of the Landenian aquifer. Subsidence starts increasing notably around 1950, peaks towards 2000 and begins to stabilize thereafter. The piezometric level declines correlate well with the periods of increased compaction and subsidence, particularly in the Landenian aquifer. The stabilization of piezometric levels and compaction rates after 2000 is a positive indicator of effective groundwater

management practices. From 1920-1950, land subsidence is minimal, reflecting the stability in piezometric levels and the low rate of aquifer compaction during this period. On the other hand, from 1950-1980, a sharp increase in land subsidence began, correlating with the rapid compaction observed in all the aquifers. This suggests that the cumulative effect of aquifer exploitation across different layers is contributing to the sinking of the land surface. From 1980-2000, the subsidence rate continues to increase, reflecting the severe compaction of aquifers, particularly the Landenian and Cretaceous aquifers, during this period. From 2000-2050, the subsidence rate begins to level off, and further compaction is becoming more limited in response to the reduced groundwater exploitation.

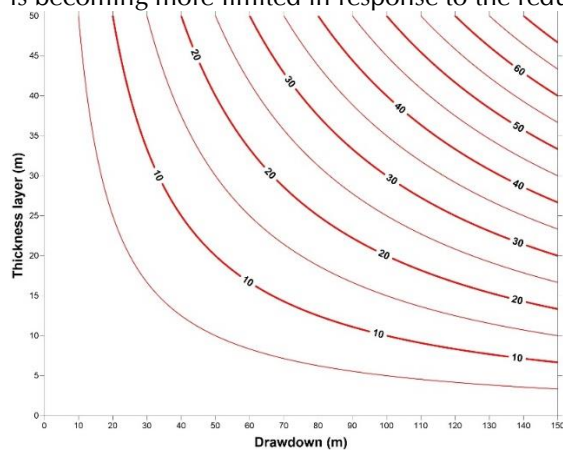


Figure 14. Compaction (in mm) as a function of aquifer thickness (m) and drawdown (m).

The simulated drawdown and compaction of the Cretaceous Aquifer in 2000 are shown in Figure 15. It is to be noted that calculated drawdowns substantially underestimate the observations. This is due to no piezometric observations being available when the model was developed. Therefore, compaction will be underestimated as well.

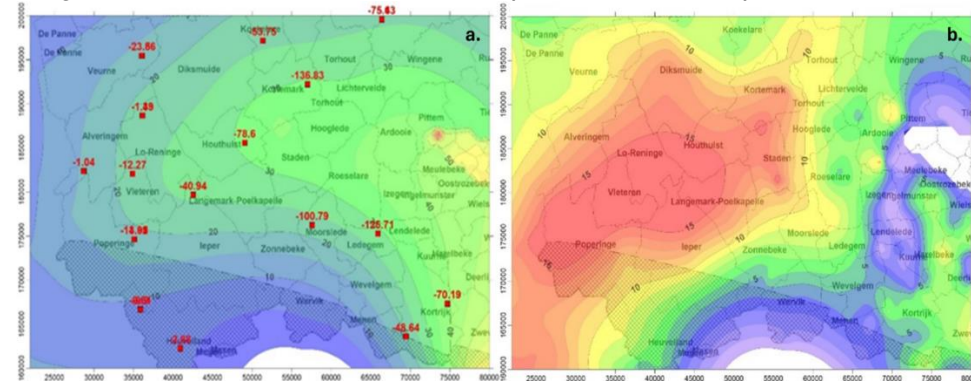


Figure 15. MODFLOW model of the DAS: a) simulated drawdown (in m) in Cretaceous Aquifer in 2000, and b) simulated compaction (in mm) of Cretaceous Aquifer in 2000.

Like the simulated compaction of the Landenian aquifer, the compaction of the Cretaceous aquifer strongly correlates with the subsidence map in the central area (Figure 15b and Figure 12b). Particularly in the areas around Langemark-Poelkapelle and Houthulst, a compaction rate of about 15-20 mm corresponds with a subsidence rate of about -2.5 to -4 mm per year. This shows that the compaction of the Cretaceous aquifer also plays a role in the subsidence bowl observed in this part of the study area. However, the compaction in the southeast (e.g. Wevelgem area) is moderate to low (about 5-10 mm) contrary to the high subsidence observed by the ERS map. This shows that the compaction of both Landenian and Cretaceous aquifers in the southeast area was not the main cause of the subsidence bowl observed there.

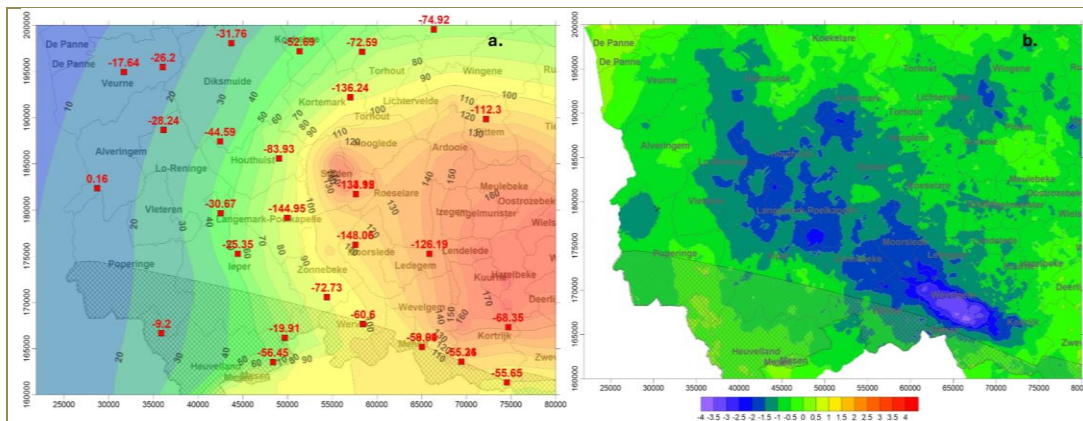


Figure 16. a) simulated drawdown (in m) in Paleozoic Basement Aquifer in 2000 with piezometric observations, and b) subsidence calculated from ERS images in the years 1992-2001 (mm/year).

The simulated drawdown map of the Paleozoic basement aquifer in 2000 (Figure 16a) shows a significant depression in the groundwater levels centered around the eastern part of the map, particularly near Kortemark, Roeselare, and Izegem, with values reaching as low as -148.06 m. The subsidence map (Figure 16b) highlights significant subsidence primarily in the central and southwestern areas, particularly around Wevelgem and the surrounding regions, with subsidence rates reaching -2.5 to -4 mm/year. Notably, this area does not correspond directly to the area of maximum drawdown (Figure 16a). The drawdown map's area of most significant groundwater depression is located more to the east, while the highest subsidence rates detected by the ERS images are situated more towards the southeastern, particularly around Wevelgem. This geographical mismatch suggests that the subsidence observed in the southwestern region is not directly related to the drawdown of the Paleozoic Aquifer. This implies that other factors, possibly related to surface activities, different geological conditions, or other aquifers/aquitards, are contributing to the observed subsidence in those areas.

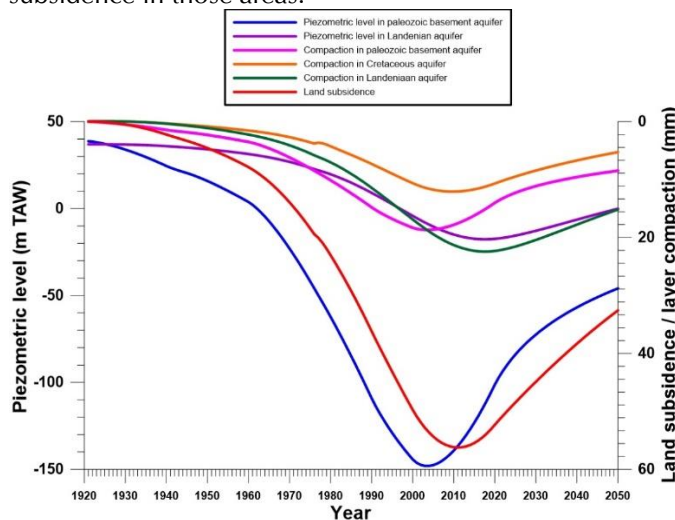


Figure 17. Evolution of the simulated piezometric levels and compaction in all aquifers of the DAS, and land subsidence, in the center of the depression cone in the Paleozoic Basement aquifer.

The simulated drawdowns of the year 2000 (Figure 16a) are not matched with subsidence calculated from the ERS image of 1992 to 2001 (Figure 12b). The center of the depression is located more to the east than the region with a high simulated subsidence rate. The subsidence pattern is not correlated with the exploitation of the Paleozoic aquifer. While the high drawdowns are about double for the Brabant Massif, compared to the Landenian Aquifer, the greatest compaction is only about half. This is due to the low compressibility of the consolidated rocks of the Brabant Massif, compared to the unconsolidated sediments of the Landenian.

The piezometric level in the depression cone of the Paleozoic basement aquifer (Figure 10a) shows a significant decline from 1920 to around 2000, indicating substantial groundwater extraction in the Paleozoic Basement aquifer (Figure 17). The decline starts to stabilize and recover after 2005, reflecting reduced extraction rates.

The piezometric level in the Landenian aquifer shows a similar declining trend, with a more pronounced drop starting around the 1950s due to increased groundwater use during the industrial boom. After 2000, the decline slows and begins to recover, due to reduced extraction. Compaction in the Paleozoic basement is significant, especially from the

mid-20th century onward. The rate of compaction stabilizes slightly after 2005. Compaction in the Cretaceous aquifer is notable and starts later than in the Paleozoic basement aquifer, indicating delayed impacts from groundwater extraction. This compaction also stabilizes after 2010. The Landenian aquifer shows substantial compaction, aligning with significant piezometric level drops. Compaction stabilizes after 2010, following the trend of piezometric levels. Land subsidence closely follows the compaction trends, particularly in the Landenian aquifer. Subsidence rates increase significantly around the mid-20th century, peak towards 2000, and then stabilize after 2010.

In conclusion, the comparison of the simulated drawdown and compaction rates of the three aquifer systems show a significant geographic mismatch with the southeastern subsidence bowl. This lack of direct correlation suggests that factors other than the drawdown in the Paleozoic Aquifer are driving the subsidence observed in this area. On the other hand, the subsidence in the central area corresponds to the compaction by the Landenian, and by the Cretaceous aquifers.

3.3. Compaction of Ypresian aquitard by simulations with 1D compaction/subsidence model

The sensitivity of compaction of the Ypresian aquitard on kv and elastic/inelastic storage was tested with a 1D compaction/subsidence model. This model was based on Well 3-0521b, located to the west of Langemark-Poelkapelle (Figure 5a). The evolution of the hydraulic head in this well is given in Figure 18b. The thickness of the model layers: ground surface is at 7.5 m TAW; thickness of Quaternary is 5.4 m (layer base at 2.1 m TAW); thickness Ypresian aquitard is 105.3 m (base at -103.2 m TAW); thickness Landenian aquifer is 43.6 m (base -146.8 m TAW); thickness Cretaceous 70.5 m (base is -217.3 m TAW); and Paleozoic basement at -217.5 m TAW.

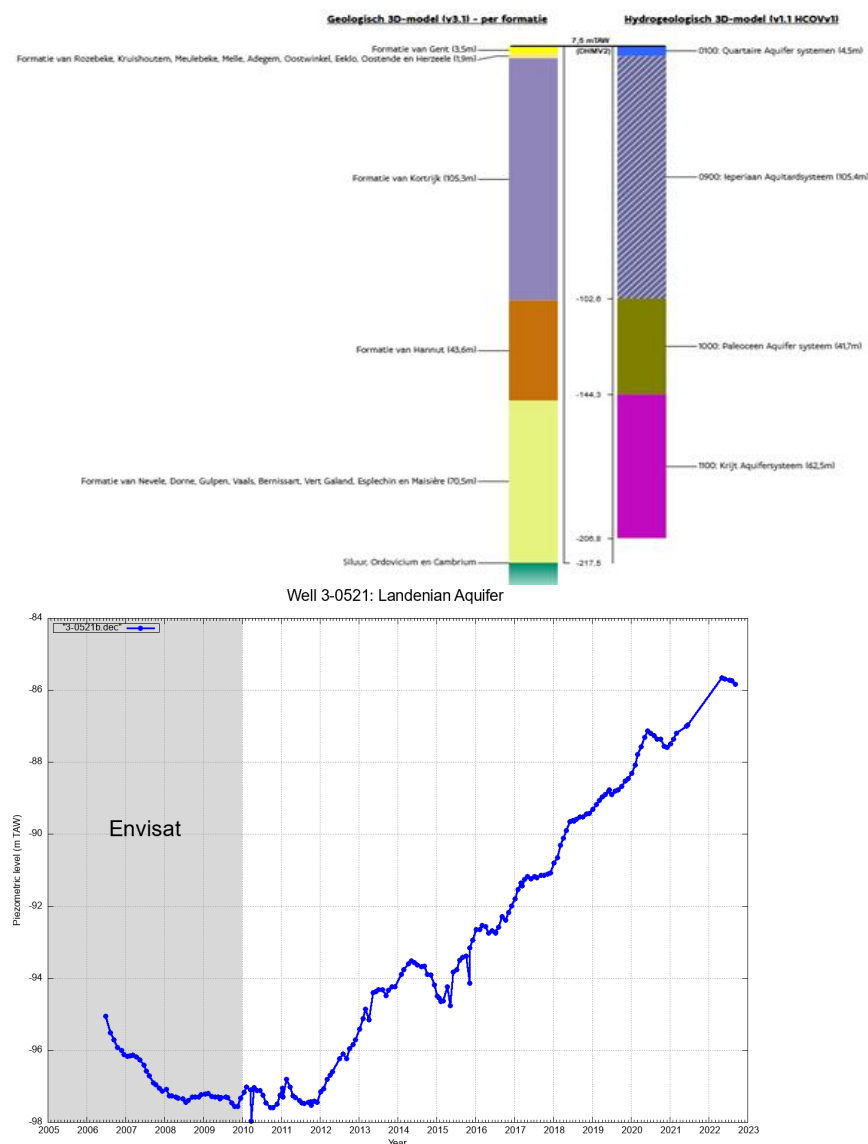


Figure 18. Well 3-0521b (primary network of VMM) in the Landenian Aquifer: a) geological and hydrogeological structure, and b) evolution of hydraulic head.

The graph (Figure 18) illustrates the piezometric level in the Landenian Aquifer as measured at Well 3-0521 from 2005 to 2023. The data also include the period when Envisat satellite observations were available (shaded area). The piezometric level in the Landenian Aquifer shows a consistent decline of about 3 m during the period of 2005-2011 down to almost -98 m TAW. Around 2011-2012, the decline in piezometric levels stabilized and began to show a slight upward trend. This period marks the end of the Envisat observation period and the beginning of a recovery phase. From 2012 onwards, there is a noticeable and consistent rise in the piezometric levels. By 2023, the piezometric level has risen to approximately -86 m TAW (about 12 m rise). This recovery phase suggests effective groundwater management practices, with reduced extraction rates.

Compaction calculation scenarios

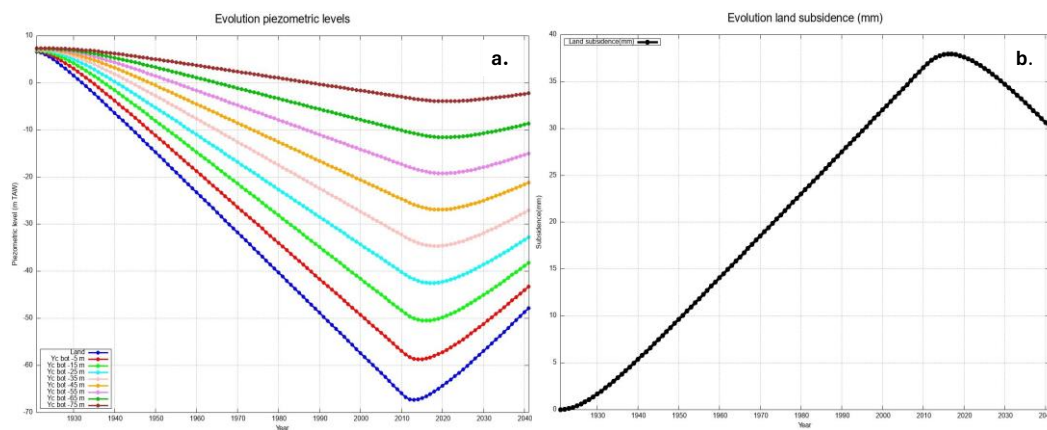
Model parameters for the different compaction calculation scenarios are presented (Table 1). The storage coefficient (S_a) for Ypresian clay at Well 3-0521b is calculated by using Equation 2 using the depth values of the Ypresian clay mentioned above. For the vertical hydraulic conductivity values, values of 10⁻⁵ m/d and 10⁻⁶ m/d are considered in the scenario.

Figures 19 & 20 present the piezometric levels in the Landenian Aquifer and different layers of the Ypresian clay under scenarios with varying vertical hydraulic conductivity (k_v) values. The scenarios explore the effects of both elastic and inelastic storage types on compaction and subsidence.

Scenario	k_v Ypresian (m/d)	S_a Ypresian	storage type
A	10 ⁻⁵	10 ⁻⁵	100% elastic
B	10 ⁻⁶	10 ⁻⁵	100% elastic
C	10 ⁻⁵	10 ⁻⁵	100% inelastic
D	10 ⁻⁶	10 ⁻⁵	100% inelastic
E	10 ⁻⁵	10 ⁻⁵	50% elastic
F	10 ⁻⁶	10 ⁻⁵	50% elastic

Table 2. Values of hydraulic conductivities, specific storage and storage types for the different scenarios.

Compaction in the 10 layers of the Ypresian clay is calculated, and the results are summed to provide the subsidence of the ground surface due to the compaction of the clay. Figure 19 shows the results for scenarios A, C, and E, with $k_v = 10^{-5}$ m/d and thus, hydraulic resistance $c = 100000$ d/m.



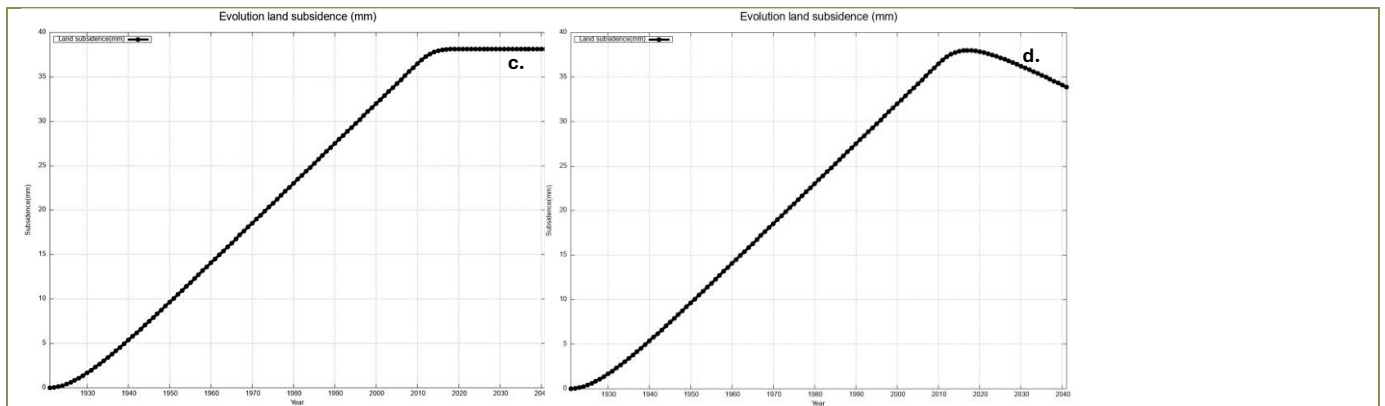


Figure 19. Evolution of piezometric levels in the Landenian Aquifer and the different layers of the Ypresian clay for $k_v = 10^{-5}$ m/d for the clay (a); land subsidence caused by compaction of the clay for $k_v = 10^{-5}$ m/d and $S_a = 10^{-5}$ m⁻¹ for 100% elastic (b), 100% inelastic (c) and 50% elastic (d) storage type.

The piezometric levels show a significant decline initially due to intense groundwater extraction (Figure 19a). Over time, there is a recovery phase where piezometric levels rise, indicating a reduction in extraction. The recovery is relatively quicker due to the higher vertical hydraulic conductivity, allowing faster water movement through the clay layers.

The K_v is equal to 10^{-5} m/d and the 100% elastic storage scenario shows moderate subsidence as the clay layers can recover elastically when the stress (water extraction) is removed (Figure 19b). On the other hand, more significant subsidence is observed in a 100% inelastic storage scenario (Figure 19c). This is because inelastic compaction is permanent and does not recover when the stress is removed. Intermediate subsidence values have been observed in the 50% of elastic scenarios, reflecting partial recovery and partial permanent compaction (Figure 19d).

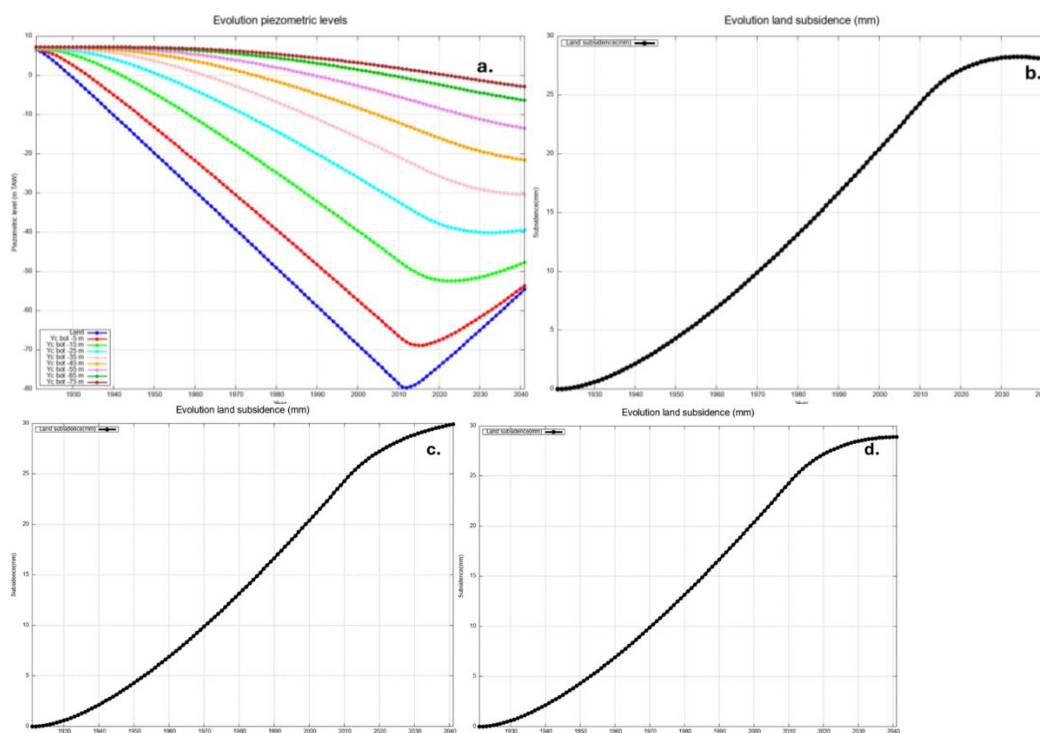


Figure 20. Evolution of piezometric levels in the Landenian Aquifer and the different layers of the Ypresian clay for $k_v = 10^{-6}$ m/d for the clay (a); land subsidence caused by compaction of the clay for $k_v = 10^{-6}$ m/d and $S_a = 10^{-5}$ m⁻¹ for 100% elastic (b), 100% inelastic (c) and 50% elastic (d) storage type.

With a scenario of K_v equal to 10^{-6} m/d and 100% elastic storage, the piezometric levels show a slower decline and recovery compared to the higher k_v scenario (Figure 20a). The low vertical hydraulic conductivity restricts water movement, causing delayed and prolonged effects on the piezometric levels.

With 100% elastic storage, slower and less severe subsidence are simulated as the clay layers can still recover elastically

(Figure 13b). The process is slower due to lower k_v . On the other hand, in the 100% inelastic storage, significant and sustained subsidence was simulated as the compaction is permanent and the low k_v value prolongs the impact. With 50% elastic storage, intermediate subsidence results with the first case are obtained, but the recovery is much slower due to the lower vertical hydraulic conductivity. For the same magnitude of changes in effective stress, inelastic compaction of fine-grained sediments can be one to two orders of magnitude larger than elastic compaction (Riley, 1969, 1998).

It is noted that for low k_v values (e.g. 10-6 m/d, Figure 20), compaction can continue even when groundwater levels in the Landenian are rising again or have stabilized.

Higher k_v (10-5 m/d) allows quicker adjustments in piezometric levels and faster recovery of subsidence effects, whereas lower k_v (10-6 m/d) results in prolonged impacts due to restricted water movement. Elastic storage types allow for recovery of subsidence when groundwater levels rise again, while inelastic storage leads to permanent compaction, causing lasting land subsidence.

A mixed storage type (50% elastic, 50% inelastic) shows that even partial inelastic behavior can result in significant subsidence. The graph underscores that subsidence can continue even when groundwater levels are rising, especially in low k_v scenarios. This indicates the importance of long-term monitoring and management to mitigate lasting subsidence impacts. Effective groundwater management should consider both the type of storage (elastic/inelastic) and the hydraulic conductivity of the layers to predict and mitigate subsidence accurately.

The 1D model shows that, given the exploitation history of the DAS, the maximal calculated subsidence due to compaction of the Ypresian clay in the center of the depression cone of the Landenian aquifer, for $k_v = 10^{-5}$ m/d for the clay, is about 38 mm. This has to be added to the maximal subsidence calculated with the 3D model for the compaction of the DAS aquifers, which is about 73 mm, in the center of the depression cone of the Landenian Aquifer. This shows that both components contribute appreciable contributions, and together result in a land subsidence of about 11 cm. Yet, this remains small compared to the InSAR subsidence of around 2 mm/year for this area, and considering that the subsidence must have occurred over a period of an estimated 50 years.

Reducing extraction rates is essential to prevent prolonged subsidence, especially in areas with low vertical hydraulic conductivity.

In summary, this study provides critical insights into the dynamics of groundwater extraction and land subsidence, highlighting the need for careful consideration of geological properties and storage types in groundwater management strategies to mitigate long-term subsidence effects.

Conclusions

The intensive exploitation of the Landenian, Cretaceous, and Paleozoic aquifers since the 1960s has led to substantial declines in piezometric levels, with drops exceeding 100 meters in some areas. The economic boom of the 1960s significantly increased groundwater extraction, further lowering the piezometric levels and contributing to the development of extensive regional depression cones.

The drawdown of piezometric levels has caused compaction of the aquifer layers, resulting in regional land subsidence. The combined effect of compaction in all affected layers has led to significant subsidence on a regional scale. The compaction of the Ypresian aquitard by pumping from the underlying Landenian aquifer has also been impactful. The study shows that compaction can continue even when groundwater levels begin to recover or stabilize, especially in scenarios with low vertical hydraulic conductivity (k_v).

The high subsidence rates derived from InSAR data for the period 1992-2001 and 2003-2010 show a consistent spatial pattern, with the highest subsidence rates observed in a NW-SE oriented zone in SW Flanders. The high subsidence rates in the NW part of the region correlate well with the intense groundwater exploitation in the Landenian aquifer, as supported by piezometric time series and the groundwater flow model. However, the high subsidence rates in the SE zone do not correlate with the Landenian aquifer exploitation. This discrepancy may be due to an underestimation of the extension of the Landenian depression cone or unaccounted local groundwater exploitations, although this seems unlikely, as there are no such indications from the piezometric observations in the aquifer.

The groundwater flow model for the DAS does not accurately reproduce the piezometric depression cone in the Cretaceous aquifer, likely due to gaps in the pumping rate data used in the model. The lack of spatial correlation with the deep regional piezometric depression cone in the Paleozoic basement aquifer suggests that the rigid rocks in the basement have low elasticity and thus limited compaction.

Target site 2: The Tertiary Aquifer System (TAS) under the central part of Flanders (i.e. the Merchtem area) - (Deliverables: D.2.1./D.2.1.2./D.4.4./D.4.4.2.)

Introduction

In the central part of Flanders, the Tertiary deposits form an important aquifer system that has been used for a long time in different industrial sections, including beer breweries. Locally, land subsidence could probably be related to the exploitation of some of the aquifers. In this region, a long tradition of beer breweries that capture their water from the

Ledo-Paniselian and Ypresian aquifers exist. Some of them are well-known and popular, like Palm, with its brewery in Steenhuffel. This study investigates if the brewery exploitations could have caused these subsidence trends.

According to Declercq et al. (2017), in a region NW of Brussels InSAR measurements indicate land subsidence trends. In this region, the Tertiary sand layers of the Ledo-Paniselian and Ypresian aquifer systems are the main productive aquifers and have been used for a long time, e.g. by local breweries which have a centuries old tradition. To investigate the relation between groundwater exploitation and land subsidence, a groundwater flow model coupled to a compaction module that calculates layer compaction can give a good insight and quantitative relations. As a result, a transient, multi-layered, 3D MODFLOW groundwater flow model has been used to estimate the compaction and the subsidence of the different lithological layers and the ground surface, respectively, in the Merchtem area.

Methodology

To investigate the relation between groundwater exploitation and land subsidence, a groundwater flow model was developed and coupled to a module that calculates layer compaction.

A transient, 3D multilayered MODFLOW model, considering all the lithological layers (both aquifer and confining layers) has been applied, so that compaction, and then the subsidence of the ground is depicted. With the implemented model, simulations were done with the licensed pumping rates in the Ledo-Paniselian and Ypresian aquifers. Only one intensive exploitation exists with a pumping rate of half a million m³/year (a brewery), most other exploitations are much smaller.

Hydrogeology, boundary condition and spatial discretization

Using the 3D geological model of Flanders, available through the DOV web portal, the whole geological and hydrogeological buildup above the Ypresian clay are included in the model (figure 21). The Ypresian clay itself, a very thick compact clay unit, can be considered here as the substratum in the groundwater system. The Tertiary layers are dipping to the northeast and groundwater flow was originally, in the predevelopment state, also to the northeast. Large-scale exploitation of the Ledo-Paniselian aquifer north of the modelled region has created a regional scale depression cone and caused a northward hydraulic gradient in this layer.

In the model appropriate boundary conditions at the north side were derived from observed water level series. Local exploitations were added.

Using the 3D geological model of Flanders, available through the DOV web portal, the whole geological and hydrogeological buildup above the Ypresian clay is included in the model (see figure 5). The Ypresian clay itself, a very thick compact clay unit, can be considered here as the substratum in the groundwater system. The tertiary layers are dipping to the northeast and groundwater flow was originally in the predevelopment state, also to the northeast. Large scale exploitation of the Ledo-Paniselian aquifer north of the modelled region has created a regional scale depression cone and caused a northward hydraulic gradient in this layer. In the model appropriate boundary conditions at the north side were derived from observed water level series. Local exploitations were added.

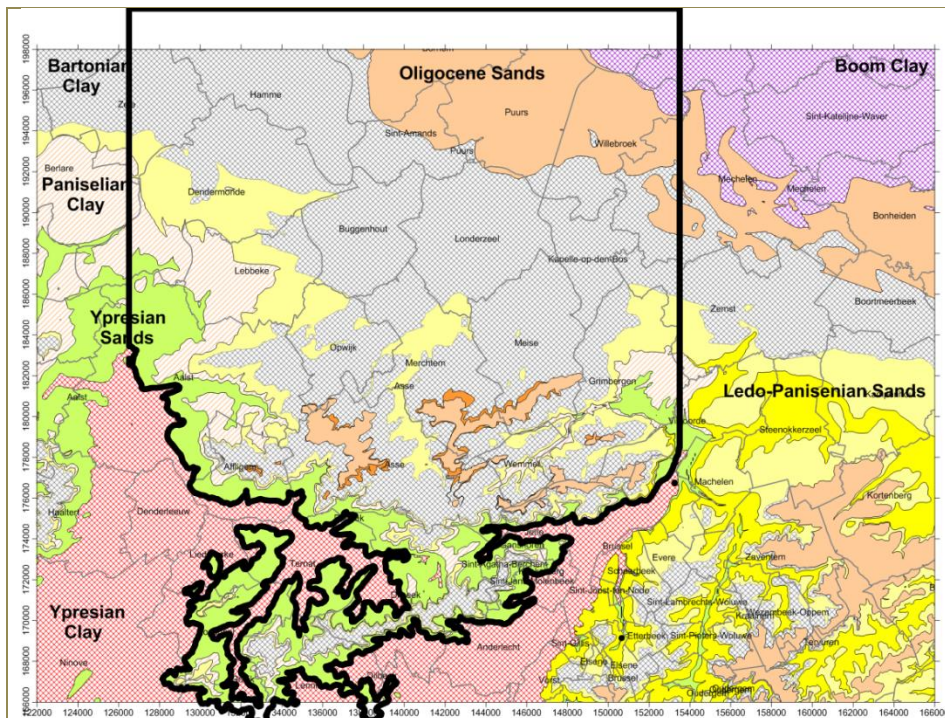


Figure 21. Geological map and model borders of Merchtem region.

South border = southern limit of Ypresian aquifer (HCOV 0800)
 West/east borders = at northward outcrops of Ypresian clay
 North border = arbitrary at Y = 200000

The exploitation is compiled as follows: Brewery Martinus Ginder-Ale, which operated from 1871 to 1991, was in the center of Merchtem but has since ceased operations. Brewery De Block, established in 1887 in Peizegem, currently does not hold a license as of 2021. From 1991 to 2011, however, it had a license permitting 7,500 m³ of water extraction per year. Brewery Bosteels, founded in 1791 in Buggenhout, is licensed for 29,500 m³ per year and sources its water from the Ledo-Paniselian Aquifer via two wells drilled to a depth of 37 m. Finally, Brewery Palm, dating back to 1686 and based in Steenhuffel, has had several extraction licenses: 475,000 m³ per year from 1990 to 1998, 500,000 m³ per year from 1998 to 2011, and the same volume from 2011 to 2031. Palm operates 21 wells (locations not specified) that tap into the Ledo-Paniselian Aquifer. Thus, it is possible to consider only this intensive exploitation which has a pumping rate of half a million m³/year, most of the above other exploitations are much smaller.

Finally, the MODFLOW SUBSIDENCE package is applied to calculate compaction within each layer that results from the induced drawdown. This computation includes all changes in layers' thickness, which collectively determine the overall land subsidence at the surface. In other words, the land subsidence at the surface is the cumulative subsidence that considers the sum of layer-by-layer compaction from top to bottom.

Model results

Groundwater flow and piezometric levels

With this model configuration, the recent evolution of piezometry was simulated. The model uses monthly time steps, so it can reproduce seasonal fluctuations. The propagation of the seasonal cycle can also be used as a calibration target, as the cycle has been identified in many observation wells. From this model run, it was seen that, with the estimated hydraulic parameterization, the equilibration time required to obtain a near-steady state flow situation is not too long, no more than a few years for large groundwater extractions. The simulated piezometric levels both in the Ledo-Paniselian and Ypresian aquifers are presented in Figures 22a and b, respectively.

Using the licensed pumping rates (true pumping rates are not available for the public), the drawdowns around the exploitations were simulated. Maps of the drawdowns after 10 years of pumping show that these are rather limited, e.g. maximum of 3 m in the Ypresian aquifer (Figure 22a) and a maximum of 2 m in the Ledo-Paniselian aquifer (Figure 22b).

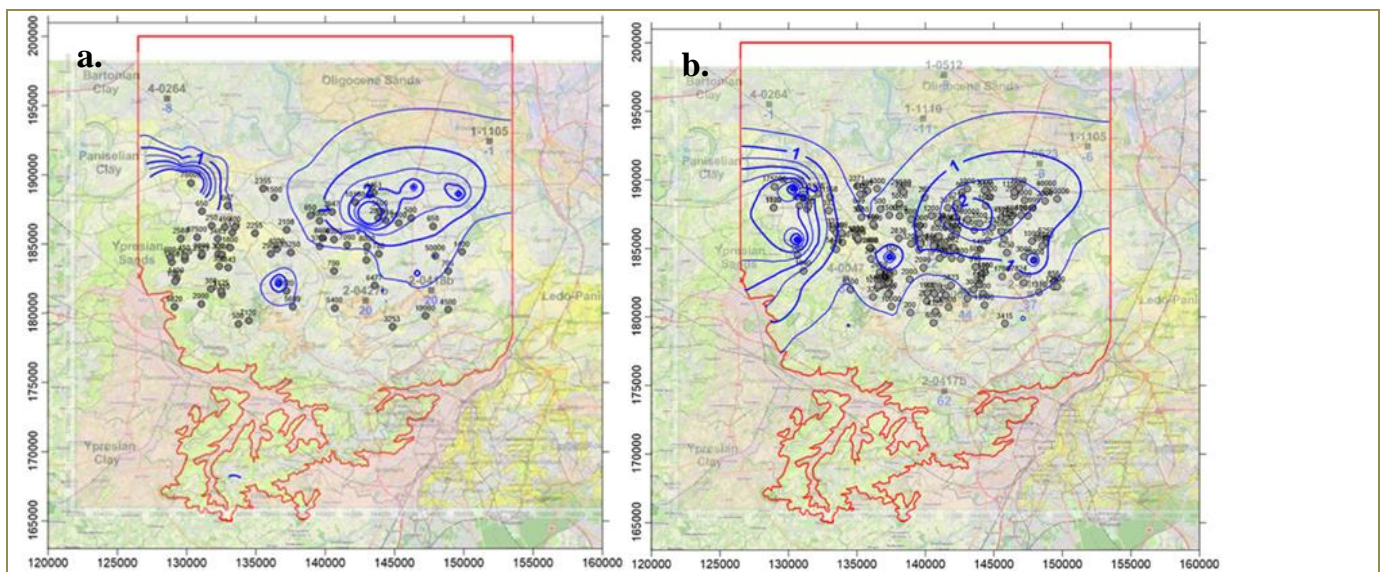


Figure 22. a) calculated drawdowns in Ypresian aquifer after 10 years of pumping, b) calculated drawdowns in Ledo-Paniselian aquifer after 10 years of pumping.

Layer compaction and land subsidence

The flow model is extended with the MODFLOW IBS (“Interbed Storage”) module that allows calculation of layer compression and compaction due to elastic storage, by the presence of compressible thin layers inside the aquifers. In the future the IBS module can be replaced by the SUB (“Subsidence”) module to allow more flexibility. The IBS module produces the compaction in the different layers and total subsidence at the land surface. With initial estimates of the hydraulic and elastic parameters, preliminary results for subsidence rates were already obtained. The model will be further adapted, and model results will be compared with the interpretation of InSAR data.

With the implemented model, as described, simulations were done with the licensed pumping rates in the Ledo-Paniselian and Ypresian aquifers. Only one intensive exploitation exists with a pumping rate of half a million $m^3/year$ (a brewery), most other exploitations are much smaller. The calculated drawdowns are therefore rather limited and cannot cause large compaction in the pumped layers and land subsidence is therefore limited to a range of only 1 mm (fig 2). As the Modflow simulations and results of the SUB module show, observed trends in land subsidence must have another origin.

Layer compaction and land subsidence

The flow model was extended with the MODFLOW SUBSIDENCE module (SUB package) that allows the calculation of layer compaction and land subsidence.

The model calculates a layer compaction of about 0.2 mm in the Ypresian Aquifer (Figure 23a) and 0.5 mm in the Ledo-Paniselian Aquifer (Figure 23b), yielding a cumulative land subsidence of less than 1 mm at the surface (Figure 23c).

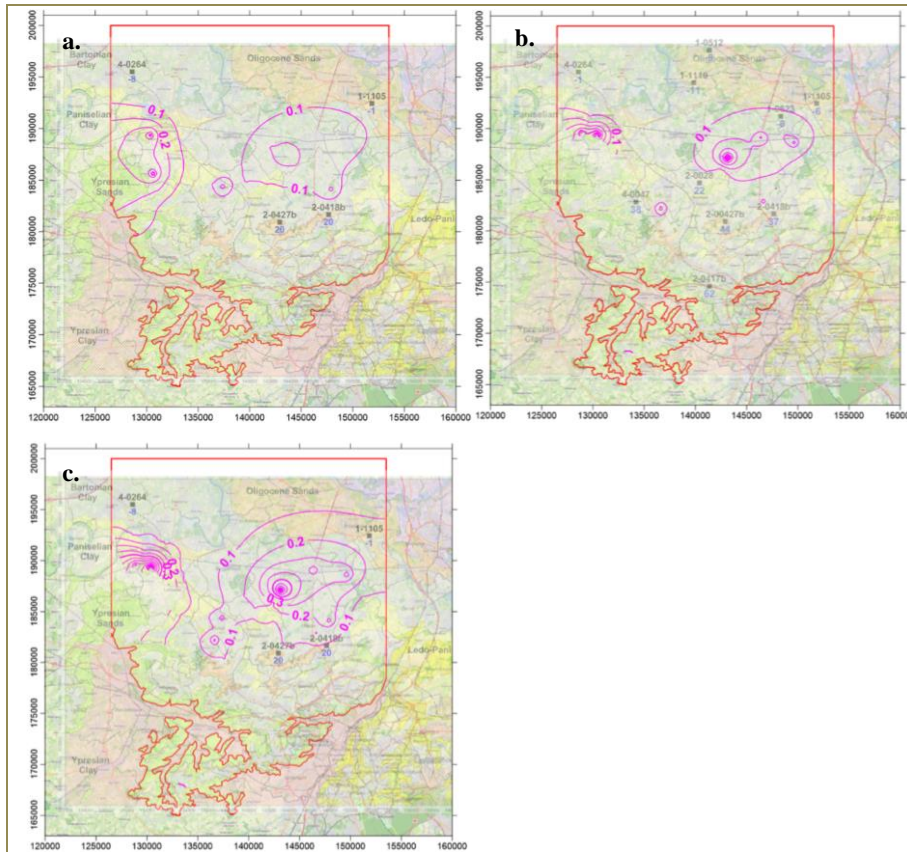


Figure 23. a) calculated layer compaction (in mm) after 10 years of pumping with a specific storage value of $10^{-5}/m$ a) for the Ypresian aquifer, b) for the Ledo-Paniselian aquifer. c) calculated land subsidence (mm) after 10 years of pumping.

However, the INSAR data in the region around Merchtem show a subsidence rate of about 1 mm/year to 4 mm/year in localized zones (Figure 24). Comparing the model results (under 1 mm total over 10 years) to satellite observations (1 mm/year to 4 mm/year) suggests that groundwater extraction is not likely the major driver of this surface subsidence.

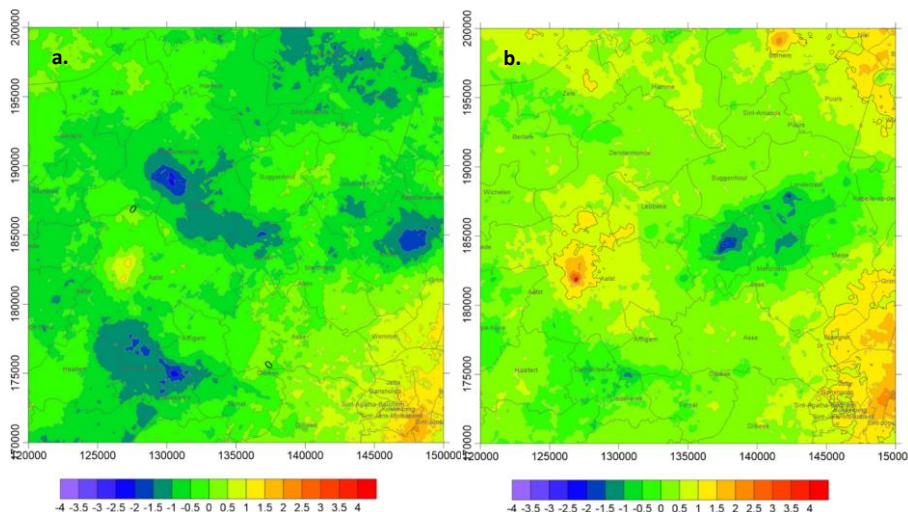


Figure 24. a) Land subsidence trend in the region around Merchtem as derived from the ERS data (1992-2001), and b) land subsidence trend in the region around Merchtem as derived from the ENVISAT data (2003-2010).

Conclusions

After ten years of pumping, the Ypresian and Ledo-Paniselian Aquifers show drawdowns of about 3 m and 2 m, respectively, with total model-predicted subsidence remaining below 1 mm. On the other hand, the InSAR data reveal higher subsidence rates, indicating other factors than groundwater extraction must be involved.

References used for these case study areas

- Boonstra, J., de Ridder, N.A., 1981. Numerical modelling of groundwater basins: A user-oriented manual. ILRI, Wageningen, The Netherlands.
- Bucur, I., Dinu, C., & Popescu, M. (2016). Eocene Deposits of the North Sea Basin: Geology and Paleoenvironments. *Journal of Geology*, 124(5), 537-552.
- Chowdhury, F., Gong, J., Rau, G.C., Timms, W.A., 2022. Multifactor analysis of specific storage estimates and implications for transient groundwater modelling. *Hydrogeology Journal* 2183–2204. <https://doi.org/10.1007/s10040-022-02535-z>
- Dassargues, A., Zhang, J., 1992. Land Subsidence in Shanghai: Hydrogeological Conditions and Subsidence Measurements. *Bulletin of the International Association of Engineering Geology*.
- De Breuck, W., Van Burm, P., Steyaert, M., & Van Camp, M., (1988). *Hydrogeologische studie van de Sokkel en het Landenaan onder het oostelijk gedeelte van Oost-Vlaanderen en het westelijk gedeelte van Vlaams-Brabant - Inventarisering gegevens*. Study for Ministerie van de Vlaamse Gemeenschap. (Report TGO 87/33).
- De Breuck, W., Wattiez, R., De Ceukelaire, M., & Van Burm, P. (1986a). *Hydrogeologische studie van de gespannen watervoerende laag in het massief van Brabant onder West en Oost Vlaanderen*. Study for Gewestelijke Ontwikkelingsmaatschappij West Vlaanderen. (Report TGO 84/15).
- De Breuck, W., Lebbe, L., Van Camp, M., De Ceukelaire, M., & Van Burm, P. (1986b). *Hydrogeologisch mathematisch model van de grondwaterstromingen in de gedeeltelijk afgesloten watervoerende lagen onder West-, Oost-, Zeeuws- en Frans-Vlaanderen*. Study for Ministerie van de Vlaamse Gemeenschap. (Report TGO 86/53).
- Declercq, P.-Y. (2020). A study of long term and slow ground movements in Belgium using Multi-Temporal InSAR satellite data [Doctoral thesis, ULiège - Université de Liège]. ORBi-University of Liège.
- Declercq, P.Y., Choopani, A., Dassargues, A., Devleeschouwer, X., 2021. Areas Prone To Land Subsidence and Their Evolutions in Belgium During the Last 30 Years. *International Geoscience and Remote Sensing Symposium (IGARSS)* 8448–8451. <https://doi.org/10.1109/IGARSS47720.2021.9554738>
- De Paepe, R., Houthuys, R., & Van Ranst, E. (1995). Stratigraphy and Sedimentology of the Ypresian in Belgium. *Geologica Belgica*, 2(1), 5-24.
- De Smedt, F. and Batelaan, O., 2001. The impact of land-use changes on the groundwater in the Grote Nete river basin, Belgium. *Future Groundwater Resources at Risk: Lisbon, Portugal*, pp.151-158. Figueroa-Miranda, S., Tuxpan-Vargas, J., Ramos-Leal, J.A., Hernández-Madrigal, V.M., Villaseñor-Reyes, C.I., 2018. Land subsidence by groundwater over-exploitation from aquifers in tectonic valleys of Central Mexico: A review. *Eng Geol* 246, 91–106. <https://doi.org/10.1016/j.enggeo.2018.09.023>
- Fitts, C.R., 2013. *Groundwater Science* (2nd ed.). Academic Press (Elsevier). Academic Press (Elsevier), Oxford.
- Gogu, R.C. and Dassargues, A., 2000. Sensitivity analysis for the EPIK method of vulnerability assessment in a small karstic aquifer, southern Belgium. *Hydrogeology Journal*, 8, pp.337-345.
- Maréchal, J.C., Dewandel, B. and Subrahmanyam, K., 2004. Use of hydraulic tests at different scales to characterize fracture network properties in the weathered-fractured layer of a hard rock aquifer. *Water resources research*, 40(11).
- Melger, H., 2018. Hydrogeological and hydrochemical study of the Brabant Massif. MSc thesis. Ghent University.
- Van Camp, M. and Walraevens, K., 2009. Recovery scenarios for deep over-exploited aquifers with limited recharge: methodology and application to an aquifer in Belgium. *Environmental Geology*, 56, pp.1505-1516.
- Van Houtte, E., Van Camp, M., & Verheyen, A. (2017). Groundwater Management in the Context of Aquifer Vulnerability: The Role of the Ypresian Clay. *Journal of Hydrology*, 547, 97-110.
- Walraevens, K., & Van Camp, M., (2004). *Grondwatermodellering voor Landenaan, Krijt en Sokkel. Uitbouwen van beheersinstrument: Sokkelmodel: Simuleren van een predictieve scenario's*. Study for AMINAL, Afdeling Water. (Report TGO 02/01).
- Walraevens, K., Van Camp, M., & Martens, K., (2000). *Grondwatermodellering voor Landenaan, Krijt en Sokkel: uitbouwen van beheersinstrument (PBO 97/32/119)*. Study for Ministerie van de Vlaamse Gemeenschap. Administratie Wetenschapsbeleid en Innovatie. (Report TGO 98/30).
- Walraevens, K. (1997). Hydrogeology and hydrogeochemistry of the Ledo-Paniselian aquifer (Flanders, Belgium). First Annual report, pp. 15–17. <https://biblio.ugent.be/publication/270340>

Target site 3: Land subsidence in the Leuven area - (Deliverables: D.2.1./D.2.1.3./D.4.4./D.4.4.3.)

This target site is a newly defined area from the original submitted project as the previous area was not suitable from different points of view to fulfill the expectations of the project.

1. Introduction

In the region of Leuven, two zones of land subsidence have been identified by PS-InSAR in the North of the city. In this area, the subsidence could be linked to the presence of many historical and ongoing pumping wells. Leuven is lying on a multilayer aquifer system called locally 'Brulandkrijt', consisting of interbedded chalk and sandy aquifers with clayey aquitards. The hypothetical cause of the subsidence, linked to pumping, is the consolidation of the clay layers over time. A 3D regional groundwater flow model coupled with a 1D geomechanical model is developed to understand the local consolidation processes and verify the assumptions.

A two steps modelling approach was followed. First a 3D regional groundwater flow model was developed to better characterize the regional groundwater flow. Secondly, a local model was built using results from the regional model as boundary conditions. This local model was then coupled to a 1D geomechanical model.

2. Description of the study area

2.1. Delineation of the study area

In Figure 25, maps of the ground deformation as provided by InSAR (Interferometric Synthetic Aperture Radar) measurements for ERS, ENVISAT and Sentinel 1A intervals show significant land surface deformations in the Leuven area. More particularly, two areas where significant deformation is observed are highlighted. This subsidence is assumed to be related to the drop in groundwater levels resulting from the pumping activities.

2.2. Geology

In the Leuven area, geological layers correspond to Quaternary and Tertiary deposits, (Cenozoic era) overlying Mesozoic formations. The different considered geological formations (**Error! Reference source not found.**) considered are, from top to bottom, the:

- Gent Formation: mainly aeolian cover sands,
- Brussels Formation: mix of fine to medium carbonate sand with glauconite,
- Kortrijk Formation: mainly clay with silt,
- Hannut Formation: mix of clay-rich sand with silt, glauconite and sandstone,
- Heers Formation: sand with glauconite,
- Gulpen Formation: composed by chalk and sand.

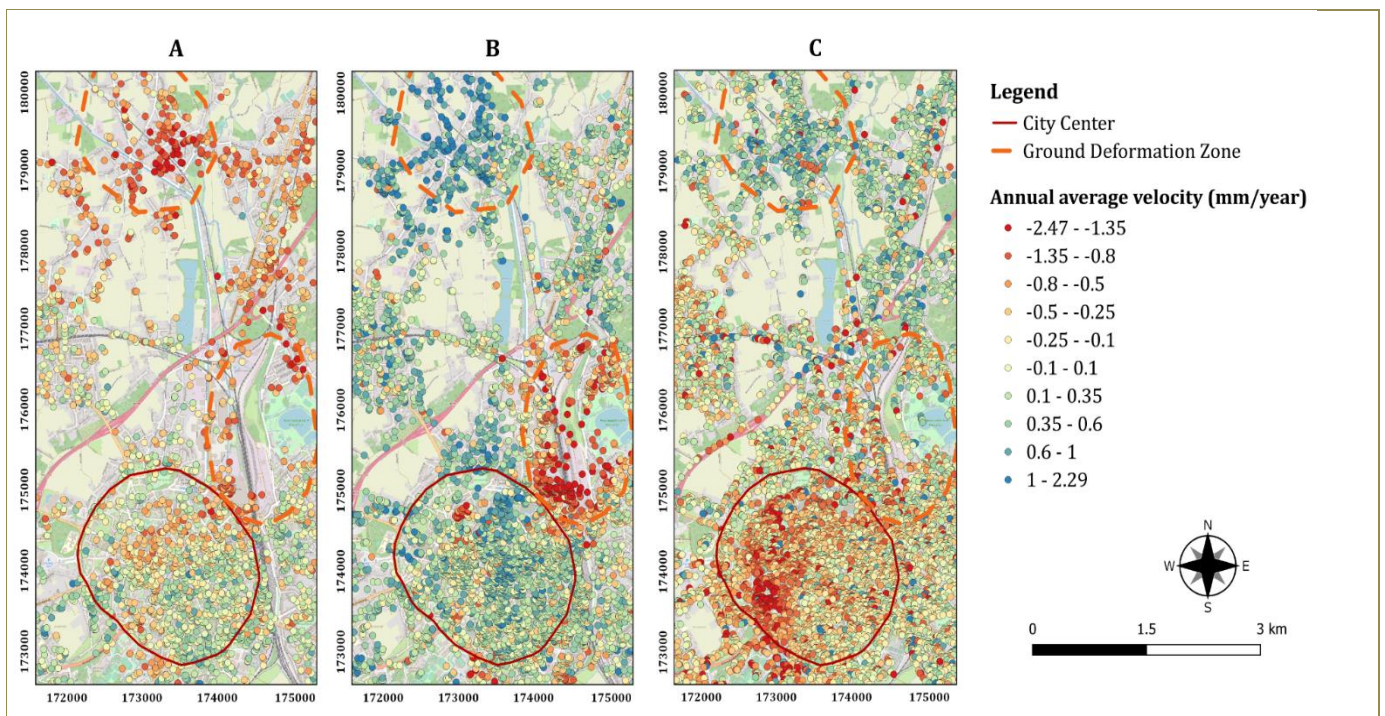


Figure 25. InSAR measurements around Leuven area for satellites ERS 1/2 (A) (1992-2001), ENVISAT (B) (2003-2010) and Sentinel 1A (C) (2016-2022).

2.3. Hydrogeology

2.3.1. Hydrogeological units

The area of Leuven is in the « Brulandkrijt » system. The main units of interest are represented by the HCOV code in **Error! Reference source not found.** They are listed from top to bottom as: Quaternary aquifer system (HCOV 0100), Oligocene aquifer system (HCOV 0400), Bartoon aquitard system (HCOV 0500), Brusselian aquifer system (HCOV 0600), Ypresian aquitard system (HCOV 0800), Paleocene aquifer system (HCOV 1000) and Cretaceous aquifer system (HCOV 1100).

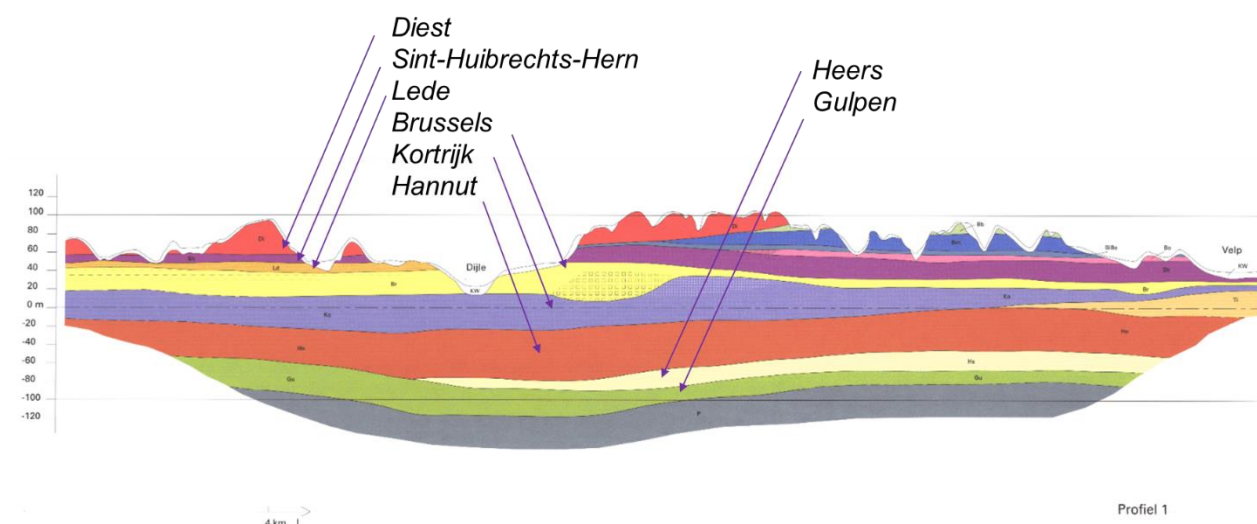


Figure 26. Geological cross-section across the area around Leuven (Toelichtingen bij de geologische kaart van België-Vlaams gewest-kaartblad 32, Leuven).

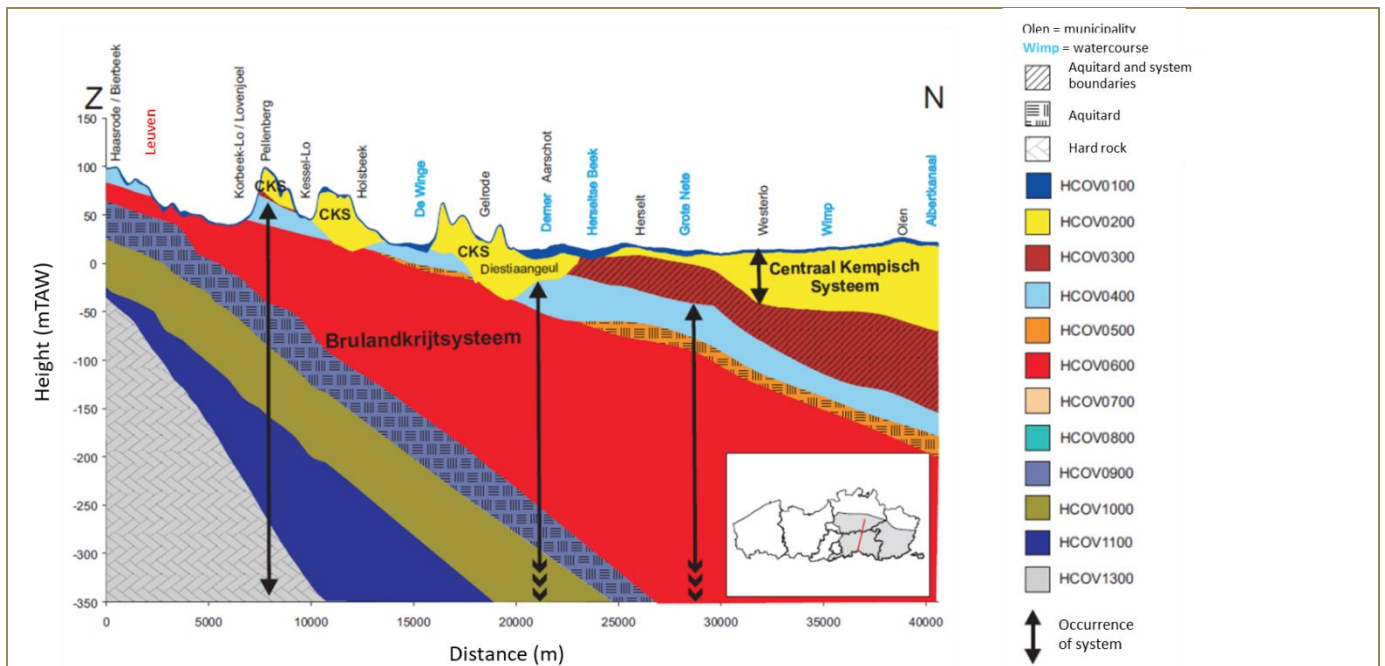


Figure 27: Hydrogeology of the “Brulandkrijt” system (VMM, Operational Water Management Department).

2.3.2. Pumping wells and piezometric head

Based on the DOV database, most of the pumping wells around Leuven are drilled in the Brusselian and the Paleocene aquifers. There are also a few important pumping wells in the Cretaceous aquifer system (Figure 28). Similarly, most of the monitoring wells (piezometers) are also found in these geological layers. Unfortunately, difficulties occur when collecting information concerning the location and pumping rates mostly for the oldest wells.

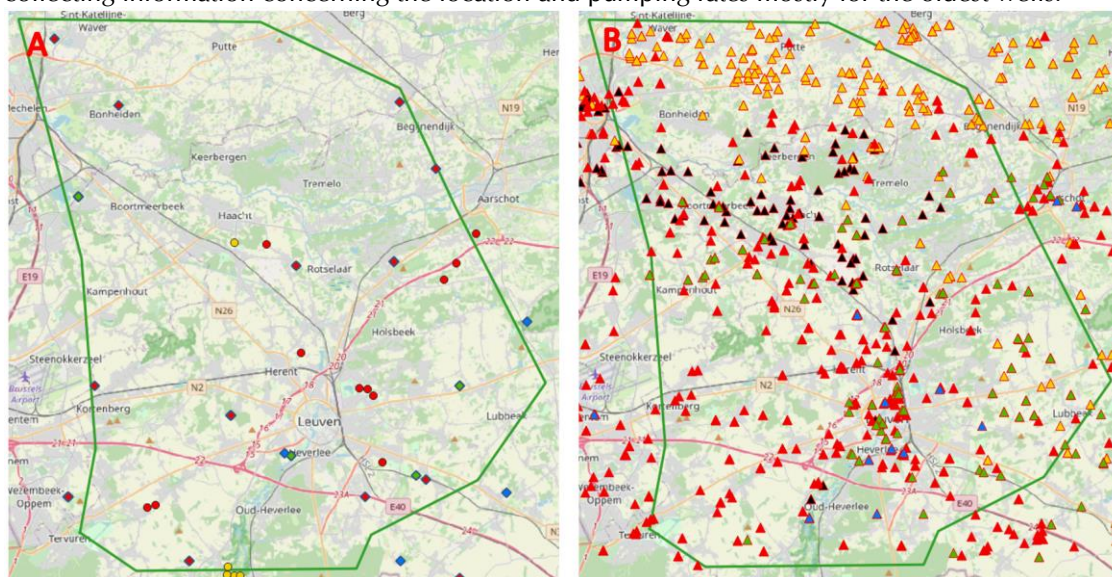


Figure 28: A) Location of the monitoring wells. B) Location of the pumping wells. Points in black are in the Quaternary, yellow in the Oligocene, red in the Brussel, green in the Paleocene and blue in the Cretaceous.

3. 3D regional groundwater flow model

3.1. Objectives of the model

The objectives of the 3D regional groundwater flow model were to simulate the main trends in the regional flows both in terms of spatial distribution and temporal trends. A steady state model based on observed data in 1990 was developed and calibrated to characterize the main groundwater flow directions. A transient model was then developed for the period 1990-2020.

3.2. Conceptual model

Different conceptual models have been tested during the project. First runs in steady state of the developed models have shown that some conceptual choices were not totally appropriate. The conceptual model was thus adapted. The last version of the conceptual model is presented below.

3.2.1. Spatial extension of the model

Using the piezometric map of 2012 for the Brusselian, the Paleocene and the Cretaceous aquifers (from "Stroomgebiedbeheerplannen voor Schelde en Maas 2016-2021 - Grondwatersysteemspecifiek deel Brulandkrijtstelsel"), the limits of the model have been chosen (Figure 29) to be able to prescribe as far as possible no flux boundary conditions along assessed directions of groundwater flow and on the groundwater divide lines.

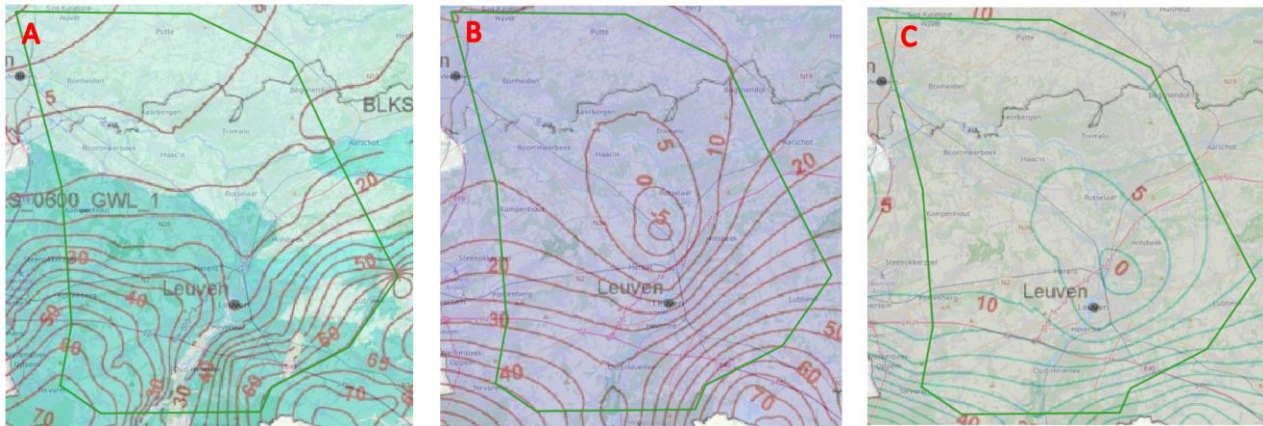


Figure 29: Piezometric maps of the Brusselian aquifer (A), Paleocene aquifer (B) and Cretaceous aquifer (C).

3.2.2. Vertical extension and vertical discretization of the model

The model includes the geological layer from the ground surface until the Mesozoic formations. The main hydrogeological units, including the low permeable and most compressible layers, are explicitly represented. The current model contains 8 different layers (Table 3).

Layer	Extension	Name	Type	Material based on DOV
1	North	<u>Quaternary</u>	Aquifer	Mainly aeolian cover sands
2	North	Boom, Oligocene and Bartoon complex	Aquifer and Aquitards	Clay, sand and silt
	South	<u>Quaternary</u>	Aquifer	Mainly aeolian cover sands
3	Whole model	<u>Brusselian</u>	Aquifer	Fine to medium limestone sand with glauconite
4	Whole model	<u>Ypresian</u>	Aquitard	Mainly clay with silt
5	Whole model	<u>Paleocene (Hannut)</u>	Aquifer	Clay-rich sand with silt, glauconite and sandstone
6	Whole model	Paleocene (Hannut clay base)	Aquitard	-
7	Whole model	Paleocene (Heers)	Aquifer	Sand with glauconite
8	Whole model	Chalk	Aquifer	Chalk and sand

Table 3: Hydrogeological parameters of the different hydrogeological layers of the numerical model. The values in red are the values of hydraulic conductivity optimized during the calibration of the steady state model.

To better represent the complexity of the geology appearing in the North of the studied area (Table 4), two different layers were used in the model (Table 3). The first layer of the model has a surface equal to the zone A (**Error! Reference source not found.**). It represents the Quaternary formations, which are found on top of the more clayey formations of

the aquitards. The second layer of the model (Figure 31) is divided into 3 areas. Zone A represents the association of the Boom aquitard, the Oligocene aquifer and the Bartoon aquitard. Zones B and C represent the Quaternary formations as in the first layer.

Geological formation		Hydrogeological unit
Name	Material based on DOV	
Gent	Aeolian cover sands	Quaternary aquifer
Boom	Clay and silt	Boom aquitard
<u>Bilzen</u>	Sands with clay interbed	Oligocene aquifer
<u>Sint-Huitbrechts-Hern</u>	Sands rich in clay	
Maldegem	Clay and sand	<u>Bartoon aquitard</u>

Table 4. Summary of the geological formations, and related hydrogeological units, appearing in the North of Leuven.

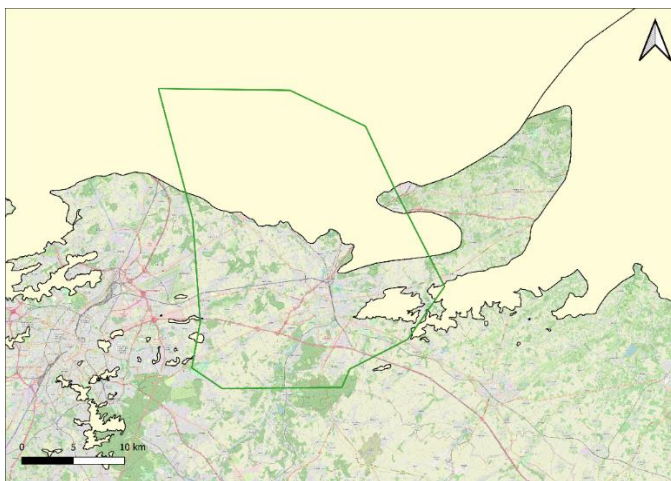


Figure 30. The yellow surface shows where the Boom and Bartoon aquitards and the Oligocene aquifer exist in the studied area. The green lines are the limit of the numerical model.

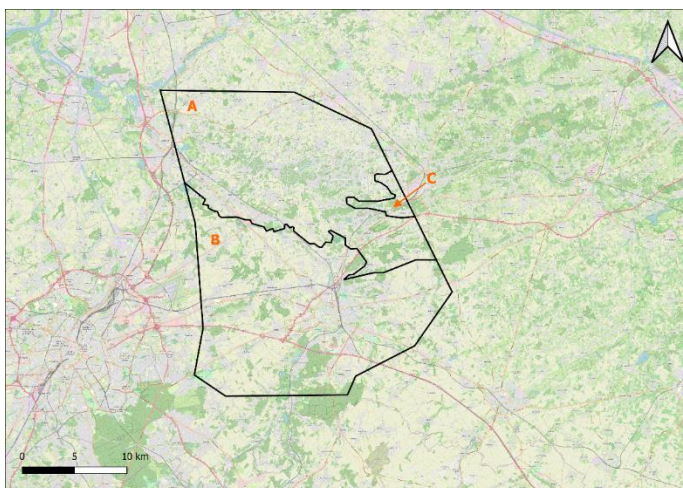


Figure 31. Zonation of the second layer of the model. The zone A represents a complex area where the aquitards of Boom and Bartoon and the aquifer of the Oligocene are present. In zones B and C only the Quaternary formations are present.

Groundwater exchange between the Heers and Hannut Formations is limited due to the presence of a thin clay layer at the bottom of the Hannut Formation that reduces the interactions between these formations. A 3-meter-thick layer of low permeability was added between the Hannut formation and the Heers Formation in the numerical model to take it

into account (layer 6 in Table 3).

3.2.3 Boundary conditions

The boundary conditions prescribed in the model had to be representative of the year 1990. However, they are based on the piezometric map from 2012, the only regional map available for the area. Based on the first results of the simulations, these boundary conditions have been updated to represent the main groundwater flows observed in 1990.

For clarity, boundary conditions applied to each layer are detailed separately.

In the first layer, representing the Quaternary aquifer, based on the topography of the area, the groundwater flow direction, and the existence of many waterways in the surrounding area, a Dirichlet boundary condition, 2 meters below the ground level, is prescribed in the Northwest corner of the boundary (Figure 32, Table 5).

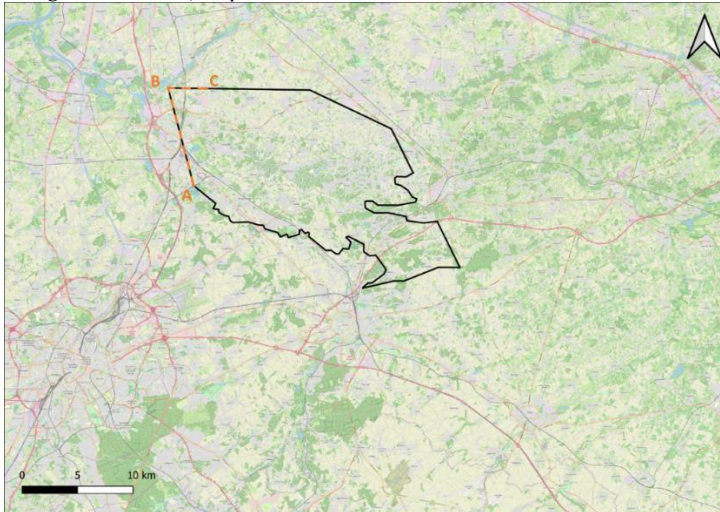


Figure 32. Boundaries conditions prescribed to the first layer (Quaternary aquifer) of the numerical model. The orange dotted lines show on which portion the Dirichlet condition is applied.

Point	A	B	C
Value (m)	8	3	6

Table 5. Values of prescribed head in the first layer. The location of the different points is shown in Figure 32.

In the third layer, representing the Brussel aquifer, Dirichlet boundary conditions are applied to the North and South boundaries (**Error! Reference source not found.**33). The values of prescribed head are based on the piezometric map of 2012. In the southern part of the model, where the Brussel formation was eroded by the Dyle River the values are updated based on the topography (Figure 1, Table).

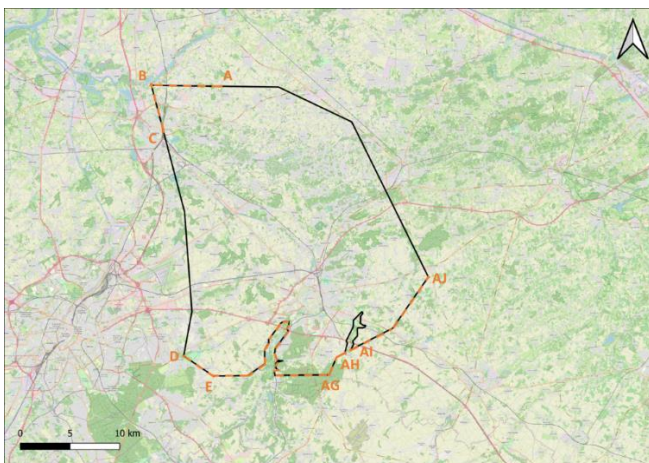


Figure 33. Boundaries conditions prescribed to the third layer (Brussel aquifer) of the numerical model. The orange

dotted lines show on which portions the Dirichlet conditions are applied.

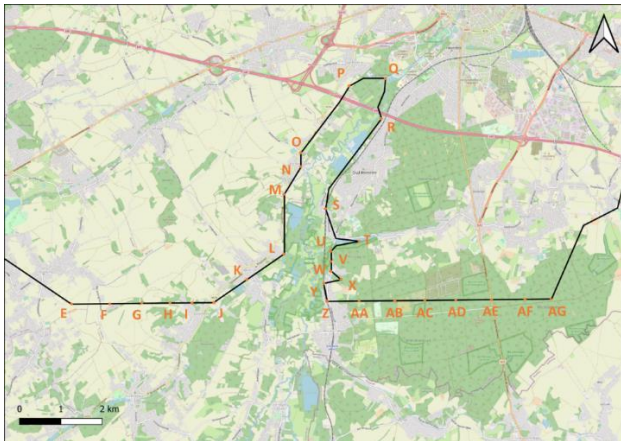


Figure 1. Zoom in Figure 33, on the Dirichlet conditions, in the area where the Brussel aquifer was eroded by the Dyle river.

Point	A	B	C	D	E	F	G	H	I	J	K	L	M	N	O	P	Q	R
Value (m)	0	-5	0	66	65	60	55	50	45	40	35	30	35	30	30	30	26	24

Point	S	T	U	V	W	X	Y	Z	AA	AB	AC	AD	AE	AF	AG	AH	AI	AJ
Value (m)	26	29.9	29.3	29.5	29.7	29.8	28.7	30.7	31	35	40	45	50	55	60	60	60	60

Table 6. Values of prescribed head in the third layer. The location of the different points is shown in Figure 33 & 34.

In the fifth layer, representing the Hannut Formation, a part of the Paleocene aquifer, Dirichlet boundary conditions were also applied on the North and South boundaries to represent the main groundwater flow directions (Figure 35, Table 7).

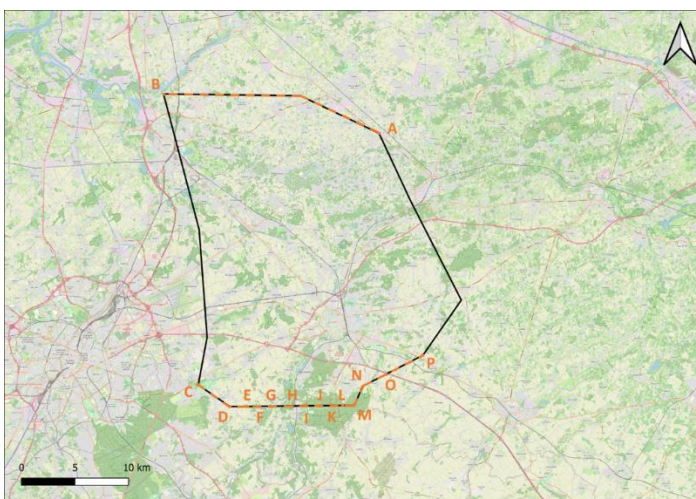


Figure 35. Boundaries conditions prescribed to the fifth layer (Hannut Formation) of the numerical model. The orange dotted lines show on which portions the Dirichlet conditions are applied.

Point	A	B	C	D	E	F	G	H	I	J	K	L	M	N	O	P
Value (m)	10	10	45	45	40	35	30	30	35	40	45	50	55	55	60	55

Table 7. Values of prescribed head in the fifth layer. The location of the different points is shown in Figure 35.

The same boundary conditions are applied to the Heers Formation and the chalk aquifer as they are not separated by a low permeability layer (Figure 36). The examination of the evolution of the piezometric levels between 1990 and 2012 in the surroundings, in and outside the study area, shows that the groundwater levels were systematically lower in 1990 for the northern boundaries. The values of prescribed head on the northern boundary in the seventh and the eighth layers that were defined based on the 2012 piezometric map are then decreased by 3 meters (Table 8).



Figure 36. Boundaries conditions prescribed to the seventh layer (Heers Formation) and eighth layer (chalk aquifer) of the numerical model. The orange dotted lines show on which portions the Dirichlet conditions are applied.

Point	A	B	C	D	E	F	G	H	I	J	K	L	M
Value (m)	7	7	31	35	38	35	30	35	40	42	33	30	25

Table 8. Values of prescribed head in the seventh and eighth layers. The location of the different points is shown in Figure 36.

Transient boundary conditions are implemented for the seventh and the eighth layers. Values were determined using piezometers near the boundaries, inside and outside of the study area. (Table 9).

Point	A	B	C	D	E	F	G	H	I	J	K	L	M
Min and max of the value over 30 years (m)	5-9	7-13	31-33	35-37	37-40	34-37	29-31	34-36	38-40	40-42	32-34	29-31	24-26

Table 9. Amplitude of the variation of the boundaries conditions through 30 years prescribed in the seventh and eighth layers. The location of the different points is shown in Figure 36.

On the boundary of the aquitards (layers 2, 4 and 6), no flow boundary conditions are prescribed. In these layers, due to the low permeability, groundwater flow is assumed to be mainly vertical.

3.2.4. Recharge

In steady state, a single value of recharge of 7×10^{-9} m/s, coming from the WetSpas model (Vrije Universiteit Brussel, 2004), is applied over the entire model surface for the recharge.

In transient simulation, to represent the dynamic of the groundwater levels in the first layer of the model, a transient recharge must be considered. Precipitation data are available only for the period 2005-2020 on the Waterinfo website for different meteorological stations in or around the studied area. Values of precipitation that were not available before 2004 are updated with precipitation data coming from the RAM model (Fettweiss et al., 2013). The recharge applied to the model is computed by multiplying these annual values of recharge by an infiltration coefficient calculated by the Wetspass model (Vrije Universiteit Brussel, 2004) equals to 0.29 for this area (Figure 2).

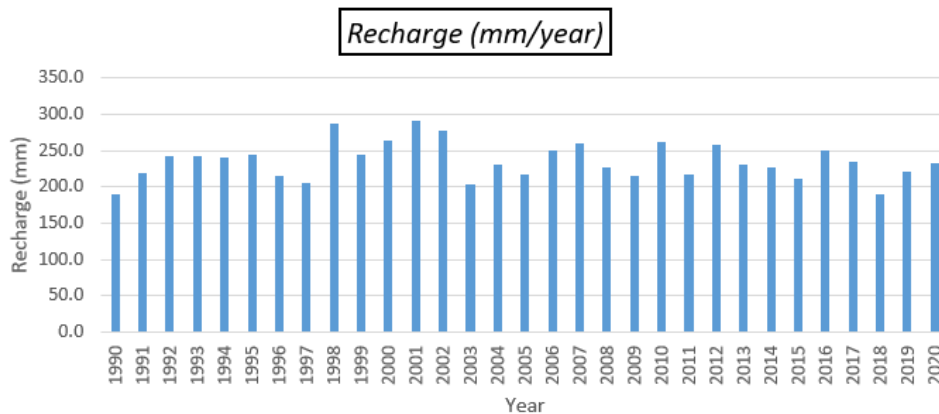


Figure 2. Calculated annual recharge between 1990 and 2020 in mm/year.

3.2.5. Groundwater-surface water interactions

In the modelled area the drainage network is dense and as a key role in controlling the groundwater levels in the first layers. A good representation in the model of the river network is thus of primary importance. Boundary conditions were added to the model to better represent the interactions with the surface waters (Figure 39). Interactions between groundwater and surface water are represented by Cauchy boundary conditions. With this type of boundary condition, the exchanged fluxes are computed based on the groundwater – surface water gradient and a conductance coefficient depending on the hydraulic conductivity of the river sediments.

In MODFLOW, two types of boundary conditions can be applied to represent groundwater-surface water interactions:

- River boundary conditions simulate groundwater inflow or outflow depending on the gradient between the groundwater level and the level of the river. The latter can thus act as a drain or allow groundwater to enter the model, based on the groundwater – surface water gradient.
- Drain boundary conditions that are unidirectional. The river acts only as a drain.

The watercourses represented in the model are considered as drains because they are often dry in this area and to avoid introducing artificially too much water in the model. Only the main branch of the river Dyle and the 'canal' are considered as rivers in the model. The conductance value of the 'canal' has been modified to reach the value of 10^{-7} m/s while the other streams have a conductance of 10^{-4} m/s.

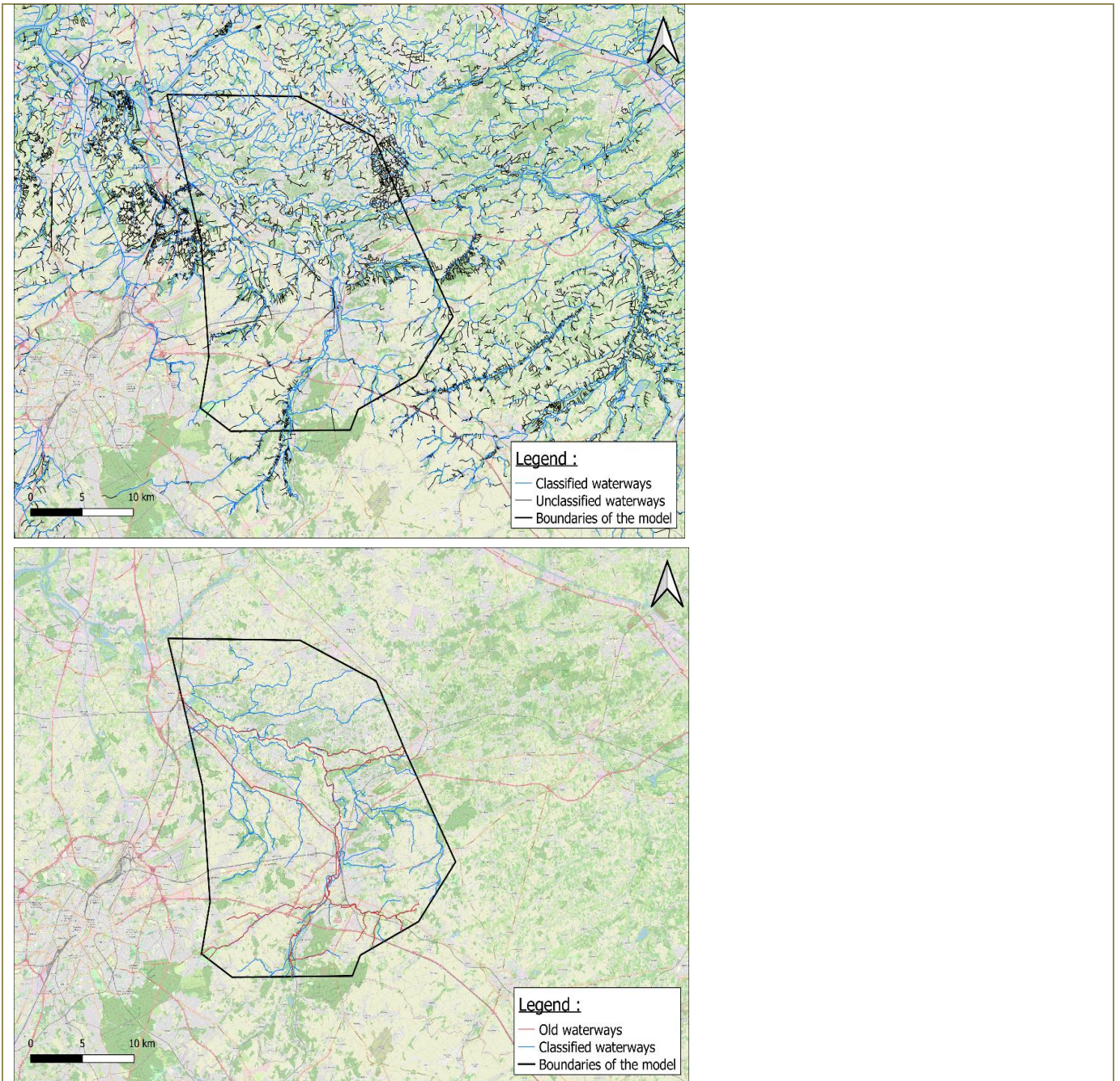
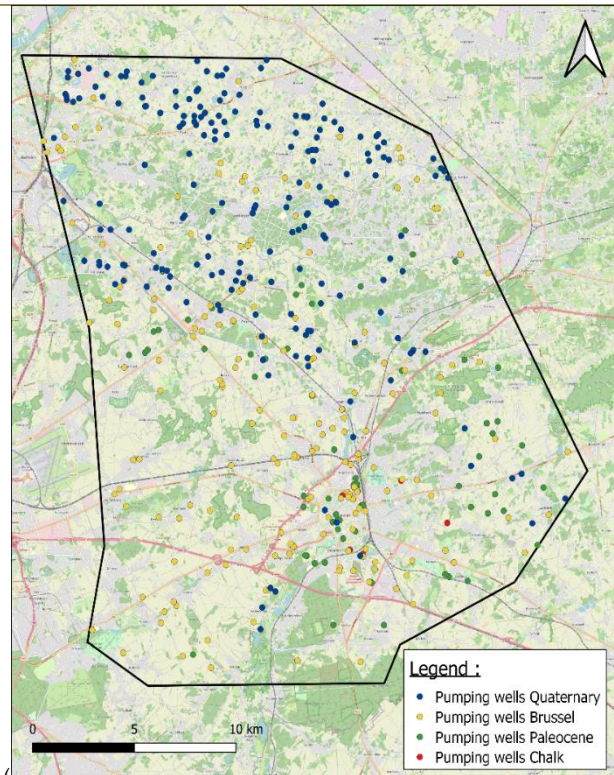


Figure 38. On the top, the map of all the waterways in the studied area delineated by a green line (source: Waterinfo). On the bottom, a map of the waterways in blue lines represented in the numerical model.

3.2.6. Pumping wells



In the studied area, there are many pumping wells (Figure 3) but most of them have a low flow rate. Only the pumping wells with the highest pumping rate, covering 97% of the total pumping rate in each layer, were modelled.

In the Brussel aquifer where the largest number of pumping wells are found, most of them have also a low pumped rate. In this layer only, to better represent the large number of pumping wells, the modelled pumping wells represent 98.5% of the total volume of pumped groundwater.

The difficulty of collecting data on pumping wells and abstraction rates must be mentioned, especially for the oldest period.

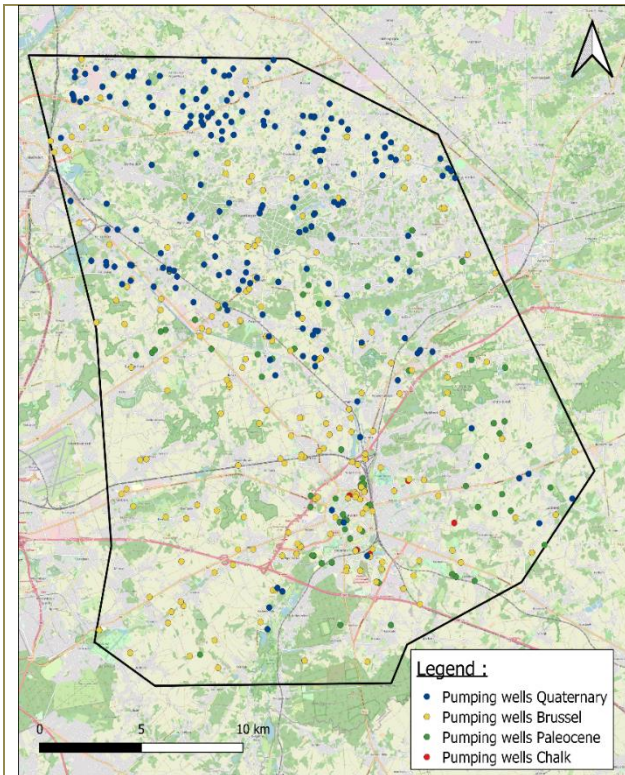


Figure 3. Existing pumping wells in the area between 1990 and 2020.

3.2.7. Parametrisation of the model

Local data on the hydraulic properties (hydraulic conductivity, specific yield and specific storage) of the subsurface are scarce. Data from the literature has been considered. First, all the layers are considered homogeneous, and a unique value of each property is assigned to each layer.

3.2.8. Spatial discretization

A 3D grid was built with the GMS interface. The generated grid of the model has cells with a minimum size of 100 meters around Leuven and a maximum size of 250 meters at the limits of the model (Figure 39).

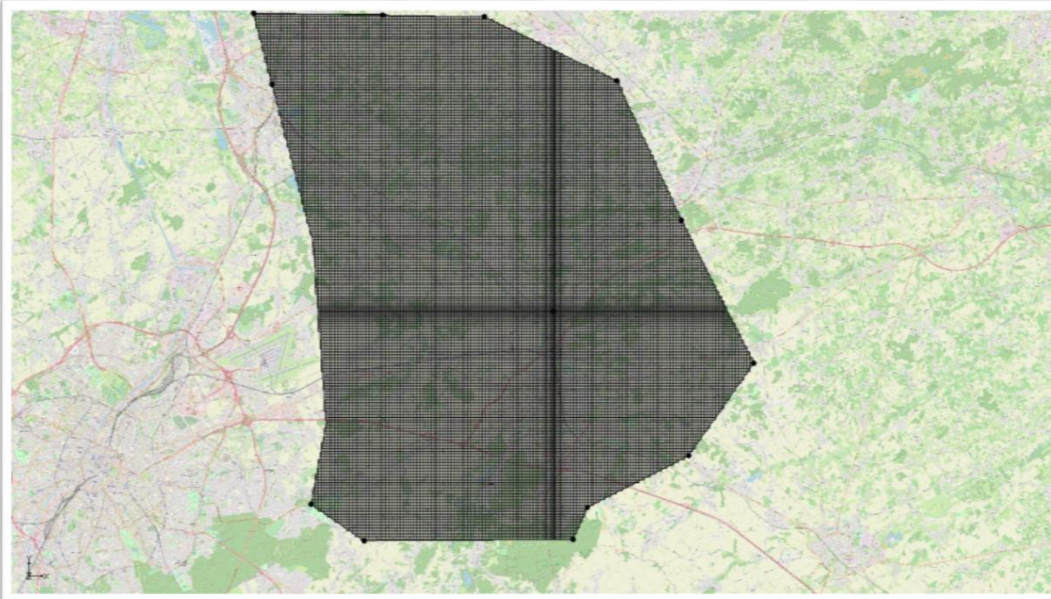


Figure 40. Discretization of the studied area in a 3D Grid.

3.3. Calibration of the steady-state model

Using the code MODFLOW, a steady state simulation has been performed simulating averaged situation of the year 1990. This model provides average piezometric heads that will represent the initial conditions (IC's) for the transient model.

The calibration of the model has been performed using PEST based on observed groundwater levels in 1990. The hydraulic conductivity in each layer is optimized during the calibration. The comparison between the observed and computed groundwater levels is shown in Figure 4. During the calibration works, it was necessary to spatially distribute the hydraulic conductivity in the third layer to better represent the cone of depression visible in the areas of deformation and in the city of Leuven. This layer is then divided in 3 zones (Figure) and a value of hydraulic conductivity was optimized in each zone.

The optimized values of hydraulic conductivity are summarized in the **Error! Reference source not found..**

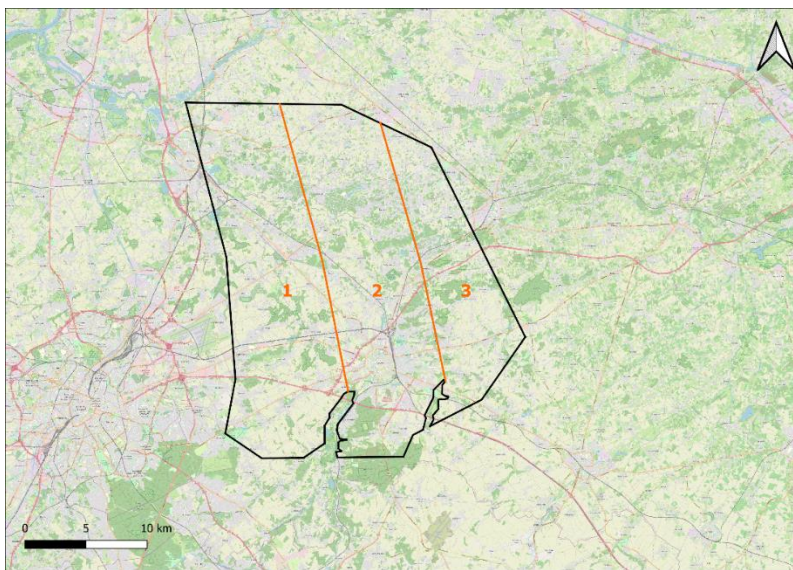


Figure 41. Division of the third layer representing the Brussel aquifer into 3 zones with different hydraulic properties.

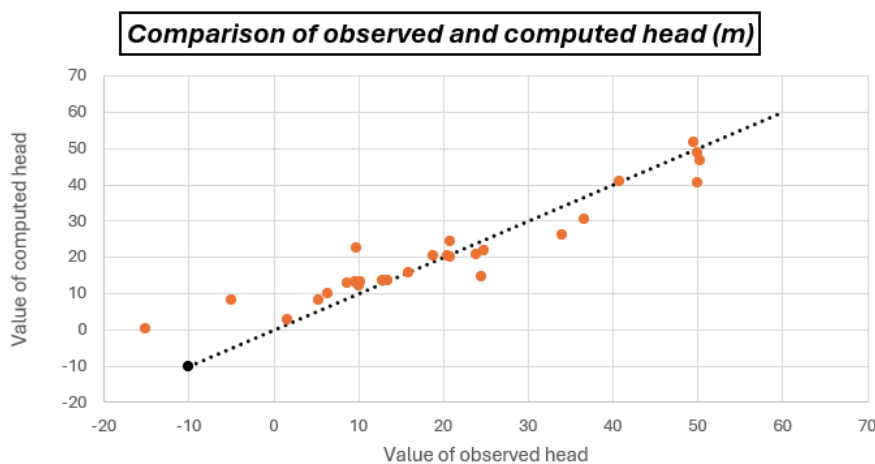


Figure 4. Comparison of computed head over observed head after calibration of the steady state model.

Layer	Extension	Name	Type	Material based on DOV	Horizontal hydraulic conductivity (m/s)
1	North	<u>Quaternary</u>	Aquifer	Mainly aeolian cover sands	1×10^{-4}
2	North	Boom, Oligocene and Bartoon complex	Aquifer and Aquitards	Clay, sand and silt	2.16×10^{-8}
	South	Quaternary	Aquifer	Mainly aeolian cover sands	7.74×10^{-5}
3	Whole model	<u>Brusselian</u>	Aquifer	Fine to medium limestone sand with glauconite	1: 7.83×10^{-5} 2: 9×10^{-4} 3: 1.35×10^{-4}
4	Whole model	Ypresian	Aquitard	Mainly clay with silt	7×10^{-9}
5	Whole model	Paleocene (<u>Hannut</u>)	Aquifer	Clay-rich sand with silt, glauconite and sandstone	1.57×10^{-6}
6	Whole model	Paleocene (<u>Hannut clay base</u>)	Aquitard	-	1×10^{-9}
7	Whole model	Paleocene (Heers)	Aquifer	Sand with glauconite	1×10^{-5}
8	Whole model	Chalk	Aquifer	Chalk and sand	5×10^{-4}

Table 10: Optimized values of hydraulic conductivity of the different hydrogeological layers, after the calibration of the steady state model.

3.4. Calibration of the transient model

As our InSAR measurements and most of our data are over a period of 30 years, starting in 1990, the transient model is developed to model the period between 1990 and 2020. The initial conditions of this model are the results of the steady-state model.

The calibration of the transient model is carried out by trial and error and by using PEST based on available time series of observed groundwater levels. It must be noticed that the amount of available data is limited, concerns only the aquifer and that the data doesn't cover the whole period of simulation. Examples of comparisons of the evolution of computed and observed groundwater levels, for piezometers close to the deformation areas, in the different aquifers are given in Figure 5. Comparison of observed (orange) and computed (blue) time series of groundwater levels in different piezometers for the period 1990-2020. Even if the absolute values of groundwater levels are not exactly simulated, this comparison shows that the model is able to reproduce the main trends in the time evolution of the groundwater levels and the variations of the groundwater levels over time that are the main drivers of the ground subsidence.

Values of the hydrogeological parameters of the transient model, including the horizontal hydraulic conductivity, the specific storage and the specific yield are optimized (Table 10).

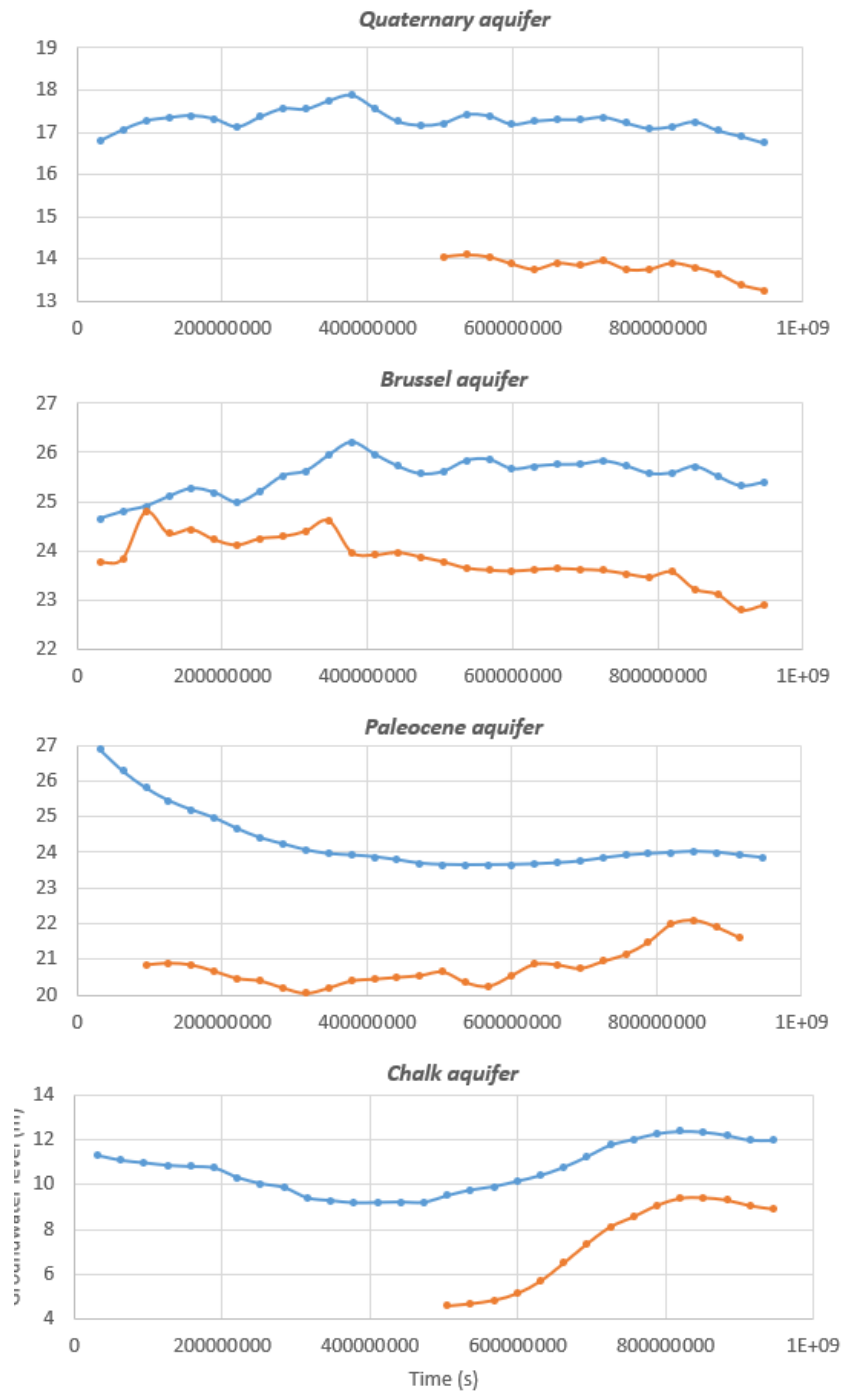


Figure 5. Comparison of observed (orange) and computed (blue) time series of groundwater levels in different piezometers for the period 1990-2020.

Layer	Extension	Name	Type	Material based on DOV	Horizontal hydraulic conductivity (m/s)	Specific storage (1/m)	Specific yield (/)
1	North	<u>Quaternary</u>	Aquifer	Mainly aeolian cover sands	1×10^{-4}	5×10^{-4}	2.42×10^{-2}
2	North	Boom, Oligocene and <u>Bartoon</u> complex	Aquifer and Aquitards	Clay, sand and silt	9×10^{-8}	5×10^{-4}	1.49×10^{-3}
	South	Quaternary	Aquifer	Mainly aeolian cover sands	5.48×10^{-5}	4.95×10^{-3}	6.62×10^{-2}
3	Whole model	<u>Brusselian</u>	Aquifer	Fine to medium limestone sand with glauconite	1: 3.4×10^{-4} 2: 2.58×10^{-4} 3: 1.27×10^{-4}	5×10^{-5} 6.84×10^{-6} 5×10^{-5}	9.98×10^{-2} 6.92×10^{-2} 5.68×10^{-2}
4	Whole model	Ypresian	Aquitard	Mainly clay with silt	1.53×10^{-8}	1.96×10^{-4}	4.5×10^{-1}
5	Whole model	Paleocene (<u>Hannut</u>)	Aquifer	Clay-rich sand with silt, glauconite and sandstone	1.67×10^{-6}	5×10^{-5}	3×10^{-2}
6	Whole model	Paleocene (<u>Hannut</u> clay base)	Aquitard	-	1×10^{-9}	1×10^{-3}	1×10^{-3}
7	Whole model	Paleocene (Heers)	Aquifer	Sand with glauconite	1×10^{-5}	5×10^{-6}	3×10^{-2}
8	Whole model	Chalk	Aquifer	Chalk and sand	5×10^{-5}	9.28×10^{-7}	4×10^{-2}

Table 11. Optimized values of the hydrogeological parameters of the different layers after calibration of the transient model.

4. 3D local groundwater flow and geomechanical model

4.1. Objectives of the local model

The regional model is used to represent the regional behavior of the groundwater flows. It allows to define boundary conditions that are close to the actual boundaries of the groundwater system or far enough away from the zone of interest to avoid too much impact of the boundary conditions in this zone of interest. However, the coarse discretization used in this regional model doesn't allow to represent the groundwater levels and their temporal evolution with great accuracy. To have an optimal and more precise representation of this dynamic, a local model was created based on the parameters and the computed groundwater levels of the regional model. The evolutions of the groundwater levels were then used to compute the ground deformations.

4.2. Development of a local groundwater flow model

The local model lies on a rectangular area close to the two deformation zones visible in Figure 25. The generated grid built using GMS has cells with a minimum size of 10 meters around the two deformation areas and a maximum size of 50 meters at the limits of the model (Figure 43). The grid is refined near the two deformation zones.

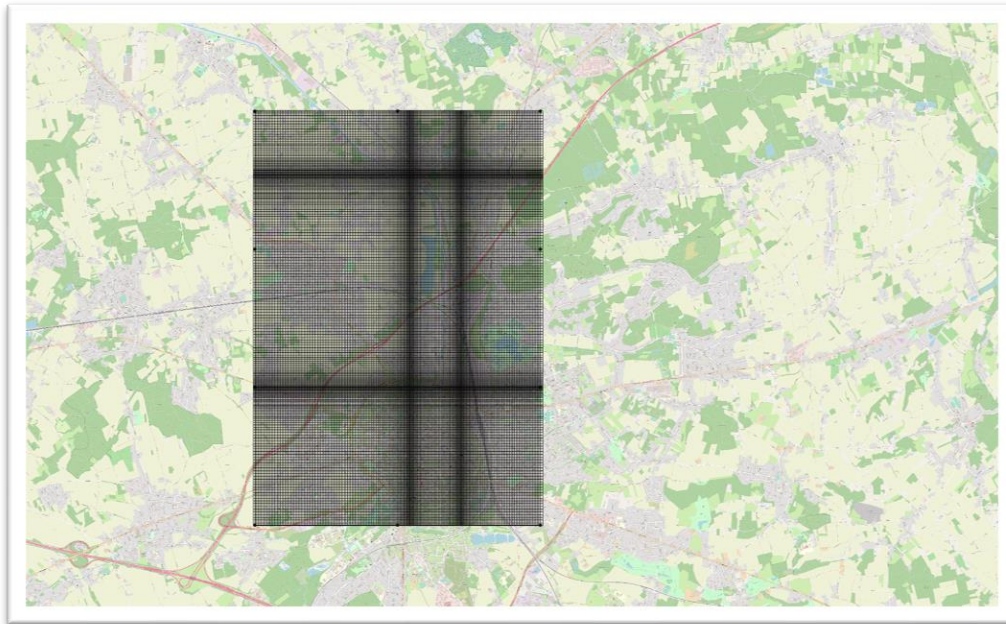


Figure 44: Spatial extension and grid of the local model with two refinement points.

4.3. Local steady state model

While the regional model contains 8 layers to consider the clayey formations appearing in the North, the local model does not overlap these geological formations. Thus, it only contains 7 layers, from top to bottom: the Quaternary aquifer, the Brussel aquifer, the Ypresian aquitard, the Hannut Formation, the clay layer of the previous formation, the Heers Formation, and the chalk aquifer.

Dirichlet boundary conditions are prescribed on the four sides of the model. Values of the prescribed head are defined from the steady state regional model (Figure 44). Only the layers for the Ypresian clays and the fin clay layer at the bottom of the Hannut Formation have a zero-flux condition on their boundaries, like the regional models.

A uniform recharge rate of 7×10^{-9} m/s is applied to the model. The horizontal hydraulic conductivity values from the steady state regional model are applied and calibrated using PEST. Furthermore, the watercourses, pumping wells and piezometers active in the area are replicated identically.

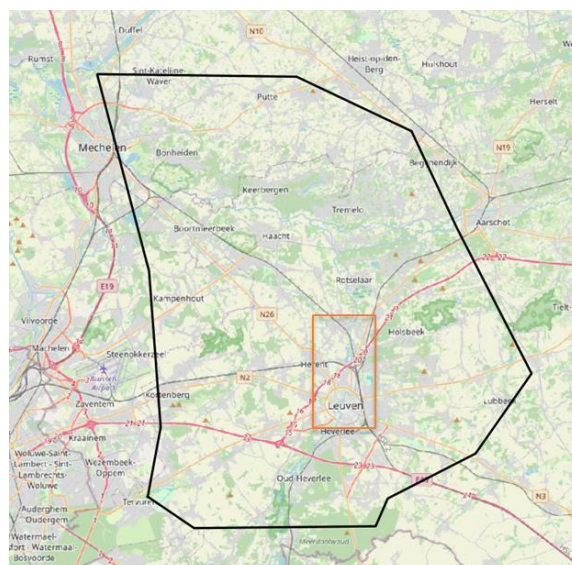


Figure 45: Limits of the regional model (black) and the local model (orange).

4.4. Local transient groundwater flow model

Transient Dirichlet boundary conditions are applied, and the values of prescribed heads are taken from the computed groundwater levels of the regional transient model (Figure 45). The values of the recharge are based on the precipitation values of RAM and the infiltration coefficient of 0.29 calculated by the Wetspass model. For the existing pumping wells in the area, values are the same as those applied in the regional transient model.

The initial conditions used for the local transient model are the groundwater levels computed by the local steady state model. This model is run through the same conditions as for the regional transient model. It starts in 1990 and is modeled for a period of 30 years.

An example of computed map of groundwater level in the Hannut aquifer is provided Figure 6. On this map, the impact of the pumping wells in the Hannut aquifer is clearly visible.

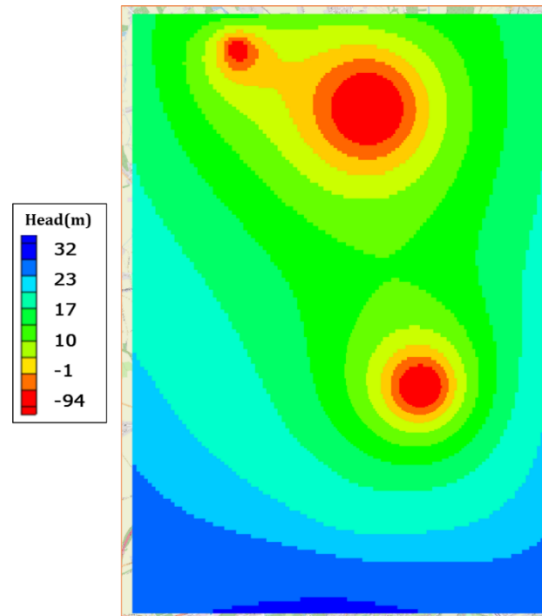


Figure 6. Computed groundwater levels in the Hannut Formation in 2015 by the transient local model. The two main subsidence areas correspond to piezometric (head) depressions.

4.5. Geomechanical model using the SUB package

The vertical displacement of the soil resulting from the modification of the pore pressure computed with the transient local model is computed with the SUB package include in the GMS Software (Hoffmann et al., 2003).

To calculate the compaction in each cell of the model, the SUB package requires several parameters whose values are summarized in Table 12. Unit mass values are determined using the literature (Dassargues, 2018) and the general lithology of each formation. Compression and swelling coefficient values, over different forms, are taken from DOV and borehole survey report data (Hjuler M.L. and Fabricius I.L., 2009; Collin F. et al., 2008; Nguyen H.D. et al., 2007).

Because of the characteristically low vertical hydraulic conductivity of aquitards, the equilibration of hydraulic heads in the aquitards typically lags head changes in the surrounding aquifer. The resulting compaction of these layers is delayed in comparison to the pressure's changes in the surroundings aquifer. In the SUB package, each layer must be defined as non-delayed or delayed regarding compaction. Aquiclude formation (Ypresian clays and the fine clay layer at the bottom of the Hannut Formation) are considered as 'delayed formations.

Compaction of the geological layers is also dependent of the previous stresses sustained by these layers depending on whether the effective stress exceeds the previous maximum effective stress, termed the preconsolidation stress (for example Jorgensen, 1980). If the effective stress remains less than the preconsolidation stress, a further increase in effective stress (or decrease in hydraulic head) causes elastic compaction. This compaction is recoverable if the effective stress returns to its initial value. If the effective stress exceeds the preconsolidation stress, layers compact also inelastically. All layers, except layer 1 are considered as overconsolidated.

Layer	Aquifer or aquitard name	Unit mass (kg/m ³)	C	A	C _c	C _s
1	Quaternary	2100	24.46	108.34		
2	Brussel	2100	35.53	205.79		
3	Ypresian	2000			0.3	0.1
4	Hannut	2100	35.53	205.79		
5	Clay layer	2000			0.25	0.11
6	Heers	2100	35.53	205.79		
7	Chalk	2100			0.31	0.12

Table 12. Values of the parameters applied to the different layers of the geomechanical model during the SUB package calculation process. C and C_c are respectively the compression constant and compression index reflecting the non-reversible inelastic behavior of the considered layer. A and C_s are respectively the swelling constant and swelling index reflecting the reversible elastic behavior of the considered layer.

The results shown in the **Error! Reference source not found.** are the computed compaction for a cell located in the middle of the area of deformation close to the center of Leuven. The values are compared with the evolution of groundwater levels. In this figure, it can be observed that most of the compaction occurs in the layers 1 and 3. Layer 1 is assumed to be not overconsolidated and the deformation is inelastic. In layer 3, the important compaction can be explained by (1) the important variation of groundwater level and (2) Layer 3 corresponds to a thick compressible clay layer.

The vertical displacement was computed using the SUB package of MODFLOW and compared to InSAR measurements:

- For the deformation close to the city center, the trend of the total compaction curve is like the estimates from InSAR measurements and shows a significant subsidence over 30 years.
- However absolute values of subsidence are different. This may be due to uncertainties related to the parameterization, conceptualization and calibration of the models (3D groundwater flow and 1D geomechanical models). This can also come from inaccuracies in the coupling of the models because the SUB uses parameters with constant values.
- At this stage, the results are less conclusive for the deformation zone located north of Leuven. There, we observe a lack of data on existing pumping wells and therefore a lack of data about actual groundwater pumping and potentially induced changes in groundwater pressure in the aquifers.

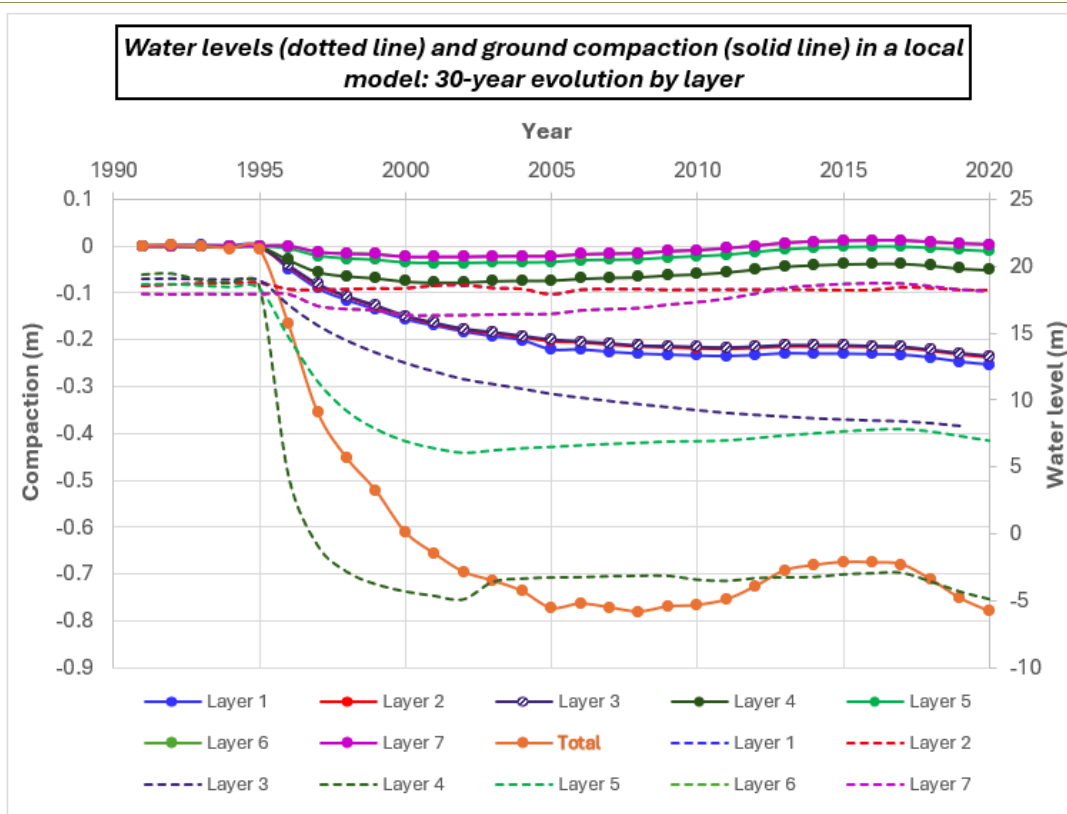


Figure 47: Comparison of the groundwater levels (dotted line) and of the compaction (solid line) computed by MODFLOW and the SUB package in each layer of the model, in a cell located in the zone near the center of Leuven. The total compaction for the same cell is represented in orange.

5. Conclusions

In the region of Leuven, two zones of land subsidence have been identified by PS-InSAR in the North of the city. In this area, the subsidence could be linked to the presence of many historical and ongoing pumping wells. A 3D regional groundwater flow model coupled with a 1D geomechanical model (SUB model) was developed to understand the local consolidation processes and verify the assumptions.

The compaction computed using the SUB model overestimates the subsidence observed using the InSAR measurements. This may be due to uncertainties related to the parameterization, conceptualization and calibration of the models (3D groundwater flow and 1D geomechanical models). This can also be due to the difficulty of comparing InSAR measurements with the results of underground models.

6. References used in this chapter

- Assessment, U.E.N.C. for E., 2009. Groundwater Contamination [WWW Document]. URL https://hero.epa.gov/hero/index.cfm/reference/details/reference_id/2259998 (accessed 5.10.23).
- Carter, M., Bentley, S.P., 1991. Correlations of soil properties. Pentech Press, London.
- Collin, F., De Gennaro, V., Delage, P., Priol, G., 2008. An elasto-viscoplastic model for chalk including suction effects. Presented at the 1st European Conference on Unsaturated Soils (E-UNSAT 2008), Taylor & Francis, London, United Kingdom.
- Dassargues, A., 2018. Hydrogeology: Groundwater Science and Engineering. CRC Press.
- Fettweis, X., Franco, B., Tedesco, M., van Angelen, J.H., Lenaerts, J.T.M., van den Broeke, M.R., Gallée, H., 2013. Estimating the Greenland ice sheet surface mass balance contribution to future sea level rise using the regional atmospheric climate model MAR. *The Cryosphere* 7, 469–489. <https://doi.org/10.5194/tc-7-469-2013>
- Freeze, R.A., Cherry, J.A., 1979. Groundwater. Prentice-Hall, Englewood Cliffs, N.J.
- Ha Dat, N., Gennaro, V., Delage, P., Sorgi, C., 2008. Retention and compressibility properties of a partially saturated mine chalk. <https://doi.org/10.1201/9780203884430.ch34>
- Hjuler, M.L., Fabricius, I.L., 2009. Engineering properties of chalk related to diagenetic variations of Upper Cretaceous onshore and offshore chalk in the North Sea area. *Journal of Petroleum Science and Engineering* 68, 151–170. <https://doi.org/10.1016/j.petrol.2009.06.005>

- Hoffmann, J., Leake, S., Galloway, D., Wilson, A., 2003. MODFLOW-2000 Ground-Water Model—User guide to the subsidence and aquifer-system compaction (SUB) package. USGS Ground-Water Resour. Program Open-File Rep. 55.
- Jorgensen, D.G., 1980, Relationships between basic soils-engineering equations and basic ground-water flow equations: U.S. Geological Survey Water-Supply Paper 2064, 40 p.
- Stroomgebiedbeheerplannen, P., n.d. Stroomgebiedbeheerplannen voor Schelde en Maas 2016-2021.
- Vandenberghe, N., Cullentops, F., 2001. Toelichtingen bij de geologische kaart van België-Vlaams gewest-kaartblad 32, Leuven. Belgische Geologische Dienst (Brussel).
- Welkom bij Databank Ondergrond Vlaanderen | DOV [WWW Document], n.d. URL <https://dov.vlaanderen.be/> (accessed 5.10.23).

Target site 4: Land subsidence in the Antwerpen area - (Deliverables: D.2.1./D.2.1.4./D.4.4./D.4.4.4.)

This target site is a newly defined area from the original submitted project as the previous area was not suitable from different points of view to fulfill the expectations of the project.

4. Introduction

4.1. Purpose and Scope

The following report presents the annual findings of our project, focusing on the regions of Antwerp and Saint Vaast, located in North Flanders and Northwest of Wallonia in Belgium respectively. The purpose of this report is to present a comprehensive summary of the research activities undertaken in the past year, with a specific focus on the updates made to the PS-InSAR measurements of land surface deformation. The report provides an in-depth analysis of the updated time series data up to 2023 for both case studies.

Within a small region of the square located in the Antwerp region, we developed a one-way 3D-hydrogeological model coupled to a 1D-geomechanical model to distinguish the effects of different drivers of deformation in different sublayers. We tried to compare the accumulation of deformations estimated in all layers in the one-way coupled model with the deformation values estimated from PS-InSAR.

Moreover, in the Saint Vaast region, we analyzed the deformations observed through PS-InSAR and compared them to the data obtained from piezometric wells to find the correlation between the time series of deformation and water level head at the location of piezometric wells.

The scope of this report is to present the outcomes of these analyses, discuss their implications, and provide recommendations based on the findings. By doing so, we aim to contribute to the understanding of geotechnical dynamics and their applications in these regions.

4.2. Background

Geotechnical studies and monitoring play a vital role in understanding and managing ground deformations, which are crucial for various objectives. Our research in the last year focuses on two key regions: Saint Vaast and Antwerp, both of which are characterized by unique hydrogeological and geotechnical conditions.

In recent years, the application of advanced remote sensing techniques has helped the field of geotechnical monitoring by providing additional data from land surface deformation. One such technique is the PS-InSAR algorithm, which utilizes radar data to detect and estimate ground deformations with high precision and accuracy. This algorithm has proven to be a valuable tool for assessing surface displacements over large areas, helping valuable insights into subsurface processes.

An old drainage adit under the Saint-Vaast region allows the mine water discharge to the Haine River. As far as our knowledge goes, the Saint-Vaast area has already been affected at least twice (in 2009 and 2018), by a clogging rupture in the drainage adit. This event has induced a displacement at the surface which is observed by PS-InSAR.

In the Antwerp region, our objective is to determine the contribution of shallow and deeper layers to observed surface deformations. Using the integration of the PS-InSAR estimation and one-way 3D hydrogeological model coupled to the 1D-geomechanical model, we aim to differentiate between deformations originating from the shallow layers and those associated with the deeper layers. This distinction is crucial for understanding the area's geomechanical behavior and gaining insights into subsurface processes.

The significance of this project lies in its ability to bridge the gap between theoretical understanding and real-world applications by integrating radar data analysis, geotechnical modeling, and field measurements. Our findings have the potential to provide valuable insights into the differentiation of deformations between shallow and deeper layers in the Antwerp region, contributing to the advancement of geotechnical knowledge and practical solutions. Moreover, the findings in the Saint-Vaast region could help future hazard assessments.

4.3. Methodology

4.3.1 Multi-temporal InSAR (MTI) Algorithm

The analysis process for MTI can be categorized into two workflows: (1) creating differential interferograms and (2) generating displacement time series. The first workflow in MTI analysis involves downloading SLC and orbit data, co-registering the SLC stack, configuring image pairs, generating interferograms, and performing phase unwrapping. The interferogram's phase components, related to SAR imaging geometry and surface topography, are calculated using satellite orbital parameters and a digital elevation model (DEM). Subtracting these components from the interferometric phase produces the differential phase, which ideally represents ground displacement. However, it can also contain non-displacement factors like atmospheric delay and residual errors. The goal is to isolate the deformation signal by analyzing a stack of differential phase observations (Figure 48).

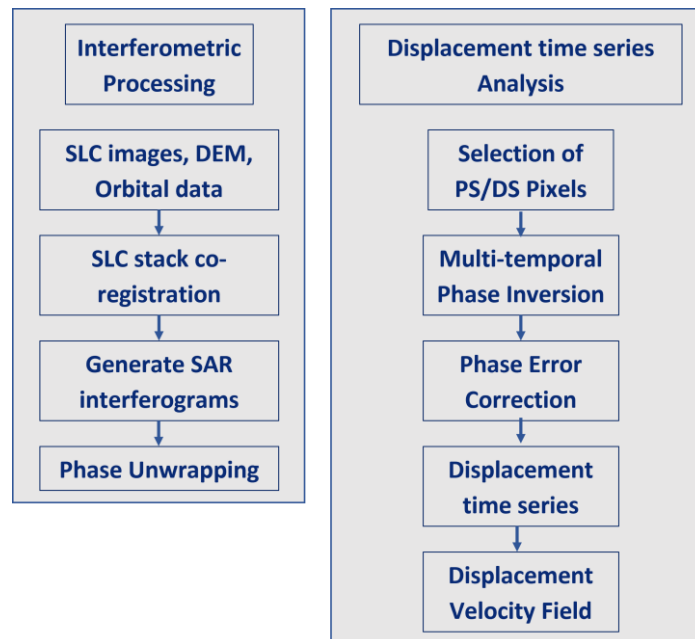


Figure 48. A generalized processing chain for retrieving ground displacement velocity and time series data from SAR imagery by multi-temporal InSAR analysis.

There are two main categories in established MTI (Multi-Temporal InSAR) approaches: (1) Persistent Scatterer InSAR (PSI) and (2) Small Baseline Subset (SBAS) InSAR. These classifications have been discussed in previous studies (Casu et al., 2006), (Ferretti et al., 2001), (Hooper, 2008), (Sadeghi et al., 2021), and (Shanker et al., 2011). PSI is particularly well-suited for areas characterized by localized, high-reflectivity radar backscatters. This makes it highly effective in urban regions and man-made infrastructure where there are numerous permanent radar targets. The LASUGEO Project has leveraged the benefits of PSI for its analysis and applications in Antwerp and Saint-Vaast areas.

The PSI or Persistent Scatterer Interferometric Synthetic Aperture Radar (PS-InSAR) algorithm is a technique that uses radar satellite imagery to measure and monitor surface deformation. It identifies stable reflection points on the Earth's surface, called persistent scatterers, from a series of radar images. By analyzing the phase differences between these images, the algorithm accurately calculates surface movement with millimeter-level precision.

InSAR data can be processed by several commercial or open-source software packages. In this study, we used open-source software InSAR Scientific Computing Environment (ISCE) (Rosen et al., 2012) for generating interferograms and the Stanford Method for Persistent Scatterers (StaMPS) (Hooper, 2008) for PSI analyses.

4.3.2. One-way 3D-Hydrogeological Model Coupled to 1D- Geomechanical Model; Antwerp Area

The conceptual model for the coupled 3D-hydrogeological and 1D-geomechanical model was developed through a systematic approach that considered the available geological, hydrogeological, and geotechnical data for the Antwerp area. A comprehensive review of existing literature and previous studies served as the foundation for the model development. An extensive review of existing literature, research papers, and reports related to hydrogeology and geomechanics in the Flanders region was conducted. This review provided valuable insights into the geological and

hydrogeological characteristics, as well as previous conceptual models or frameworks proposed by other studies. The term "One-way 3D-Hydrogeological Model Coupled to 1D-Geomechanical Model" refers to a modeling approach that integrates a three-dimensional (3D) hydrogeological model with a one-dimensional (1D) geomechanical model. This approach aims to simulate and understand the interaction between groundwater flow (hydrogeology) and subsurface deformation (geomechanics) within a specific region.

In the previous year, the annual report centered on gathering hydrogeological data from various reports and sources relevant to the Antwerp area. These data were employed to construct a three-dimensional hydrogeological model using the MODFLOW software, which models the flow of groundwater. The model incorporated geological data, measurements of groundwater levels, and other hydrogeological parameters. Known hydraulic conditions were represented by assigned values at the boundaries of the model, referred to as prescribed head values. These achievements, which involved the integration of MODFLOW, established the groundwork for the subsequent stages of the ongoing study. Furthermore, the methodology employed in the previous year will be omitted in the current report. As a result of groundwater extraction, changes in pore pressure caused by fluctuations in piezometric head induce variations in effective stress within the 1D model column. This hydromechanical coupling is responsible for the observed deformations at the land surface (Lo et al., 2022). A decrease in pore pressure corresponds to an increase in effective stress. Pore pressure propagation occurs rapidly in aquifers but may be delayed in low permeability layers. In this project, we utilized the SUB module of MODFLOW, which enabled us to simulate both recoverable (elastic) and non-recoverable (inelastic) interbed compactions. This simulation could be conducted considering scenarios with and without delayed drainage.

For the SUB package, if there is a small change in effective stress and we assume that all deformation is caused by the change in hydraulic head, the deformation of the layer can be estimated using the following linear approximation:

$$\Delta b = S_{sk} b \Delta h \quad (1)$$

$$S_{sk} = \begin{cases} S_{ske} & \sigma' < \sigma'_{max} \\ S_{skv} & \sigma' > \sigma'_{max} \end{cases} \quad (2)$$

Where Δb is the change in the thickness of a given layer with the starting thickness of b , and S_{sk} is the skeletal specific storage. S_{ske} and S_{skv} are the elastic and inelastic (virgin) skeletal specific storage respectively. σ'_{max} is the highest previous effective stress expressed in terms of preconsolidation stress (Hoffmann et al., 2003).

In the terminology of SUB package, interbeds denote a poorly permeable bed within a relatively permeable aquifer. When the SUB Package is incorporated into a MODFLOW-2000 simulation and delay interbeds are employed, the equations that describe the diffusion process from the interbeds (Eq. 3) are interconnected with the equations that depict three-dimensional groundwater flow (Eq. 4).

$$\frac{\partial^2 h}{\partial z^2} = \frac{S'_s}{K'_v} \frac{\partial h}{\partial t} \quad (3)$$

S'_s is the specific storage of the interbed,

K'_v is the vertical hydraulic conductivity of the interbed, and

t is time.

$$\frac{\partial}{\partial x} \left(K_{xx} \frac{\partial h}{\partial x} \right) + \frac{\partial}{\partial y} \left(K_{yy} \frac{\partial h}{\partial y} \right) + \frac{\partial}{\partial z} \left(K_{zz} \frac{\partial h}{\partial z} \right) - W = S_S \frac{\partial h}{\partial t} \quad (4)$$

x is the Cartesian coordinate in the x direction,

y is the Cartesian coordinate in the y direction,

z is the Cartesian coordinate in the z direction,

K_{xx} is the component of the hydraulic conductivity tensor in the x direction,

K_{yy} is the component of the hydraulic conductivity tensor in the y direction,

K_{zz} is the component of the hydraulic conductivity tensor in the z direction,

W is the volumetric flux per unit volume of sources and (or) sinks of water, and

S_S is the specific storage.

The assumption behind the SUB package sometimes is extreme and far from reality. For example, SUB package assumes that the subsurface materials exhibit linear elastic behavior, meaning the deformation is directly proportional to the applied stress. This assumption simplifies the modeling of subsidence-induced deformation. The approach also includes the assumption of constant geomechanical parameters over time. It's important to note that these simplifications and

assumptions allow for efficient modeling of displacements effects but may introduce some limitations and potential deviations from real-world conditions. The ongoing review research manuscript conducted by a group from the University of Liege comprehensively discusses the challenges and limitations associated with subsidence modeling, including the assumptions and potential constraints encountered. Additionally, two other abstracts related to this topic have been published in scientific conferences. (Moreau et al., 2023b), (Moreau et al., 2023a).

4.4. Data and measurements

4.4.1. PS-InSAR Observation in Antwerp

During the past year, the PS-InSAR data of Sentinel-1A were updated to include observations up until January 2023 in the Antwerp area. By incorporating this updated dataset, our study benefits from the most recent information on ground movements, contributing to a more accurate understanding of the dynamics and geohazards within the Antwerp area. Table 13 provides a concise overview of the current radar data availability, highlighting their specific characteristics and the status of their processing.

Sensor type	Antwerp			
	Spanning time	Mode	Track number	Status
ERS 1	1992-2001	Descending	423	Processed
Envisat	2003-2010	Descending	423	Processed
Sentinel	2016-2023	Ascending/ Descending	88/37	Processed
TerraSAR-X	2019-2021/ 2014-2016/ 2019-2020/ 2019-2021	Ascending/ Descending/ Descending/ Ascending	25/48/48/116	Raw Data Received

Table 13. Concise overview of the current radar data available in Antwerp region.

A proposal was submitted, funded and accepted by the German Space Agency (DLR) to request the acquisition of commercial high-resolution TerraSAR-X radar data. The proposal outlined the objectives of the study and highlighted the need for high-quality radar imagery to support the research. Following the submission of the proposal, the request was approved, and the data acquisition was initiated.

During the past year, the PS-InSAR data of Sentinel-1A were updated to include observations up until January 2023 in the Antwerp area. By incorporating this updated dataset, our study benefits from the most recent information on ground movements, contributing to a more accurate understanding of the dynamics and geomechanical procedures within the Antwerp area.

In 2022-2023, we reached out to SkyGeo, reputable company based in the Netherlands, to enhance the quality of our research findings. While we had already collected and processed Sentinel-1A satellite data, SkyGeo's advanced commercial software, DePSI, enabled us to achieve superior results in our analysis. Comparing to our own processing (from ISCE-STAMPS chain), the time series of deformation provided by SkyGeo exhibited significantly lower levels of noise compared to our initial results. The results obtained from their software demonstrated lower noise levels in the time series of deformation, providing us with more accurate and reliable measurements. Additionally, the number of observed PS points increased, allowing for a more comprehensive analysis of surface deformation patterns. The PS data provided by SkyGeo covers a significant time, from 2017 to 2022, and encompasses the entire Antwerp area.

4.4.2. Geomechanical Data (in Antwerp)

In 2022, we requested access to the geotechnical data in Flanders from the Geotechnics unit at the Department of Mobility and Public Works (MOW). This data was essential for our research project, as it allowed us to gain insights into the shallow layer (first 5 meters) of the soil. The geotechnical data provided by the MOW primarily consisted of information obtained from boreholes. These boreholes were strategically drilled across various locations in Flanders (Figure 49). For the objectives of this study, swelling and compression constants values were extracted from geotechnical reports and were used in 1D-geomechanical modelling of Antwerp local Model. Due to the lack of corresponding parameters for the deeper layers, we had to extract them from the studies conducted in the other areas distant from Antwerp region (Deng et al., 2011; Nguyen et al., 2014). It is important to acknowledge the limitations and potential uncertainties associated with utilizing data from different locations. However, given the absence of direct measurements for the deeper layers in the Antwerp region, this methodology served as a practical solution to gather relevant

information.

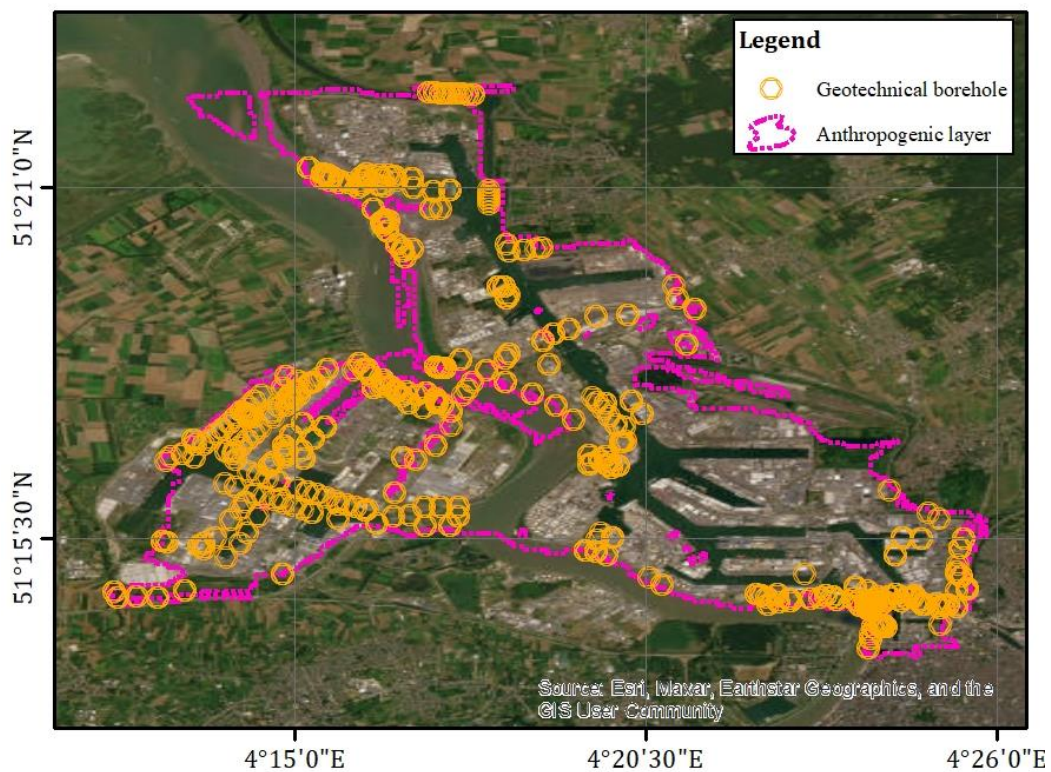


Figure 49. Distribution map of geomechanical boreholes in the Antwerp harbour

4.4.3. Evolution of Monthly Pumping Rate (in Antwerp)

In the past year, a key aspect of our research involved calculating the monthly pumping rates of wells in the Antwerp area, specifically focusing on three aquifers that are considered significant in our modeling approach. To achieve this, we calculated the cumulative monthly rate of all pumping wells in each aquifer.

4.5. Results and discussion

4.5.1. PS-InSAR Observations in Antwerp

In our study, we utilized two distinct datasets of PS-InSAR observations, each providing valuable insights into surface deformation patterns over different time periods. The first dataset, which was processed by our team, includes data from ERS1/2 (1992-2001), Envisat (2003-2010), and Sentinel (2016-2022). In the past year, this dataset was updated to include Sentinel acquisitions up until 2023, further extending the temporal coverage and enabling a more comprehensive analysis of deformation trends. Additionally, we integrated a second dataset processed by SkyGeo company, which focuses on Sentinel acquisitions from 2017 to 2022 in both ascending and descending modes.

4.5.2. PS-InSAR Data Processed in the LASUGEO Project at the Location of Antwerp Local Model.

In the past year, we have utilized the power of Python programming, along with the vast array of Python libraries, to perform extensive data analysis on PS-InSAR results. This analysis was targeted at identifying and understanding ground deformation patterns in the local model of Antwerp.

The program was designed to analyze three different sets of data: ERS, ENVISAT, and Sentinel data. The PS-InSAR data was transformed into a format that can be easily analyzed, and further filtered based on a user-defined geographical area in Antwerp. The data was then processed to calculate the average deformation over time within the specified area. By shifting the entire time series data by subtracting the value at the first date, we managed to create a more relatable and understandable visualization of deformation trends and considerations of first date as the reference date instead of single master acquisition date.

Each dataset produced its own unique plot, showcasing the average LOS deformation timeseries of the points located

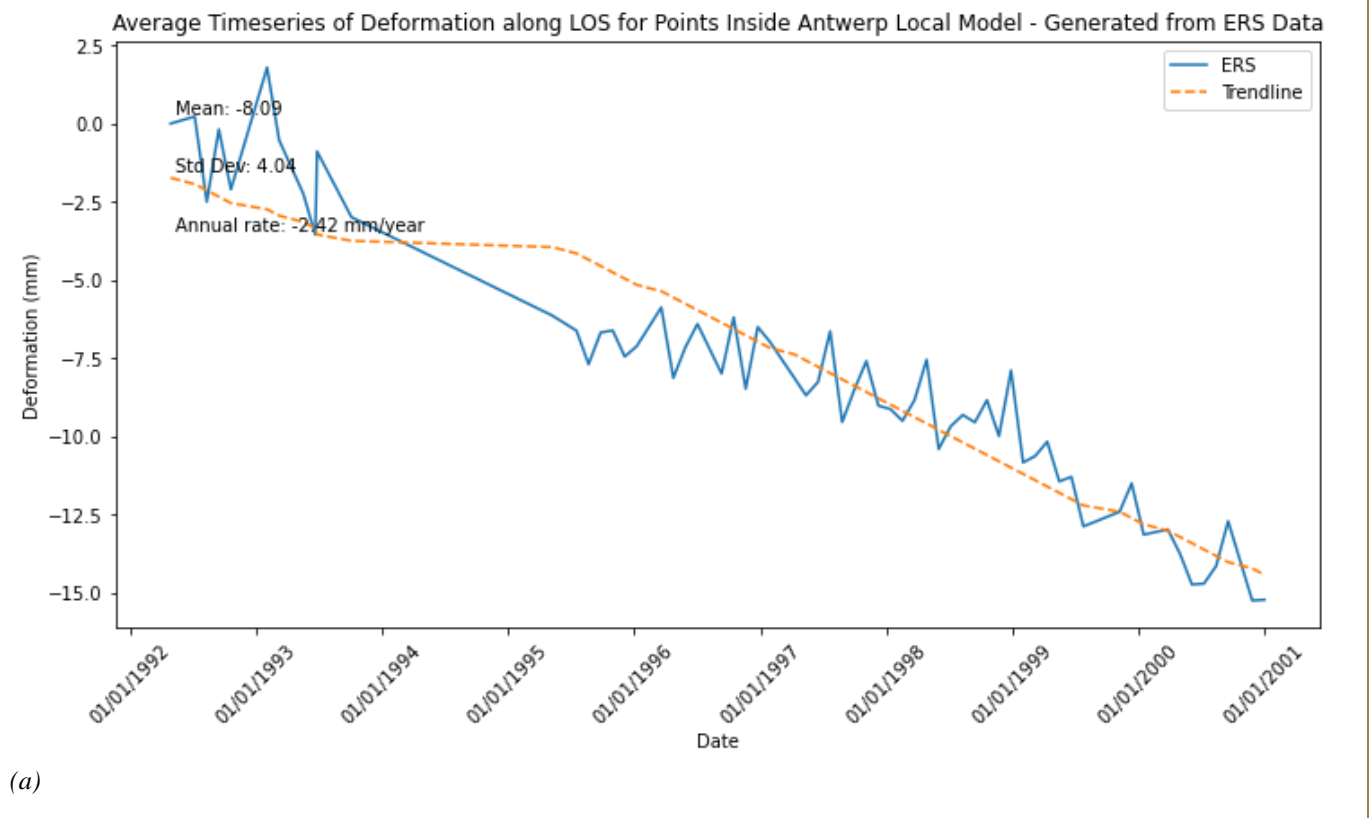
in the border of local model of Antwerp, and a corresponding trendline. This allowed us to perceive the evolution of the deformation over time clearly.

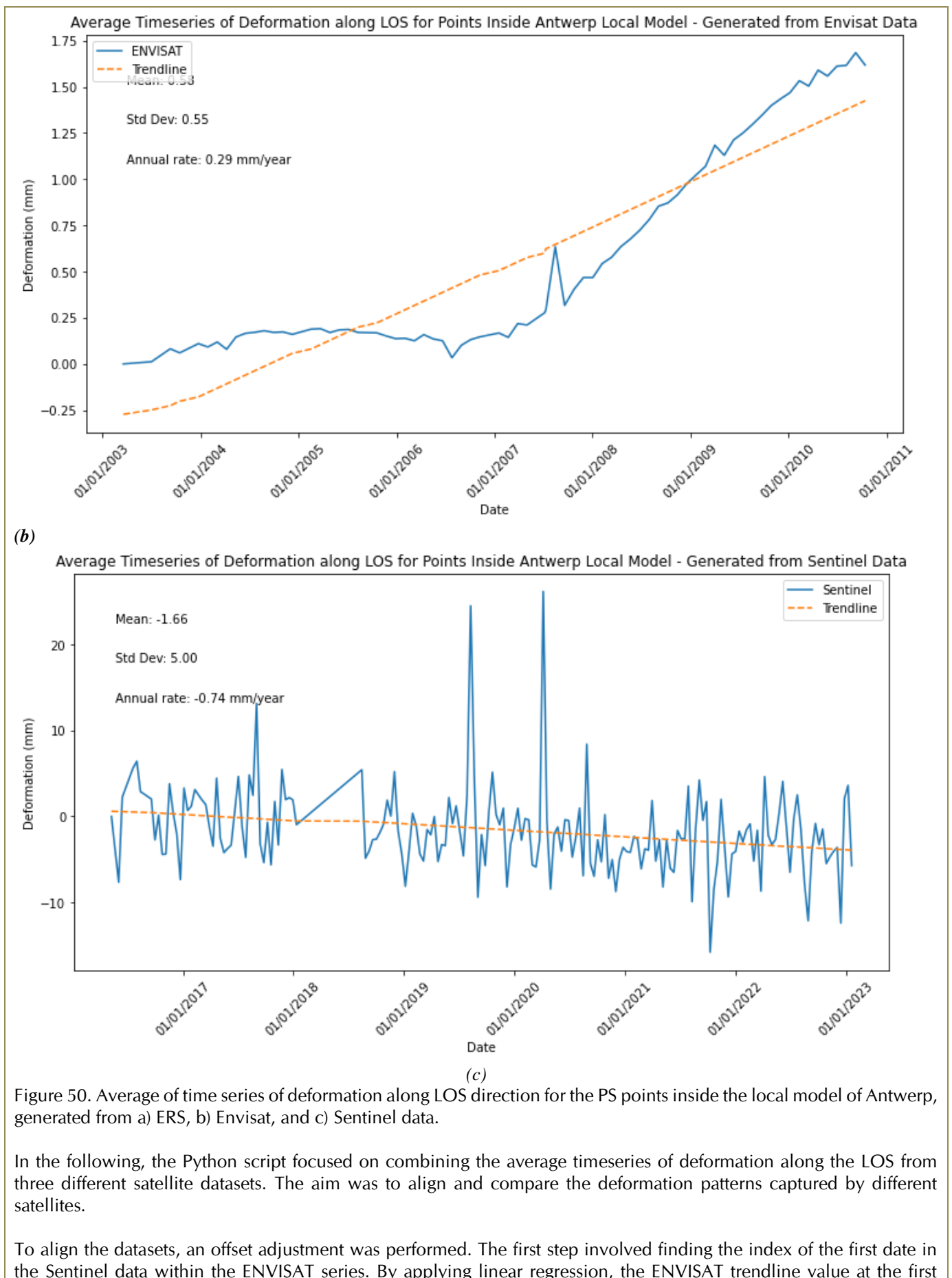
For the ERS data, trendline starts at around -1.73 mm and ends at about -14.43 mm, showing a general decrease over time. The timeseries data also displays a decrease, going from 0.00 to -15.24 mm (Figure 50a).

For the ENVISAT data, the trendline starts at approximately -0.27 and ends at approximately 1.43 mm, showing an overall increase with very small rate. The shifted data also exhibits a general increase from 0.00 to 1.61 mm (Figure 50b).

Looking specifically at the Sentinel data, the trendline shows a gradual decrease over time (from 0.60 to -3.93 mm), indicating that there is a general downward trend in the deformation timeseries. This could potentially suggest that there is a consistent subsidence occurring within the specified area in Antwerp over the period from 2016 to 2023 (Figure 50c).

Values of annual rate are specified on Figure 50.





Sentinel date was determined, enabling alignment at the common starting point. Additionally, an offset was calculated to align the ENVISAT series with the ERS series at its first date. This offset was based on the difference between the ERS and ENVISAT trendlines at time zero. Both the ENVISAT and Sentinel series were then shifted by this calculated offset. The combined shifted timeseries for ERS, ENVISAT, and Sentinel were plotted, showcasing the deformation patterns captured by each satellite. The ERS data was plotted in blue, ENVISAT data with the offset adjustment in red, and Sentinel data with the offset adjustment in green. Furthermore, trendlines were plotted for each dataset separately. The ERS trendline was shown in blue, the shifted ENVISAT trendline in red, and the shifted Sentinel trendline in green, all using dashed lines. (Figure 51).

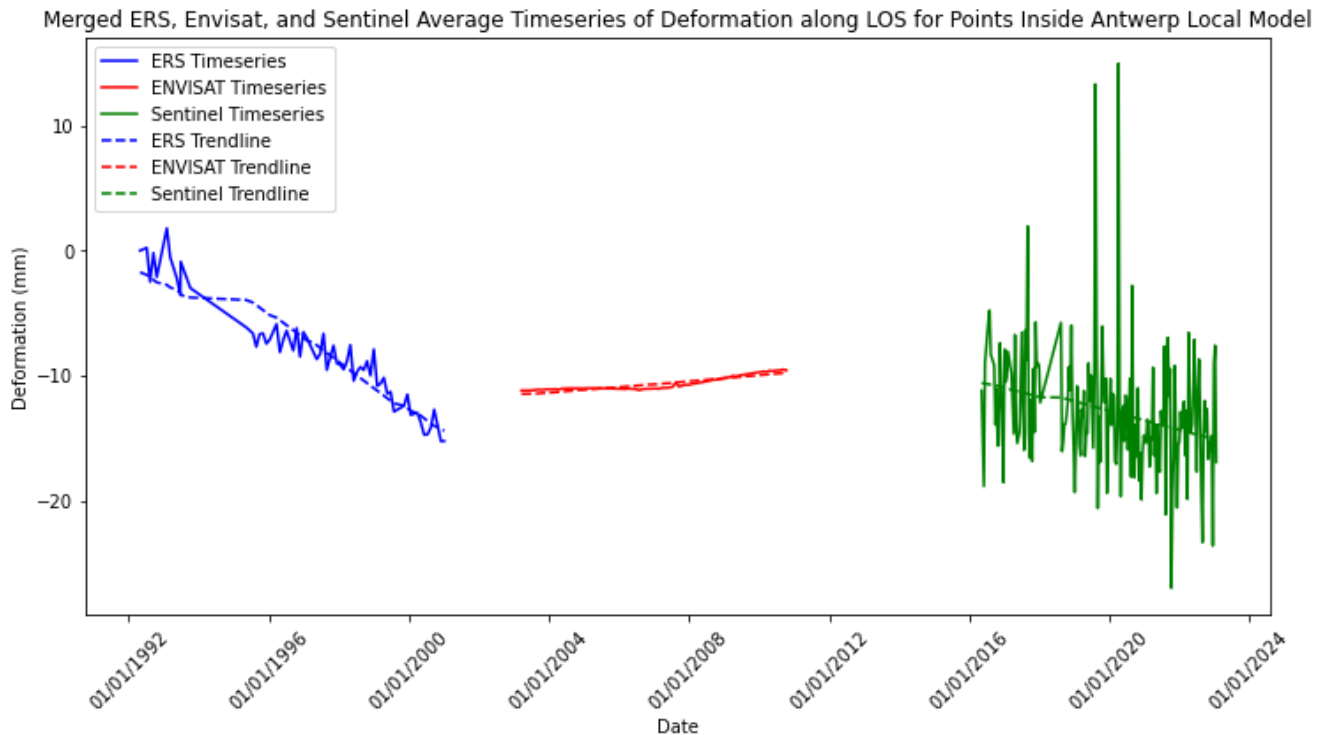


Figure 51. Merged average LOS timeseries of deformation generated from ERS, Envisat and Sentinel PS-InSAR results for PS points inside the Antwerp Local Model.

These findings lay the foundation for further investigations and the comparison with results which are conducted in the future parts. It is worth mentioning that the shifting alignment approach used in this analysis provides a practical way to compare and visualize the deformation patterns from different satellite datasets. However, the shifting alignment involved calculating offsets for second and third timeseries based on the linear trendlines of the first and second timeseries respectively. Therefore, due to dissimilar trendlines of three different datasets, the offset calculation is not truly representative for the offsets between them in the reality.

As part of our efforts in the last year, we analyzed the vertical deformation time series of Sentinel Data within the border of Antwerp local model. We applied several smoothing techniques, including Moving Average Smoothing, Exponential Smoothing, and Savitzky-Golay Filtering. Figure 52 shows the smoothed time series for each of these techniques. We also calculated the annual linear deformation rate based on the smoothed data. The linear rates calculated were:

Original Vertical Data: -0.57 mm/year

Moving Average Smoothed: -0.56 mm/year

Exponential Smoothing: -0.50 mm/year

Savitzky-Golay Filter: -0.56 mm/year

These values will be compared to the linear rate calculated by the SkyGeo Company.

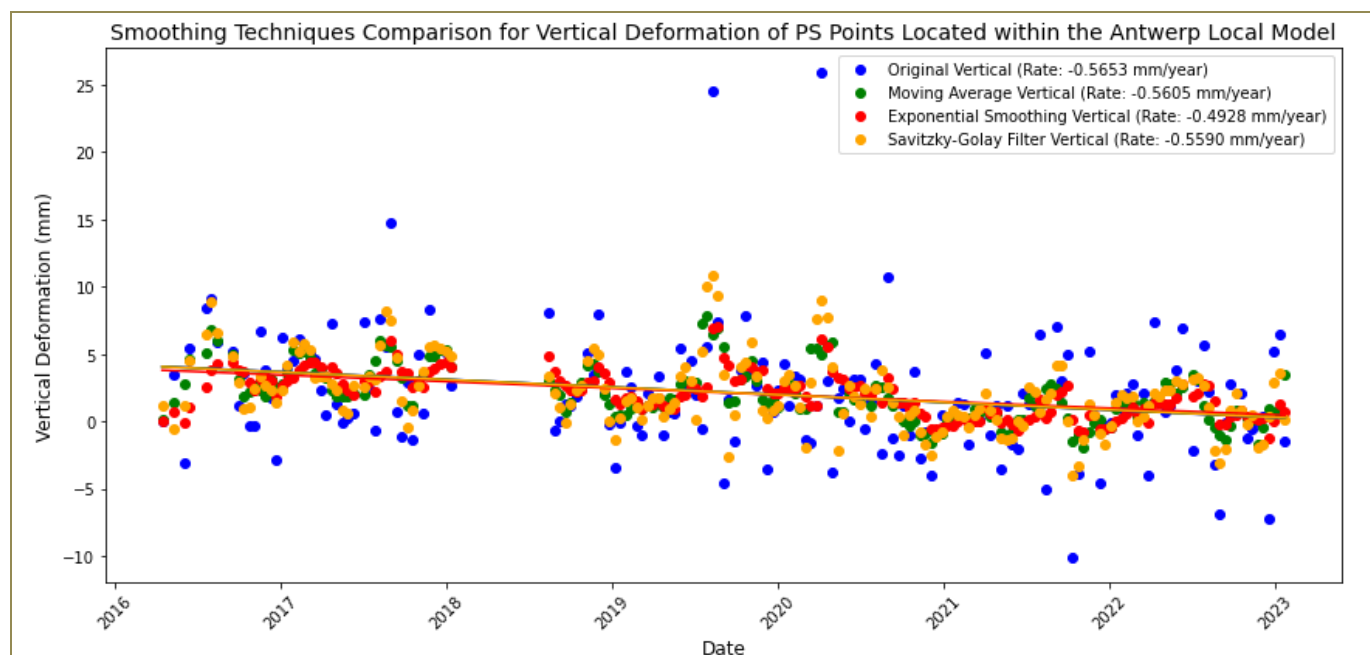


Figure 52. Comparison of different smoothing techniques for noise reduction of average timeseries of vertical deformation of PS points located within the border of Antwerp local model.

The four different datasets from SkyGeo provided us with many points across multiple acquisition periods, allowing accurate monitoring of deformation in the Antwerp area, particularly Antwerp local model (Table 14). The estimated models (linear, quadratic, seasonal) provided valuable insights into the deformation patterns and trends.

Midden - 1 (S1 dsc T37)	Midden - 2 (S1 asc T88)	West - 1 (S1 dsc T110)	West - 2 (S1 asc T161)
Satellite: Sentinel-1	Satellite: Sentinel-1	Satellite: Sentinel-1	Satellite: Sentinel-1
Pass direction: Descending	Pass direction: Ascending	Pass direction: Descending	Pass direction: Ascending
Incidence angle: 39.1°	Incidence angle: 38.2°	Incidence angle: 36.9°	Incidence angle: 38.9°
Resolution: 13.2 x 3.5 meters			
Acquisition period: October 4, 2017 - October 26, 2022	Acquisition period: October 1, 2017 - October 29, 2022	Acquisition period: October 9, 2017 - October 31, 2022	Acquisition period: September 30, 2017 - October 22, 2022
Number of acquisitions: 152	Number of acquisitions: 155	Number of acquisitions: 152	Number of acquisitions: 150
Number of points: 73,353,321	Number of points: 61,911,475	Number of points: 54,073,190	Number of points: 60,226,698
Estimated models: Linear, quadratic, seasonal.			
Reference date: October 4, 2017	Reference date: October 1, 2017	Reference date: October 9, 2017	Reference date: September 30, 2017

Table 14. Characteristics of four different datasets provided by SkyGeo.

A comparison was made between the number of PS points resulting from our PS-InSAR processing conducted as part of the LASUGEO project and the PS-InSAR processing by SkyGeo. The comparison revealed that the SkyGeo results contained a higher number of PS points compared to our own processing. In the local model of Antwerp, our processing identified 97 PS points, while SkyGeo's processing identified 213 PS points. This significant difference in the number of PS points suggests that the SkyGeo dataset provides a more extensive coverage of the study area (Figure 53).

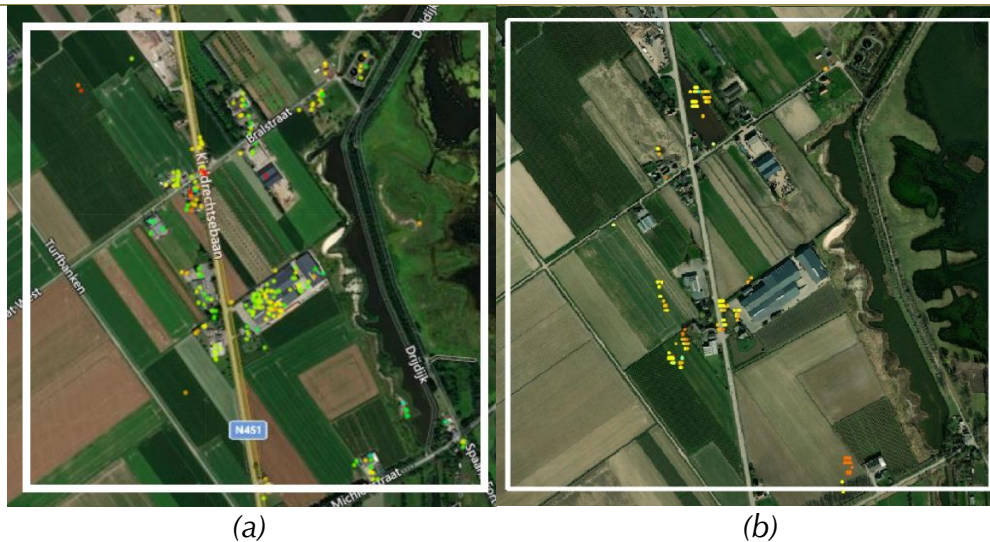


Figure 53. Comparison between density of PS points located in the border of Antwerp local model, from processing of a) SkyGeo and b) LASUGEO project.

Data provided by the SkyGeo portal, which considered the area of 1.0900 km² within the local model of Antwerp, resulted in an average linear displacement rate of -1.6 mm/year. The range of displacement rates provided by SkyGeo varied from -6.2 mm/year to 4.2 mm/year (Figure 54).

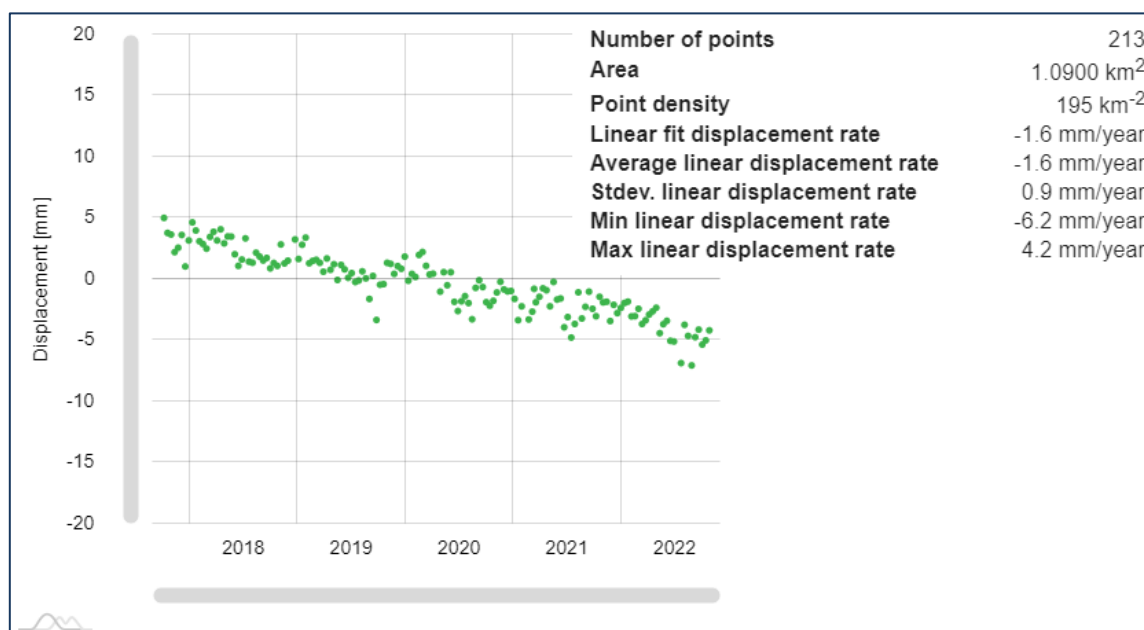


Figure 54. Timeseries of deformation for the PS points located within the border of Antwerp local model provided by SkyGeo.

While comparing the data from our project and the SkyGeo portal, which are based on the same geographical area, a subtle difference is noticeable in the average linear displacement rates derived from both methods. In our project, we observed an average rate of -0.56 mm/year, whereas the SkyGeo data suggested a rate of -1.6 mm/year.

Given the scale and context of these measurements, a discrepancy of approximately 1 mm/year, while present, may not be significantly impactful. Both measurements indicate a similar trend of displacement, providing assurance that the observed phenomena are consistent between both methodologies. The difference of 1 mm/year could be within the acceptable range considering the inherent uncertainties in the measurement, processing, and analysis of such geospatial data.

This slight discrepancy could be attributed to variations in the methodologies adopted for data processing and interpretation. Moreover, it's important to note that this kind of geospatial analysis is more about identifying and understanding broad trends and patterns than about matching precise rates. From that perspective, the key takeaway here is that both our project and the SkyGeo analysis confirm a similar trend of displacement.

4.5.3. Hydrogeological Model Coupled to 1D-Geomechanical Model in Antwerp.

The aim of the present report was to consider the nature of land subsidence in the Antwerp region, by employing a 3D-flow model coupled to a 1D-geomechanical model. Having incorporated the piezometric data presented in the preceding report, our focus in this year report has been on the structural and geomechanical behaviour of the various layers during the simulation period of 2007 to 2016.

The land surface deformation in this part of the work, was evaluated using a 3D finite-difference groundwater flow model, MOFLOW, coupled to a 1D geomechanical model, SUB. This model aimed to estimate the consolidation over time in various hydrogeological layers within a 1 square kilometer area in Antwerp.

Hydrogeological parameters, such as horizontal and vertical hydraulic conductivity values, were taken from previous studies. They were then used to simulate the piezometric head changes in the various model layers over 2007-2016. The results show a decrease in the piezometric head in the top six layers and an increase in the bottom three layers over the period 2007-2016. It was also found that the layers demonstrated varying levels of compaction and rebound, with the Polder deposits (Layer 1) and the Tongeren aquitard (layer 5) experiencing the most significant consolidation and the Bartoon aquitard (layer 7) and the Wemmel-Lede aquifer (layer 8) and sands of Brussels layers having the strongest rebound (Figure 55).

Time Series of Deformation in Different Layers of the 1D-Geomechanical Model of Antwerp

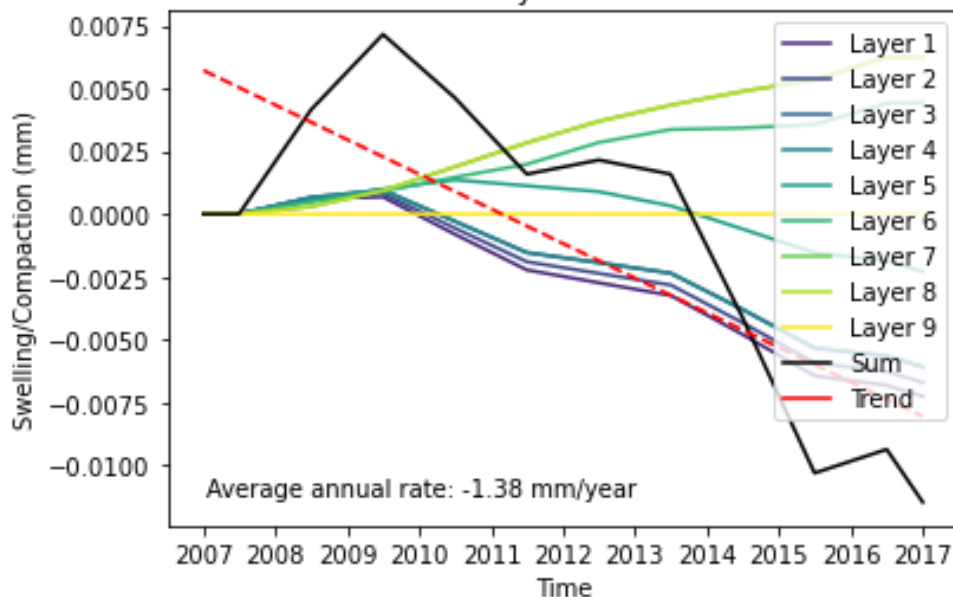


Figure 55. Timeseries of deformation in different layers of the 1D-geomechanical model simulated by SUB package.

The observed annual linear rate of cumulative deformation, as indicated by the geomechanical model simulation (Figure 55), was found to be -1.38 mm/year over the simulation period. This timeseries was compared directly with the combined timeseries of deformation unveiled by the PS-InSAR for comparative analysis. Due to temporal overlap constraints, only the Envisat PS-InSAR data could be directly compared with the geomechanical model simulation. Furthermore, the time of overlap was limited to the period between 2007 and 2010. The Envisat timeseries, with its linear annual rate of 0.23 mm/year, was relatively close to the average rate observed in the geomechanical model simulation, highlighting a degree of consistency across the two methodologies (Figure 56). Nevertheless, the observed patterns across the two timeseries did not exhibit a direct correlation. This could potentially be attributed to the inherent limitations and simplifications associated with the SUB package utilized for 1D-geomechanical modelling. Despite this, the comparative values generated by the two methods were found to be reasonable. In the light of these results, it is essential to note that while the numerical discrepancy in rates and divergence in pattern might initially suggest a degree of divergence, it is within a range that can be reasonably expected given the simplifications involved in the SUB

package. This comparison underscores the importance of multiple observation techniques to understand complex geomechanical processes, while taking into consideration the potential limitations of each method. These limitations have been discussed in a forthcoming review paper, which is currently in the process of being submitted.

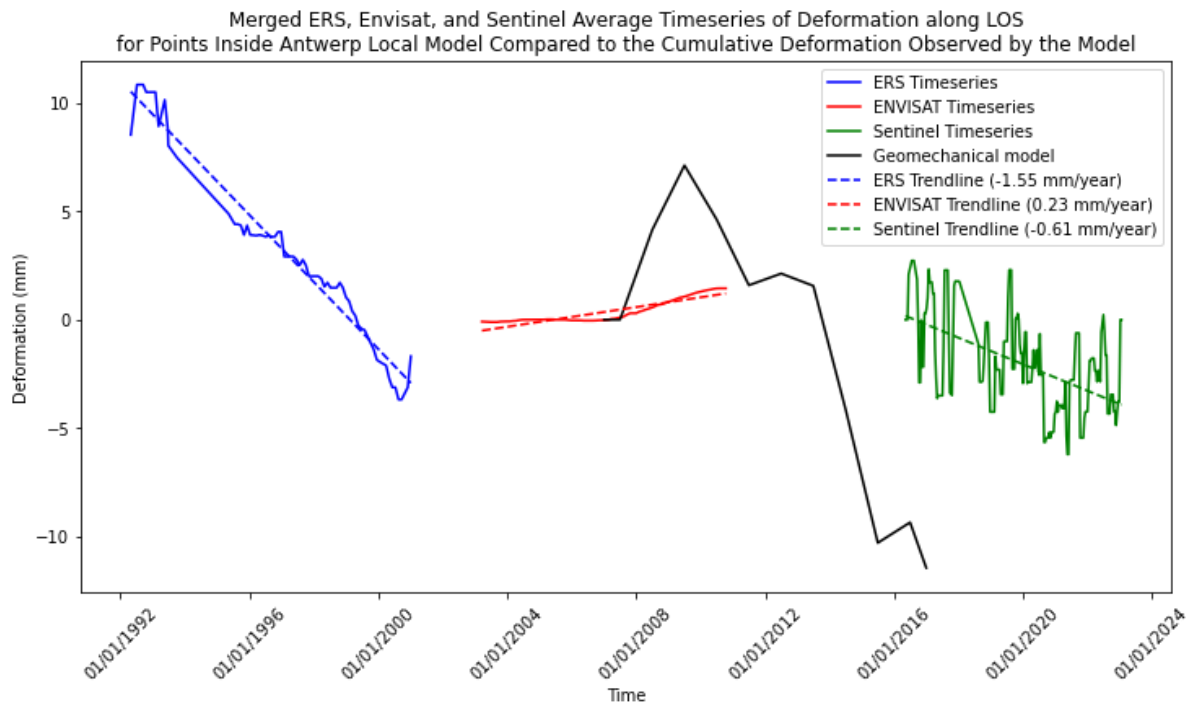


Figure 56. Merged ERS, Envisat, and Sentinel average timeseries of deformation along LOS for points inside Antwerp local model compared to the cumulative deformation observed by the geomechanical model.

4.5.4. Discussion on Geomechanical Model Using Additional Data

In our study, a comparative analysis between PS-InSAR observations and Geomechanical model simulations revealed a degree of correlation. However, this association was not uniformly consistent across the entirety of the examined period. Geomechanical modeling detected evidence of swelling and compaction across various strata, including the Boom Clay layer. Given our understanding of this layer as an over-consolidated formation, we must approach these results with a degree of circumspection. In fact, over-consolidated clay, like Boom Clay, typically undergoes significant prehistoric stress, causing it to compress and release much of its water content. This process results in a highly dense and stiff clay formation. Thus, conventional expectations for this type of clay would involve minimal additional compaction or swelling. The detected deformations in the Boom Clay layer, as per our geomechanical model, hence, raise questions that warrant further investigation.

Moreover, our investigation discovered an intriguing instance of stability at a location of a power tower station. In our PS-InSAR analysis for the LASUGEO project, this site was not detected as a PS point. However, data from the SkyGeo dataset contradicted this by clearly identifying this stable trend during 2017-2022 (Figure 57). Given the inherent depth of the power tower's foundation, typically around 10 to 15 meters, the observed stability in the deformational behavior could imply the presence of stable underlying geological structures. It's noteworthy that the power tower station is situated 5.5 kilometers away from the Antwerp local model's location, yet it is precisely on identical geological formations. This observation could potentially challenge the outcomes of the local geomechanical model of SUB package. Nonetheless, the short duration of both the geomechanical model simulation and the comparative study with PS-InSAR limits our ability to make definitive assertions about these findings.

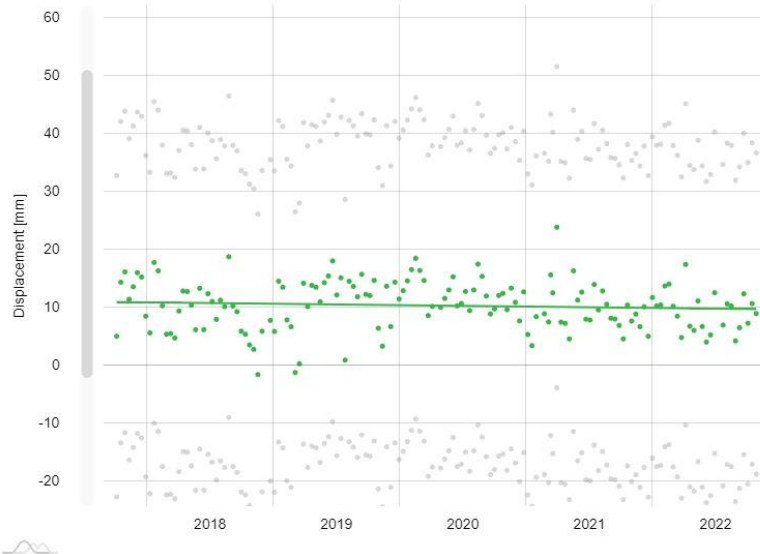


Figure 57. Timeseries of deformation at the location of power tower station located in 5.5 km from Antwerp local model provided by SkyGeo website.

Additionally, although there was not any pumping well in local model, we provided the pumping rate evolution graphs of three different aquifers of Quaternary, Campine and Oligocene (HCOV 0100, 0200, and 0400) over 2003-2023 in whole Antwerp region (Figure 58). The analysis of pumping rate evolution reveals different patterns and trends in different aquifers. Over this period, all three aquifers have seen substantial increases in pumping rates, indicative of intensified extraction activities. In summary, the data suggests an escalating trend of groundwater extraction from Quaternary and Campine aquifers over the past two decades, particularly in the latter half of the study period (2015-2023). The Oligocene aquifer experiences the least substantial pumping rate increases. These trends could be indicative of various factors such as increasing demand due to population growth or industrial needs, or potential decreases in alternative water sources.

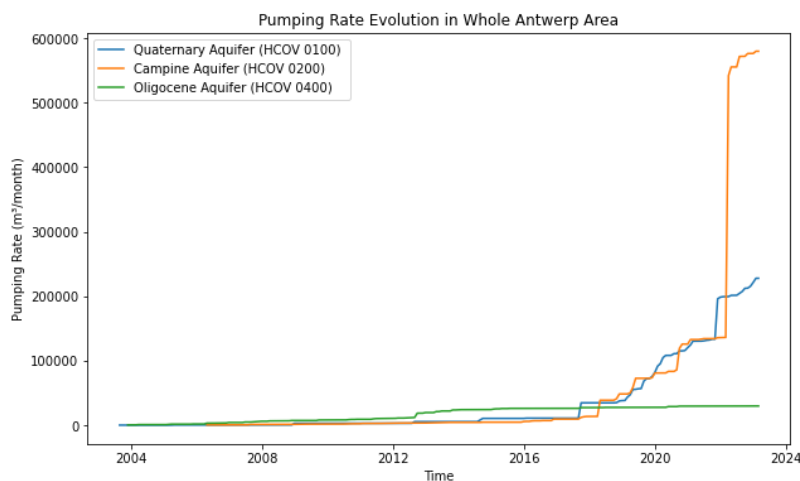


Figure 58. Pumping rate evolution in whole Antwerp Area.

To find if there is any relation between pumping rate evolution graphs and timeseries of deformation in whole Antwerp, we provided the correlation matrix which brings insights into the relationships between deformation timeseries revealed by PS-InSAR and monthly evolution of pumping rate in different aquifers (Figure 59).

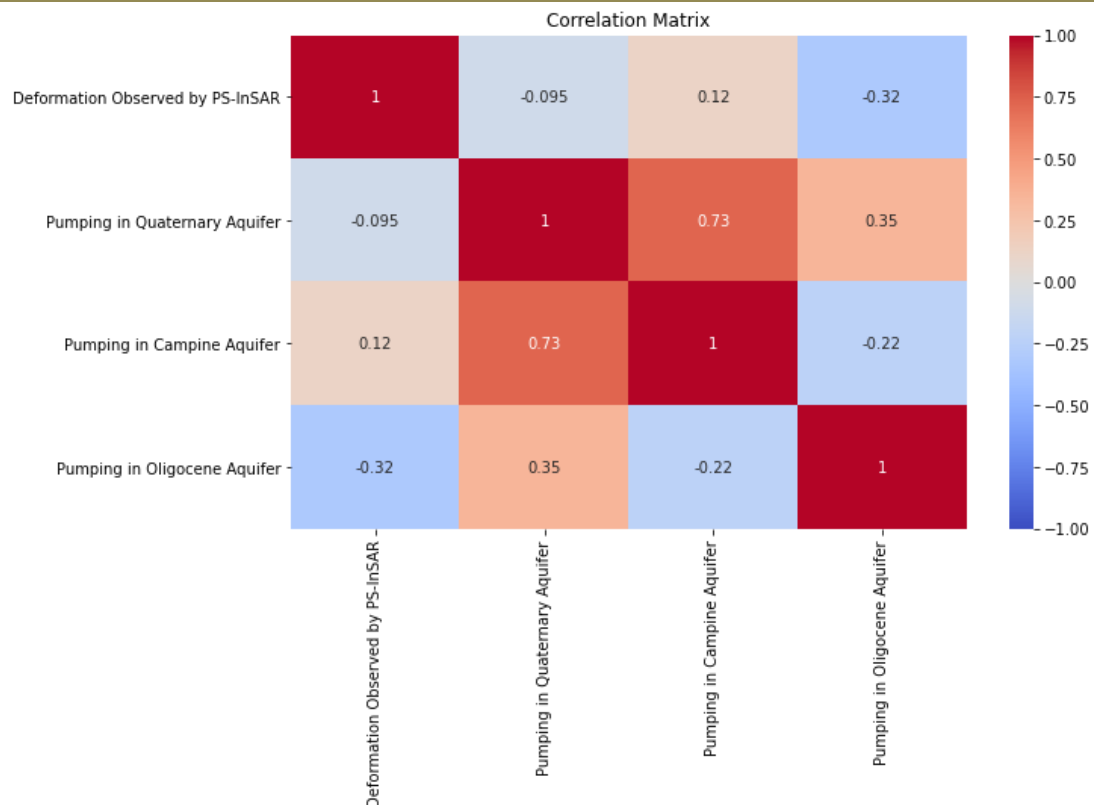


Figure 59. correlation matrix between deformation timeseries revealed by PS-InSAR and monthly evolution of pumping rate in different aquifers.

The deformation observed by PS-InSAR does not show a strong correlation with any of the pumping variables in the three aquifers. The correlation coefficient between deformation and pumping in each aquifer is relatively low, indicating a weak linear relationship. This suggests that the pumping activities in the aquifers probably are not the primary driver of the observed deformation. These findings highlight the complexity of the groundwater system and suggest that factors other than pumping, such as geological characteristics or natural subsidence, may play a role in the observed deformation.

4.6. Conclusions

In conclusion, our study has provided valuable insights into the ground deformation patterns in the Antwerp region through the analysis of PS-InSAR data and hydrogeological investigations.

In the Antwerp region, the analysis of PS-InSAR data revealed varying deformation patterns over time, indicating a complex deformation behavior. The combination of different satellite datasets allowed for the comparison and visualization of deformation patterns. However, the observed correlation between deformation and pumping activities in the aquifers was weak, suggesting that factors other than pumping may contribute to the observed deformation. The geomechanical model simulations in the Antwerp region raised questions regarding the detected deformations in the over-consolidated Boom Clay layer. The presence of stable deformation at a power tower station location challenged the local geomechanical model's predictions, suggesting the influence of stable deep structures. Nonetheless, further investigation is needed due to the limitations of the short duration of the simulation period. The pumping rate evolution graphs indicated an escalating trend of groundwater extraction in the Antwerp region, particularly in the Quaternary and Campine aquifers. However, the correlation analysis between deformation and pumping variables revealed a weak linear relationship.

4.7. References

- Casu, F., Manzo, M., & Lanari, R. (2006). A quantitative assessment of the SBAS algorithm performance for surface deformation retrieval from DInSAR data. *Remote Sensing of Environment*, 102(3), 195–210. <https://doi.org/10.1016/j.rse.2006.01.023>
- Deng, Y. F., Tang, A. M., Cui, Y. J., Nguyen, X. P., Li, X. L., & Wouters, L. (2011). Laboratory hydro-mechanical

- characterisation of Boom Clay at Essen and Mol. *Physics and Chemistry of the Earth, Parts A/B/C*, 36(17–18), 1878–1890. <https://doi.org/10.1016/j.pce.2011.10.002>
- Ferretti, A., Prati, C., & Rocca, F. (2001). Permanent scatterers in SAR interferometry. *IEEE Transactions on Geoscience and Remote Sensing*, 39(1), 8–20. <https://doi.org/10.1109/36.898661>
- Hoffmann, J., Leake, S., Galloway, D., & Wilson, A. (2003). MODFLOW-2000 Ground-Water Model—User guide to the subsidence and aquifer-system compaction (SUB) package. *USGS Ground-Water Resour. Program Open-File Rep.*, 55.
- Hooper, A. (2008). A multi-temporal InSAR method incorporating both persistent scatterer and small baseline approaches. *Geophysical Research Letters*, 35(16). <https://doi.org/10.1029/2008GL034654>
- Lo, W., Purnomo, S. N., Dewanto, B. G., Sarah, D., & Sumiyanto. (2022). Integration of Numerical Models and InSAR Techniques to Assess Land Subsidence Due to Excessive Groundwater Abstraction in the Coastal and Lowland Regions of Semarang City. *Water*, 14(2), Article 2. <https://doi.org/10.3390/w14020201>
- Moreau, A., Choopani, A., Declercq, P.-Y., Orban, P., Devleeschouwer, X., & Dassargues, A. (2023a, April 19). A Summary Review Based on Case Studies of the Challenges Related to the Comparison of Displacements Measured by PS-InSAR and Simulated by Geomechanical Coupled to Groundwater Models. The Tenth International Symposium On Land Subsidence. <https://orbi.uliege.be/handle/2268/302365>
- Moreau, A., Choopani, A., Declercq, P.-Y., Orban, P., Devleeschouwer, X., & Dassargues, A. (2023b, April 26). Difficulties arising when PS-InSAR displacement measurements are compared to results from geomechanical and groundwater flow computations. EGU General Assembly 2023. <https://doi.org/10.5194/egusphere-egu23-16384>
- Nguyen, X. P., Cui, Y. J., Tang, A. M., Li, X. L., & Wouters, L. (2014). Physical and microstructural impacts on the hydro-mechanical behaviour of Ypresian clays. *Applied Clay Science*, 102, 172–185. <https://doi.org/10.1016/j.clay.2014.09.038>
- Rosen, P. A., Gurrola, E., Sacco, G. F., & Zebker, H. (2012). The InSAR scientific computing environment. *EUSAR 2012; 9th European Conference on Synthetic Aperture Radar*, 730–733.
- Sadeghi, Z., Wright, T. J., Hooper, A. J., Jordan, C., Novellino, A., Bateson, L., & Biggs, J. (2021). Benchmarking and inter-comparison of Sentinel-1 InSAR velocities and time series. *Remote Sensing of Environment*, 256, 112306. <https://doi.org/10.1016/j.rse.2021.112306>
- Shanker, P., Casu, F., Zebker, H., & Lanari, R. (2011). Comparison of Persistent Scatterers and Small Baseline Time-Series InSAR Results: A Case Study of the San Francisco Bay Area. *Geoscience and Remote Sensing Letters, IEEE*, 8, 592–596. <https://doi.org/10.1109/LGRS.2010.2095829>

Target site 5: Land subsidence in the Saint-Vaast area - (Added and new Deliverables: D.4.5./D.4.4.5.)

This target site is an added and unplanned target side based and discovered recently by SAR data observations indicating very recent land subsidence issues in that region that were processed with the help of the ISSeP services related to the ongoing work on the post-mining effect.

5.1. Introduction

While the literature predominantly highlights the environmental problems of abandoned mines, it pays less attention to their physical hazards, and related issues (Salom and Kivinen 2020; Mhlongo 2023). To address this gap, our study focuses on the complex interactions between historical mining activities and ongoing deformations leading to hazards, with a specific emphasis on the Saint-Vaast region in Belgium. In particular, the Saint-Vaast region offers a unique case where subsurface hydrological variations, structural changes, and presence of a drainage adit from past coal mining led to complex, recurring deformation events. This work integrates advanced Persistent Scatterer Interferometric Synthetic Aperture Radar (PS-InSAR) techniques with piezometric monitoring data to comprehensively analyze ground deformation and subsurface dynamics in a post-mining context. This is the first application of such a technique in this region, allowing us to understand the relationships between surface deformation patterns, groundwater fluctuations and the presence of the adit remained from mining time in the region. By doing so, we aim to provide a clearer understanding of how past mining practices continue to influence contemporary geohazards in the future.

Saint-Vaast, a municipality located in Wallonia (Belgium), is an example of challenges associated with land surface deformation as evidenced by PS-InSAR (Choopani et al. 2022). Due to extensive coal mining that began in the late 19th century, the subsurface has experienced significant changes. These changes have transformed the region from a zone which was originally for resource extraction into the areas now characterized by high-risk of geohazards.

A drainage adit is situated approximately 30 m below the surface in Saint-Vaast. The subsurface includes confined aquifers and sublayers that have been documented to have low mechanical stability. Historically, this drainage adit played a crucial role in the coal mining period. In the present context, their existence, in combination with other

subsurface features, is responsible for a series of geohazards. In February 2009, a clog rupture occurred causing significant damage to a residential area (7 houses, the pedestrian walkways, and the road itself were affected by ground deformations implying the formation of fissure cracks in the walls of the houses). In response to this event, a drainage pipe at the mouth of the adit was installed to drain the excess water to the river Haine, providing a mitigation measure against future similar incidents. Following the 2009 event, 6 piezometric wells were installed in the region to monitor the water level in the vicinity of the adit and the ground deformations observed at the surface. There was no piezometric data available to provide evidence of increasing water levels or instability before that event. This study aims to confirm and analyze these conditions, presenting evidence of deformation occurring before 2009. By 2018, the installed pipe became obstructed due to subsurface instabilities, likely including a collapse of loose sands from the Wealden deposits leading to a new phase of rise in the water level within the aquifer. This time the pipe effectively redirected the mudflow towards the river Haine, preventing further damage to the residential areas probably after a similar clog rupture inside the adit.

Analysis of these events has indicated a strong correlation between subsurface hydrodynamics indicated by piezometric wells and surface deformations observed by PS-InSAR. Consequently, this research enables the prediction of future similar events by integrating its findings.

For this research, we used satellite data that spanning a non-continuous period of 31 years for the Saint-Vaast region, including ERS (1992–2006), Envisat (2003–2010), and Sentinel-1A (2016–2023), acquired. The deformation maps resulting from processing of radar data showed changing zones of gradual subsidence and uplift over time, closely aligning with areas historically associated with coal mining. The piezometric wells data closely align with the displacement time series obtained from PS-InSAR, indicating a strong agreement between the two.

5.2. Region of interest

5.2.1. Geographical and geological setting

The ROI is in Saint-Vaast, within the Hainaut region of Wallonia, Belgium. This region has historically been a significant coal mining zone. The ROI, situated in the Center coal basin, primarily encompasses La Louvière and extends to parts of five neighboring municipalities, including Manage, Morlanwelz, Binche, Estinnes-au-Val, and Mons. Adjacent towns include Le Roeulx, Seneffe, Chapelle-lez-Herlaimont, and Anderlues (Figure 60a).

Geologically, the subsurface consists of a Paleozoic basement corresponding to the NamurianWestphalian series (Upper Carboniferous) overlain by sedimentary series from the Meso-Cenozoic, Pleistocene, and Holocene eras. These latter deposits are primarily composed of colluvial and alluvial materials. The location of cross-section AA' has been added to Figure 60a.

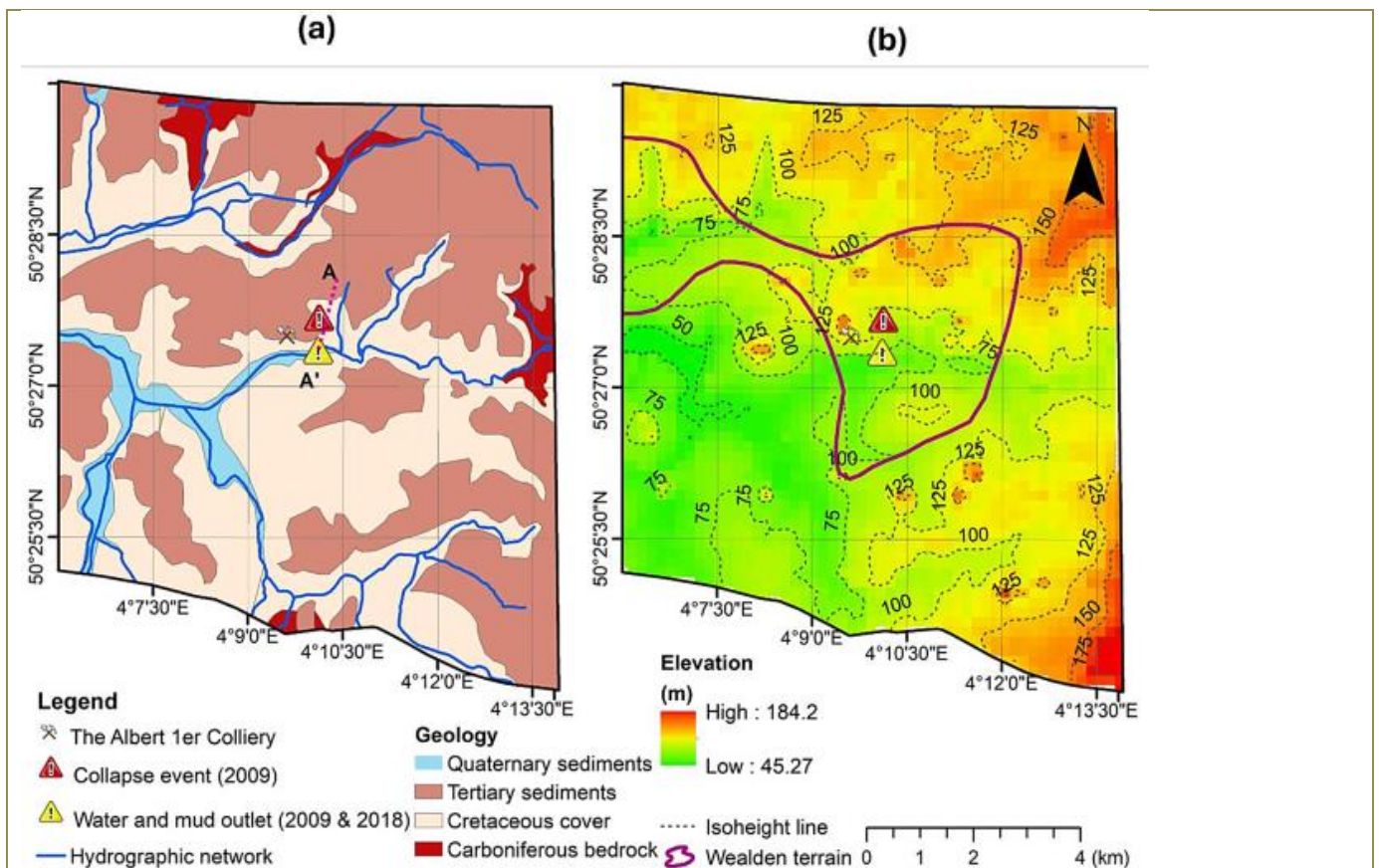


Figure 60. (modified from (Fripiat et al. 2013) (a) highlighting hydrographic networks and watersheds. The location of cross-section AA' has been specified, (b) topographical map from Shuttle Radar Topography Mission (Farr et al. 2007), highlighting Wealden terrains. Location of both 2009 and 2018 events on a geological map from Wallonia geoportal.

The Saint-Vaast area is overlain by Pleistocene loam deposits and alluvial sediments along the alluvial plain of the Haine River. The Wealden deposits are Lower Cretaceous sediments, but their age is changing throughout the Mons Basin from the western side (Barremian) to the eastern side (Albian) (Yans 2003). The Wealden sediments are generally found in kilometric lenses trapped in the depressions of the Palaeozoic basement but also inside natural karstic features distributed throughout the Paleozoic carbonate top surface. The Wealden deposits were mapped originally by Marlière (1946) and more recently from core descriptions allowing to propose of a revised cartography of the Wealden deposits around Saint-Vaast (see Figure 60) (Drevet et al. 2010).

Hydrographically, the region lies in the Haine sub-basin of the Scheldt basin, which reaches the Canal du Centre to the north and is flowed by the Haine from east to west (Figure 60b). Prominent tributaries include the Ruisseau des Estinnes and Ruisseau de la Princesse. The Haine originates in Anderlues and is fed by multiple smaller streams, like the Olive stream and Marais stream. Urbanization is most prevalent in the north, where the Canal du Centre intersects the region. This area is marked by the Strépy-Thieu boat lifts and the Canal du Centre Historique. Waterway routes in this zone, such as the Thiriau du Luc and its tributaries, often intertwine with the Canal du Centre Historique path (Drevet et al. 2010).

The study area relief is affected by traversing watercourses and is marked by colliery spoil heaps, some even exceeding 190 m in height (Figure 60b) (For detailed information on the Albert 1er spoil heap, see Destination Terrils: Terril Albert 1er.). Its average altitude is around + 100 m, but this varies with + 75 m elevations to the northwest and about + 150 m to the southeast (Figure 60b). The river Haine is the predominant hydrological feature in the study area, situated 608 m to the south of the initial incidence point. Central to the study area is drawn the mapping of an underground adit corresponding to an old adit located in the upper part of the thick lens of Wealden deposits. A detailed view of the geological features, including the direction and approximate depth of the adit, along with the schematic location of drilled piezometric wells is shown in the cross-section (Figure 61).

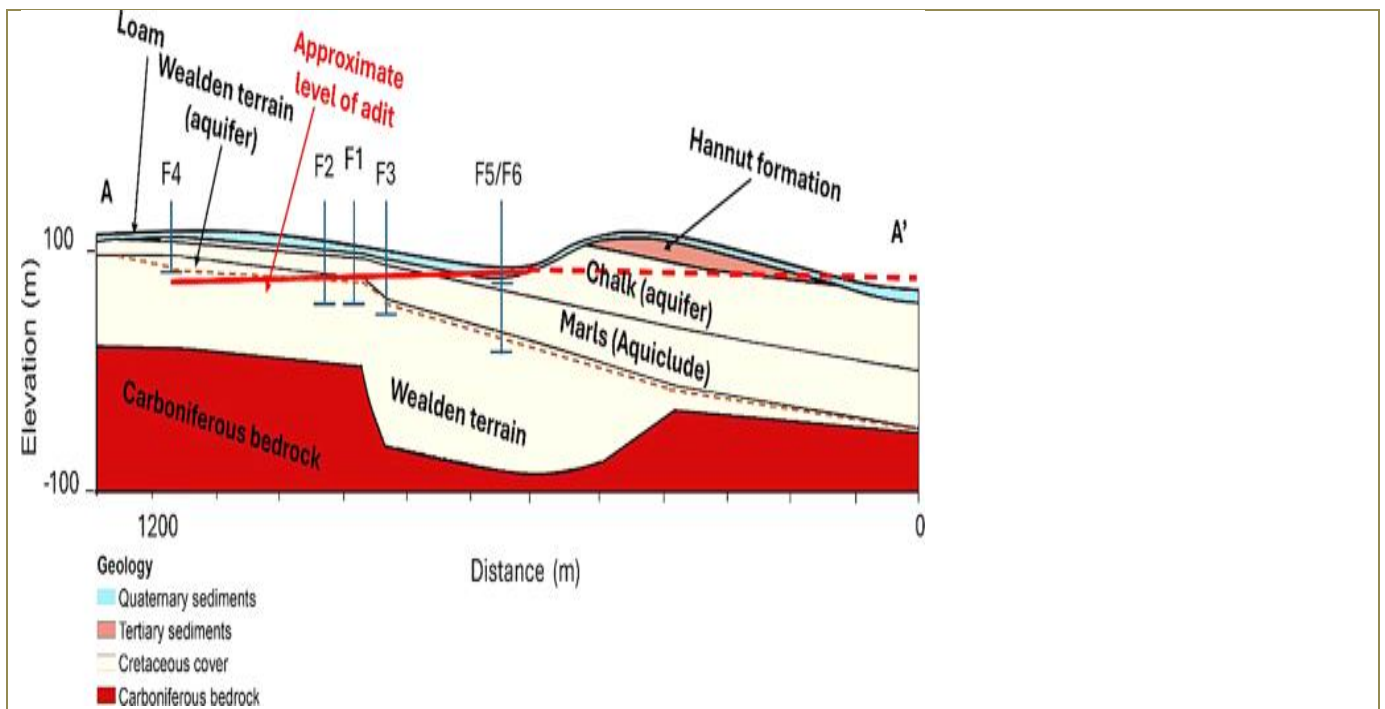


Figure 61. Cross-section AA' (highlighted in Figure 60a) illustrating the geological layers and the position of the drainage adit. The section highlights the direction and approximate depth of the adit relative to the Wealden deposits, as well as the overlying Turonian marls and Cretaceous aquifer

This mining adit is horizontal or slightly inclined and was possibly excavated to access a water-bearing storage level inside the Saint-Vaast hill. The “Charbonnages de La Louvière et Sars-Longchamps” colliery with the mine shafts 9 and 10 of the coal extraction site Albert 1er, started in 1914 and stopped in 1961, is the nearest active colliery in Saint-Vaast (Nicau [2024](#)). The latter colliery ceased the same year and was included in a bigger operational colliery named “Charbonnages de Ressaix-Mariemont-La Louvière” still supervised administratively by the regional Walloon administration. Given the proximity of the adit drainage with the active coal exploitation Albert 1er site, there is an issue most probably in relation to underground water fluxes from the nearby hill area containing the Cretaceous aquifer (chalks) and aquiclude (Wealden and Turonian marls). Turonian marls constitute a relatively impervious cover with a thickness of 20–30 m acting as a hydraulic barrier and confining the Wealden underground water located in the sandy layers, potentially located at the top of the Wealden deposits (Fripiat et al. [2013](#)). The significance of this adit is further highlighted by its evident role in the documented events and the geospatial estimations of land subsidence and uplift as revealed by PS-InSAR data. Given its importance, our focus will narrow to the region surrounding this adit, offering more detailed research and discussions (Figure 62).

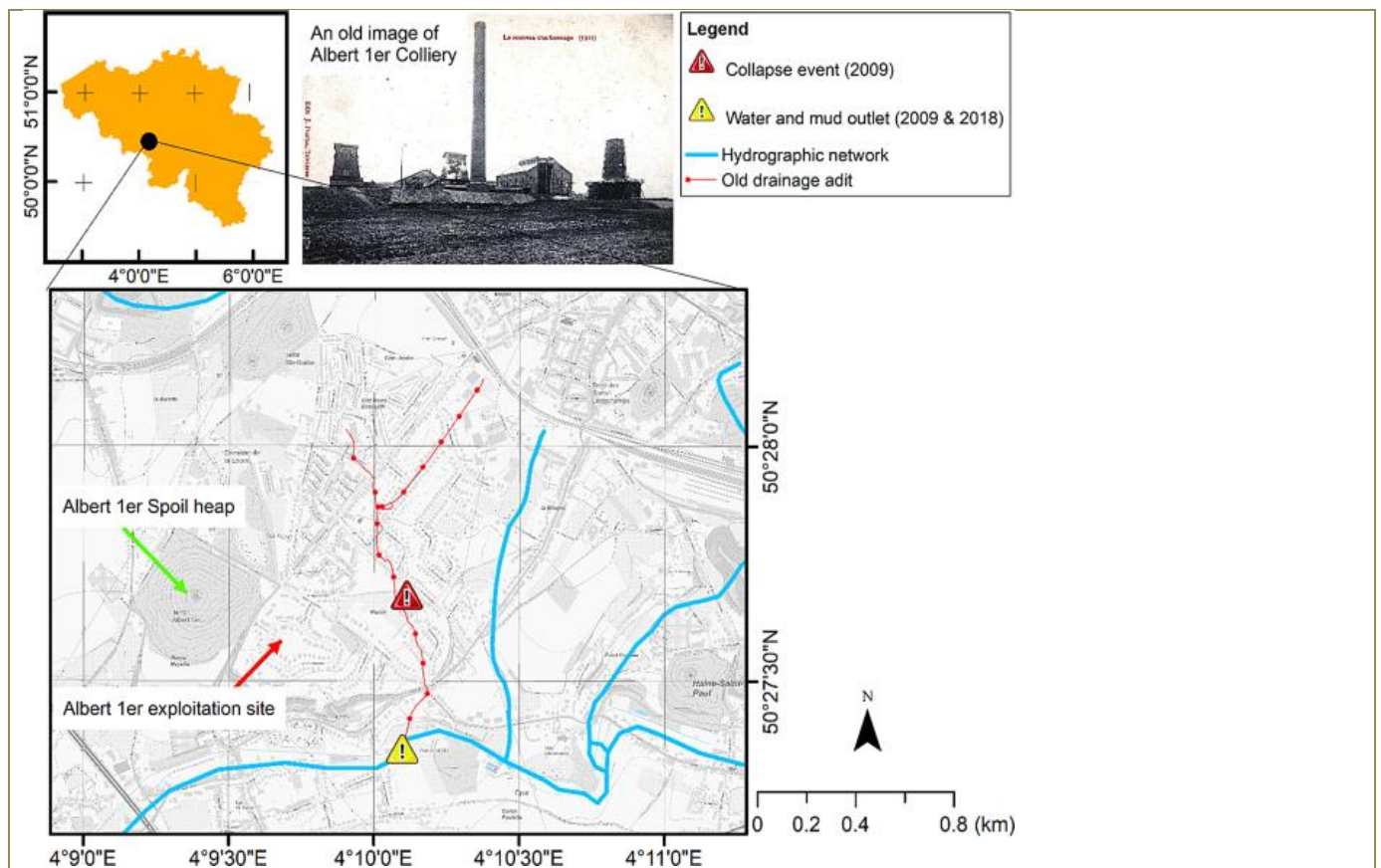


Figure 62. Detailed geospatial mapping of the historical underground gallery near Albert 1^{er}Colliery. The topographical background map is sourced from CartoWeb (NGI). Insert black and white photo adapted from (Hudson Institute of Mineralogy, n.d.) showing the Albert 1er colliery in Saint-Vaast (photo copyrighted to J. Duriau, Trivières)

5.2.2. Saint-Vaast incidents of 2009 and 2018

The most important geological feature in the Saint-Vaast subsurface is the presence of the Wealden terrains (Figure 60a). The Wealden geological layer features a complex stratigraphical sequence, with clayey horizons at the top transitioning to more mixed sandy-clay compositions at depth. These deposits are kilometeric lenses located in very localized depressions of the Paleozoic basement in general and specifically present here in the Saint-Vaast area. Their formation resulted from continental sedimentary processes and environments during the Early Cretaceous period, characterized by alternating deposition of clay and sandy layers. The clayey horizons are originally located in the middle and lower part of the sequence, while the mixed sandy-clay deposits are found at the top. The sandy portions have high permeability and can store and transmit substantial volumes of water. In contrast, the clayey sections act as impermeable barriers, often trapping and isolating water bodies in sandy lenses inside the clay horizons. Alongside these terrains, coal-bearing aquifers are present, which are essentially water-bearing layers associated with the exploited coal seams. These aquifers play a pivotal role in the hydrogeological dynamics of the region although the top of the Paleozoic basement has been strongly affected by the weathering with clay sequences that are sometimes very difficult to distinguish from the clay layers of the Wealden deposits itself. Their interactions with the overlying and underlying terrains, especially the Wealden clayey horizons, determine much of the subsurface water flow and storage patterns (Drevet et al. 2010). Given the geological characteristics of the Wealden terrain, this study examines the incidents that occurred in 2009 and 2018 in Saint-Vaast where Cretaceous chalk layers overlay impermeable Turonian marls above the loose sands of the Hainaut Group. These sands, saturated and under excessive pressure, put the gallery at risk due to the pressure difference between the upper underground aquifers and the high level of the Haine River. Over long periods, such conditions can accumulate significant potential energy. A natural or anthropogenic disruption in the Wealden clay horizon could cause the pressurized water from the Wealden confined aquifer to be released suddenly, as observed in the 2009 and 2018 incidents. The pressurized release can be even more pronounced if the coal aquifer, at any given point, directly interfaces with the sandy Wealden terrains. Considering the extensive mining history of the region, abandoned mining galleries and shafts may have served as potential pathways or reservoirs for groundwater flow. Given their expansive and interconnected nature, this adit plays a crucial role in subsurface hydrodynamics. To better understand these dynamics, a cross-section showing the hydrogeology of the region, including the locations of piezometric wells and the variabilities in the lithology of the Wealden terrain at each piezometer, has been created

(Figure 63).

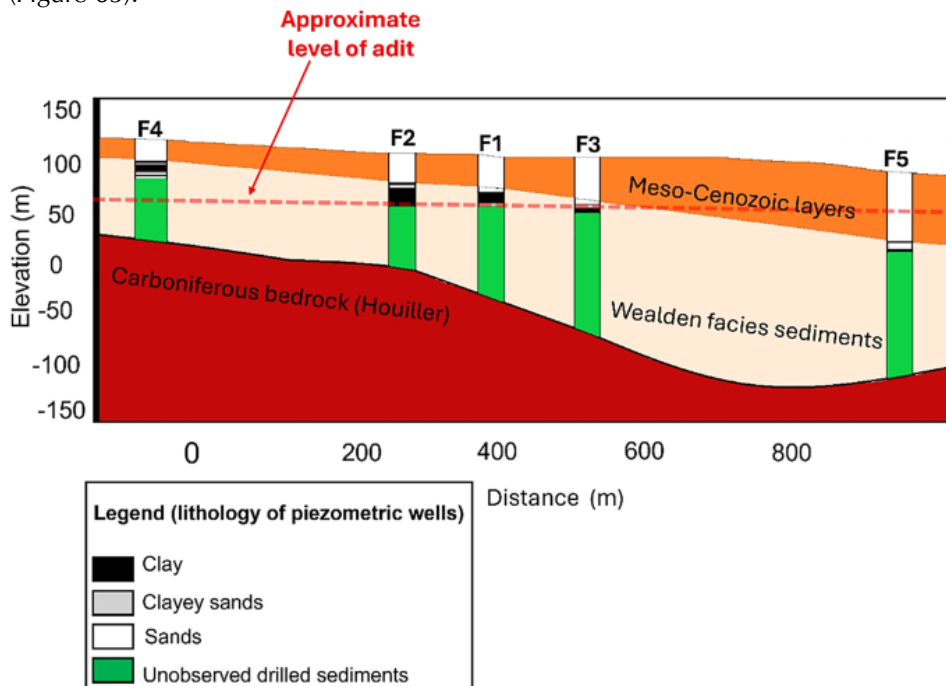


Figure 63. Geological cross-section over the piezometric wells F1 to F5 in the Saint-Vaast region, illustrating the lithological variability of the Wealden terrain across different piezometric wells, modified from (Drevet et al. [2011](#))

5.3. Methods

Synthetic Aperture Radar (SAR) data, when analyzed through the PS-InSAR technique, has significantly advanced the monitoring of ground deformations from space. A challenge, however, arises when there is an absence of man-made structures in the study area, or when the deformation does not conform to a predefined temporal model (Crosetto et al. [2016](#)).

The fundamental inputs for PS-InSAR are interferograms – products that include the phase difference between two SAR acquisitions, thus revealing ground displacements that occurred between the two acquisition times. To produce these interferograms, a set of SAR images is required, where a specific image is chosen as a 'reference' and the others are termed 'secondary'. The difference in phase between the reference and each of the secondary images generates individual interferograms (Dehghani and Nikoo [2019](#)).

In our study, the Delft Object-oriented Radar Interferometric Software (Doris) (Kampes [1999](#)), was used for interferometric processing of Single Look Complex (SLC) data of both the ERS and Envisat satellites. While Doris can handle Sentinel-1A data, for our research goals, Sentinel-1 A data was processed using the InSAR Scientific Computing Environment (ISCE) (Rosen et al. [2012](#)).

Upon interferogram generation, PS-InSAR protocol, driven by the StaMPS, employs a two-step approach for identifying Persistent Scatterer (PS) points. The initial selection of PS candidates is performed based on amplitude dispersion analysis (Ferretti et al. [2001](#); Hooper et al. [2007](#); Osmanoglu [2011](#); Chen et al. [2018](#)). These selected points are candidates as PS due to their very stable phase response. Pixels with lower amplitude dispersion are considered more stable and are chosen as initial candidates. After selecting a subset of pixels as initial candidates, the phase stability for each pixel is estimated using phase analysis, based on the assumption that deformation is spatially correlated (Zhang et al. [2015](#); Ansar et al. [2022](#)). This involves filtering out spatially correlated noise and assessing the remaining phase consistency across multiple interferograms. In this step we identified PS candidates by applying a threshold, set at a value bigger than 0.7. This threshold is considered as specific criteria, which assess the reliability of scatter points based on their consistency in reflecting radar signals across multiple acquisitions (Kenner et al. [2016](#); Chen et al. [2018](#)). This method ensures that the detected deformation signals belong only to those scatterers exhibiting stability, thus refining the accuracy and reliability of the resultant deformation insights. An external Shuttle Radar Topography Mission (SRTM) Digital Elevation Model (DEM) was used to mitigate topographic distortions inherent in the interferometric phase data. StaMPS uses a technique called 3D phase unwrapping to resolve the ambiguity in phase measurements, which are initially wrapped within the interval $[-\pi, +\pi]$. This method is designed to work effectively in the context of PS-InSAR by employing the phase gradients in x , y , and time t directions (Hooper and Zebker [2007](#)). This technique is implemented within a software package called Statistical-Cost Network-Flow Algorithm for Phase Unwrapping (SNAPHU) (Chen and Zebker [2000](#), [2001](#); [2002](#); Hooper et al. [2012](#)). After phase unwrapping, filtering in space is

applied to mitigate spatially correlated errors such as atmospheric and orbital effects. The remaining signal represents deformation and spatially uncorrelated errors, which can be modeled as noise (Sousa et al. [2010](#), [2011](#)).

5.4. Materials

5.4.1 SAR datasets

To measure the expansion and dynamics of ground deformation in Saint-Vaast, we integrated three C-Band SAR datasets spanning three decades.

Our study started with an analysis of ERS1/2 satellite imagery spanning the period from 1992 to 2001. This was succeeded by ENVISAT images, covering the years from 2003 to 2010. We subsequently incorporated Sentinel-1 A imagery from the years 2016 through 2023 into our dataset. The resolution of these data is presented in Table 15 (Zebker et al. [1994](#); Small et al. [2003](#); Bourbigot [2016](#)).

We used 75 descending ERS, 74 descending Envisat, and 204 Sentinel-1 A ascending images spanning between April 1992 to January 2001, March 2003 to October 2010, and June 2016 to April 2023 respectively. Figure 64 shows the perpendicular baseline against temporal baselines of the generated interferograms.

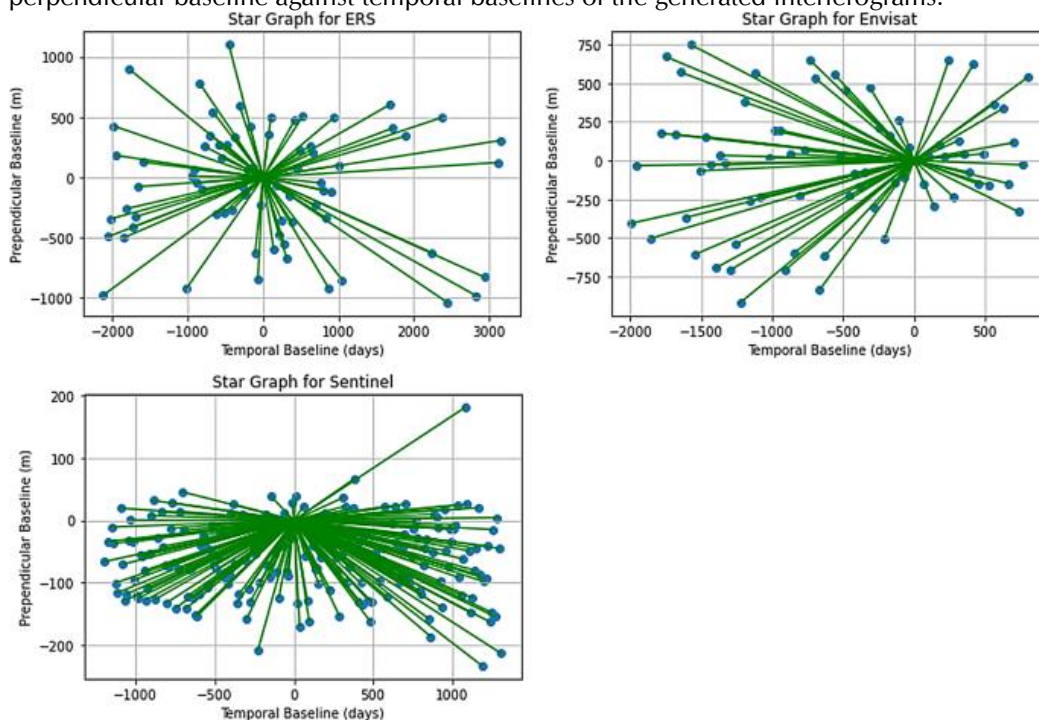


Figure 64. Star graphs showing perpendicular baselines (in meters) against acquisition dates for three SAR-image datasets, spanning the ERS, ENVISAT, and Sentinel-1A periods.

5.4.2. Water level data

To assess the risk of an accident of this type recurring in Saint-Vaast a detailed study of the piezometry of the aquifers was conducted by the Public Service of Wallonia. Piezometric wells, monitoring the Wealden and Chalk aquifers in the Saint-Vaast area, offer insights into the subsurface hydrology influenced by historical mining activities. Five piezometers (F1 to F5) near the collapsed area were cored in the Wealden facies to assess the potential influence of historical mining activities on groundwater pressures. Piezometer F6 in the vicinity of the collapse region was specifically set up to monitor the water level in the chalk aquifer to understand its hydrological behaviour and interactions. The location of the different available piezometers in the studied area is shown in Figure 65.

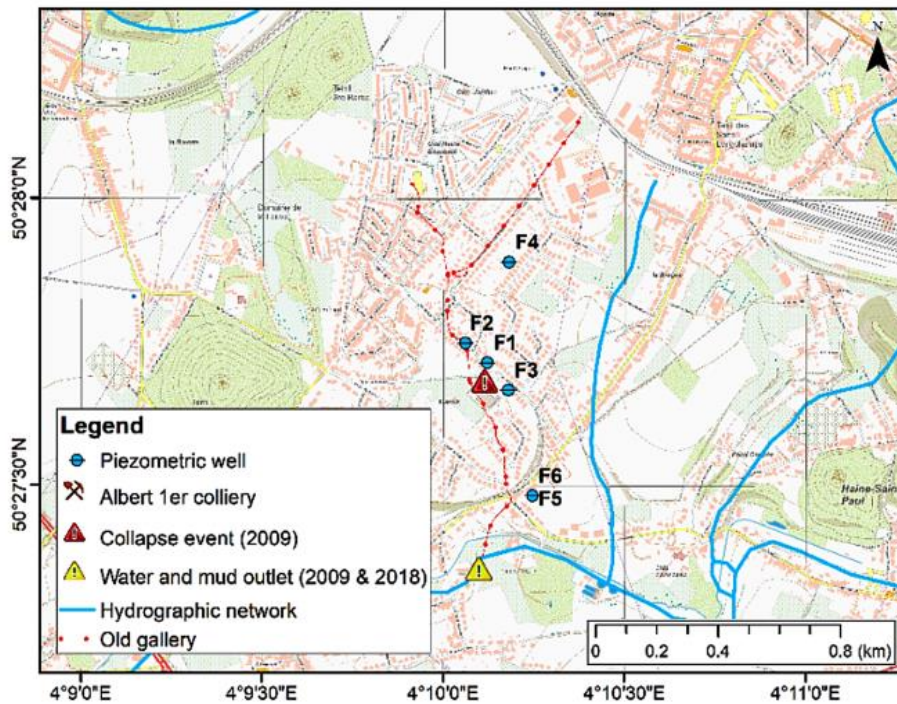


Figure 65. Location map of piezometric wells concerned with the study. The map background is sourced from CartoWeb (copyrighted to NGI)

5.5. Results

In this part of the paper, we present the results and discussion of our study on land surface deformation of the Saint-Vaast region. Our analysis using 3 decades of SAR data and 13 years of piezometric wells monitoring, explains the ground deformations and its hydrogeological drivers. Comparison between the SAR estimations with hydrogeological measurements shows a significant correlation between groundwater level variations and surface displacement during specific intervals within the study period.

5.5.1. PS-InSAR analysis

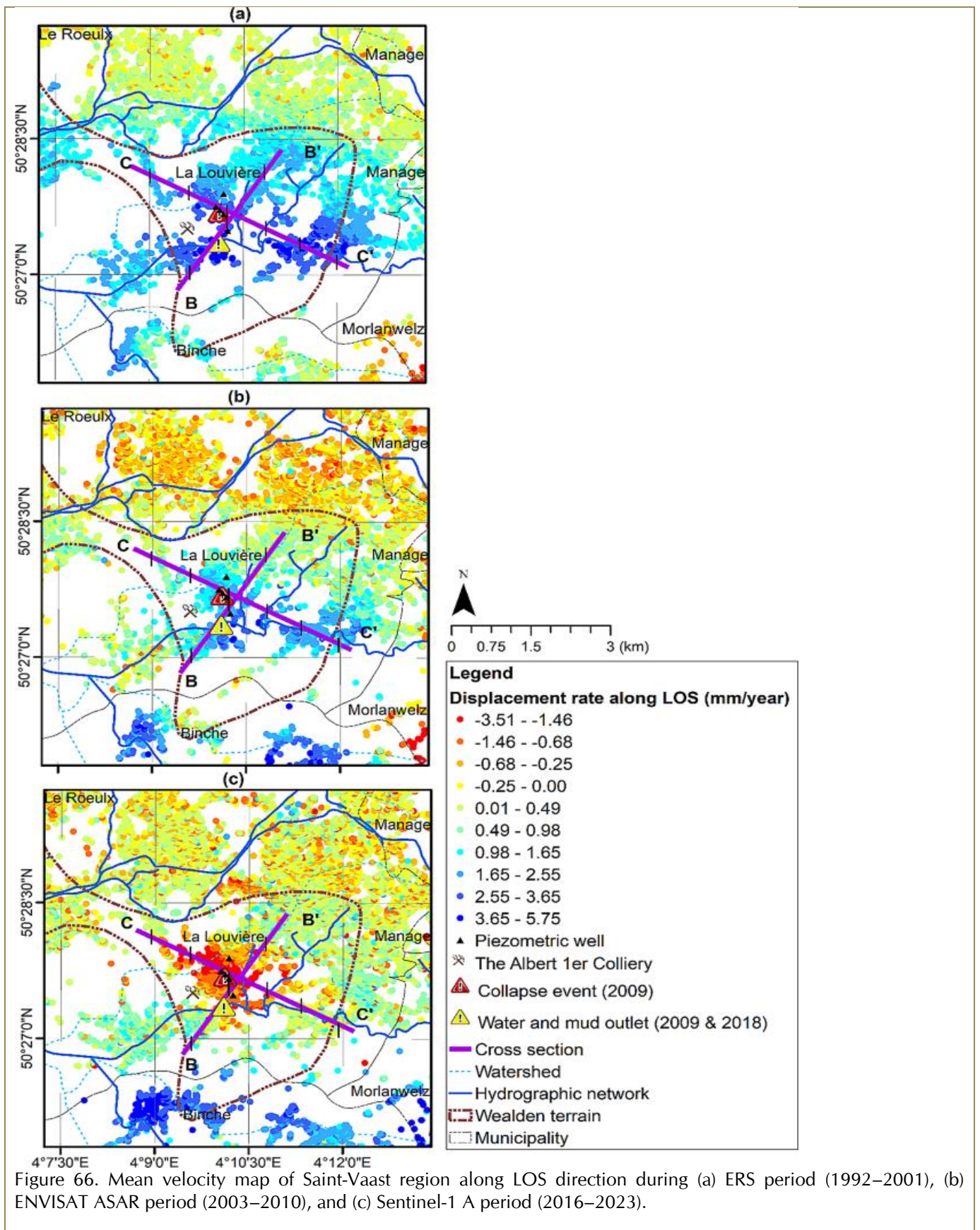
In our investigation of ground displacement in the Saint-Vaast area, we used PS-InSAR analysis across three distinct radar datasets from 1992 to 2023. We estimated significant displacement trends within a 5.7 square kilometer region of historical mining activity. Initially, from 1992 to 2001, this zone exhibited uplift movement with an average displacement of 2.65 mm/year, peaking at 4.49 mm/year along the satellite Line Of Sight (LOS) (Figure 66a). The period between 2003 and 2010 showed a stabilization in LOS displacement rates, averaging 0.94 mm/year. During this time, fluctuations range from a slight subsidence of -0.96 mm/year to an uplift of up to 1.5 mm/year along the LOS (Figure 66b). This period indicates a transient equilibrium within the subsurface structures. Contrasting to these periods, the recent years from 2016 to 2023 marked a notable shift to land subsidence, with an average LOS displacement rate of -1.24 mm/year, descending to a minimum of -3.65 mm/year (Figure 66c). The velocity values along the LOS illustrated in Figure 66 provide a ground displacement velocity but should be interpreted with caution, as they may not fully represent the deformation dynamics over the entire estimation period. (A time-lapse of yearly changes in LOS velocity maps is provided in the supplementary materials). While the mean LOS velocity during the Sentinel-1 A satellite monitoring period suggests a trend of subsidence, a closer examination of the recent time series data shows a beginning pattern of an uplift.

This emphasizes the complexity of deformation processes in the Saint-Vaast region, where short-term fluctuations can significantly deviate from longer-term trends. Figure 7 also illustrates how the pattern of deformation, including both uplift and subsidence phases, symmetrically aligns along the boundaries of the Wealden terrains. This alignment revealed by PS-InSAR time series analysis, emphasizes the geological influence on deformation dynamics. Additionally, Figure 66 shows the location of piezometric wells to highlight their position in relation to the pattern of deformation.

For the PS points located within a 200 m buffer area from the cross-sections BB' and CC' (solid purple lines in Figure

66), the LOS velocity during the three satellite periods is further estimated and illustrated (Figure 67).

As shown in Figure 67a, a consistent positive peak of deformation along the cross-section BB' during both the ERS and Envisat periods is centered around the longitude at 4.17. with increasing and decreasing LOS values respectively before and after the peak. The ERS data indicate a higher uplift at this peak, while during the Envisat period, the general deformation pattern across the region tends towards stability, yet a slight uplift is still estimated along the cross-section, with a lower peak compared to the ERS period. Conversely, Sentinel-1 A data reveal a transition to subsidence displaying the highest rate of land subsidence along the cross section around the longitude 4.175.



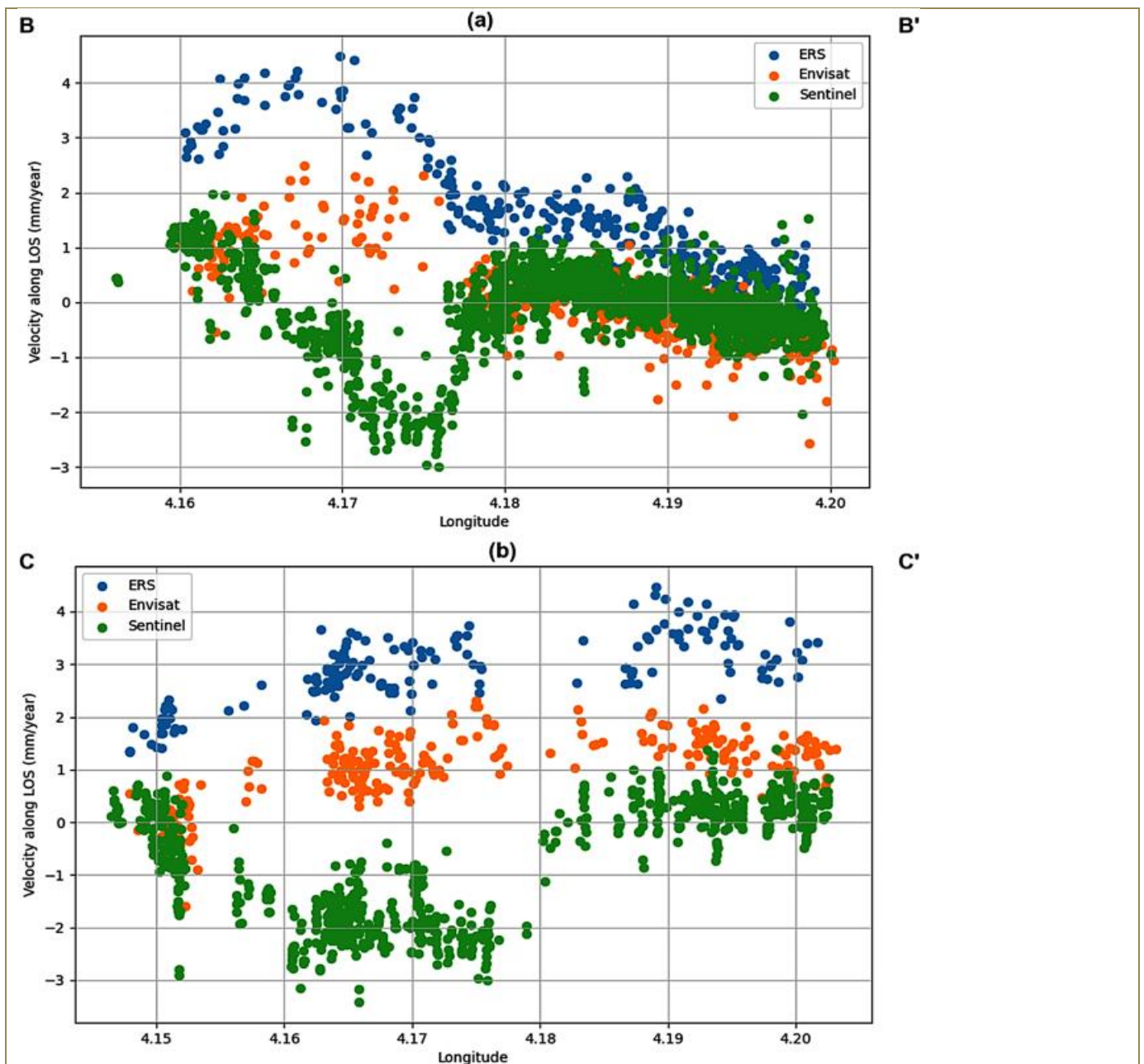


Figure 67. Average LOS velocity for PSs located within a 200 m buffer along a) cross section BB' b) cross section CC' (highlighted in Figure 66) passing over the deformation zone during three periods

This deformation pattern, with an increasing trend towards the centre of the land subsidence bowl, and the center of maximum movement shifting slightly over time compared to the peak in the uplift, indicates a dynamic subsurface process, evolving from uplift to land subsidence. It must be noted also that the three periods have a significant stability area from the longitude interval 4.1775 to the end. An increasing trend in the LOS velocity values is also visible before the longitude 4.1775 starting from the lowest negative LOS velocity values. The end of the cross-section reached the urbanized area of La Louvière where the subsurface data seems to indicate a very reduced amount of Wealden deposits with a reduced cover of Meso-Cenozoic deposits.

CC' is along the axis of the semi-symmetrical shape of the Wealden terrains, running in a northwest-southeast direction. As shown in Figure 67b, during the ERS period, like BB', there is an uplift along the cross-section. However, moving from C to C', the value of uplift increases towards the lobe of the Wealden border. Unlike BB', the uplift at the end of the cross-section does not turn into subsidence but continues to show uplift, though at a lower rate. During the Envisat period, similar uplift is observed along CC'. However, the uplift rate is slower, and the general deformation pattern shows a gradual decrease in uplift. By the end of the cross-section at C', the deformation stabilizes. Sentinel-1 A data

reveal a transition to subsidence displaying the highest rate of land subsidence along the cross-section from C to C', like BB'. The value of the peak subsidence is the same as observed in BB'. However, in BB', the minimum peak is very sharp, indicating that the subsidence sharply reaches its lowest point around longitude 4.175, transitioning from stability at the beginning of B. In contrast, along CC', the subsidence smoothly reaches the same peak, maintaining this peak until around longitude 4.185, and then gradually stabilizes. The displacement values obtained from PS-InSAR are calculated relative to a reference point. This reference point, assumed to be stable, is a key factor in PS-InSAR processing. For the ERS data (1992– 2001), the reference point was located at a specific latitude and longitude (4.54° E 50.932° N), part of a broader regional processing. For the Envisat (2003– 2010) and Sentinel-1 A (2016–2023) datasets, a stable reference region was identified near the dynamic deformation area based on the stability observed during the ERS period. Specifically, the reference point for Envisat and Sentinel-1 A data was located at a specific latitude and longitude (4.05° E 50.51° N) with a 50-meter buffer around it. All displacement values in analyses of deformation during three different missions were calculated relative to these reference points which are assumed stable.

Analysis of cross-sections BB' and CC' suggests that the deformation processes in the region are influenced by the orientation and distribution of the Wealden terrains, leading to more uniform deformation patterns along CC'.

The second by-product of running StaMPS is LOS time series of deformation. These timeseries correspond to the average timeseries of PSs located within a 100 m radius of five piezometers, which are illustrated (Figure 68). Our analysis concentrated on identifying and interpreting breakpoints within the time series data to gain a deeper understanding of the relation between displacement values and incidents in the region. Breakpoints are those dates where significant shifts in the deformation rate are observed, indicative of underlying hydrogeological processes and their influences that change the deformation dynamics. The identification of these breakpoints is crucial for understanding the temporal evolution of land deformation, as they signify periods where the deformation trend undergoes notable changes.

To identify these breakpoints, we employed a trial-and-error method that involved fitting linear trends to segments of the time series. When the goodness-of-fit, measured by the R2 factor, showed a noticeable decrease, it indicated that the linear trend was no longer a suitable representation for subsequent segments of the time series, thus suggesting a potential breakpoint. The R2 factor, also known as the coefficient of determination, is a statistical measure used to evaluate how well a regression model represents the data. This approach, while iterative and influenced by the presence of atmospheric fluctuations, allowed us to pinpoint periods where the deformation trend underwent significant changes.

This observation is significant as these breakpoints are consistently present across all five displacement timeseries (Figure 68). These timeseries correspond to average timeseries of PSs located within a 100 m radius of five piezometers, labelled F1, F2, F3, F4, and F5/F6—the latter two being co-located (Figure 65). Incorporating these points helps explain the clog ruptures that occurred in 2009 and 2018. The ERS satellite data spanning from April 1992 to January 2001 provided the first estimations of displacement in the region. Throughout this period, the time series data indicated a consistent uplift until April 1998, after which a phase of relative stability was observed across all piezometric wells until 2001 except for F4, which showed subsidence after April 1998. (Figure 68). Although no specific incidents were documented during this stable phase from April 1998 to January 2001, the historical context and subsequent deformation patterns suggest the possibility of an unreported subsurface event occurring during that time. From March 2003 to the end of January 2009, our analysis of Envisat satellite data revealed a notable uplift in all 5 timeseries, with rates reaching 3.46 mm/year near F5/F6 wells and reducing to 1.3 mm/year around F4. The locations of these piezometers are shown on the velocity map (Figure 66). The last year of the Envisat period (January 2009- October 2010) showed a stabilization in the trends across the all-time series. This phase of relative stability ended just before the first documented clog rupture event in February 2009. This suggests a correlation between the end of the uplift phase and the hydrogeological disturbances.

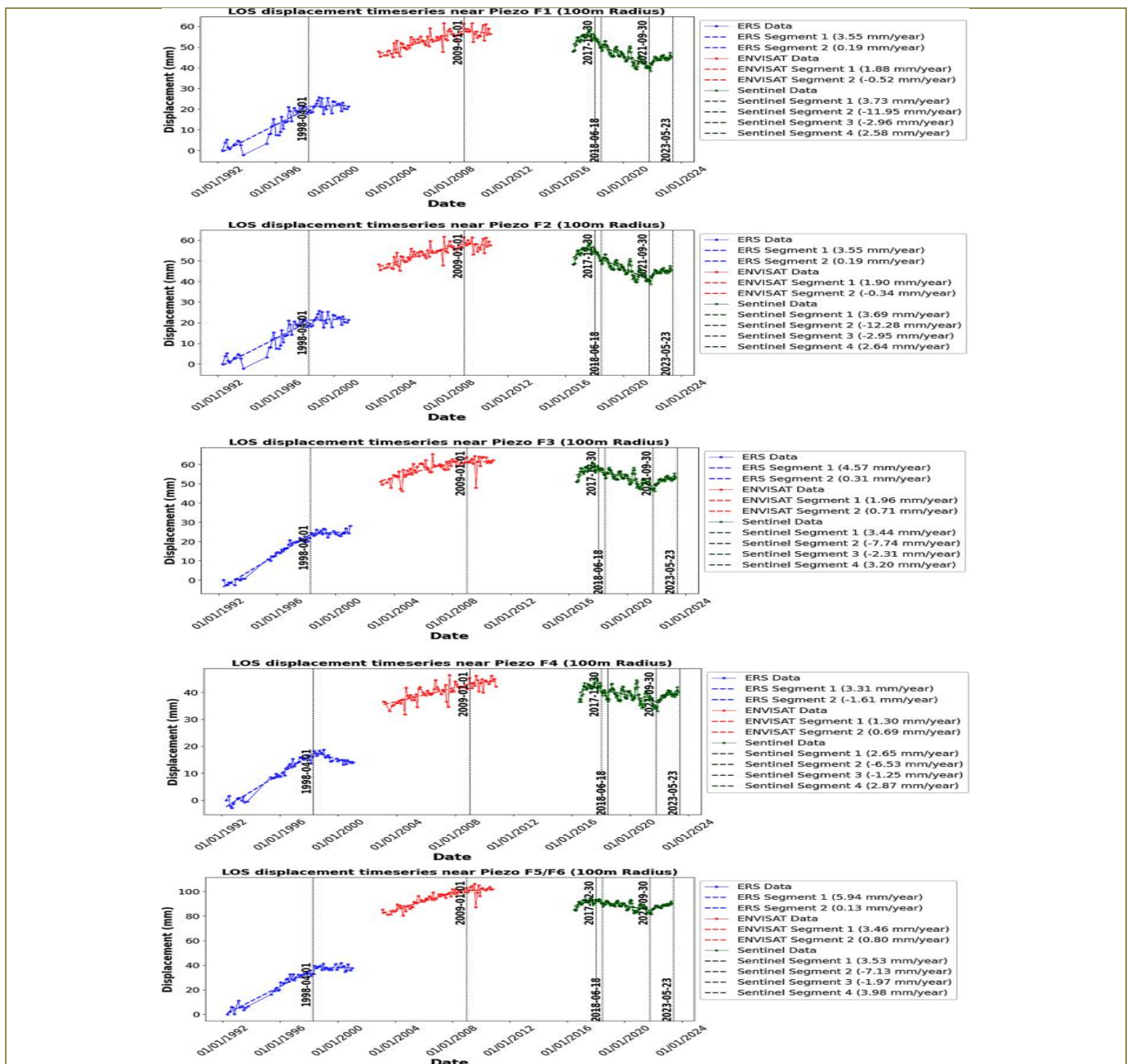


Figure 68. LOS displacement timeseries from ERS, Envisat, and Sentinel-1 A data for the PS points in the vicinity of piezometric wells, averaged for all PS points located within a radius of 100 m from each piezometer

The SAR data showed that a regional pattern is visible and most probably in relation to the subsurface activities of the coal mines in this part of the basin. The cessation of the groundwater pumping activities due to mining closure led to a gradual rise of the groundwater levels, increasing pore water pressure and reducing effective stress in the subsurface, weakening the soil or rock structure. This long-term evolution is illustrated by a regional uplifting trend in the studied area that is still visible during the ERS period. The ENVISAT period is still highlighting this trend in the southern area while the northern area showed negative LOS velocities suggesting a land subsidence affecting the urban areas of Le Roeulx, La Louvière, and Manage. The end of this uplifting trend is clearly visible during the Sentinel-1A data where the LOS velocity values indicate stable conditions mostly for the central and northern areas while the southern area continued to show uplifting conditions.

Looking now to the studied area of Saint-Vaast, a different pattern is visible with strong positive, slightly positive to almost stable, and negative LOS velocity values respectively during the ERS, ENVISAT, and Sentinel-1A time interval. This process illustrated the change of the behaviour from uplifting conditions to the progressive development of the land subsidence bowl. The rising trend indicates the progressive influx of groundwater that can accumulate in the

confined Wealden water-bearing sandy lenses causing an initial uplift (2003–2010), followed by a period of stability (January 2009–October 2010) as pressures balanced. Eventually, the continuous pressure buildup exceeded the subsurface material strength, triggering the 2009 clog rupture through sudden pressure release. The radar data gap from October 2010 to June 2016 limited direct estimations, yet it is possible that the ground surface initially subsided during this time. This resulted from the expulsion of large volumes of water and mud due to the 2009 rupture. Not only the release of water but also the transition of the materials of sand and clay from the Wealden terrain contributed to this subsidence. This temporarily reduced the sub-surface pressures, leading to land subsidence. However, with the clog of the pipe, which was installed after the event of 2009, pressures would have gradually built up again, initiating a new uplift phase. The exact onset of this uplift is uncertain, but Sentinel-1A data from June 2016 onwards captures the final phase of this uplift period till December 2017. During this period maximum and minimum uplift of 3.73 and 2.65 mm/year in the vicinity of F1 and F4 was observed respectively. This was followed by a shift to subsidence (around June 2018). The start of this subsidence phase coincided with the second clog event in the pipe installed post-2009, leading to an increase in pore pressure once again. However, unlike the previous incident, no rupture occurred this time due to the effective water and mud transfer by the same pipe to the river Haine. This managed discharge initiated a rapid subsidence phase post-2018, with the subsidence rate peaking at -12.28 mm/year near F2 in the first half of 2018, the highest among all other piezometric vicinities. The subsidence rate then decelerated significantly in the latter half of 2018 and continued at a reduced pace until September 2021. Among the piezometric wells, the highest and lowest subsidence rates were observed near F1 and F4, at -2.96 and - 1.25 mm/year, respectively. After September 2021, a new uplift phase started, observable across various parts of the region. This uplift, occurring around all piezometric wells, exhibits a consistent positive displacement rate estimated between 2.58 and 3.98 mm per year. Given the historical patterns described so far, it is reasonable to anticipate another significant event in the near future. The next section explores the relationship between deformation and piezometric wells, highlighting their interconnected dynamics.

5.5.2. Analysis of piezometric wells

Concerning the relationship between piezometric wells and incidents, several key insights were identified. The hydrogeological characterization of the Wealden terrain with a variable composition is critical for understanding the subsurface water dynamics and their influence on surface deformation. The installation of piezometers F1 to F5 after the 2009 incident and the subsequent monitoring of water table levels provided a direct insight into the aquifer response to external pressures and events. Piezometer F6 was also installed but to monitor the chalk aquifer. Notably, the water table levels show distinct trends and anomalies.

A time series visualization of water levels across six piezometric wells, with Wells F5 and F6 situated in the same location, is provided (Figure 69). In the figure, the legend clarifies which data comes from which company or method, identifying the different sources of data collection. Visual examination of the fluctuation reveals not only unexpected events but also potential measurement issues. Initial data from F2 appear accurate, yet exhibit unusually high fluctuation rates, possibly due to installation issues with the piezometer. Rates exceeding 10 cm/h are unlikely to be natural, suggesting sensor malfunctions or external disturbances. F1 exhibited rapid water level rises in early October 2009, early March 2010, and early November 2010 (red vertical dashed lines in Figure 69). The first one aligns with a tracer test based on our knowledge, providing a clear explanation for this fluctuation. However, the origins of the subsequent increases in March and November 2010 are not as readily identifiable.

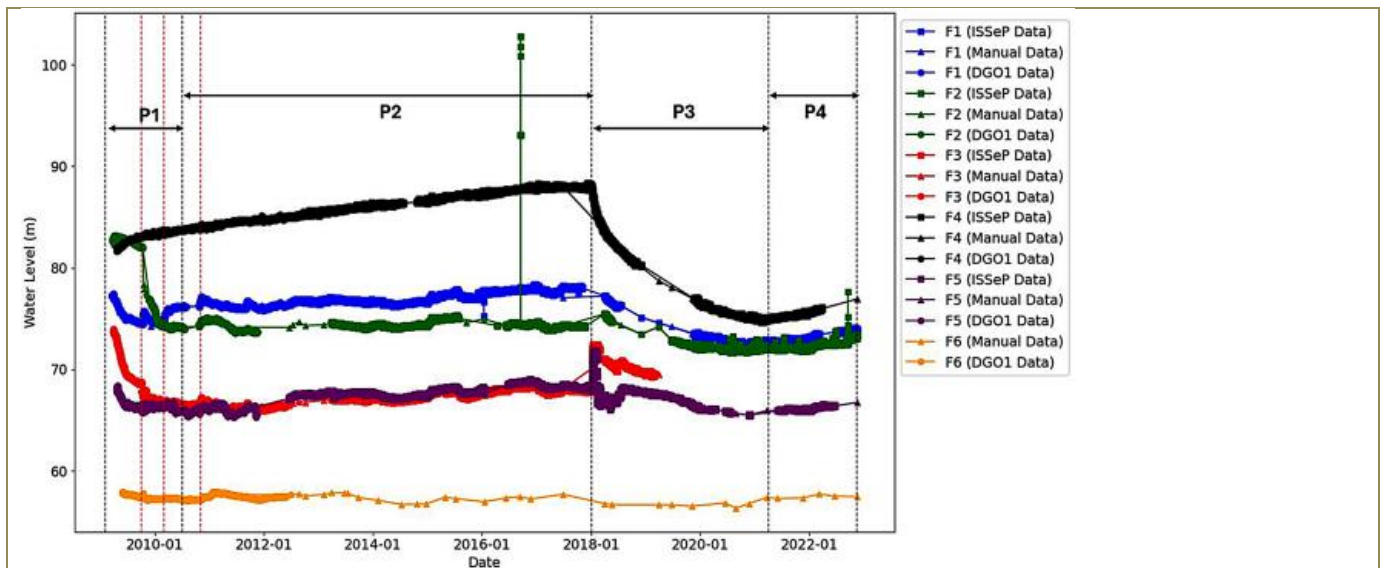


Figure 68. Time series of the 6 piezometric wells installed near the location of the mudflow outburst and the damages at the surface in the residential area of Saint-Vaast after the first event in 2009. The red dashed lines indicate rapid water level rises observed in F1 during early October 2009, early March 2010, and early November 2010

The water table at F5 in the Wealden terrain stands roughly 10 m above the chalk aquifer level at F6. With the lower sampling frequency of F6, yet it exhibited no significant fluctuations within the chalk aquifer throughout the entire observation period, suggesting that the chalk strata were probably not a contributing factor to the documented incidents. It makes sense as the chalk aquifer is separated from the Wealden aquifer by a thick aquiclude comprising the Cretaceous formations and the thickness of this aquifer is reduced on the hill of Saint-Vaast residential area compared to the southern area on the other side of the Haine river. Five piezometers, even F2, despite its considered lower reliability, exhibited remarkably consistent responses, indicating a coherent hydrogeological behaviour across the monitored area. Within this dataset, critical breakpoints are highlighted with vertical dashed black line marking key dates in the monitoring timeline. They are segmented into four distinct phases: beginning with the initial setup in 2009 after the first clog rupture event, leading into Phase 1 (P1) which continues until mid-2010. It is then followed by Phase 2 (P2) from mid-2010 to February 2018, Phase 3 (P3) from February 2018 to April 2021, and Phase 4 (P4), from April 2021, through to the end of our dataset in late 2022. To investigate the water level fluctuations, a more detailed analysis of the piezometric time series between these breakpoints is provided (Figure 70).

Immediately after the 2009 incident, a substantial release of water and mud was observed, leading to a decline in water levels across all piezometers, except for F4, during Phase 1 (P1). F4 exhibited a gradual increase in water level at a rate of 1.58 m/year, different from the general pattern observed in the other wells. The negative water level trends observed in P1 across all wells except F4 transitioned in P2 to either stabilization, as seen in F2, or to recovery, with rising levels in F1, F3, and F5. The rising trend in F4 persisted during P2, at a reduced rate of 0.58 m/year.

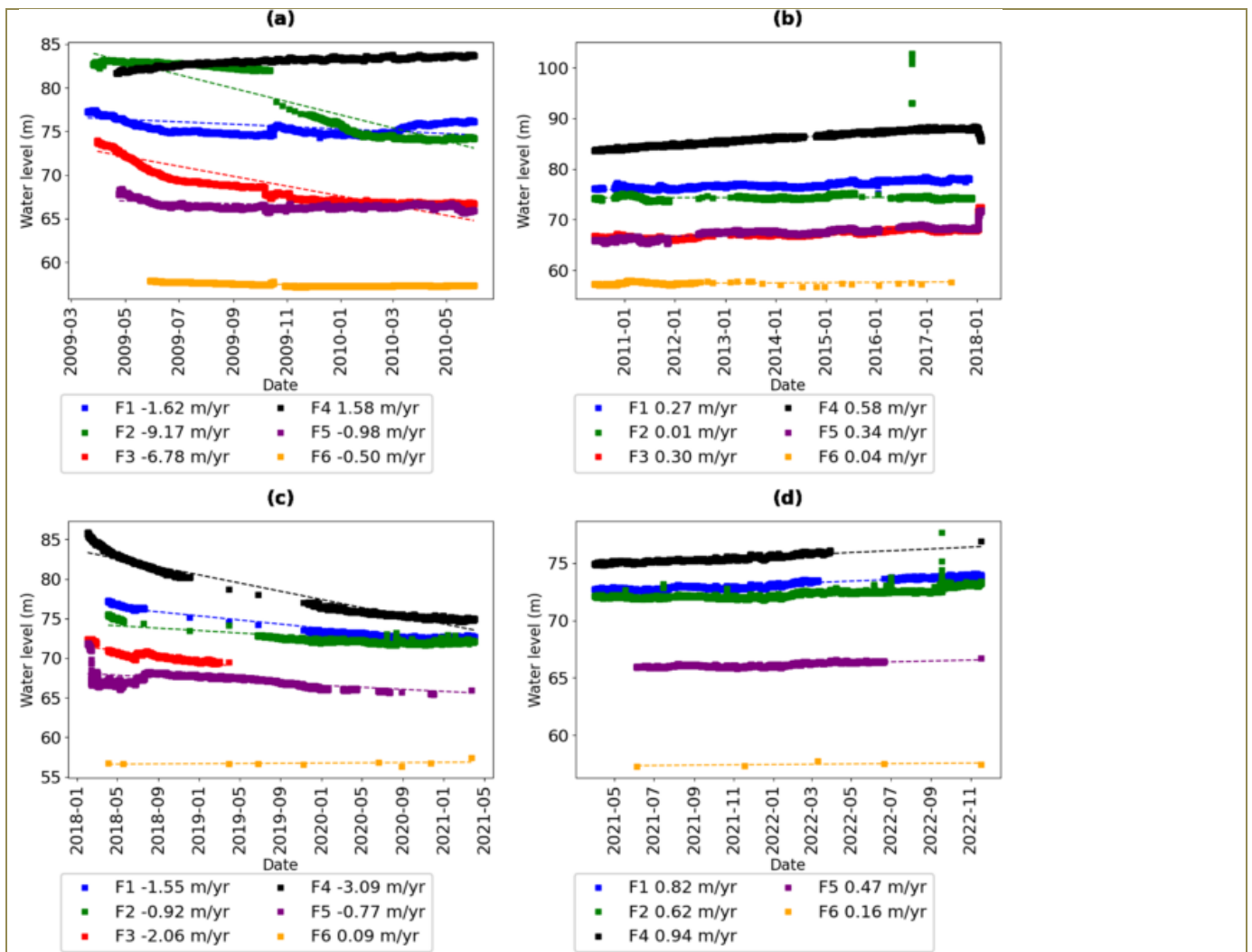


Figure 69. Water level evolution in piezometric wells installed near the incident site after the first event in 2009. The figure is segmented into four distinct phases: **a** initial setup to mid-2010 (P1), **b** mid-2010 to February 2018 (P2), **c** February 2018 to April 2021 (P3), and **d** April 2021 to late 2022 (P4), showing detailed fluctuations during these significant phases

A strange observation was made towards the end of 2018. A sudden and pronounced rise in water levels in F3 and F5, accompanied by a sharp decline in F4, indicates an anomalous hydrogeological event or a potential shift in subsurface dynamics. The second incident coincided with this hydrological behaviour observed at the end of the P2 and beginning of the P3 phases. Initially, in early 2018, there was a sharp increase in water levels in F5 and F3, which suddenly transitioned to a decline, followed by a gradual decrease. A similar pattern was noted in F1 and F2, although data for the initial phase of the drop in F3 and F5 are missing for these wells due to irregular sampling during that time. F4 water level fell sharply, at a rate of 3.09 m/year, yet showing a different steeper decline compared to the other wells, despite a similar downward trend. The different behaviour of F4, compared to F1, F3, and F5, despite all being situated within the Wealden terrains, could be explained by lateral variations in the geological composition of these sites. The Wealden terrains are generally characterized by sandy layers at shallower depths transitioning to clay materials with increasing depth, as observed in F1, F3, and F5. However, drillings at F2 and F4 have more clayey horizons closer to the surface (Figure 63). This could explain F4 unique hydrogeological response, and the different water level trends observed. The clay layers, known for their lower permeability compared to sandy formations, could restrict water movement, thereby decoupling F4 water level responses from those observed in the more permeable, sandy environments of F1, F3, and F5. Another potential explanation could rely on the aspect of a lateral clog issue more to the northern part in the adit, implying that another clog was created after the 2009 event in between the positions of the F1-F2-F3 piezometers and the F4 piezometer. This other clog related to a collapse event inside the adit, might have initiated a change in the hydrogeological response to groundwater accumulation much further to the North of the adit implying already a pressure change leading to an uplift. If this scenario is correct, it might explain why the 2018 event is characterized by a strong water level decline in the F4 area while the F1-F2-F3 are also following the same pattern with a smaller

amplitude. Nevertheless, the potential lateral location of the second clog associated with the 2018 event has not created damage to the surfaces in another part of the residential area of Saint-Vaast nor right at the surface of the 2009 event. P4 marks a potentially new hazardous phase, characterized by a noticeable rise in water levels, signalling the risk of a new incident. This period, showing the start of an upward trend in water levels aligns with uplift estimations from the recent Sentinel-1A data. Essentially, the rising water levels, with limited outlets for relief, could escalate subsurface pressure, heightening the risk of further incidents.

5.6. Discussion

The events experienced in Saint-Vaast typically follow a pattern of progressive clogging, rupture, and subsequent surface deformation. However, rather than occurring at a fixed interval, the recurrence of these events is highly dependent on hydrological conditions, particularly infiltration rates. During periods of significant water infiltration, the confined aquifer system becomes pressurized, leading to uplift. When the water cannot escape due to clogging, pressure continues to build until rupture occurs, releasing water, mud, and the transition of sediments out, which in turn initiates a subsidence phase. The duration of each phase—uplift, stability, and subsidence—can vary considerably, depending on local weather patterns and groundwater recharge rates. Since late 2021, the region has shown signs of uplift again, suggesting a potential recurrence of clogging events like those in the past. This poses a recurring geohazard issue in this densely populated urbanized area of Saint-Vaast that requests a detailed monitoring approach in the long term to follow up a post-mining hazard.

Piezometric analysis showed significant correlations between water level fluctuations in the Wealden aquifers and instances of ground deformation. The events of 2009 and 2018 highlight the region's vulnerability to hydrogeological hazards due to post-mining activities. The combination of piezometric well evolutions and PS-InSAR time series of deformation provides a comprehensive explanation for these events.

The temporal analysis identified critical breakpoints in displacement trends and piezometric well time series, offering insights into subsurface processes. These breakpoints align with observed hydrogeological events, indicating a direct link between subsurface water pressures and ground stability.

Starting from these considerations, a simple approach is here proposed to continue the monitoring of the whole area by combining the two techniques (i.e. piezometric wells and PS-InSAR data). The purpose of this approach is to give an overview of the collapse risk and clogging effect inside the abandoned mined adit considering how to tackle input data uncertainty. Frequently, in risk analysis a strong interference between uncertainty and decision-making is present and therefore it is crucial to generate an easy, accessible and transparent decision procedure capable of solving also complex problems characterized by poor local information. The case of Saint-Vaast is associated to the presence of an adit structure that has been mapped on old mine documents and to a long period of digging using many shafts to reach the level. The adit is potentially precisely located while the depth and the size (height and dimensions of the adit) are almost unknown. The lithology of the Wealden facies has been recently investigated through the 5 piezometric levels but only on a very limited depth implying a strong uncertainty in the presence, thickness and numbers of water-bearing sandy lenses inside the Wealden deposits through the entire thickness of the series but also in the lateral facies variations that might be very relevant for such kind of continental deposits. The depth of the adit and the dimensions do not allow visual inspections neither while it would be very suitable to have a clear view of the stability of the roof along the entire length of the adit. The 5 piezometers are also not very well distributed, and their number is insufficient to cover the entire adit. The unknown lithologies forming the roof of the adit are also creating large uncertainties in the places where mechanical instabilities might create roof collapses leading to clogging issues. Depending on the location of the potential future clog issue, the incident might be either almost not visible or generate again surface displacements. The management of post-mining hazards associated to such kind of features at shallow depth requires a combined monitoring system as the one used in this paper by two different technologies. It is potentially worth the time to check the other mapped adit features found in the area and associated with the Wealden deposits to determine whether other areas might also be influenced by similar surface displacements.

5.7. Conclusions

The analysis of land surface deformation in the Saint-Vaast region, Belgium, over three decades (1992–2023), using PS-InSAR techniques and correlating these findings with piezometric well data, has enhanced our understanding of the hydrogeological dynamics and associated geohazards of post-mining activities. This study highlights the relationship between subsurface water dynamics and resulting land deformation due to the presence of an old mining gallery.

The PS-InSAR time series analysis shows the temporal progression of ground displacement across three radar datasets. ERS data mainly (1992–2001) exhibit an uplift phase from 1992 until 1998, transitioning into stability from 1998 to 2001. Envisat observations (2003–2010) continue the uplift from 2003 to 2009, followed by stability in 2009–2010. Sentinel-1A data (2016 onwards) show an uplift phase from 2016 to 2018, a dramatic subsidence after 2018, and a reduced subsidence rate until 2021. From 2021, a new uplift phase is observed. Velocity maps align with the geological features of the Wealden terrains, emphasizing subsurface hydrogeological processes impact on ground deformation.

This investigation demonstrates the importance of integrated SAR and piezometric analyses in understanding and predicting geohazards in the post-mining region of Saint-Vaast. The dynamic interaction between geological structures, historical mining activities, and hydrogeological processes presents a complex but understandable pattern of ground deformation. This approach is crucial for early detection and mitigation of potential geohazards, safeguarding communities and infrastructures in this vulnerable post-mining region. Historical piezometric and PS-InSAR data show a clear correlation. Whenever there was an increase in the water level, an uplift was monitored. This is linked to sand and clay roof collapse in the gallery, leading progressively to a clog. Mudflow outbursts are associated with water floods and eventually cause subsidence.

The list of references can be found inside the publication itself cfr list of the LaSUGEO project publications later in this report.

Target site 6: Ground deformation in the Brussels area - (Added and new Deliverables: D.4.6./D.4.4.6.)

6.1. Introduction

The Brussels area is affected by movements of the ground surface. InSAR analyses have revealed that the centre of Brussels has been rising since 1992 at speeds of up to several millimetres per year (Declercq et al. 2017). These uplifts are mainly located in the northwest and the Senne valley. They are more significant before 2010 (Figure 70). A clear correlation between these uplifts and the rise in piezometric heads in the Palaeozoic bedrock and Landenian aquifers can be seen following the de-industrialization of the centre of Brussels and the shutdown of many pumping wells. The piezometric head in the bedrock and chalk aquifers is now close to 10 m above sea level but was -40 m in the 1960s. Land subsidence was linked to the historic pumping and the subsequent piezometric drawdowns, and we are now seeing an elastic rebound as the piezometric heads of the aquifers are rising.

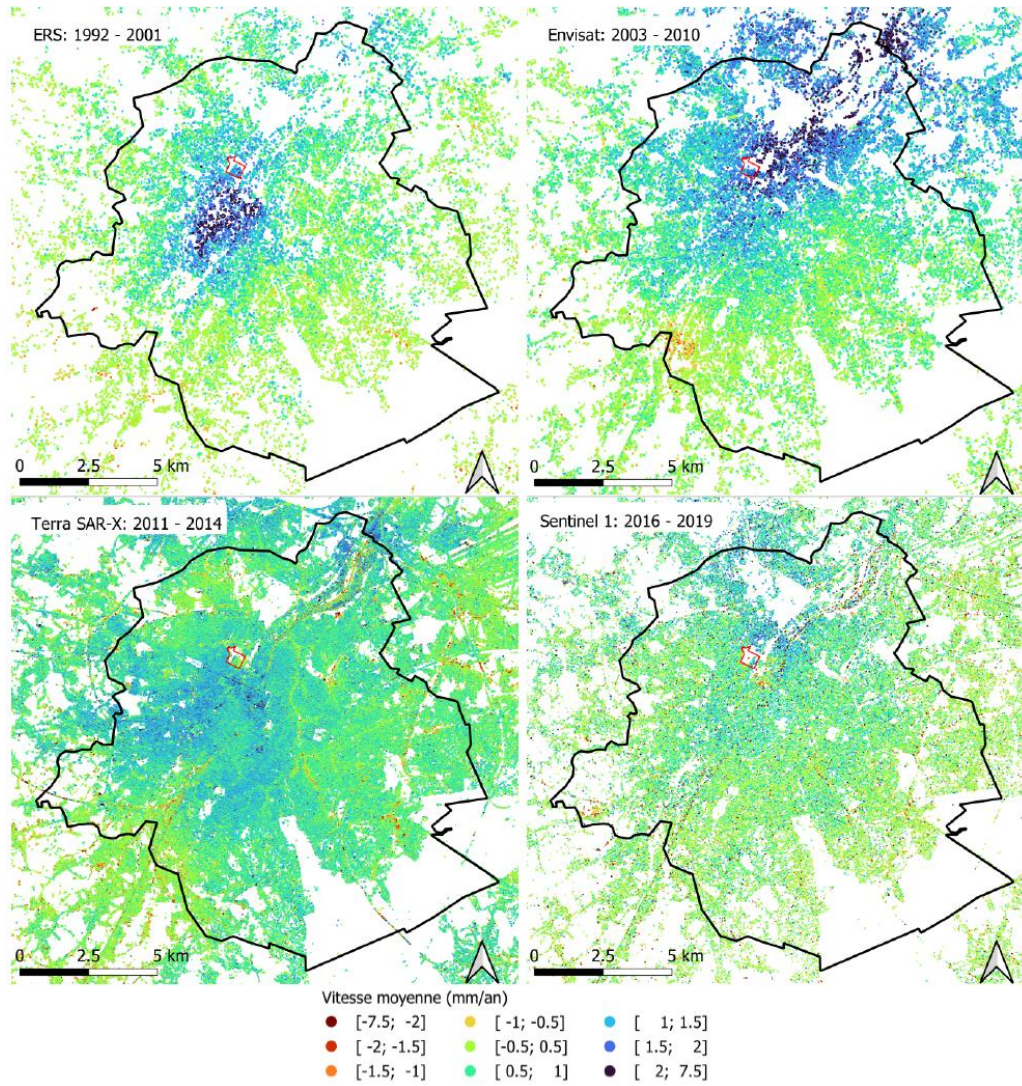


Figure 70: Land movement velocities estimated from different InSAR measurement periods (Declercq, 2017 & 2019). Delineation in red of the Tour & Taxis zone used further as a reference for comparisons.

6.2. Summary of the geological context (Figure 71, Table 15)

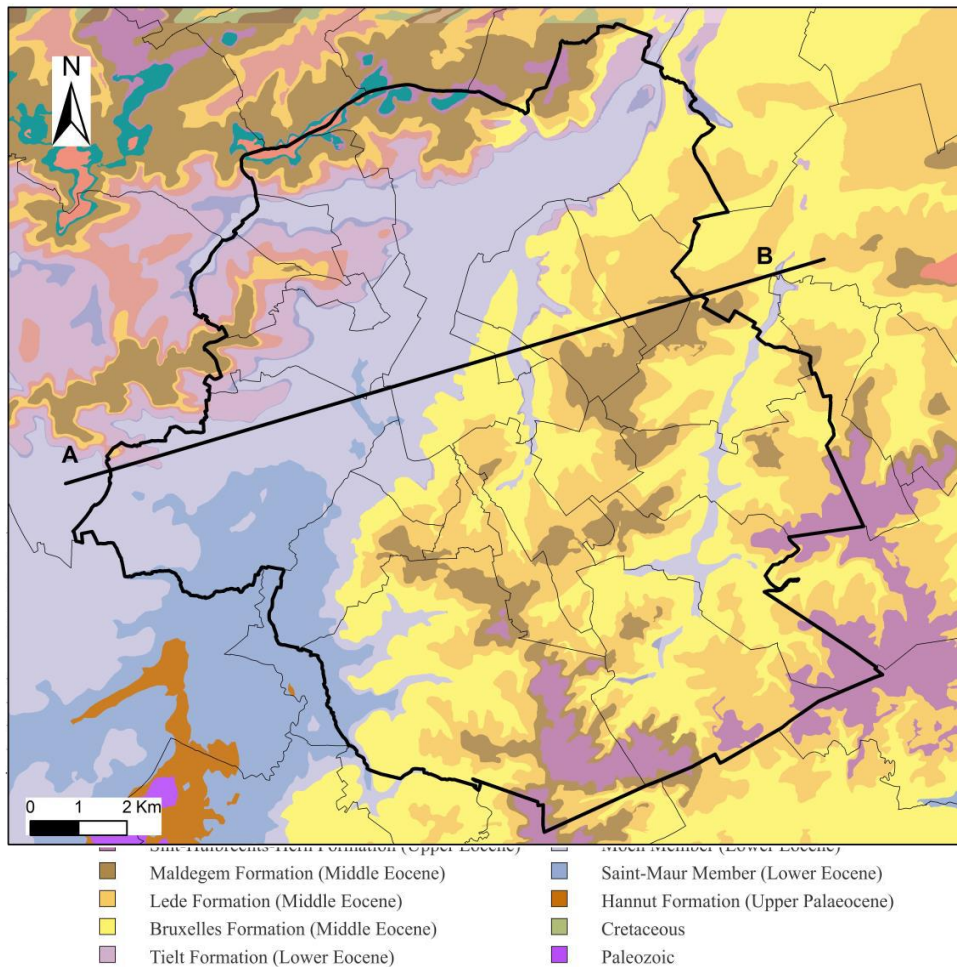


Figure 71: Geological map and cross-section profile (A–B) through the Brussels Region (limits in bold black lines) (Buffel and Matthijs, 2009).

The Moen sands and clays are also drained by the Senne valley. Most importantly, the groundwater flow in the Landenian aquifer (Hannut Formation) is directed in a northwestern direction (Figure 72) (Hydroland model, 2016). The bedrock aquifer is mostly slightly confined, and its recharge area is in the Walloon Brabant. The groundwater flow is also mostly in a northwestern direction as shown by the different measured piezometric heads (Figure 73). This aquifer was used extensively by industry in Brussels, with withdrawals greater than the recharge. This has led to a significant drop in the piezometric heads of about 60 to 70cm/year. This situation lasted until the 1960s, when the trend was reversed following a reduction in pumped groundwater flowrates.

ERA	SYSTEM	SERIES	Stratigraphic	Hydrogeological Unit	Type	Nature
			FORMATION/Member			
CENOZOIC	QUATERNARY	HOLOCENE	-	Aquifer system of the Quaternary	AQUIFER/AQUITARD	Unconfined to confined
		HOLOCENE	-		AQUICLUDE	
		PLEISTOCENE	-		AQUIFER	
	NEOGENE	Upper MIOCENE	DIEST	Perched aquifer system with sands	AQUIFER	Unconfined to locally confined
		Lower MIOCENE	BOLDERBERG		AQUIFER	
	PALEOGENE	Upper EOCENE	SINT-HUIJBRECHTS-HERN	Perched aquifer system with sands	AQUIFER/AQUITARD	Unconfined to locally confined
			MALDEGEM/Zomergem		AQUICLUDE	
			MALDEGEM/Onderdale		AQUIFER	
		Middle EOCENE	MALDEGEM/Orsel and Asse	Aquiclude (clays)	AQUICLUDE	
			MALDEGEM/Wemmel	Aquifer system with sands	AQUIFER	Unconfined to locally confined
			LEDE		AQUIFER	
			BRUSSEL/BRUXELLES		AQUIFER	
		GENT/Vierzele	AQUIFER			
		Lower EOCENE	GENT/Merelbeke	Aquiclude (clays)	AQUICLUDE	
			TIELT	Aquitard with alternating sands and clays	AQUIFER/AQUITARD	Unconfined to locally confined
	KORTRIJK/Aalbeke		Aquiclude (clays) not very thick	AQUICLUDE		
	KORTRIJK/Moen		Aquifer system with sands	AQUIFER/AQUITARD	Unconfined to locally confined	
	KORTRIJK/Saint-Maur		Aquiclude (clays)	AQUICLUDE		
	HANNUT/Lincint		Aquifer system with sands	AQUIFER	Confined	
	Upper PALEOCENE	HANNUT/Grandglise	Aquifer system with sands	AQUIFER	Confined	
HANNUT/Lincint		Aquiclude (clays)	AQUICLUDE			
MESOZOIC		Upper CRETACEOUS	NEVELE	Aquifer system combined with the top part of the Paleozoic	AQUIFER	Confined
PALEOZOIC		Lower CAMBRIAN	TUBIZE	Aquifer system of the Paleozoic with a weathered/fractured top zone	AQUIFER/AQUITARD	Confined
					AQUICLUDE	

Table 15: List of the different geological formations in Brussels Region with the stratigraphical position and the type/nature of the different aquifers and aquitards (Meyus et al., 2000).

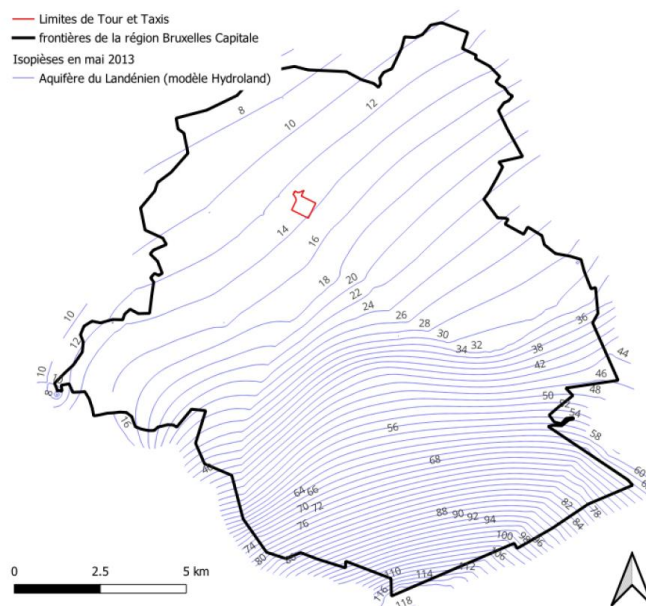


Figure 72: Computed piezometric map of the Landenian aquifer in May 2013 (from Hydroland Model, 2016).

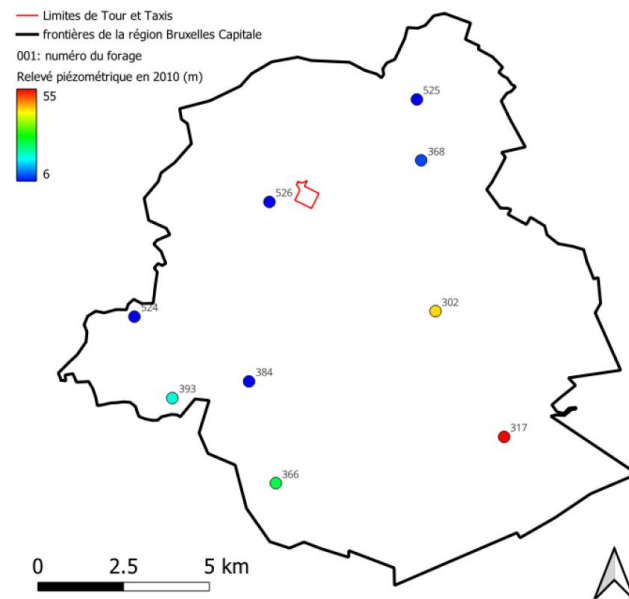


Figure 73: Location of the monitoring wells in the bedrock aquifer for piezometric head measurements.

6.3. Local situation at the reference site of Tour & Taxis

A 3D transient groundwater flow model of the Brussels region was judged too ambitious for this study. The main reasons are the following: (1) the lack of data about the actual transient stress-factors (i.e., the pumping wells); (2) the complex geometry of the upper aquifer and aquitards that are drained by the Senne valley. So, it was decided to focus on the site of Tour & Taxis. This site located in the Senne valley next to the Canal, to the north-west of the historic heart of the city is particularly interesting as it corresponds to the greatest values of uplift measured between 1992 and 2010. In this site the succession of layers is the following (Figure 74):

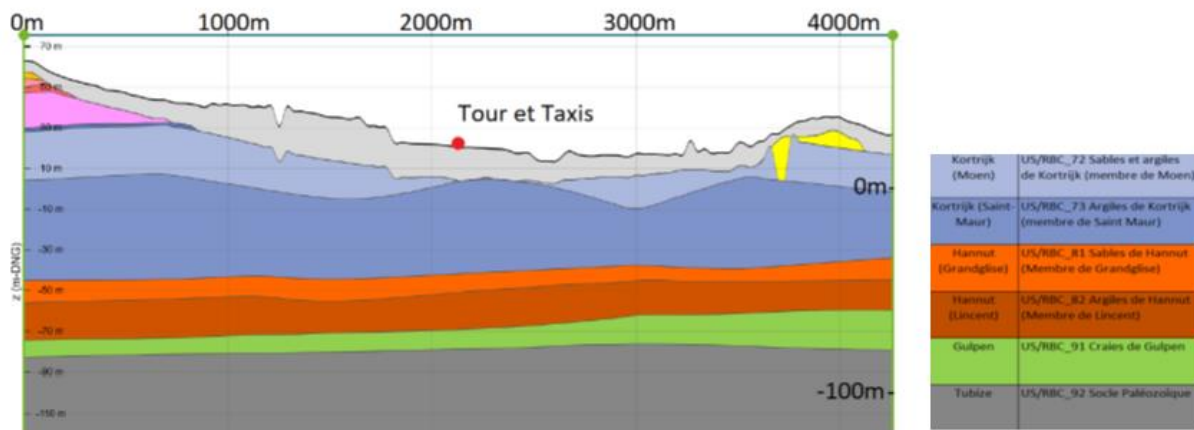


Figure 74: West-East cross-section through the site of Tour & Taxis showing the different hydrogeological units. Three aquifers can be considered: (1) alluvial sediments; (2) Landenian sands; (3) Palaeozoic bedrock.

6.4. InSAR measurements

InSAR (Interferometric Synthetic Aperture Radar) measurements are interpreted on the basis of 5 to 20 m radar images for the ERS, Envisat and Sentinel 1 satellites and 3 m for Terra SAR-X, which means that if there are several reflectors close together but at different distances from the satellite, the signal returned will be a combination of several combination of several signals with different phases.

For each pixel, a coherence value is calculated, enabling its reliability to be assessed on a scale ranging from zero for an unreliable pixel to one for a reliable pixel. Only pixels with a coherence greater than 0.7 were retained. These pixels are called Persistent Scatterers (PS) (Figure 6). Based on a time-displacement curve, a displacement velocity is calculated (Table 16).

	Period	Number of selected PS	Uplift velocity
ERS	1992 - 2001	57	1.15
Envisat	2003 - 2010	38	1.67
Terra SAR-X	2011 - 2014	437	0.32
Sentinel 1	2016 - 2019	20	0.4

Table 16: Uplift velocities as estimated from InSAR measurements for different period in time at Tour &Taxis.

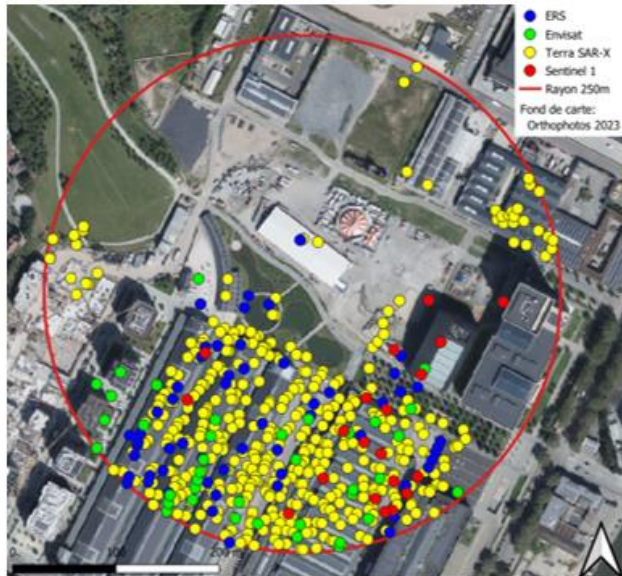


Figure 75: Location of the PS for the different measurement periods.

A time-displacement curve was generated for each series by taking the average of the curves for each SP. Then, a four-point moving average was applied to smooth out variations and a linear regression was used to determine the uplift velocity shown in Table 2. The measured velocities for the first two series are particularly significant, with an uplift between 1 and 2 mm/year, whereas they are less than 0.5mm/year for the last two series, after 2011 (Figure 76).

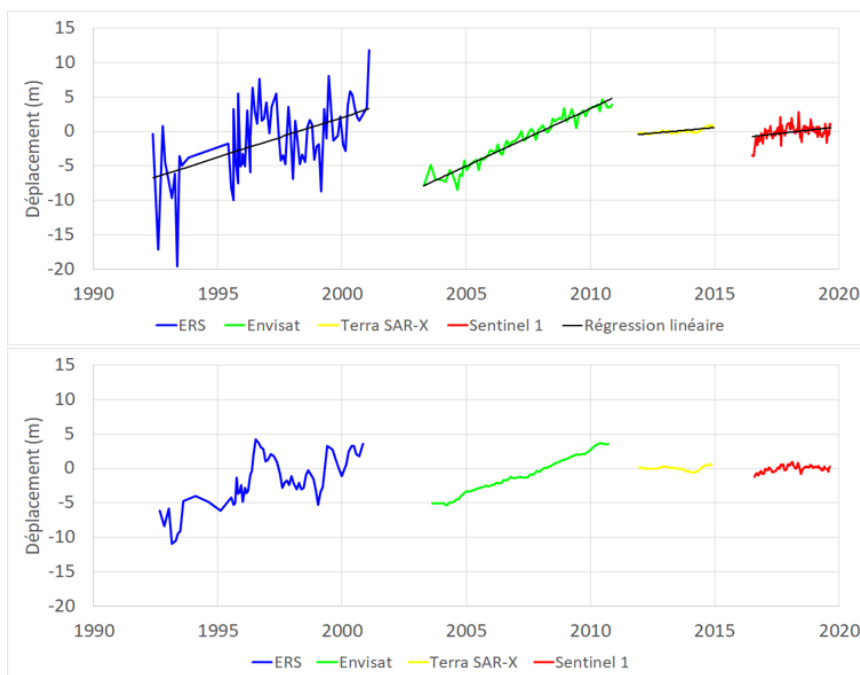


Figure 76: Time-displacement curves for the different InSAR measurement periods without moving averaging (above) and with the four-point moving average (below) (Poncelet, 2024).

6.5. Hydro-geomechanical model concepts

We used a 1D hydro-geomechanical model using the finite element method (LAGAMINE code) coupling the groundwater flow equations to the geomechanical equations. Computed water pressures (i.e., from the calculated piezometric heads) are translated, at each time step, into effective stresses using the Terzaghi principle. Deformations are calculated using a non-linear elastoplastic model for settlements and a non-linear elastic model for swelling. The layers modeled are over-consolidated so that only the elastic behavior is considered. The following elastic law is used:

$$\epsilon_v = -\kappa / (1 + e) \ln \left(\frac{[\sigma']_1}{[\sigma']_0} \right) \quad (1)$$

where ϵ_v is the relative vertical deformation, κ is the elastic compressibility factor, e is the void ratio, and $[\sigma']_1$ and $[\sigma']_0$ the initial and final effective stress respectively.

Indeed, any other deformation component than the vertical one is neglected.

The relation between the elastic compressibility factor κ and the swelling constant A , and the swelling coefficient C_s is the following:

$$\kappa = (1 + e_0) / A = C_s / 2.3 \quad (2)$$

where e_0 is the initial void ratio linked to the porosity with $e_0 = n / (1 - n)$

An initial value of $\kappa = 0.0168$ is taken for the Saint-Maur Formation (Ypresian clays) which is the harmonic mean of the different values from various studies (Poncelet, 2024, Bolle et al., 2006, Dam et al., 2009).

Initial values for the vertical hydraulic conductivity are taken as the geometric means from the data of the geotechnical maps (Poncelet, 2024, Dam et al., 2009).

Numerical discretization

One of the challenges in such calculation lies in the adequate simulation of the delayed water pressure changes in the low permeability layers. Linear approximation of the water pressures in the aquitards is to be avoided. Many finite elements (i.e., thus many nodes) must be discretized to represent the smooth and delayed water pressure distribution at any time in these layers. The model uses the finite element method with elements that have three nodes and two integration points vertically, which allows a non-linear calculation of the pressure within an element. Additionally, we have defined many elements per layer. As shown in Table 17, the size of the elements is between 25 and 50 cm.

	Thickness (m)	Number of elements	Size of elements(cm)
Ypresian aquitard	49	191	25.7
Landenian aquifer	8.5	18	47.2
Landenian aquitard	18.75	41	45.7

Table 17: Details about the vertical discretization of the different hydrogeological units (Poncelet, 2024).

The initial water pressure profile of 1960 is difficult to be reconstructed. A hydrostatic profile can reasonably be imposed in the Landenian aquifer, but representing the situation in the aquitards by linear interpolation is not realistic, as 1960 marks the end of a period of increasing drawdowns that began around 1900, and the pressure at the center of the aquitards was not decreasing as fast as at the contact with the aquifer. The more realistic solution is to simulate the whole period from 1900 and taking really into account only the most recent results. The initial effective stresses in the column are calculated based on the volumetric mass of the geological formations and the initial water pressure profile. As mentioned previously, the horizontal groundwater flow through the side walls of the model is zero because the model is 1D vertical. The pressures at the base of the alluvial aquifer and the top of the chalk/bedrock aquifer are prescribed at the nodes located at the two extremities of the column. The pressures of the Landenian aquifer are prescribed at the center of that layer. Reconstructed evolutions of the piezometric heads have been used (Figures 77, 78, and 79). Details can be found in Poncelet (2024).

Calibration

The time-displacement curves represent relative displacements with respect to the master image. To compare these curves with the ground displacements calculated by the model, they have been shifted upwards by aligning the master image with the deformation curve calculated by the model (Figure 79).

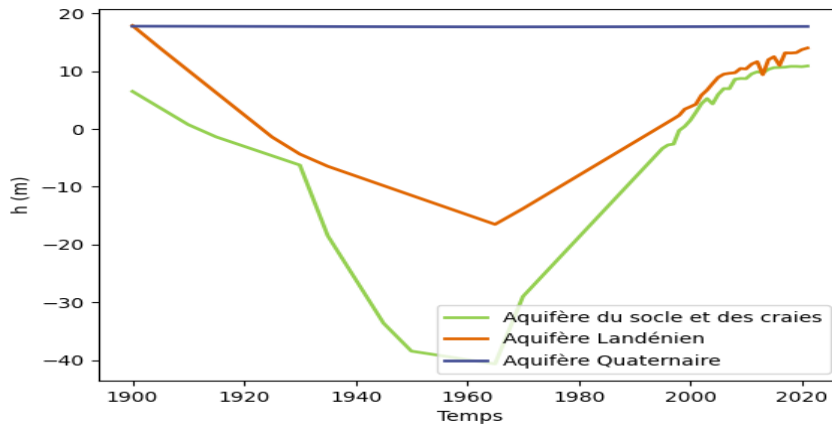


Figure 77: Reconstructed/aggreated piezometric evolution in the aquifers from 1900 until now (from Poncelet 2024).

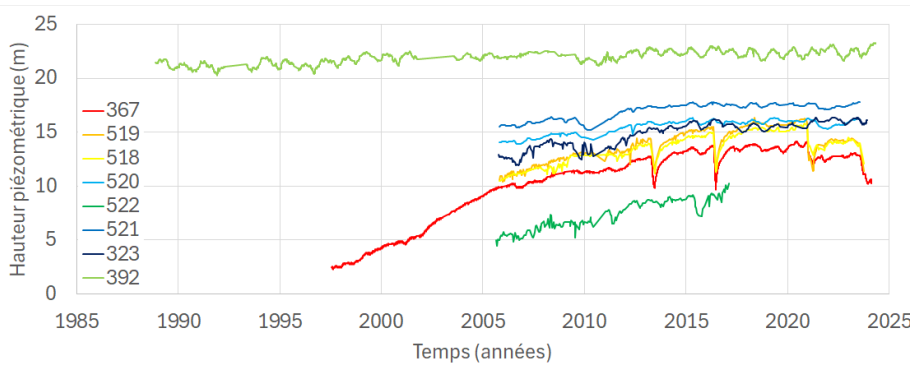


Figure 78: Recent piezometric evolution in the Landenian aquifer as measured in different piezometers (Poncelet, 2024).

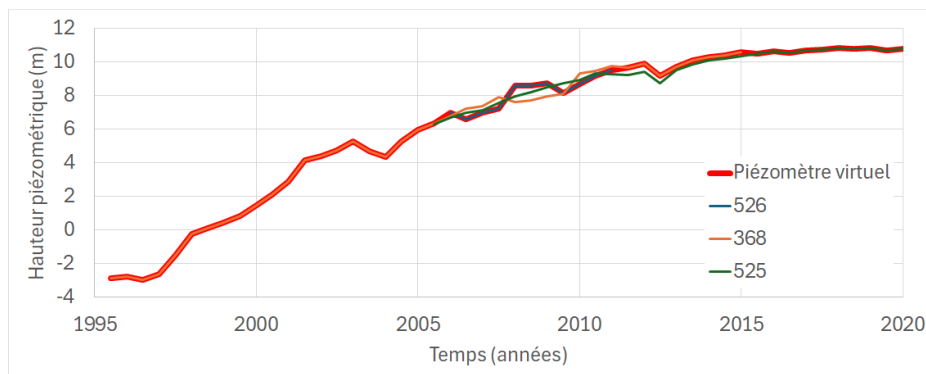


Figure 79: Measured and reconstructed recent piezometric evolution in the Chalk/bedrock aquifer.

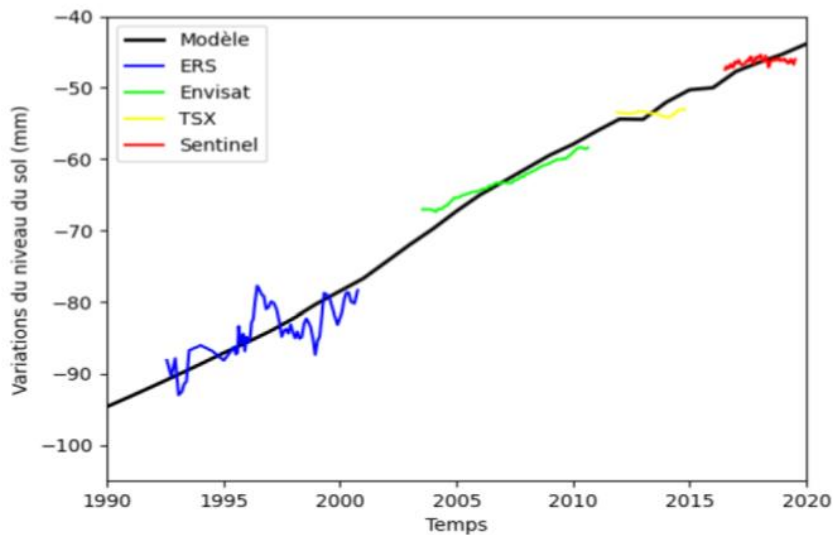


Figure 80: Comparison between the calculated land subsidence (before calibration of the model) and the time-displacement curves from InSAR measurements.

Calibrating a model involves varying its parameters to get calculated results as close as possible to field observations and measurements in the field. In this case, we can consider that the observations are the time-displacement curves obtained using the InSAR method (Figure 11). Indeed, the risk of calibrating with little data and a lot of parameters is to have a system that is not constrained enough.

Here, we limited the calibration to values adaptation for only the main two parameters: elastic compressibility factor κ and the vertical hydraulic conductivity of the aquitards. To avoid multiplying the number of parameters, all the aquitards will be given the same compressibility value and the hydraulic conductivity values will be multiplied by a common factor.

After calibration, the adapted value of the elastic compressibility factor κ is 0.008 for ball the aquitards, and the adapted hydraulic conductivity values of the Ypresian and Landenian aquitards are 2.6×10^{-10} and 1.2×10^{-10} m/s respectively. Calibration was required to increase the vertical hydraulic conductivity of the Ypresian aquitard (values from lab tests were very low).

6.5. Results

So, after calibration, the comparison between the calculated land subsidence and the time-displacement curves from InSAR measurements is better as shown in Figure 81.

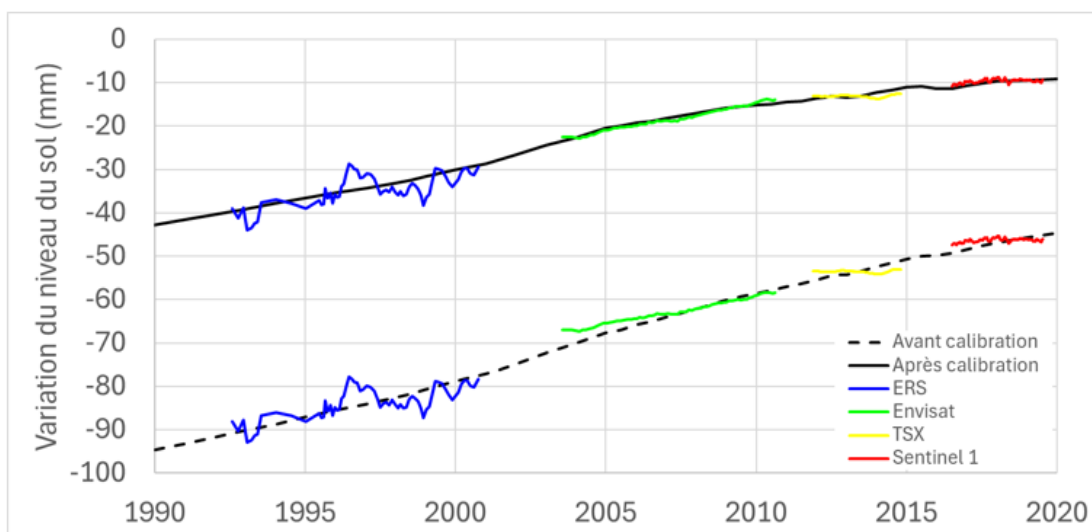


Figure 81: Comparison between the calculated land subsidence and the time-displacement curves from InSAR measurements: before calibration (below) and after calibration (above).

The water pressure evolution in the different layers in function of time (from 1900 until 2020) (Figure 82) shows the delayed propagation of the pressure changes in the aquitard layers. This is particularly interesting to explain the delayed response in terms of land subsidence and uplift with regards to the timing of the main pumping and the cessation of them.

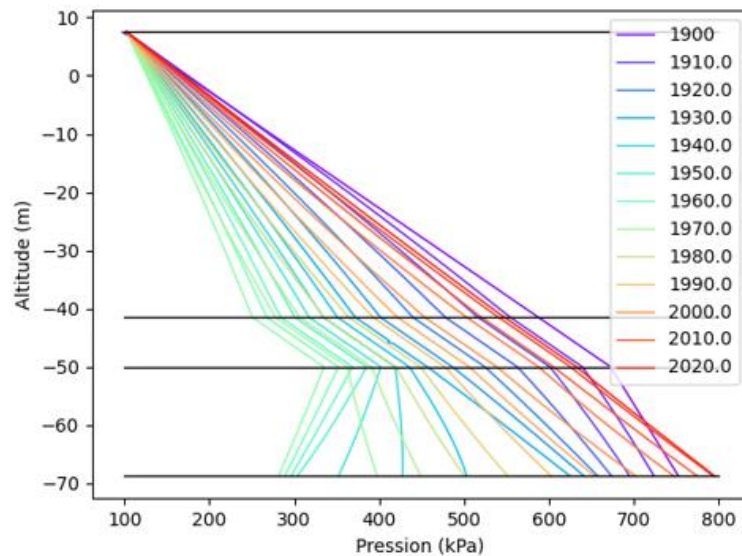


Figure 82: Water pressure evolution in the 1D column in function of time from 1900 until 2020.

The corresponding deformation from 1900 until 2020 in each geological unit is shown in Figure 83.

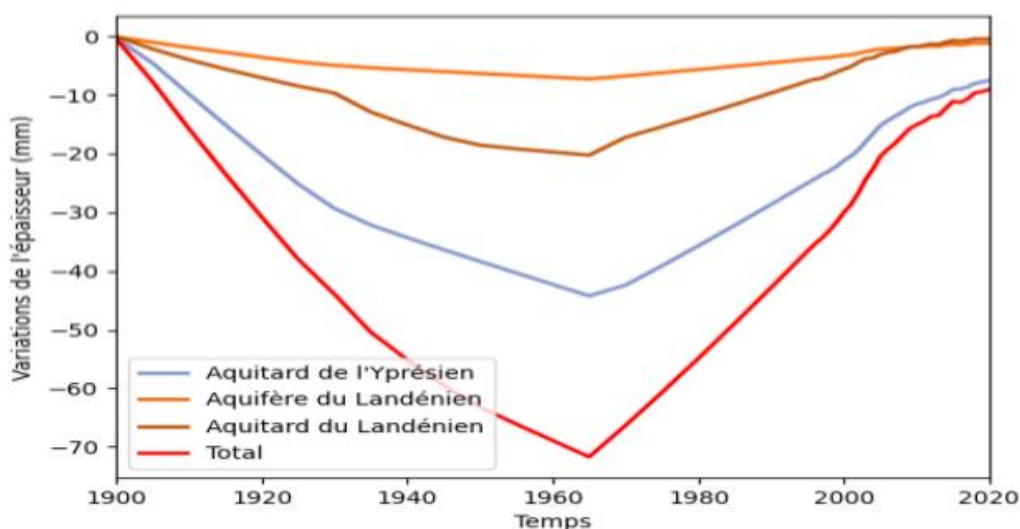


Figure 83: Thickness variation in each main geological unit and in total.

A sensitivity analysis has been performed by Poncelet (2024). As for the calibration, the analysis considered changes in the elastic compressibility values and the hydraulic conductivity values of the aquitards. It has been shown that the model results were quite more sensitive to the values of the elastic compressibility factor than to the permeability of the aquitards. When decreasing the permeability, an additional delay is introduced between the water pressure conditions and the geomechanical consolidation/swelling.

6.5. Conclusions

The industrialization of the city of Brussels in the 19th and early 20th centuries, in the area near the canal and railway facilities such as the site of Tour & Taxis, led to the overexploitation of confined aquifers, resulting in a significant drop in piezometric heads influencing the water pressures in the overlying loose sediments. During the 20th century, industries gradually moved out of the city, reducing the pumped groundwater flowrates. Since the 1960s, the heads

have been rising and are now tending to be stabilized. The induced water pressure variations in the overlying compressible low permeability layers initially led to the subsidence of part of the city, and then, since 1960s the subsequent elastic rebound of around 1 mm/year.

We succeeded in simulating with a 1D hydro-geomechanical model the trend of land subsidence and uplift at the site of Tour & Taxis. We compared successfully the time-displacement curves and displacement velocities as estimated by processing InSAR measurements for the period 1992 - 2019. Indeed, this has required a calibration of the compressibility and permeability properties of the main geological compressible layers.

Future perspectives include building a 3D groundwater flow model to be coupled to multiple 1D hydro-geomechanical models to simulate more accurately the actual hydrogeological conditions. This would require a huge amount of data concerning not only the spatially distributed properties of the different layers but also a reliable data set of pumping records.

6.6. References

- Bolle, I., Buysse, M., De Beer, E., De Breuck, W., DeCeukelaire, M., De Moor, G., Desmet, D., D'Huyvetter, J., Franceschi, G., Maertens, J., Mahauden, M., Meyus, I., Tavernier, R., Van Burm, Ph. and W. Van Impe. Grondmechanische kaarten van Gent, 1976 - 1993.
- Buffel, P., Matthijs, J. 2009. Kaartblad 31-39 Brussel-Nijvel. Departement Leefmilieu, Natuur en Energie, Dienst Natuurlijke Rijkdommen, Vlaamse overheid.
- Dam, J.P., Nuyens, J., Roisin, R. et V. Thonnard. Carte géotechnique de Bruxelles, planche 31.3.5, 1977.
- Deckers, J., Matthijs, J. 2017. Middle Paleocene uplift of the Brabant Massif from central Belgium up to the southeast coast of England. *Geol. Mag.* 154, 1117–1126. <https://doi.org/10.1017/S001675681600073X>
- Declercq, P.-Y. 2017. Persistent scatterer interferometry on ERS, Envisat and Terra SAR–X pictures, Unpublished raw data.
- Declercq, P.-Y. 2019. Persistent scatterer interferometry on Sentinel 1 pictures, Unpublished raw data.
- Declercq, P.-Y. 2020. *A study of long term and slow ground movements in Belgium using Multi-Temporal InSAR satellite data*. PhD thesis, ULiège - Université de Liège, 2020.
- Declercq, P.-Y., Walstra, J., Gérard, P., Pirard, E., Perissin, D., Meyvis, B. and X. Devleeschouwer. 2017. A study of ground movements in Brussels (Belgium) monitored by persistent scatterer interferometry over a 25-year period. *Geosciences* 7(4). 10.3390/geosciences7040115.
- Hydroland Model Brussels. 2016. Aquila. Modèle hydrogéologique de la masse d'eau souterraine du Landénien, Hydroland v1.0
- Meyus, Y., Batelaan, O., De Smedt, F. 2000. Concept Vlaams Grondwater Model (VGM), technisch concept van het VGM, Deelrapport I: Hydrogeologische Codering van de Ondergrond van Vlaanderen (HCOV). Rapp. Opdr. Van AMINAL Afd. Water Brussel.
- Piessens, K., De Vos, W., Herbosch, A., Debacker, T., Verniers, J. 2004. Lithostratigraphy and geological structure of the Cambrian rocks at Halle-Lembeek (Zenne Valley, Belgium), Geological Survey of Belgium, Professional Paper.
- Poncelet, A. 2024. Modèle hydrogéologique et géomécanique pour la simulation de la subsidence et/ou du soulèvement dans la zone de Bruxelles. Master thesis, ULiège.
- Sintubin, M., Everaerts, M. 2002. A compressional wedge model for the Lower Palaeozoic Anglo-Brabant Belt (Belgium) based on potential field data. *Geol. Soc. Lond. Spec. Publ.* 201, 327–343. <https://doi.org/10.1144/GSL.SP.2002.201.01.16>
- Vercoutere, C., Van Den Haute, P. 1993. Post-Palaeozoic cooling and uplift of the Brabant Massif as revealed by apatite fission track analysis. *Geol. Mag.* 130, 639. <https://doi.org/10.1017/S001675680002094X>

WP3: Gravimetry data and models – Deliverables (D.3.1)

1. Introduction

One of the goals of the LASUGEO project is to exploit Synthetic Aperture Radar Interferometry (InSAR), Global Navigation Satellite Systems (GNSS), and absolute gravimetry (AG) measurements to detect and quantify groundwater exploitation in Belgium. Correctly exploiting the observations retrieved by each geodetic technique requires an appropriate statistical methodology. Over the past year, most efforts were devoted to (1) providing reliable estimates of deformation and (2) developing statistical methodologies allowing a better detection of groundwater exploitation from geodetic techniques. In the following chapters, we provide an overview of the research work carried out to exploit gravity, GNSS and InSAR deformation time series.

Collecting gravity data

The ROB gravimetry data were not collected during the Covid crisis period and the measurements in all sites in Belgium and France has been stopped in 2023 with the departure of Dr Michel Van Camp to become the new General Director of the RBINS. Since then, no further ROB activities related to the LASUGEO project have been done. See WP4.

Time series analyses of the gravity measurement data – Deliverable (D.3.2.- See WP4)

WP4: Ground deformation monitoring using PSInSAR and other geodetic techniques – (Deliverables D.4.1./D.4.2./D.4.3./new D.4.5. for IGR antennas)

1. PSI chain software methodological tool development and processing and SAR cartography

1.1. Introduction on SAR interferometry

For over two decades, multi-temporal radar interferometry (MT-InSAR) has been employed by research teams worldwide to measure ground movements with millimeter-per-year precision using radar satellite images captured from an altitude of approximately 800 km. This technique offers numerous advantages, including high accuracy, frequent image acquisition intervals of 6 to 12 days for SENTINEL-1, open access to nearly 30 years of ESA archives, and a high spatial density of measurements. The density varies based on factors such as image resolution, wavelength, and the number of reflective objects in the scene, which in Belgium is strongly influenced by urbanization.

However, the method also has some limitations. It requires substantial computational resources and expertise to produce reliable measurements. Additionally, the high cost of acquiring and processing high- or very high-resolution radar images can pose challenges for expensive research projects. Another limitation is the lower measurement density in rural areas, although this can be partially mitigated using artificial reflectors. Despite these challenges, the strengths of this technique underpin this study, which focuses on long-term monitoring of small-scale ground movements in Belgium.

InSAR

Radar Remote Sensing.

In 1978, NASA launched SEASAT a pioneering satellite mission dedicated to the Earth observation. It was equipped with the first civilian radar sensor. The SEASAT program terminated after 110 days due to a failure but it clearly demonstrated the potential of the radar for studying our planet. In the beginning of the 1970s, Richman (Richman, 1971) developed the idea of using radar satellites for interferometry purposes. The first InSAR application on earth occurred more than a decade later with the work of Zebker and Goldstein (Zebker & Goldstein, 1986). In 1991, the launch of ERS-1 by ESA brought a huge number of SAR data to the scientific community and corresponded to an actual kick-off of the SAR techniques.

The RADAR systems:

The word RADAR is an acronym for “Radio Detection And Ranging”. In the beginning of the 20th century, the radars were essentially developed for ship tracking and collision avoidance in the 1930s and 1940s the military purposes took over the development (Hanssen, 2001). The radar is an instrument that emits electromagnetic pulses with high power in the radio and microwave wavelengths regime and records the echoes of the backscattered signal in a sequential way (Moreira et al., 2013).

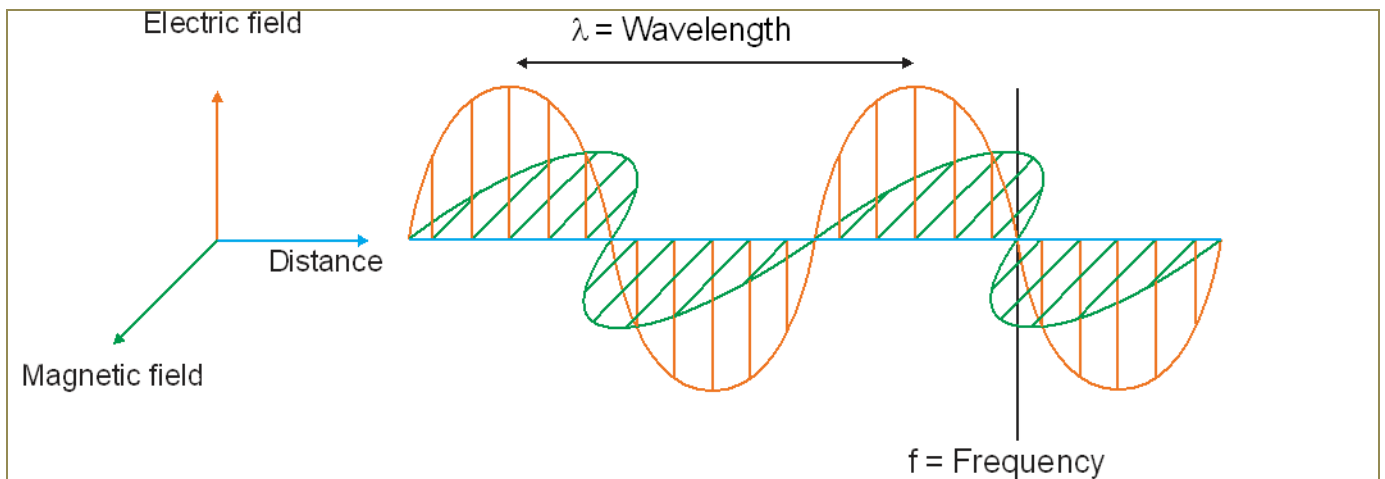


Figure 84. Electromagnetic wave.

Fundamentally, the radar consists of a transmitter, a receiver, an antenna and electronic devices to record and process the data (NRC 2019). It operates by measuring the two-way travel time of the pulse or the time delay between the pulse transmission and the reception of the echoes from the targets. Consequently, their distances from the radar antenna and thus their location can be determined. Since the radar uses monochromatic electromagnetic waves the backscattered signal of the illuminated objects carries an Amplitude, a Phase and is also characterised by a Polarisation. An electromagnetic wave is a self-propagating signal consisting of coupled oscillating electric and magnetic fields, which are perpendicular (Figure 84.). Wavelength (λ) is the distance in space between any two successive points on the wave that have the same phase and amplitude. The polarisation corresponds to the vertical (V) or horizontal (H) propagation of the signal. The part of the electromagnetic spectrum used by radar systems ranges from millimetric to 1-meter wavelengths (Figure 84.). Several wavelength ranges or bands of particular interest are designated by code letters since the WWII.

The most used bands for radar imagery are listed below:

X-band: 2.4 to 3.75 cm (12.5 to 8 GHz). Used mainly for military reconnaissance.

C-band: 3.75 to 7.5 cm (8 to 4 GHz). Used on multiple spatial SARs such as ERS-1, ERS-2, ENVISAT, RADARSAT and Sentinel-1A/1B.

S-band: 7.5 to 15 cm (4 to 2 GHz). Used mainly by weather radar surveillance satellites.

L-band: 15 to 30 cm (2 to 1 GHz). Used on SEASAT and JERS-1 satellites.

P band: 30 to 100 cm (1 to 0.3 GHz). Used on the AIRSAR

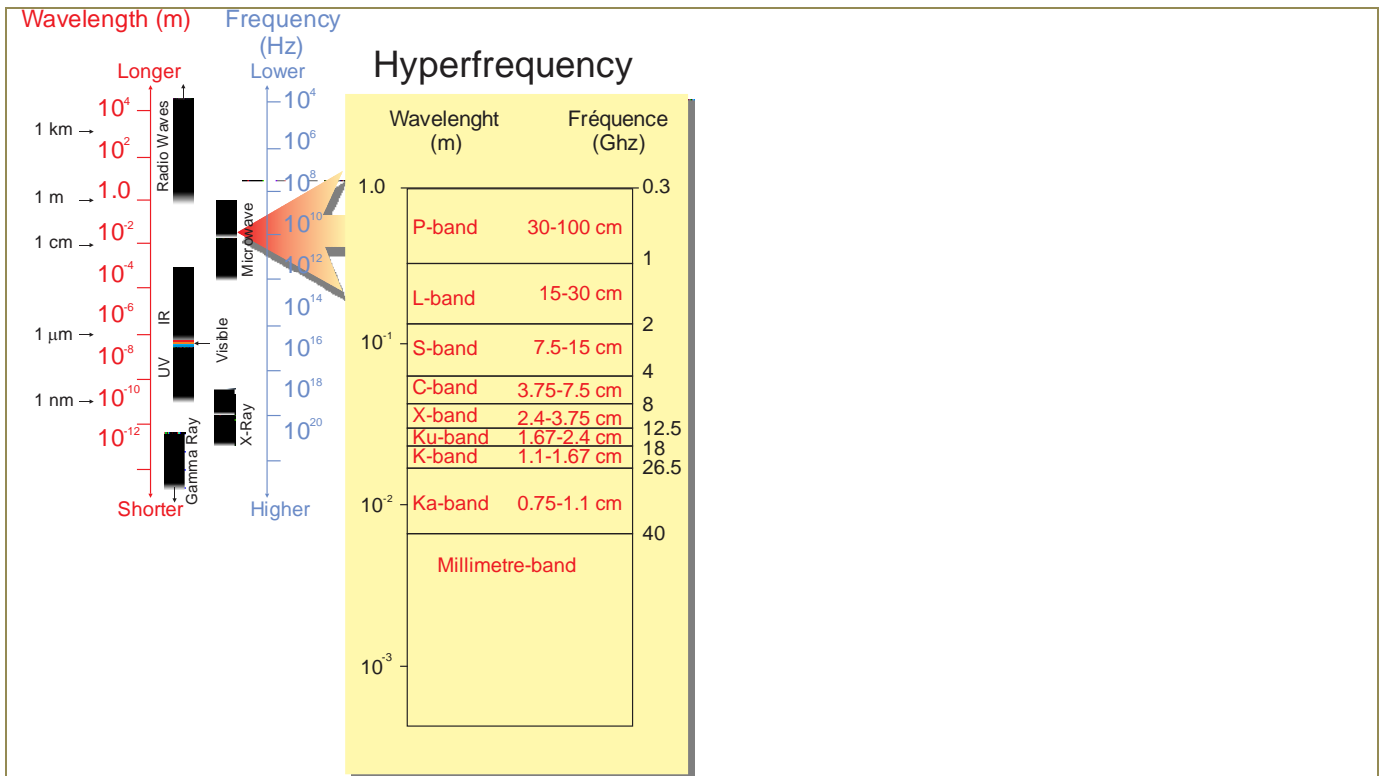


Figure 85. Electromagnetic spectrum (modified from: Natural Resources Canada, 2014).

The Figure 86 clearly shows that atmospheric transmission is almost maximum for wavelengths ranging from 1 cm to 30 cm. On the contrary, the atmosphere is nearly opaque to the Infrared wavelengths. Therefore, the radar's long wavelengths, microwave radiation can penetrate through the atmosphere, cloud cover, and is not sensitive by dust particles. Radars can operate under almost all weather and day/night conditions.

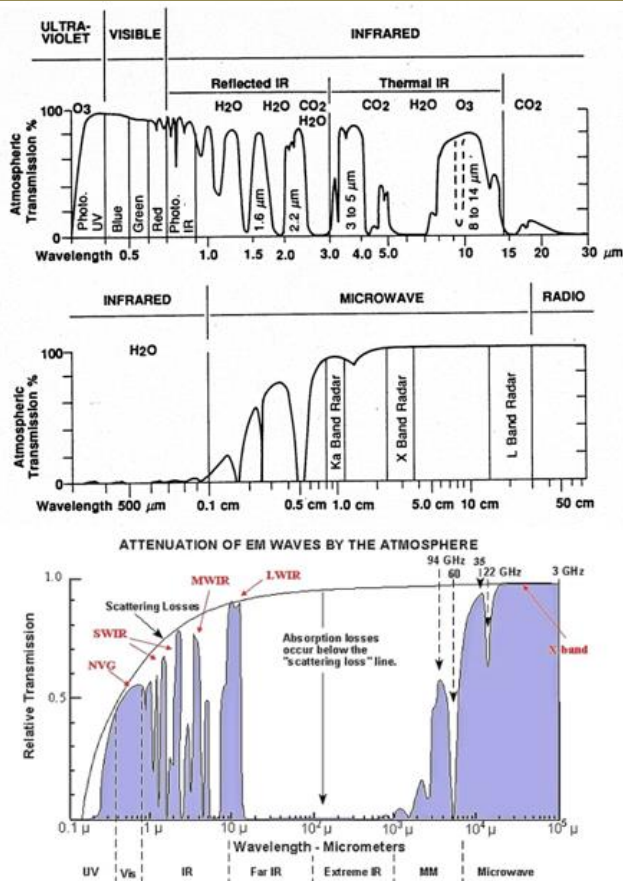


Figure 86. Atmospheric attenuation in the electromagnetic spectrum. EM, electromagnetic; IR, infrared; LWIR, longwave infrared; MM, millimetre; MWIR, medium wave infrared; NVG, Night-Vision Goggle area; SWIR, short wave infrared; UV, ultraviolet; Vis, visible (from Sabins, 1987).

Synthetic Aperture Radar.

The Synthetic Aperture Radar (SAR) is affiliated to a specific class of radar systems called the imaging radars (Hanssen, 2001; Moreira et al., 2013) for which a large antenna is synthesised to increase the azimuthal direction (Figure 87).

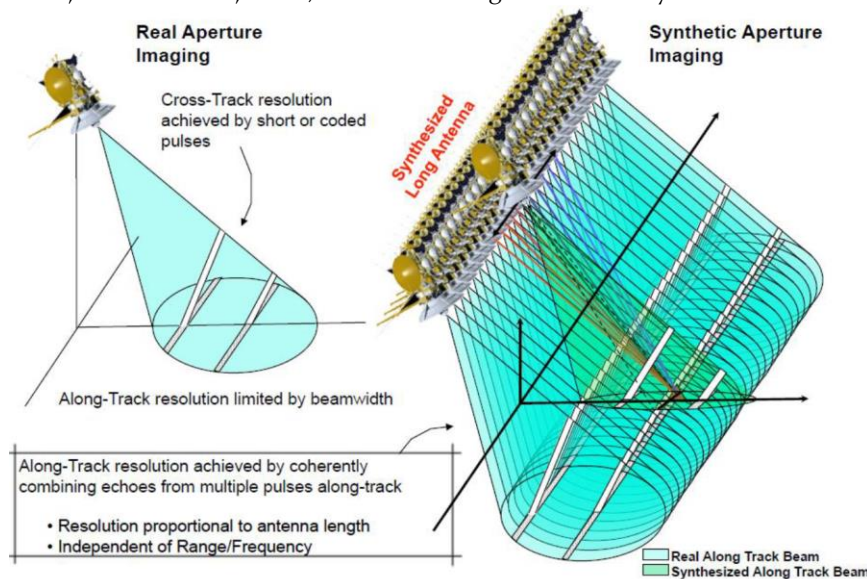


Figure 87. Real aperture vs Synthetic aperture (©JPL).

SAR is an active illumination system that has a side-looking imaging geometry oriented towards the earth surface. The antenna can be mounted on an aircraft or on a satellite. The electromagnetic wave signals are emitted by the antenna and the backscattered echoes from the illuminated surface are recorded by the antenna as the spacecraft moves. SAR systems use the Doppler history of the returned echoes produced by the movement of the aircraft to synthesise a large antenna. The Figure 88 represents the geometry of a radar mounted on a moving platform. The ground range or range direction corresponds to the direction perpendicular to the flight direction. The near range is closest to the nadir and the far range is farthest from the antenna. The azimuth direction is on the opposite parallel to the SAR flight path. The slant range is the oblique distance between a point on the ground and the SAR antenna.

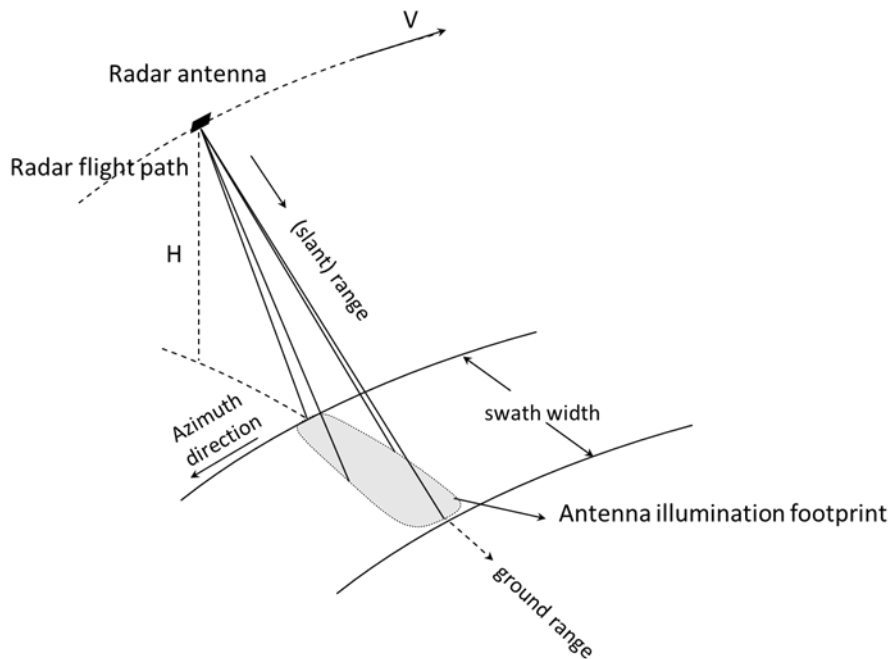


Figure 88. RADAR geometry modified from SAR-EDU, 2019.

In a radar system, the resolution is defined for both the azimuth and range directions. For Real Aperture Radar (RAR), the Range resolution is defined by:

$$resRange = \frac{c \cdot \tau}{2} \text{ or } \frac{c}{2 \cdot B_{chirp}} \quad (\text{EQ 1-1})$$

where c is the speed of light, τ corresponds to the pulse duration of the emitted signal and B_{chirp} is the bandwidth of the chirp. To improve range resolution, radar pulses should be as short as possible. It is also necessary for the pulses to transmit enough energy to enable the detection of the reflected signals (keeping the radiometric resolution). However, the equipment needed to transmit high-energy pulses is demanding. For this reason, a CHIRP (Figure 89) is used to compress the signal, and a long pulse is emitted with a modulated frequency. For ERS, $B_{chirp} = 15.555 \text{ MHz}$, the Range resolution is equal to 9.6 m.

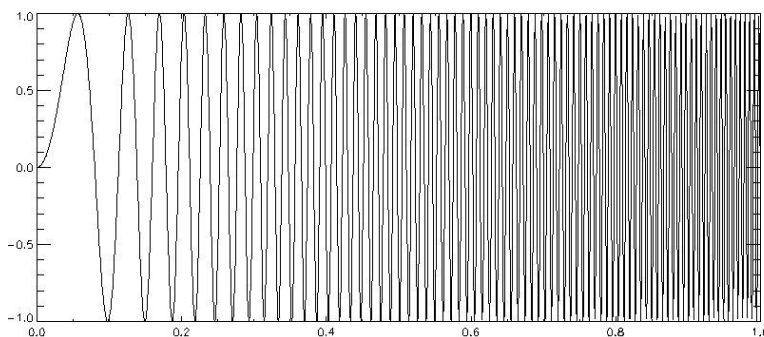


Figure 89. Linear CHIRP. X : Time, Y : Amplitude.

In the azimuth direction, the resolution is defined as the capability of the system to differentiate two scattering objects located at short distance. The azimuth resolution is proportional to the ratio between the wavelength and the length of the antenna. The following equation defines the azimuth resolution:

$$resAzimuth = \frac{\lambda * R}{L} \text{ and } R = \frac{H}{\cos \theta} \text{ (EQ 1-2)}$$

where L is the length of the antenna, R the distance between the antenna and the object in the slant range, θ the incident angle and λ the wavelength. For example, we can estimate the resolution of ERS in the case of RAR. The wavelength is $5.6 \cdot 10^{-2}$ m, the altitude is $785 \cdot 10^3$ m, the incidence angle is 23° and the length of the antenna is 10 m (Curlander & McDonough, 1991). Therefore, the azimuth resolution would be equal to $16 \cdot 10^3$ m. Such a resolution is not appropriated for imaging remote sensing application. Another possibility would consist in increasing the length of the antenna to several hundred metres which is in practice not possible for spacecraft. To bypass this limitation and increase the azimuth resolution, the SAR technique was developed rather than by the actual use of a long antenna. The forward displacement of the spacecraft with the antenna is used in SAR to synthesise a long antenna and therefore increase the azimuth resolution (Chan & Koo, 2008). During the movement, a pulse is transmitted, the backscattered echoes are received by the antenna and finally recorded for further processing (Figure 90). This treatment is based on the Doppler effect, based on pulse compression. The recorded echoes from two different scatterers illuminated by the same beam have different Doppler shifts. By knowing exactly the route of the spacecraft, the system computes the phase history of each target. When the target begins to be illuminated, it is ahead of the radar and returns a frequency (Doppler frequency) slightly higher than the one received. This frequency decreases as the satellite moves along his path towards the target, becomes zero (Zero Doppler frequency) when the target is in the direction perpendicular to the azimuth, and then becomes negative until the illuminated area exits the beam. The combination of those multiple echoes creates the synthetic longer aperture that permits the differentiation of the targets within the same illuminated beam (Agram, 2010). In conclusion, the linear modulation of the frequency naturally induced by the Doppler effect of the relative movement between the source and the target is exploited.

After processing, the synthetic azimuthal resolution depends only on the length of the antenna: $resAzimuth' = \frac{L}{2}$. For ERS, the synthetic azimuthal resolution is 5 m.

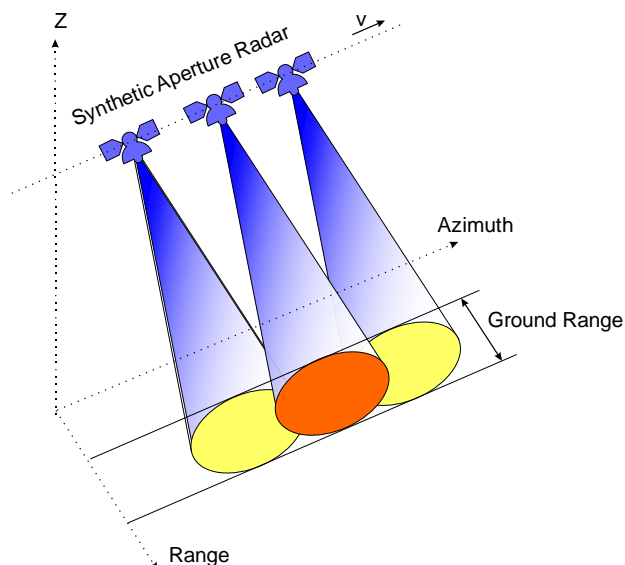


Figure Error! No text of specified style in document.-7 Synthetic acquisition geometry modified from: (SAR-EDU, 2019).

As mentioned above in SAR systems a larger antenna is synthesised to increase the azimuthal direction.

Type of acquisition.

All satellites equipped with SAR sensors orbit the Earth on a near-polar orbit at an altitude ranging from 500 to 800 km above the Earth's surface, depending on the satellite platform hosting the SAR sensor. The angle between true north-south and the satellite orbit varies slightly, depending on the satellite but, in general lies in the range of ten degrees. The satellites in a near-polar orbit at an altitude ranging from 500 to 800 km from Earth are acquiring the data from two geometries, ascending and descending (91). Ascending concerns images acquired when the satellite is going from the S to the N. Descending is the opposite. The angle between the true north-south axis and the satellite orbit varies from one satellite to another but is in general in the range of 10 degrees (Ferretti, 2014). Due the side looking geometry, the satellites see the objects on the earth surface from a different position and therefore may "record" different objects. Also using descending and ascending images permits to fully decompose the Line of Sight (LOS) velocity vectors into a 3D

displacement.

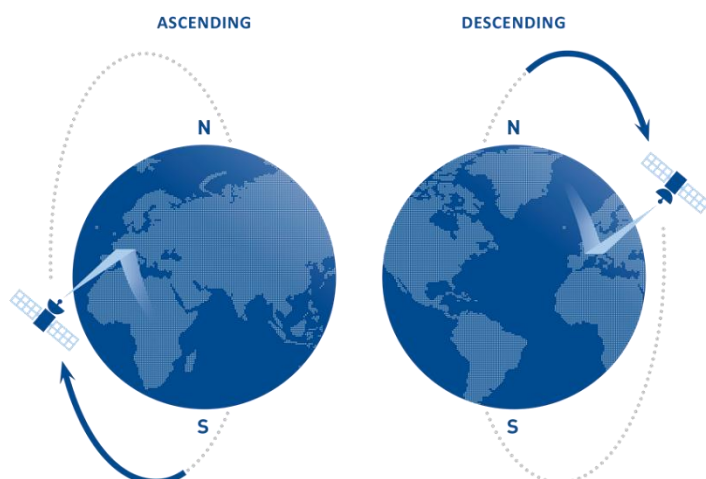


Figure 91. Ascending and Descending acquisition type (TRE ALTAMIRA, 2019).

SAR Satellites.

Error! Reference source not found. 18 shows a non-exhaustive list of SAR satellites commonly used. The indicative price for one image is also mentioned. We will see in the following chapters that the realisation of PSI processing needs at least 15 images that bring the cost of acquisition for high resolution images (TerraSAR-X) to a minimum of 30,000 € or to solicit the data via research proposals. This situation highlights the fact that in this study the number of high-resolution images is limited.

Satellite	Agency	From/To	Mode	Wavelength (cm) / Band	Incident angle (°)	Revisit time (days)	Resolution (m) Ground range	Price per image
ERS-1/2	ESA	1991/2001	Stripmap	5,6 / C	23	35	4 x 20	Free via ESA cat1 research proposal
ENVISAT	ESA	2003/2010	Stripmap	5,6 / C	15-45	35	4 x 20	Free via ESA cat1 research proposal
TerraSAR-X X	DLR	2007	Spotlight Stripmap	3,1 / X	20-45	11	1 x 3 -> 3 x 3	2250 € (/2 for 18 months old archive data) Free via research proposal
Cosmo-SkyMed	ASI	2007	Spotlight Stripmap	3,1 / X	20-60	4, 8	1 x 1 -> 3 x 3	1800 €
SENTINEL-1A SENTINEL-1B	ESA	2014 2016	TOPSAR (IW) (Stripmap)	5,6 / C	29-46	12 alone 6 SENTINEL-1 A+B 12 alone	20 x 4	Free

Table 18. SAR satellites.

SAR Images Properties.

A SAR image corresponds to a mosaic of small picture elements called pixel of which each represents a small portion of the Earth surface (known as resolution cell). Each pixel of a SAR image provides a two-dimensional array of complex number that includes amplitude and phase information about the microwave field backscattered by all the reflectors within the corresponding resolution cell projected on the ground, the ground resolution cell. The size in range of the ground resolution cell is related to the SAR image pixel resolution by the incident angle and the local topography. As the terrain slope increases, the ground moves toward the satellite, the ground resolution in range increases. This effect is known as foreshortening.

This complex image is called the Single Look Image (SLC) (Figure). The pixels indices in the matrix correspond to the azimuth and range position of the backscattering objects in the resolution cells (Agram, 2010). Each pixel contains the in-phase, reference signal (I) and quadrature, offset of $\pi/2$ from I (Q) components of the radar signal, from which the amplitude (A) and the phase (ϕ) are derived (Devan  ry Arasa, 2014):

$$A = \sqrt{I^2 + Q^2} \text{ (EQ 1-3)}$$

$$\phi = \text{atan} \left(\frac{Q}{I} \right) \text{ (EQ 1-4)}$$

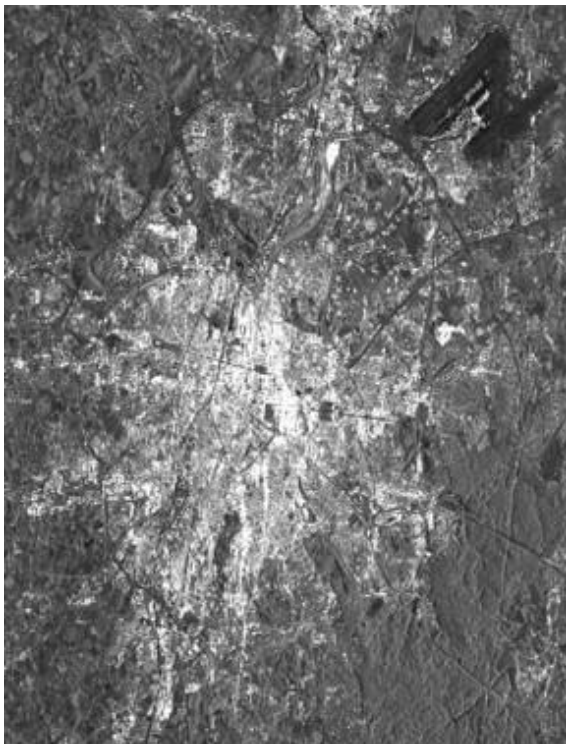


Figure 92. Mean amplitude multilook (6:2) image of Brussels. White pixels correspond to high reflectivity areas, whereas dark pixels correspond to low reflectivity zones.

Amplitude.

The amplitude of a SAR image is a measure of the intensity of the radiation backscattered towards the radar antenna by the objects (Ferretti et al., 2007). The amplitude is highly linked to the roughness of the highlighted objects. Surface roughness refers to the average height variations in the surface cover from a plane surface. Whether a surface appears rough or smooth to a radar depends on the λ and angle of incidence. When the surface height variations begin to approach the size of the λ , then the surface will become rough for the radar. Thus, a surface will appear rougher as the wavelength becomes shorter and smoother as the wavelength becomes longer. For a given λ , flat surfaces (**Error! Reference source not found.**) like lakes are subject to specular reflections, the largest part of the signal is reflected away from the antenna. Therefore, those surfaces appear black on amplitude images. On the other hand, human constructions, cities are characterised by dihedral and trihedral bounces redirecting a high intensity towards the antenna. Those areas correspond to the brighter pixels of the SAR images.

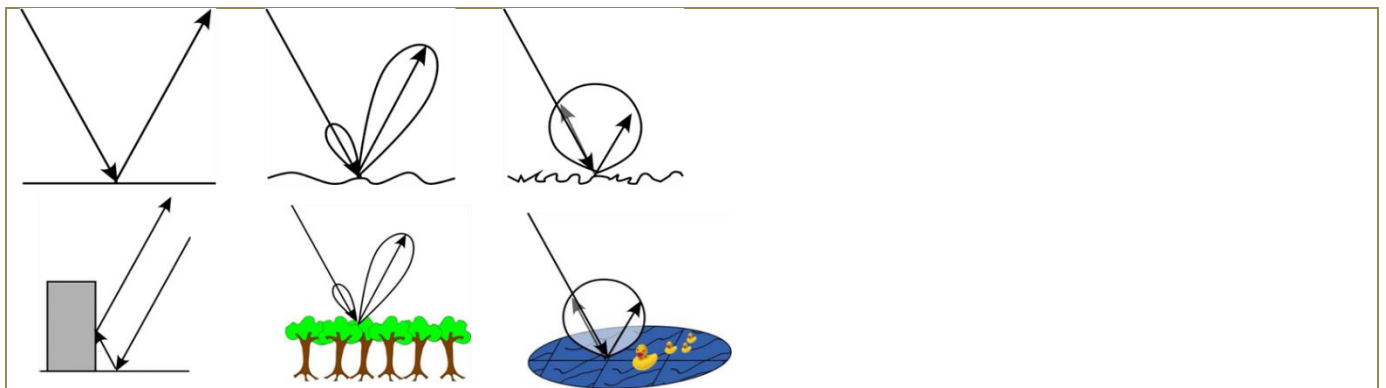


Figure 93. Reflection types depending on the surface/objects.

Phase.

The phase of each pixel of a SAR image is proportional to the two-way travel distance between the antenna and the objects backscattering the signal. It is explained by the fact that objects located at different distances from the radar antenna introduce different delays between the emission of the signal and the recording of the backscattered one. Due to the cyclicity of the signal the travel distance that differ by an integer multiple of the λ induces the same phase change (Figure 94). Therefore, the phase is always known modulo 2π (EQ 1-5)

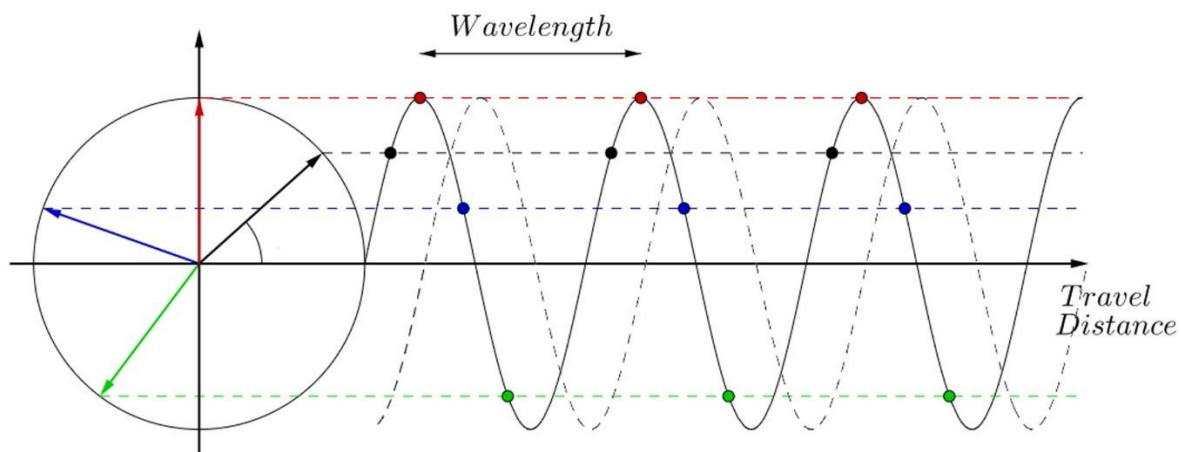


Figure 94. Complex representation of the phase (image:ESA).

Equation of the phase:
$$\varphi = \frac{-4\pi}{\lambda} R + \varphi_{scatt} + n \cdot 2\pi \text{ (EQ 1-5)}$$

Where λ is the wavelength, R is the Range distance, φ_{scatt} is the phase due to the nature and location of the objects backscattering the signal within the resolution cell, n is an integer corresponding to the modulo of the phase. The Figure illustrates how a target is seen and recorded by the radar in terms of time interval.

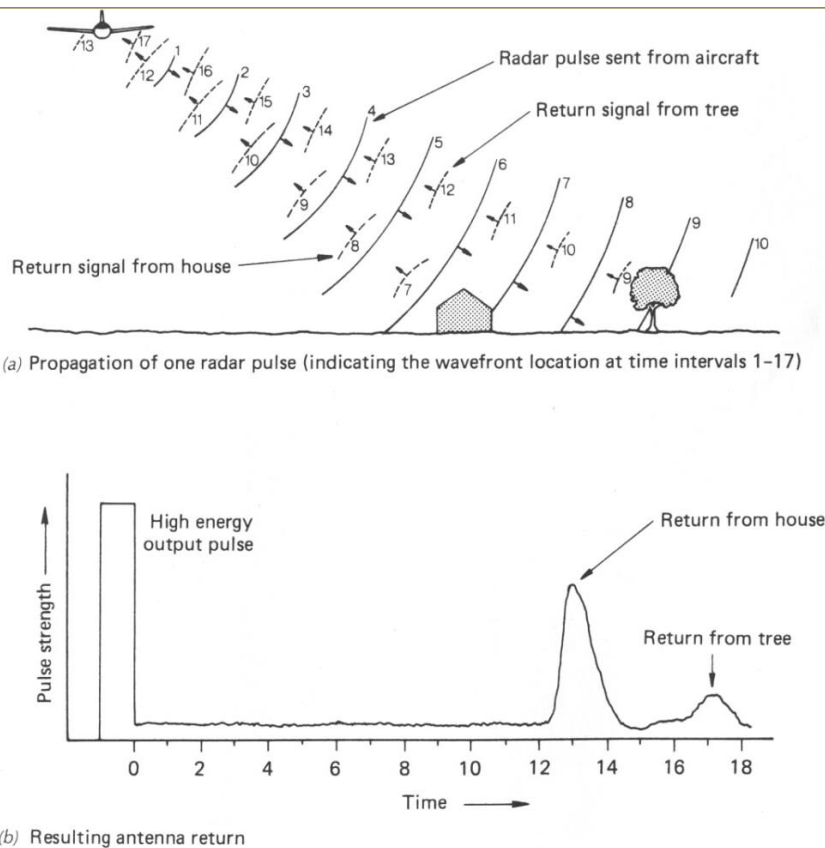


Figure 95. Illustrations of how targets are seen and recorded by a radar (image from Lillesand & Kiefer, 2000).

InSAR, DInSAR

In the case of SAR Interferometry (InSAR), the phase information for two SAR images acquired over the same area from similar but different geometries are combined to form an interferogram. The phase of the interferogram is obtained by multiplying pixel by pixel the first image (Master image) with the complex conjugate of the second image (Slave image) (Bamler & Hartl, 1998; Massonnet & Feigl, 1998). The resulting interferometric phase is the phase difference between the images and the amplitude of the interferogram corresponds to the product of the two images. To realise this operation the Slave image must be coregistered and resampled to the geometry of the Master image (Hanssen, 2001; Zebker & Goldstein, 1986).

From the equation 2-5 the phase of a complex SAR pixel is $(\varphi = \frac{-4\pi}{\lambda} R + \varphi_{scatt} + n \cdot 2\pi)$

Complex SAR image 1: $u_1[i, k] = |u_1[i, k]| \cdot \exp(j \varphi_1[i, k])$ (EQ 1-6)

Complex SAR image 2: $u_2[i, k] = |u_2[i, k]| \cdot \exp(j \varphi_2[i, k])$ (EQ 1-7)

Interferogram formation: $v[i, k] = u_1[\cdot] u_2^*[\cdot] = |u_1[\cdot]| |u_2[\cdot]| \exp(j \varphi[\cdot])$ (EQ 1-8)

Phase of the interferogram is $\varphi[\cdot] = \varphi_1[\cdot] - \varphi_2[\cdot]$ (EQ 1-9)

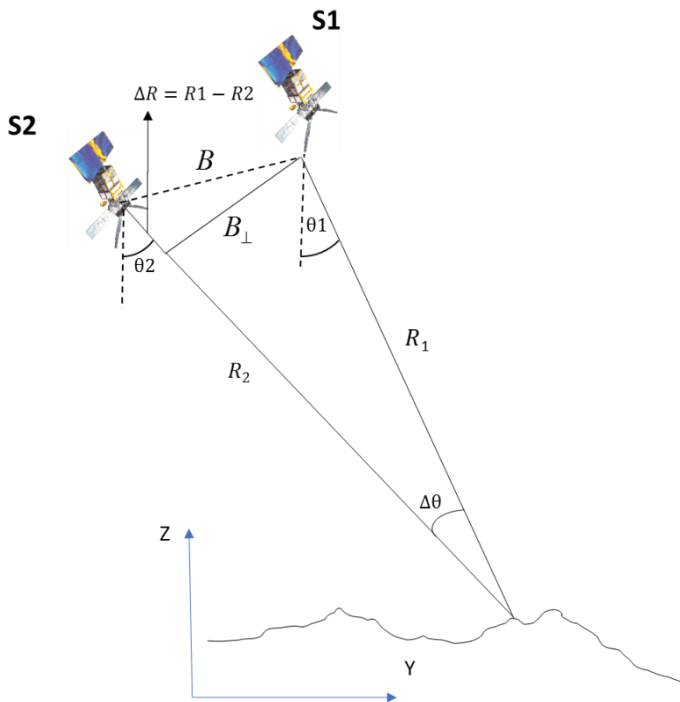


Figure 96. SAR interferometric configuration. R1 and R2 are the slant ranges, B corresponds to the Baseline, B_perp is the perpendicular Baseline and theta1 and theta2 the look angles (image: ESA).

By considering that the scattering characteristics of the illuminated objects remain the same for the Master and the Slave and ignoring any time delays in the imaging hardware, the interferometric phase is:

$$\varphi_{\text{int}} = \frac{-4\pi}{\lambda} R \quad (\text{EQ 1-10})$$

Where φ_{int} is the phase of the interferogram, λ is the wavelength and R the radar-target distance.

The interferometric phase φ_{int} is actually the sum of the following component:

$$\varphi_{\text{int}} = \varphi_{\text{def}} + \varphi_{\text{orbit}} + \varphi_{\text{topo}} + \varphi_{\text{atm}} + \varphi_{\text{noise}} \quad (\text{EQ 1-11})$$

The φ_{def} corresponds to the relative displacement of the reflecting object. The φ_{orbit} is the phase difference due to the orbital changes between the two acquisition positions. The φ_{topo} accounts for the topography. The φ_{atm} is the phase due to the Atmospheric Phase Screen (APS) provoking delays. The φ_{noise} is due to other terms and the system noise (Agram, 2010) and in case of a good (high amplitude) scatterer can be neglected. Initially, InSAR was developed to measure the Earth topography (Zebker & Goldstein, 1986). The Shuttle Radar Topography Mission (SRTM) was based on radar technology to create Digital Elevation Model (DEM) of the Earth. In the case of Differential InSAR (DInSAR) (Massonnet et al., 1993; Zebker et al., 1994), the phase due to the topography is removed using a DEM. A synthetic interferogram is generated based on the DEM to remove the phase contribution of the topography and therefore it is possible to estimate the ground displacement by considering the other phase contributions to be negligible. The different contribution to the phase of the interferogram will be detailed below. The Figure 97 is an interferogram generated using two ENVISAT SAR images taken before and after an earthquake in Bam (Iran) the 26/12/2003.

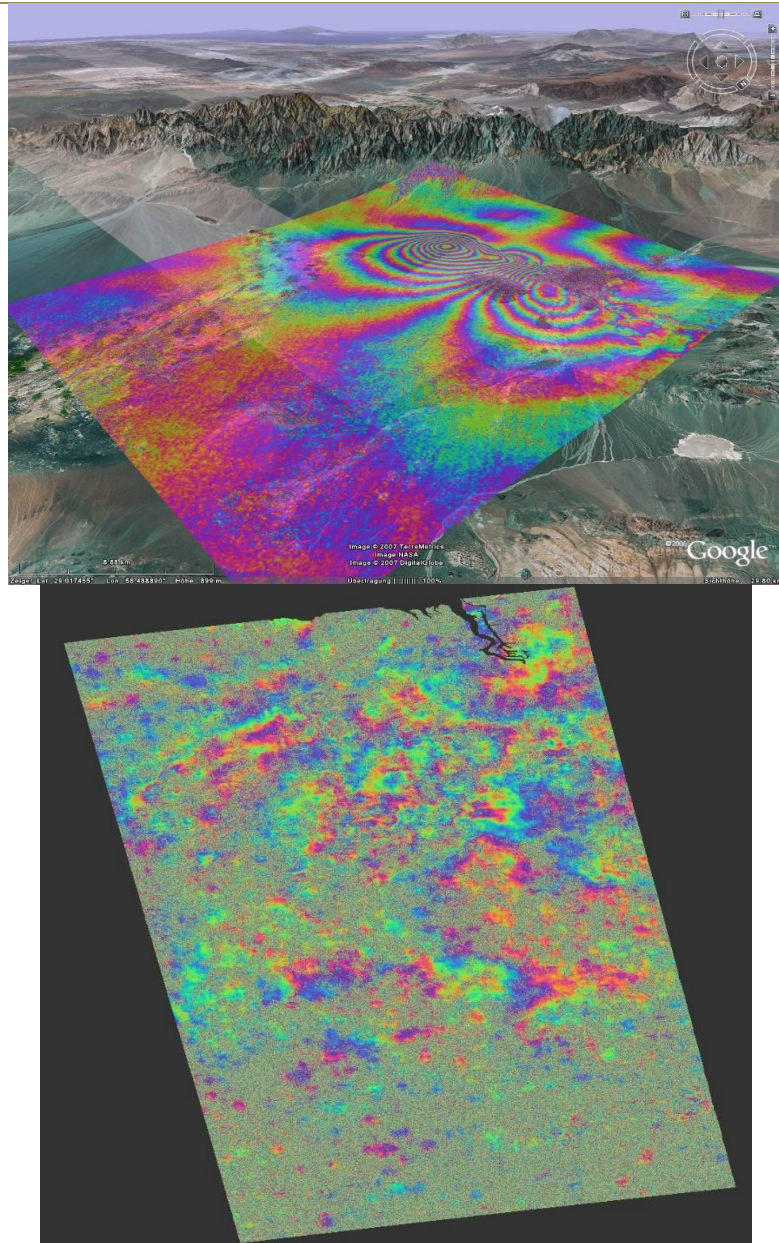


Figure 97. A. SAR interferogram observing the Bam earthquake using ENVISAT 3.12.2003/7.1.2004 images (Funning et al., 2005; SAR-EDU, 2019; Stramondo et al., 2005). Each group of fringes colour cycle corresponds to a displacement of 2.8 cm. B. Sar interferogram of Sentinel 1 from February 2018 to February 2019 of the North of Belgium.

Contribution of the different factors to the phase.

1. Contribution of the ground displacement (φ_{def})

The φ_{def} is produced by a ground displacement in the LOS during the period of time between the Master and the Slave acquisition (Hanssen, 2001).

$$\varphi_{\text{def}} = \frac{-4 \pi d}{\lambda} \quad (\text{EQ 1-12})$$

Where d is the ground displacement in the LOS and λ the wavelength. In the case of a C-band satellite like ENVISAT $\lambda = 5.6$ cm therefore a displacement of 2.8 cm corresponds to a full-colour cycle. The *Figure* illustrates the interferometric sensitivity versus the wavelength.

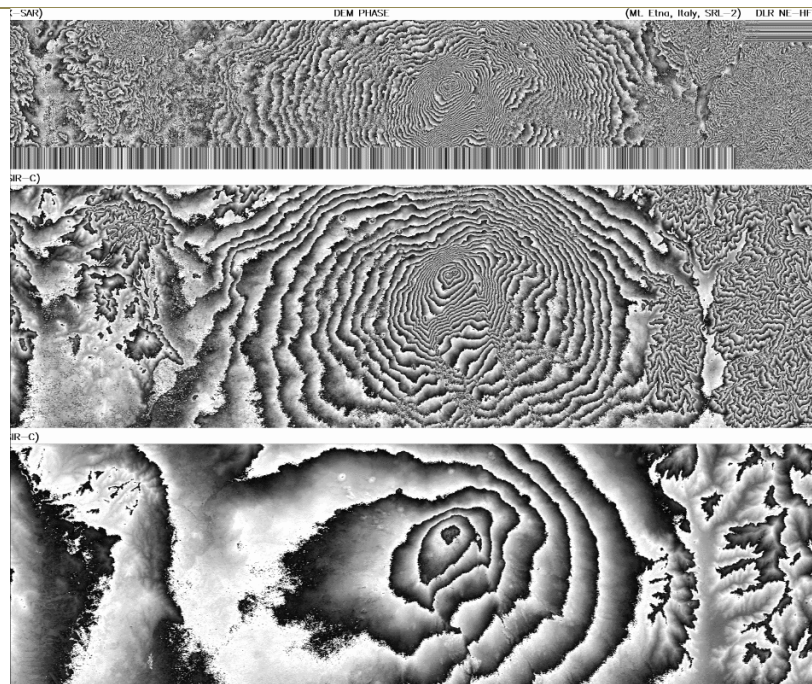


Figure 97. Mount Etna seen at different wavelengths. A). X-band. B). C-band. C). L-band. (SAR-EDU, 2019).

The displacement is calculated in the LOS geometry (Figure 99) and depends on the look angle (θ) and satellite heading on ground (θ_h) (Cuenca, 2012). The displacement in the LOS corresponds to the contribution of the Up vector (d_U), the East vector (d_E) and the North vector (d_N). Giving the equation:

$$d = d_U \cos \theta + d_N \sin \theta \sin \theta_h + d_E \sin \theta \cos \theta_h \text{ (EQ 1-13)}$$

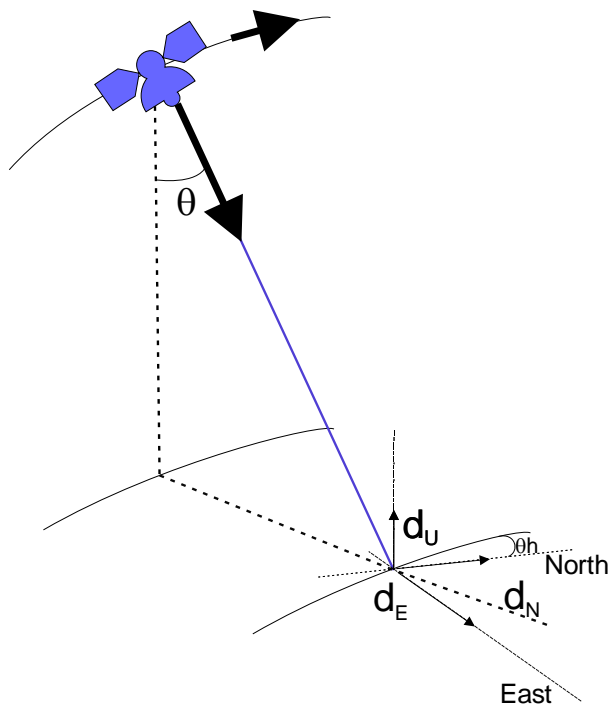


Figure 99. Satellite geometry.

Using this equation and the look angle θ value of ENVISAT (23°) and the heading angle $\theta_h = 10$, one can derive that the satellite has higher sensitivity in the vertical direction than the two other components. It is even almost not sensible in the along track direction.

2. Contribution of the baseline or Orbital errors (φ_{orbit}).

A shift in the orbital trajectory of the spacecraft between the master and the slave acquisitions induces a phase difference.

This difference is due to the change of the viewpoint and thus backscattered signal of the illuminated area. Orbital errors produce long-wavelength phase contributions to the interferogram. If the observed phenomenon produces similar long wavelength displacement, it is hard to discriminate the contribution to phase of the orbital errors from the actual displacement (Amelung & Fattahi, 2014; Massonnet & Feigl, 1998). There are various techniques available for mitigating the orbital errors, Massonnet and Feigl 1998 propose to estimate a linear or quadratic surface that fits to the interferometric phases by *a priori* knowledge of the orbits from the spacecraft instrument. This procedure is also known as deramping. Residual fringes are removed by tuning the polynomial coefficients of the “deramping” surface.

3. Contribution of the topography (φ_{topo}).

As the radar antenna sees the topography from two different points of view, the removing of the orbital phase contribution reveals a stereoscopic effect (Massonnet & Feigl, 1998). This topographic contribution is called topographic fringes that need to be quantified. The altitude of ambiguity (h_a) is defined as the altitude shift that generates one topographic change or an interferometric phase change of 2π . h_a varies from infinity if the spacecraft acquires the master-slave images from exactly the same position to 10 m corresponding to the largest orbital separation accepted for interferometry and avoiding decorrelation (Massonnet & Feigl, 1998). The altitude of ambiguity is inversely proportional to the perpendicular baseline:

$$h_a = \frac{\lambda R \sin\theta}{2 B_{\perp}} \text{ (EQ 1-14)}$$

Where h_a is the altitude of ambiguity, λ the wavelength, R the radar target distance, θ the incidence angle and B_{\perp} the perpendicular baseline. For ERS, with a 100 m perpendicular baseline a fringe (2π change) corresponds to an altitude difference of 93 m. This sensibility to the topography is used to calculate Digital Elevation Model (Zebker & Goldstein, 1986) and was the base used to map the topography during the SRTM missions in 1999. SRTM produced a near-global topography product for latitudes smaller than 60° , with the SRTM data sampled over a square grid of 3 arc-second (90 m). The relative height error is less than 10 m (Farr et al., 2007; Rodriguez et al., 2005).

However, to obtain a continuous topography the interferometric phase must be unwrapped, as the radar measures interferometric phase modulo 2π .

4. Contribution of the atmosphere (φ_{atm}).

The atmospheric phase “screen” (φ_{atm}) corresponds to the variation in the delay of the signal as it propagates through the atmosphere. Since the master and slave acquisitions are separated by several days (35 days for ERS-ENVISAT), the differences in the ionosphere (50-2500 km height) and troposphere (0-25 km height) conditions will affect differently the phase of the images as well as the water vapour and the stratification due to the topography. The φ_{atm} delays can be spatially identified as long and short wavelength signals (Bekaert et al., 2015). The ionospheric effect and the tropospheric effect are considered as long wavelength signals while the water vapour and the vertical stratification due to the topography has short one.

The ionospheric phase delays are related to the variations in free electrons along the travel path of the signal. The Tropospheric phase delays are caused by pressure, temperature and relative humidity variations. This last contribution to the total phase of the interferogram can be much larger than the tectonic signals of interest (Bekaert et al., 2015). This is a clear limitation of InSAR to precisely calculate the ground displacement.

5. Contribution of the noise (φ_{noise}).

The φ_{noise} includes the instrumental noise and the temporal change of the scattering properties of the highlighted objects. For instance, vegetated areas are subject to a rapid change of its scattering properties in comparison to outcrops for which the backscattered signal does not completely change between the two acquisitions.

Phase Unwrapping.

Since the interferometric phase in the interferogram is ambiguous due to its cyclic nature (modulo 2π), the process providing a “continuous” phase information is known as phase unwrapping. It consists via different algorithms in adding the correct integer (modulo) multiple of 2π to the interferometric fringes. However, this process (Figure 100) shows fringes corresponding to the topography of the Mount Etna as it is recorded and the unwrapped phase. This process is probably one of the most difficult aspects in radar interferometry processing mainly due to artefacts and noises. In the beginning of the 1990s, several 2D algorithms were developed (Costantini, 1998; Goldstein et al., 1988; Zebker & Lu, 1998). They mainly fall into two classes (Zebker & Lu, 1998):

1. algorithms based on identification of residues in the wrapped phase field and cuts, or “trees”, connecting a group of residues to limit the integration paths.
2. Algorithms that derive a smooth field by integrating the gradient of the observations subject to smoothness constraints as determined by least-squared-difference criteria.

Further developments of the algorithms benefiting from an increase of the computation power led to the creation of 3D unwrapping methods (Hooper & Zebker, 2007). Among the algorithms produced by the InSAR community, there is an Open Source software called SNAPHU standing for: “Statistical-Cost, Network-Flow Algorithm for Phase Unwrapping” (Chen & Zebker, 2002), which is commonly used.

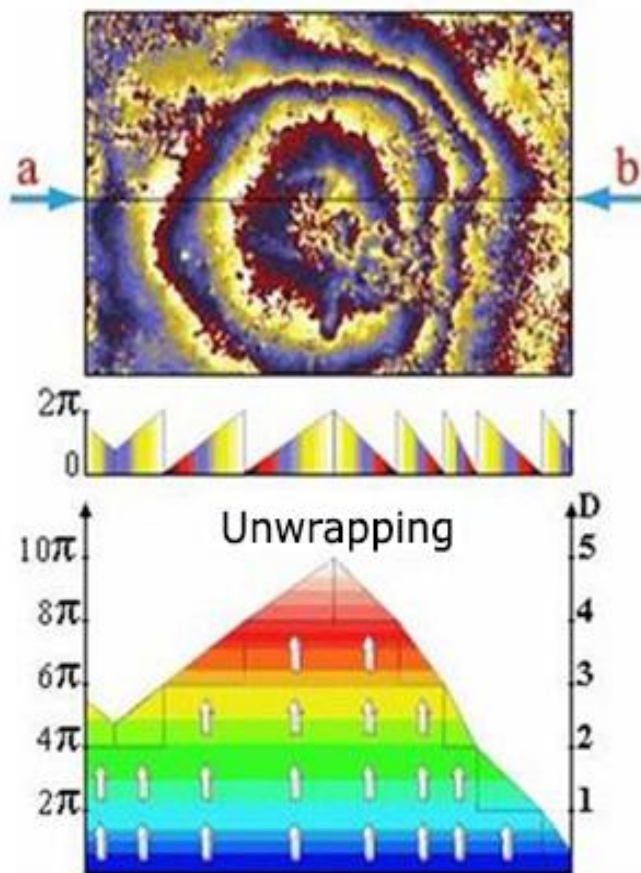


Figure 100. Illustration of the principle of unwrapping an interferogram (Image: ESA).

Limits of InSAR – DInSAR techniques.

Fundamentally, InSAR and DInSAR techniques are based on the phase difference between two SAR images that are acquired at two different time periods. The correlation is a measure of the similarity of phase between the two acquisitions. It ranges between 0 and 1, where 0 indicates no correlation. A good correlation is needed to produce valuable interferogram that could be unwrapped. Decorrelation corresponds to the loss of correlation. If the correlation is greater than 0.20, the phase information can be retrieved; between 0.15 and 0.20, it is possible but difficult to retrieve some phase information; and below 0.15, no phase information can be retrieved (Wei & Sandwell, 2010). Usually, correlation above 0.20 is expected in areas where the surface conditions of the highlighted areas do not change much with time, such as urban areas, and low correlation is probable in vegetated zones or rural areas.

Several factors are influencing the decorrelation. However, the Temporal and the Spatial decorrelation are the two main factors (Hanssen, 2001; Zebker & Villasenor, 1992). The temporal effect is related to physical changes in the surface over the time period between the two acquisitions. The change of reflectivity of the surface due to vegetation, the melting of snow, soil humidity or other phenomena, decorrelates significantly the measurements. The recorded phase becomes unreliable. Therefore, InSAR-DInSAR studies are not commonplace in Belgium but are more applicable in dry and sparsely vegetated countries.

The spatial decorrelation is due to the difference in incidence angles between the two acquisitions. All the backscattered signals from a resolution cell on the ground are added up slightly differently and the measurements are not reproduced exactly (Zebker & Villasenor, 1992).

Typical sources of decorrelation are:

- Vegetation (especially for X-band and C-band). Leaves on the trees grow, fall and move.

- Newly built areas (houses, roads, ...), erosion. The land surface is changing all the time.
- Rapid movements. Landslides and earthquakes change rapidly the earth surface due to heavy modifications and/or destruction of the area.

In general, to remove or minimise the temporal and geometric decorrelations, we use filtering algorithms and select suitable SAR Master-Slave pairs to be processed. The main criteria for the selection are the respect of a small baseline distance and a short time period between the images.

Another source of error or limitation consists in the use of inaccurate DEM. When studying surface displacements with InSAR, the topographic phase is removed using an external digital elevation model (DEM). However, the topographic component is never perfectly subtracted because of DEM inaccuracies or errors. It results in having residual topography fringes in the interferograms usually accounting for several metres. The errors introduced by the residual topography fringes can have more or less impact on the actual calculation of the displacement. For example, for ENVISAT, the wavelength is 5.6 cm, the incidence angle is 23° , for perpendicular baseline of 100 m, 10 m of residual topography corresponds to 0.3 cm of error that could have been assimilated to a displacement.

In summary, InSAR-DInSAR have three major limitations for studying the ground displacements: the effect of the atmosphere on the signal, the spatial and temporal decorrelation (low coherence interferograms) and external error sources. To overcome these limitations, time series analysis techniques (Multi-Temporal-InSAR) were developed in the late 1990's. In the following sections, the most relevant time series analysis techniques will be briefly described, the PSI-PSInSAR and Small Baseline Subset techniques (SBAS). PSInSAR is a patented name by TRE, therefore we will use the generic acronym PSI.

MT-INSAR

In this chapter, we will make a brief description of the two main families of Multi-Temporal InSAR (MT-InSAR) approaches. The aim is to provide to the reader the key points of the techniques. Recently (Crosetto et al., 2016) made an extensive review of the techniques and the different research papers linked to it.

Multi-temporal InSAR techniques are extensions of InSAR-DInSAR intended to overcome the issues caused by the spatial and temporal decorrelations and atmospheric delays. The interferogram is at the core of MT-InSAR. These techniques involve the simultaneous processing of a stack of multiple SAR images covering the same Region Of Interest (ROI) allowing the correction of uncorrelated phase noises (including APS, instrumental noise, changes of the scattering properties) (Agram, 2010). Globally, there are two main types of PSI approaches. The first one identifies pixels that have a good correlation and stable phases during a long period of time in the stack of interferograms (Ferretti et al., 2000, 2001). The second PSI technique uses the spatial correlation of the phase between the scatterers (Hooper et al., 2004). Using appropriate combinations of short orbital separation, SBAS techniques are reducing the effect of spatial and temporal decorrelation (Berardino et al., 2002; Hooper, 2008; Lanari et al., 2004).

The backscattered signal from each resolution cell on the ground varies depending on the spatial distribution and reflectivity properties of the scattering objects within the cell. Since the radar is using monochromatic signal, its backscattered record corresponds to the coherent sum of the wavelets of each distributed scatterer within the resolution cell (Figure). In this case, because all the scatterers have comparable amplitude, the phase of the interferograms are randomly distributed between $[-\pi, \pi]$ due to the decorrelation. The SBAS technique (Berardino et al., 2002) proposes to increase the Signal to Noise Ratio (SNR) by averaging the cells neighbouring phases of the interferograms. Therefore, the random phases due to the movement of scatterers cancel out (Agram, 2010). Only the phases due to the average motion of the averaged cells are kept.

In the case of a single scatterer within the resolution cell, the recorded signal only varies a little through the studied period of time. However, this situation almost never happens in nature.

Finally, if there is one scatterer that dominates the others by having a stronger amplitude, the influence of the other scatterers has a minor impact on the backscattered signal of the resolution cell. This is the base of the PSI technique. Inside the interferograms, the pixels having such properties are called PS. Physically, in urban areas, the predominant PS, are usually structures (buildings) backscattering a maximum of energy due to their geometric nature inducing double bound reflection.

Perissin and Ferretti (2007) identified six different target typologies based on their scattering properties.

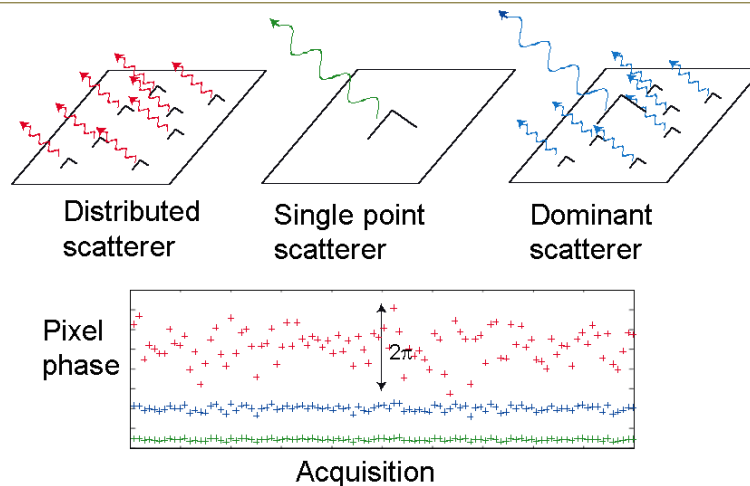


Figure 101. Scattering mechanism models for a SAR resolution element – distributed scatterers (red), ideal single point scatterer (green) and PS (blue). The persistently scattering pixel exhibits smaller phase variation than the distributed scatterer (image: Hooper 2017)

PSI.

The PSI technique consists in the identification from a stack of interferograms of single targets that are coherent during the entire time interval. It is the main family of techniques, processing chains that are used in this research. Two software were principally used to process the satellite SAR images and retrieve the ground displacements of the studied areas. SARPROZ (Perissin et al., 2011) and StaMPS (Hooper et al., 2012). Stamps could be considered as a suite composed of open sources software. ROI-PAC from Jet Propulsion Laboratory (Rosen et al., 2000) was used to process the RAW SAR images to SLC. DORIS from T.U. Delft (B. Kampes & Usai, 1999) was used to produce the interferograms. StaMPS from Stanford University was used to process the interferograms to harvest the PS.

From (Colesanti et al., 2003; Perissin, 2016) the phase components of an interferogram is:

$$\varphi_{int} = \varphi_{def} + \varphi_{topo\ res} + \varphi_{flat} + \varphi_{atm} + \varphi_{orbit} + \varphi_{noise} \text{ (EQ 1-15)}$$

Where, φ_{def} is the phase due to displacement of the point, $\varphi_{topo\ res}$ is the phase due to inaccuracy of the DEM used as reference, φ_{flat} is the phase due to the flat terrain, φ_{atm} is the phase due to atmospheric delays, φ_{orbits} is the phase due to the orbital errors and φ_{noise} is the noise due to the decorrelation.

The first term is defined by the equation:

$$\varphi_{def} = \frac{-4\pi d}{\lambda} \text{ (EQ 1-16)}$$

Where λ is the wavelength of the radar signal and d is the distance between the antenna and the target including the possible target displacement. The latter d is usually strongly correlated in time and may also show spatial correlation depending on the phenomenon responsible for the displacement.

The second term:

$$\varphi_{topo\ res} = \frac{4\pi}{\lambda R \sin\theta} B_{\perp} h \text{ (EQ 1-17)}$$

Where R is the radar target distance, θ the incidence angle, λ the wavelength, B_{\perp} the perpendicular baseline and h is the height of the radar target. $\varphi_{topo\ res}$ are also called DEM errors. They are uncorrelated in time and directly proportional to the perpendicular baseline.

The third term φ_{flat} , the flat terrain, can be calculated from orbits and removed. For the sake of simplicity, we will not consider here possible orbital errors.

The fourth term:

φ_{atm} has a strong spatial correlation but is not correlated in time. Usually, Atmosphere Phase Screen (APS) is not modelled in PSI because the phase difference between two nearby targets is, in principle, small (B. M. Kampes, 2006).

The fifth term:

φ_{orbits} contains the phase contribution due to the orbital errors.

The sixth term:

φ_{noise} contains all other phase contributions. As a time-linear model is used, any displacement of the targets that diverges from its linear trend, the part of the signal corresponding to this difference is therefore also contained in the random

noise term. In the PS technique, a temporal high-pass filter is used to separate and isolate temporally correlated displacement signal from random noise (B. M. Kampes, 2006; Perissin, 2016).

PSI techniques consist in separating the different phase terms above by exploiting their different spectral behaviour in the framework of a multidimensional joint analysis and finally extract the phase due to the displacement (Colesanti et al. 2003).

A first approach consists in considering that in the interferograms, for the pixels that are close to each other, we could consider that the phase is mainly composed by the deformation, topography (including flat) and the noise terms. The atmospheric delay and orbital errors are cancelled by the double difference. So, from the EQ 1-15:

$$\varphi_{int} \cong \varphi_{def} + \varphi_{topo\ res} + \varphi_{noise} \text{ (EQ 1-18)}$$

$\varphi_{def} + \varphi_{topo\ res}$ are then modelled, the φ_{noise} is partially removed by filtering.

For the second approach, the system exploits the spatial correlation of the deformation signal:

$$\varphi_{int} \cong \varphi_{def} + \Delta\varphi_{topo\ correlated\ res} + \Delta\varphi_{topo\ uncorrelated\ res} + \varphi_{atm} + \varphi_{flat} + \varphi_{noise} \text{ (EQ 1-19)}$$

where φ_{def} , $\Delta\varphi_{topo\ correlated\ res}$, φ_{atm} are considered as spatially correlated. Spatial filtering on a resampled grid using Combined Low-pass and Adaptive Phase (CLAP) is then applied to estimate the spatially correlated terms.

The workflow needed to perform a PSI processing using StaMPS is depicted in the *Figure*, several important steps are described hereafter and it is also worth mentioning the processing steps that differ between the temporal and spatial approaches as StaMPS is based on the second one (the spatial approach).

First, we need to produce a stack of interferograms whose phase are related to a single Master image. Usually, a minimum of 15 SAR images are needed to provide a reliable processing. The Master is selected to limit the decorrelation. The criteria for selecting the Master are a minimum temporal baseline and perpendicular baseline between one candidate Master and all the Slaves. The Figure 102, illustrates the selection of a single Master and the spreading of the Slaves in terms of temporal baseline and perpendicular baseline. This graph is also called a star graph. Then, the images are coregistered using the precise orbits of the satellites and the interferograms are calculated. The coregistration process is demanding in terms of computing power and is also a step where errors occur easily and are often not directly seen. Then, the topographic contributions are removed using an external DEM. In fact, the software reproduces the fringes corresponding to the topography and removes them from the interferogram.

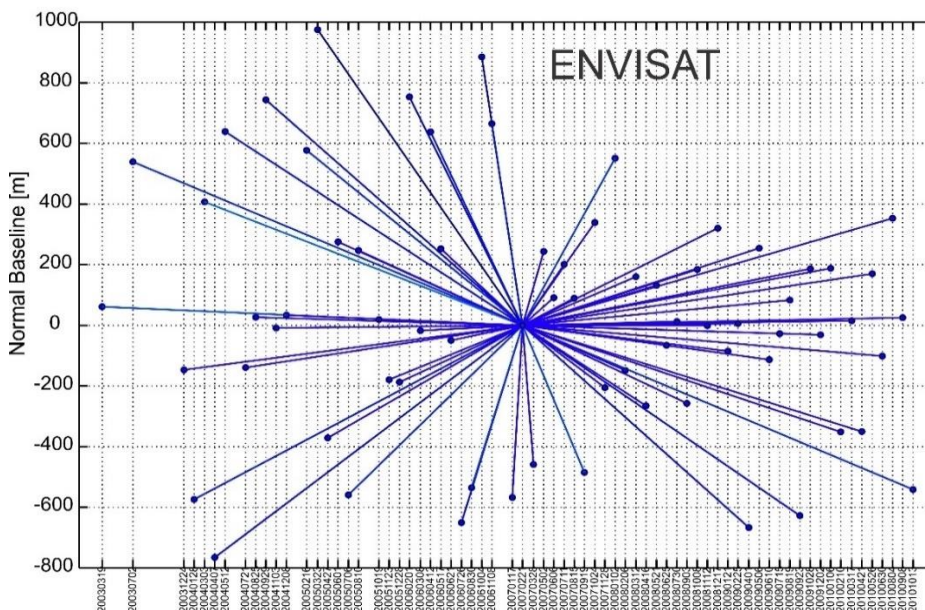


Figure 102. Star graph, single Master plot of perpendicular (normal) baselines versus temporal baseline.

The second step corresponds to a coarse selection of the PS. The aim is to calculate the atmospheric phase at these pixel positions in all the computed interferograms. This is realised by filtering of the residual phases after the estimation of the parameters such as, the DEM error and the displacement, taking advantage of the spatial correlation of the atmospheric signal (B. M. Kampes, 2006). Since the phase contributions that are not modelled need to be smaller than π (the unwrapping occurs later), this step is performed between nearby points. Persistent Scatterer Candidates (PSC) are selected based on their amplitude of dispersion index DA (Ferretti et al., 2001):

$$DA = \frac{\sigma_A}{\mu_A} \text{ (EQ 1-20)}$$

Where σ_A is the standard deviation and μ_a is the average value of the amplitude. If D_A is high, this means that the reflexion inside the resolution cells add up differently in each acquisition. This also means that this pixel is not dominated by a single scatterer. Usual values for D_A in StaMPS processing chain range from 0.40 to 0.43.

Using this network of PSC, in the first approach, the phase is unwrapped during the selection process by using a temporal model for the evolution of this double difference of phase. Usually, linear models are used to realise the unwrapping procedure. It is a forced solution. This implies that PSC phase behaviour not following the models could be rejected by the system.

For the second approach, in StaMPS, spatial filtering is applied by iteration to estimate the spatially correlated deformation, orbital errors and atmosphere delays terms (Hooper et al., 2012). Usually a low-pass and adaptative Goldstein filters (Goldstein et al. 1988) are used. In both approaches, after a filter in time and space, the ϕ_{def} is separated from the ϕ_{atm} and ϕ_{noise} .

Third, the corrected phase terms can now be unwrapped as long as the PSC density is such that the absolute phase difference between neighbouring PSC (after correction of DEM error) is lower than π (Sousa et al., 2011). The unwrapping procedure occurs using a 3D algorithm.

Finally, a flat table file (*Figure Figure*) is created containing all the PS with an ID (Lat, Lon) location, a velocity calculated from the time series and the displacement for each acquisition date with reference to the Master image and a reference point. In terms of accuracy, (Adam et al., 2009) have demonstrated that the accuracy in the case of a linear deformation can reach 1 mm.

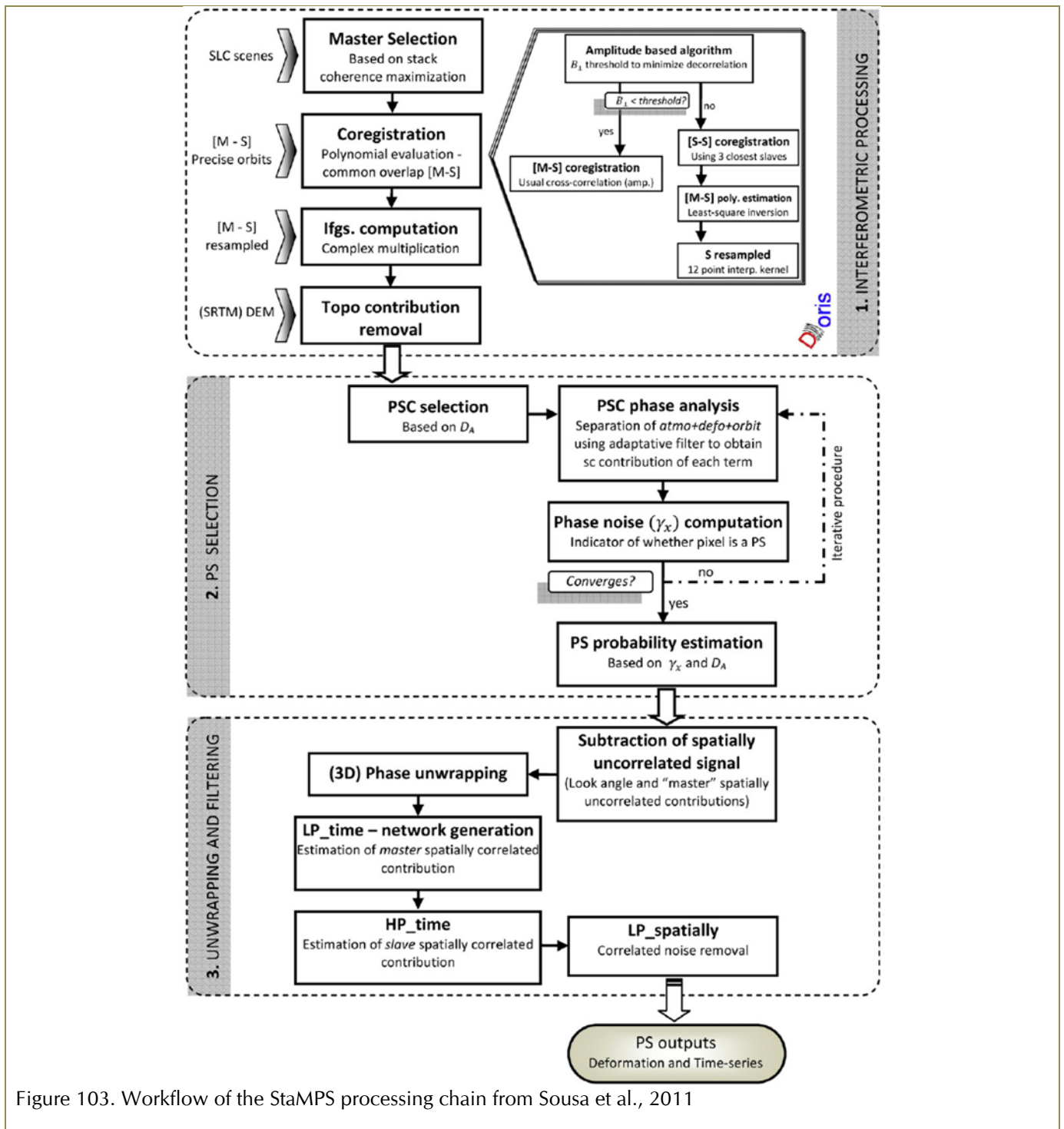


Figure 103. Workflow of the StaMPS processing chain from Sousa et al., 2011

id/code	Identifier
lon	Longitude WGS84 (°)
lat	Latitude WGS84 (°)
cohe	Coherence
vel	Velocity (mm/year)
height	Altitude from DEM (m)
TS date	Displacement from the Master (mm)

ID	LOX	LAT	COHE	VEL	HEIGHT	20160415	20160509	20160602	20160614	20160720	20160801	20160813	20160918
1	47857897.00	5068838.00	0.96	1.54	128.27	0	-3.02	2.59	0.7	3.12	0.56	2.95	0.57
2	47964383.00	5068968.00	0.9	2.57	107.37	0	-4.99	0.43	0.87	-1.11	-2.5	-1.44	-1.18
3	47965454.00	5068969.00	0.91	2.97	104.05	0	-2.45	0.8	-3.09	-3.05	-2.18	2.42	0.7
4	47966477.00	5068971.200	0.97	1.86	100.51	0	-2.22	0.86	-1.02	-1.05	-2.21	-1.33	0.96
5	48441283.00	5069552.300	0.89	2.52	84.25	0	-2.83	4.57	-4.49	2.27	4.14	4.68	3.39
6	50212893.00	5071702.200	0.82	0.89	75.7	0	0.38	1.65	-4.39	-5.15	1.2	0.45	3.73
7	50225795.00	5071717.800	0.92	0.43	76.72	0	-1.37	0.37	0.86	-2.25	0.71	1.53	3.33
8	53012703.00	5075041.200	0.97	3.68	72.94	0	-1.56	2.95	0.76	1.04	1.7	1.49	2.46
9	53040859.00	5075074.000	0.92	2.2	76.83	0	1.95	-1.65	-2.97	0.03	1.17	3.19	0.79
10	53331575.00	5075416.900	0.94	3.7	79.33	0	0.04	-1.01	-4.17	-1.59	2.34	0.46	3.05
11	48072084.00	5069113.400	0.94	2.02	91.81	0	-2.09	1.21	-1.92	-1.5	-2.26	1.58	0.45
12	48401769.00	5069516.800	0.91	3.31	80.41	0	-1.69	2.36	-4.15	0.06	1.54	3.07	0.36
13	49981112.00	5071435.400	0.93	2.06	57.53	0	-2.11	-1.66	3.02	2.67	0.85	-1.53	0.61
14	50290789.00	5071808.000	0.93	3.57	80.47	0	-1.42	-1.08	-2.88	-3.6	0.53	-2.24	1.19
15	53037543.00	5075083.200	0.96	3.42	76.03	0	2.63	0.42	0.32	6.75	4.66	4.73	6.24
16	53720133.00	5075886.200	0.82	1.92	83.27	0	0.66	0.39	-7.01	-5.86	-6.86	-6.71	-4.92
17	4752528.00	5068454.800	0.83	2.44	126.05	0	0.68	2.44	0.98	0.2	0.83	6.51	1.51
18	48158896.00	5069232.400	0.94	2.7	95.5	0	0.37	5.6	0.22	0.94	-2.22	-1.53	0.72
19	52112013.00	5074000.300	0.95	3.03	99.82	0	3.97	5	1.55	3.05	0.3	1.27	2.8
20	52974107.00	5075021.100	0.94	3.54	82.37	0	-2.05	-1.3	-1.44	0.18	0.63	2.19	-1.24

Figure 104. PSI processing results structure and actual example.

Small Baseline Processing.

The PSI approach implies the generation of multiple interferograms with respect to a single common master image. Even if the master image is selected in a way to reduce the Temporal and the Perpendicular baselines, in many cases, Master and Slave pairs are formed having a long perpendicular baseline (even longer than the critical baseline). This clearly increases the decorrelation and therefore reduces the number of PS because only highly coherent targets are considered. Those PS are mainly present in urban or rocky areas while their density decreases drastically in vegetated zones and rural areas.

The SBAS algorithms consist in creating all the possible interferograms separated by a short time interval and small difference of perpendicular baseline to reduce the decorrelation. The goal is to find pixels, which are spatially coherent in most of the interferogram stacks and retrieve in some way the temporal displacement. Different approaches were developed by several authors to extract the displacement information. (Berardino et al., 2002) proposed an SBAS algorithm based on singular value decomposition and temporal models to estimate the nonlinear displacement from a stack of multilooked interferograms. (Hooper, 2008; Lanari et al., 2004) are using full resolution interferograms that are unwrapped in 2D or in 3D (Pepe & Lanari, 2006). A least squares method was developed by (Schmidt & Bürgmann, 2003) to extract the displacement without fixing any *a priori* deformation model (linear) such as needed for PSI. (Doin et al., 2011) are using a constrained least squares methodology to retrieve the displacement called New SBAS.

The Figure 105 shows the SBAS processing workflow of the StaMPS suite. Globally the processing steps do not differ from the PSI approach until the creation of the interferogram stacks. The stacks are created by mitigating the impact of decorrelation. Proper interferometric pairs with short temporal and small perpendicular baselines are selected using threshold values. According to these selection parameters, hundreds of interferograms need to be processed for SBAS, where there were, for example, only fifty in PSI. In StaMPS, the SBAS method needs that all interferograms are connected in one single subset for using the Least-Squares (LS) adjustment. If the network does not satisfy this condition, new threshold values of temporal and perpendicular baselines must be selected. Then, the main purpose of the algorithm consists in targeting Slowly-Decorrelating Filtered phase Pixels (SDFP). These SDFP are pixels that show only limited decorrelation over short time intervals (Hooper, 2008). To achieve this, SDFP pixels are identified among candidate pixels extracted using the amplitude of dispersion. The candidates are filtered using the same filtering procedure as described in the PSI section (Hooper et al., 2007). Finally, a 3D unwrapping algorithm that exploits the spatio-temporal relationship of the redundant interferograms is used to calculate the phase of the SDFP. This phase permits finally the estimation of the displacement component.



Figure 105. Simplified processing flow chart of the SBAS chain in StaMPS.

PSI and SBAS results have been used together by many authors to map and analyse ground displacements due to subsidence (Grzovic & Ghulam, 2015; Herrera et al., 2010; Hu et al., 2014; Qu et al., 2014; Sowter et al., 2016; Yan et al., 2012; Zhang et al., 2019), to landslides (Colesanti et al., 2003; Dong et al., 2018; Lauknes et al., 2010; Qu et al., 2014), to human infrastructures (Mura et al., 2018; Qin et al., 2018)... Few studies (Dong et al., 2018; Gong et al., 2016; Mirzaee et al., 2017; Shanker et al., 2011) were realised and provided real world comparisons of the results coming from both PSI and SBAS approaches. The differences between the LOS velocity values calculated by PSI and SBAS were minimal and did not trespass 0.5 mm/year in absolute value.

Combined PSI-SBAS processing.

The StaMPS processing suite proposes to combine the PSI and SBAS approaches, since they are focusing on different models of scattering mechanisms of the ground targets. PSI techniques are targeting a single scatterer that dominates within the resolution cell while SBAS techniques are focused on cells containing many scatterers (Hooper, 2008). The algorithm combines both the PS and SDFP results before the phase unwrapping process. A 3D unwrapping is then realised on the combined dataset and further processed to estimate the displacement.

Hybrid MT-InSAR method.

A new algorithm called SqueeSAR was proposed by (Ferretti et al., 2011) to overcome the limits of the PSI technology and to avoid processing a large quantity of interferograms needed for the SBAS approach. The technique relies on a joint processing of PS and Distributed Scatterers (DS). DS corresponds to a large group of neighbouring pixels of low coherence in the interferograms that share the same scattering properties and for which the ϕ_{noise} can be mitigated by statistical methods (Even & Schulz, 2018). They usually correspond to an area with low vegetation, debris areas, rock outcrops, roads, etc. For aggregating pixels around a central one, a search window is centred on it. One of the common tests consists in comparing the backscattered amplitude. If the set of pixels inside the windows have the same distribution of amplitude, there is likely a chance that they belong to the same physical structure. It is also known as an Adaptive Multilooking (Jiang et al., 2015). Alessandro Ferretti et al., 2011, applied the SqueeSAR technique over a mountainous area, two third of the identified targets were associated to DS and the remaining to PS.

1.2. Processing of the SAR data covering Belgium

The Permanent Scatterer Interferometry (PSI),(Colesanti et al., 2003; Ferretti et al., 2000; Hanssen, 2001; Kampes, 2005;

Lanari et al., 2004; Perissin and Wang, 2012; Prati et al., 2010) is one of the first MT-InSAR techniques. Several new methodologies and software have been elaborated since then. STaMPS permit to combine a PSI and a SBAS approach (Hooper, 2008; Hooper et al., 2007, 2004). Ferretti et al. (2011) have also developed a new algorithm called SqueeSAR. For this study, only the PSI approach has been used. It consists of a time series analysis using the phase history of scatterers with a strong amplitude. It exploits “coherence islands” (e.g., buildings reflecting the radar signal emitted by the satellite) where the phases remain sufficiently stable over time. During the processing chain, the different contributing phases of each PS are removed, leaving only the phase related to the displacement. During the processing of the SAR images, precise orbits from the Delft Institute of Earth Observation and Space Systems were used to minimise orbital errors and a master scene was selected for each set (ERS, ENVISAT, TerraSAR-X and SENTINEL 1) in order to minimise the temporal and spatial baselines (B. Kampes & Usai, 1999). For the ERS and ENVISAT SAR data, the images were oversampled using a factor 2 in both range and azimuth before producing the interferograms. This was done to improve the density of the PS and thus to improve tracking of the ground movement of the ROI.

In the case of ERS and ENVISAT, the SAR images are 100 km in the azimuth direction and about 100 km in the range direction while for Sentinel-1A, the images are 250 km x 100 km in the range and azimuth respectively. The range is subdivided into 3 swaths. The following figures (Figures 106-108) show the position of the footprints of the satellite tracks that covers Belgium and the Table 19 gives a summary of the characteristics of the different processing already realized in the framework of this project. The outputs of the processing include the localization of the PS (geographic coordinates), its annual average velocity in the Line Of Sight (LOS) in mm/year, its coherence and finally the displacement in the LOS (mm) for each acquisition with regard to a reference (master) image.

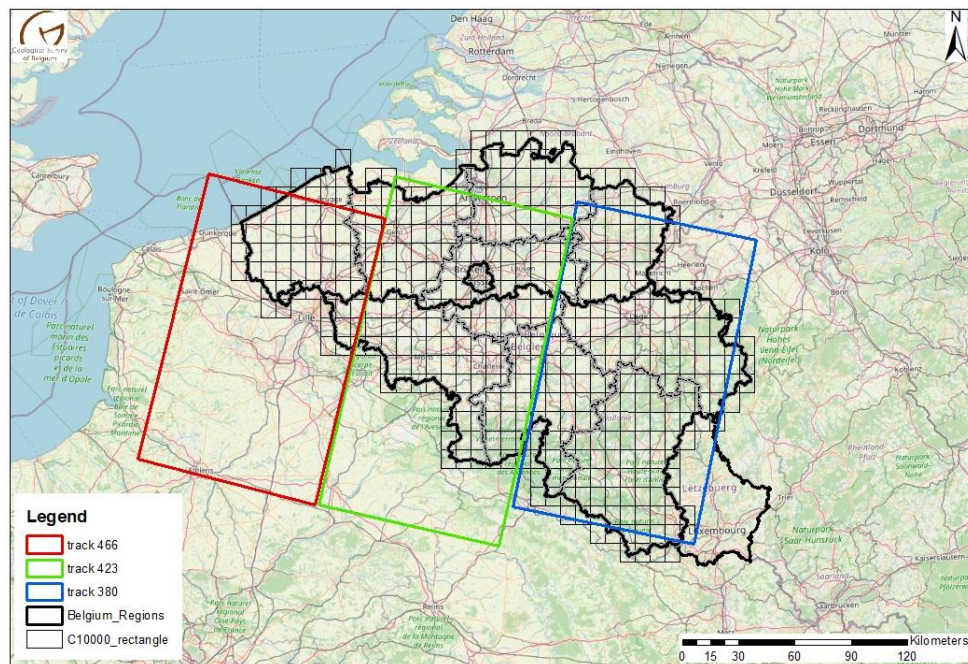


Figure 106. Footprints of the satellite SAR imagery tracks covering Belgium for the satellites ERS1/2 and ENVISAT.

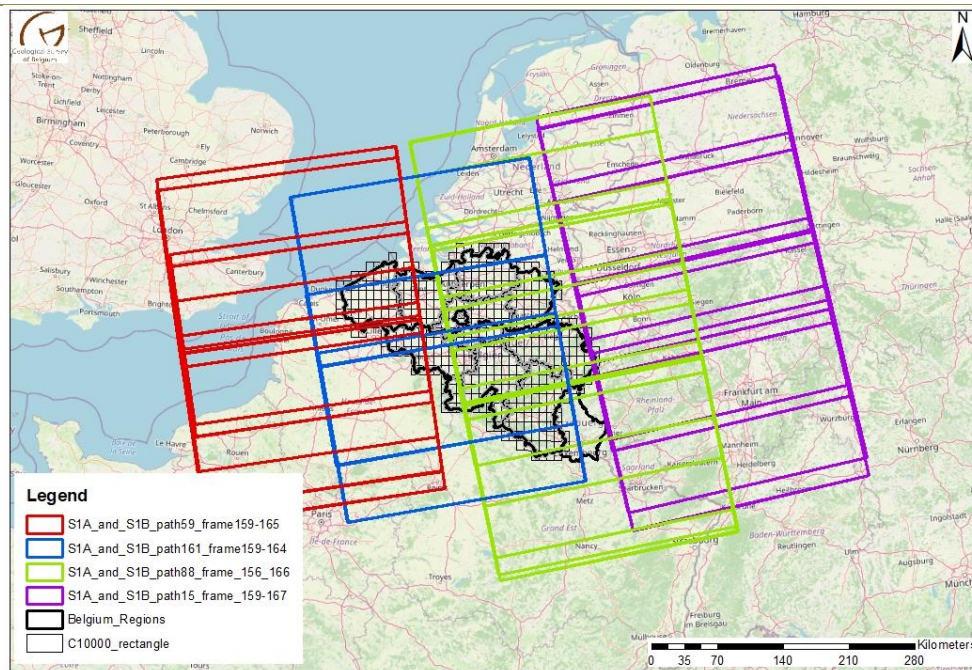


Figure 107. Footprints of the satellite SAR imagery tracks covering Belgium for the satellites Sentinel-1A and 1B in ascending orbit.

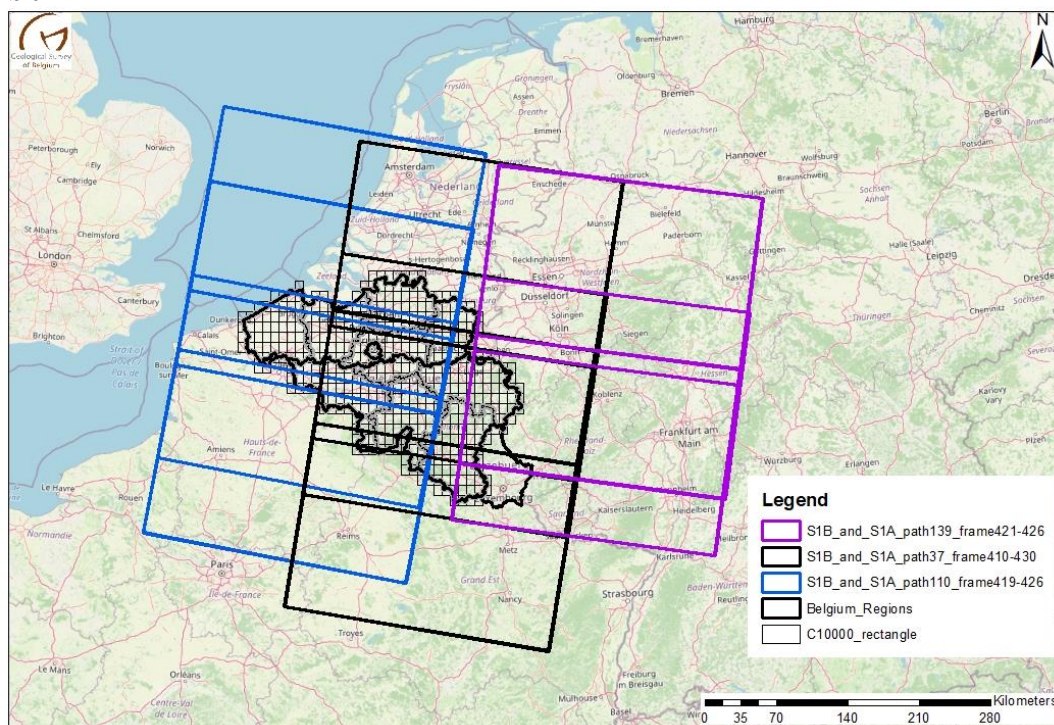


Figure 108. Footprints of the satellite SAR imagery tracks covering Belgium for the satellites Sentinel-1A and 1B in descending orbit.

T/P	S	Geom	Sat	Number of Images	Start date	End date	Master	P
380	/	descending	ERS	62	06/08/1992	31/12/2000	06/04/1997	35 days
423	/	descending	ERS	67	26/04/1992	03/01/2001	18/07/1998	35 days
466	/	descending	ERS	77	03/06/1992	07/10/2006	28/03/1998	35 days
380	/	descending	ENVISAT	60	21/12/2003	10/10/2010	12/08/2007	35 days
423	/	descending	ENVISAT	74	12/02/2003	13/10/2010	15/08/2007	35 days
466	/	descending	ENVISAT	48	27/12/2003	16/10/2010	09/05/2009	35 days
161/166	SW1- SW- 2- SW3	ascending	S1A	98	02/06/2017	08/10/2020	23/01/2019	12 days
88/157	SW1- SW2	ascending	S1A	102	02/06/2016	03/10/2020	30/01/2019	12 days
161/161	SW1- SW2- SW3	ascending	S1A	129	07/06/2016	08/10/2020	13/09/2018	12 days
88/163	SW2	ascending	S1A	110	14/06/2016	03/10/2020	25/12/2018	12 days

Table 19. Summary of the SAR images characteristics used in the framework of this project. T: Track, P: Path, S: Swath, Geom: Geometry, Sat: Satellite, P: period.

Since the time frame encompassed by each S1A stack of images is different, each stack is processed separately. S1A was launched in 2014 but ESA changed the acquisition parameters, during 2016-2017, resulting in a major change of the spatial coverage of the images. As the processing results consist of the maximum of the spatial intersection of the stack of the images, the acquisition before 2016 were not used and some shifted images between 2016-2019 were removed from the processing to keep the largest processed surface. The Table 20 summarizes the S1A in ascending geometries used for this report.

P and T	S	Geom	Sat	Number of Images	Start date	End date	Master
P161 F166	SW1- SW-2- SW3	ascending	S1A	123	14/06/2017	09/09/2021	28/06/2019
P88 F157	SW2- SW3	ascending	S1A	128	02/06/2016	04/09/2021	09/10/2019
P161 F161	SW2- SW3	ascending	S1A	155	07/06/2016	09/09/2021	28/06/2019
P88 F163	SW2	ascending	S1A	155	14/06/2016	04/09/2021	25/12/2018

Table 20. Summary of the SAR images characteristics used in the framework during the year 2021 of this project. T: Track, S: Swath, Geom: Geometry, Sat: Satellite, P: period

The Sentinel-1A and Sentinel-1B (till December 2021) SAR imagery were collected and downloaded both in ascending

and descending for archiving them in the GSB dedicated server for further processings. A regular update of the processing of the Sentinel-1A images (both in ascending and descending orbits) is done almost every 6 months during the project life. Progress will be made in the future to combine ascending and descending together to calculate the real vertical displacement vector that is different from the LOS velocities that are not vertical.

A powerful storage system composed by a LaCie 48 To with 6 big arrays disks helps to organize the 1001 SAR SLC scenes collected from Sentinel-1A (Ascending-Descending), the 779 SAR SLC scenes of Sentinel-1B (Ascending-Descending) – not fully completed in 2024. It must consider that every month, 45 new Sentinel SLC SAR images are needed representing 180 Go of data. Two processing chain stations are organized today. To give a bit of an order of the associated issues: the processing of one full frame of Sentinel-1A ascending is producing a 5 To of interferograms and 1 To of matlab tables and time series meaning 6 To of data to store at least partly. The GSB has thus developed a GSB data repository center of SAR SLC imagery scenes covering 30 years of satellite acquisition covering Belgium. On top of this additional other high-resolution SAR images are also stored but not used inside the project itself.

The results are formatted as a table (Table) in which each PS has the following information: the PS identifier (id), the longitude (lon) and latitude (lat) coordinates in decimal degree in WGS 84 (EPSG: 4326), the height (m), the coherence factor (cohe) the velocity (vel) in mm/year, and all the dates of measurements of the available S1A images. Coherence is a quality measure of the goodness of the model fit. For further analysis, the PS raw results are filtered using a coherence > 0.7 to maximise the quality of the PS data. In total four PS data files are provided corresponding to the processed Sentinel-1 ascending frames.

id	Lon (dd)	Lat (dd)	Z (m)	cohe	Vel (mm/year)	Dates
----	-------------	-------------	----------	------	------------------	-------

Table 21. summary of the database structure of the TS tables.

The period encompassed by each Sentinel-1A processing are different. A choice is necessary between keeping the maximum coverage in time vs keeping the maximum coverage in space. Sentinel-1A was launched in 2014 but ESA changed the acquisition parameters, during 2016-2017, resulting in a major change of the spatial coverage of the images afterwards. As the processing results consist of the maximum of the spatial intersection of the stack of the images, the acquisition before 2016 were not used and some shifted images between 2016-2021 were removed from the processing.

Sentinel-1A/1B uses progressive scan synthesis aperture radar (TOPSAR), which induces fundamental changes in the way to handle data and produce interferograms. To increase acquisition coverage at the expense of a loss of azimuthal resolution, TOPSAR systems are using a progressive scanning of adjacent bursts, along and across track. During each burst acquisition, the SAR beam is steered from backward to forward (Figure 109). This steering induces a strong aliasing of the Doppler spectrum and an additional quadratic phase term along the azimuthal direction. This quadratic phase term (or the corresponding linear frequency variation) must first be removed to allow data co-registration and interpolation before being reintroduced within the data. If not removed and handled classically, interpolation of aliased spectrum leads to ripples within the interferogram. In addition, corresponding burst from an interferometric data pair must be co-registered extremely precisely to cancel-out the quadratic phase term through the interferometric process. Required co-registration precision is of the order of 1/1000 of a pixel for proper quadratic phase term cancelation. If not reached, subtraction of both parabolas leads to a remaining linear phase ramp across the interferogram leading to non-continuous phase jumps between bursts.

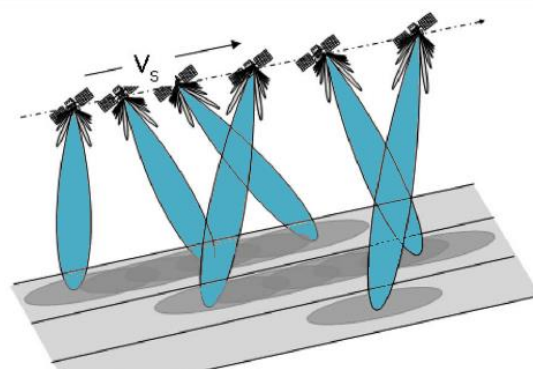


Figure 109. Burst scanning process of TOPSAR acquisition mode on Sentinel-1 satellites.

Another axis of the project is related to the fact that PS are not always identified/retrieved during the SAR image chain processing.

1.3. Overview of the ground deformation highlighted by PSInSAR technique at the regional scale in Belgium

In Belgium, the majority of the natural regional geohazards that can provoke ground movements are of the following types: earthquakes, landslides, karst, subsidence and uplift. On the other hand, human induced geohazards are those related to the overexploitation through drilling activities of underground resources (i.e. groundwater and gas exploitations) and those associated to underground mining or quarrying exploitations (i.e. coal, metallic minerals, stones, ore deposits, etc.). Most of the earthquakes are located to the east of the city of Liège and from Charleroi to Tournai (Figure 1.1-1). Although the map shows a significant number of records, the estimation of the return period of high magnitude earthquakes (> 6) ranges between 500 to 1000 years if all the Quaternary faults located in the Lower Rhine Embayment are considered (Camelbeeck et al., 2000a, 2007). On the other hand, for the Bree fault scarp in the NE of the country, the return period is estimated between 10 000 to 20 000 years (Meghraoui et al., 2000; Vanneste et al., 2001). Camelbeeck et al., 2000a consider Belgium as currently having a low seismicity profile. It is therefore not obvious to observe the effect of the earthquakes during the 30 years period of InSAR acquisitions. For instance, only two earthquakes located in Belgium had a magnitude > 3.5 , Spa in 1996 $ML = 3.8$ and Le Roeulx in 1995 $ML = 4.5$. It is worth mentioning that the high-density zone of recorded earthquakes to the east of Belgium is included in the slowly (0.5 to 1 mm/year) uplifting zone highlighted by GNSS in (Kreemer et al., 2020).

Landslides are principally known in the Flemish Ardennes an area located 20 Km SW of Brussel (Dewitte et al., 2018; Van Den Eeckhaut et al., 2010; Vranken et al., 2013) and in the "Pays de Herve" located in the eastern part of the country. The Figure 110 gives an overview of the existing geohazard of regional extension. The mapped zones affected by potential landslides are quite large, but the actual movements are limited in terms of amplitude and space. The largest karst hazard zone is situated in the western part of Belgium in Tournai although most of the lime content geological formations are potentially karstic (Figure 110). Among the largest known ground movement in Belgium, the areas associated to the exploitation of the coal mines were responsible for strong subsidence and collapses in their vicinity during their exploitation activities. For instance, Calembert, 1955 mapped the extension of the damage due to the coal extraction in the Liège district. In Limburg, during the exploitation period, the maximum mine subsidence measured was 8 m in the centre of the coal concessions (Vansteelandt, 1996). For cartographic purposes only the extension of all the coal concessions is represented in Figure 110.

The first mapping of the ground movements for the entire country was realised by (Jones, 1950) where he compared the results of the “Deuxième Nivellement Général, 1948 (Second General Levelling, DNG)” with the measurements realised in 1892 of the precise levelling points. Unfortunately, many reference points disappeared between the two levelling periods. He was anyway capable to highlight some interesting displacements such as a subsidence of 40 to 80 mm in Antwerp, 200 mm in Brussels and 300 to 600 mm in Tournai. Poitevin, 1989 introduces the great potential usage of gravimetry to study the tectonic movements and to increase the quality of the levelling by providing reference points. He also compares the levelling data of the DNG with the Re-iterated Second General Levelling (RDNG) realised in 1978. A map was realised showing the height changes at the main network nodes. Here are some interesting values, in Antwerp the change is equal to -17 mm, in Maasmechelen to -25 mm, in Kortrijk -39 mm and in Tournai -26 mm. Most of the values are negative except for the extreme south of Belgium. This fact is appealing since it does not correspond to the previous observations by Jones, 1950. Pissart and Lambot, 1989 also compared the levelling of 1948 with the one realised in 1978 and produced a map showing the isolines of the height change for the entire country. The Royal Observatory of Belgium in Uccle was again defined as the reference point for the levelling. All levelling points having a height change above 100 mm between the two period were removed. They estimate the precision at the nodes of the levelling network being comprise between ± 6 to ± 12 mm. The Table 1.1-1 summarize their observations and provides whenever available the given explanation of the movements. Pissart and Lambot, 1989 have the merit of having highlighted and provided a first cartography for ground movements in Belgium (Figure 1.1-3). However, their explanation for these movements is most often limited to observations and not to research on the triggering factor(s), whether they are of natural or human origin (Lebbe, 1995), explained the observed subsidence localised in the NW of Belgium in the Kortrijk area. Following him, the overexploitation of the semi-confined Cambro-Silurian aquifer is responsible for the 90 mm height change in this area between the two levelling periods.

Location	Height changes between 1948 and 1979 (cm)	Calculated velocity (mm/yr)	Explanation given in the paper
Limburg	-9	-2.90	Mines
Alost	-4	-1.29	
Gent	-9	-2.90	Refer to publication of (Lebbe et al., 1988) (Overexploitation of deep aquifer)
Zeebrugge	-6	-1.94	
La Louvière	+5	1.61	Mines (Hypothesis: relate the uplift to the earthquakes and possible flexure/faults)
Antwerp	-3	-1.29	
East of Belgium	-4	-0.29	Hypothesis consists of variation of the magma in the mantle at 10 to 15 km depth

Table 22. Synthesis of the observed ground movements given in Pissart and Lambot, 1989.

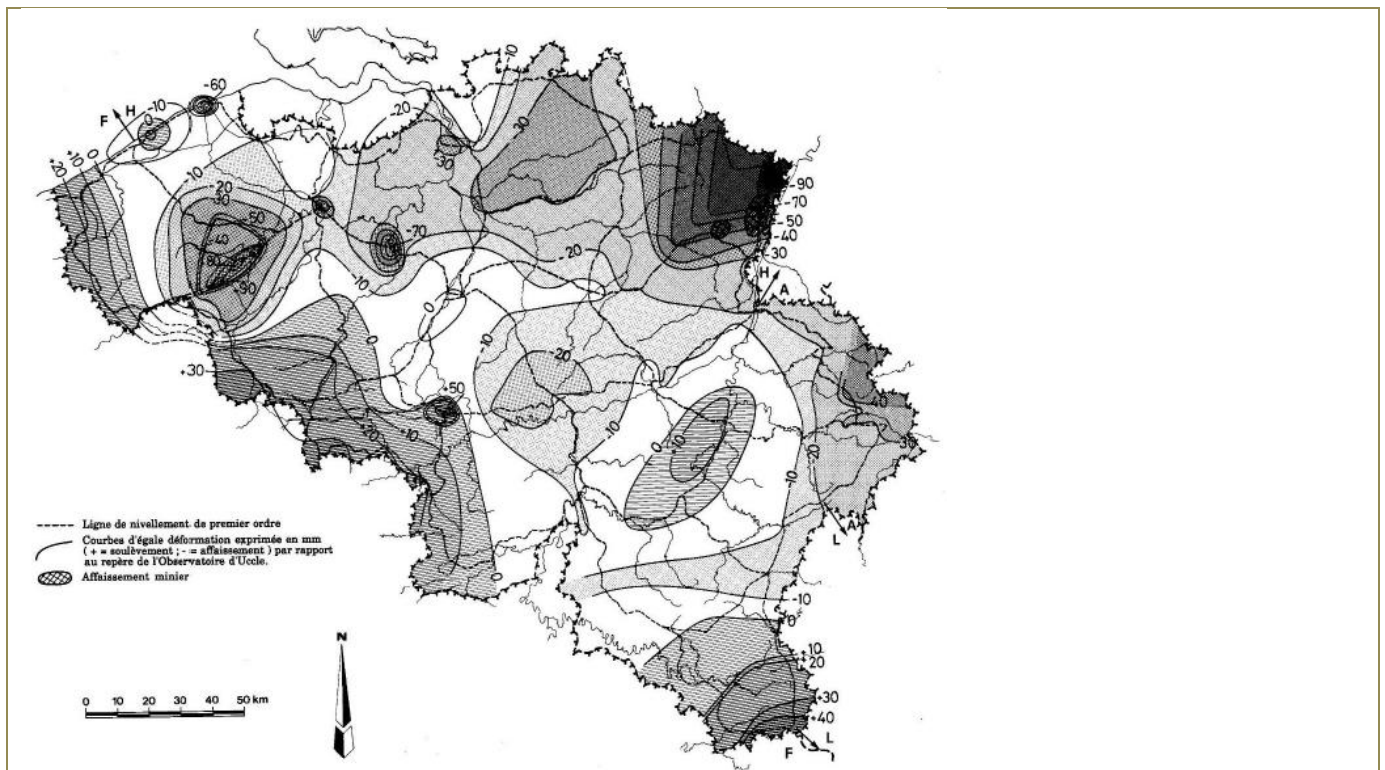


Figure 111. Altitude changes in mm between the levelling period 1948-1978 (from: Pissart and Lambot, 1989).

Demoulin et al., 1992 compared as well the two levelling campaign data (1948-1979) to provide “new indications in terms of neotectonics in Belgium”. The country was subdivided into five zones of which two are considered as stable: the Condroz-Ardenne and Flanders. The Campine and the NE of the Ardenne are related to the evolution of the lower Rhine tectonics. The central Brabant Massif corresponds to the fourth zone. Finally, the SW of Belgium is characterised by positive changes of heights. The authors also delimited four areas where the ground movements have an anthropic origin or influence (Figure 1.1-2. Geohazards identified in Belgium and cartographically plotted and potential ground movements areas recognized in Belgium. Moreover, the ground movements recorded by the GPS antennas (black arrows) and the gravimetry networks (blue and red arrows) are also reported using arrows (Data from ROB). The positive or negative ground movements and their measured amplitude (in mm/year) is also reported).

The uplift of the Ardenne is a well-known debated subject in Belgium confronting the measurements, observations and hypothesis of geoscientists having different background. The following articles present the subject without taking sides in either scenario: (Camelbeeck et al., 2002; Demoulin et al., 2005; Demoulin and Collignon, 2002, 2000; Francis et al., 2004; Sougnez and Vanacker, 2011).

Ground movements in Belgium were also studied using absolute gravimetry at eight stations during the last 8 to 15 years of data acquisition (Van Camp et al., 2011). However, after the correction of the glacial isostatic adjustment the residual gravity values are within the uncertainty level for all stations except one in Julich located in Germany. Julich is affected by a strong subsidence related to the brown coal exploitation in a deep open pit. The latest calculated rates based on gravimetric measurement are presented in Figure 110.

Belgium is also monitored using a dense network of 50+ GPS-GNSS stations distributed at the regional level between the FLEPOS, WALCORS and Uccle respectively for the Flemish Region, the Walloon Region and the Royal Observatory of Belgium. Unfortunately, up to now, there is no publication using those data at country level to map the associated ground movements.

This short review of the existing literature about small scale and slow ground movements highlighted on Belgian territory previously leads to the conclusion that local scale geohazards such as karst and landslides are already studied in detail thanks to field observations and measurements even if the combination with PSInSAR was never tried. Earthquakes and seismicity are characterised through the monitoring of the seismic stations network and the scientific research of the seismic team at the Royal Observatory of Belgium (Camelbeeck et al., 2009). The comparisons of the levelling at the different period highlighted several regional scale land subsidence and uplift that are in general only briefly described and not deeply explained nor modelled.

PS Density

In total $1.877 \cdot 10^6$ PS with a coherence > 0.7 are resulting from the processing of the S1 images. The geographical distribution of the average annual velocity values is first analysed using a 1 Km^2 grid. The density of PS (PS/Km²) is calculated by using a spatial query on both layers. The density can be used as an indicator of the relative confidence for interpreting the results at the regional scale. Since the PSI technique relies on the backscattering of the radar signal by an object, in cities there are much more PS.

Since Flanders has a higher population density than Wallonia, a higher PS density in the northern part of the country is observed (Figure 112). It has to be noticed as well that, in Wallonia, large areas are devoted to dense forest, agricultural or natural areas where almost no reflectors are present and therefore barely no PS can be identified (The Fens, Stavelot Massif).

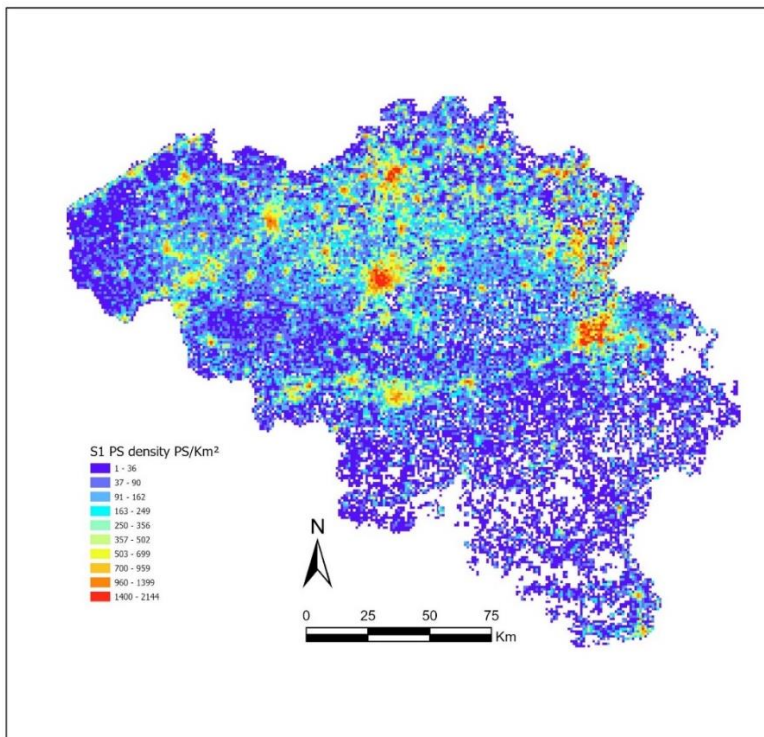


Figure 112. PS density grid (1 km^2) given for the Sentinel 1A satellite data for the Belgium territory displaying a colour code associated to PS density ranging between $1\text{-}26 \text{ PS/km}^2$ (blue) to $1440\text{-}2144 \text{ PS/km}^2$ (red). Remote areas do not contain PS data and remain in white. It is obvious that more remote areas are identified in the south and southeastern part of Wallonia.

1.4. The improvement of PS-InSAR use by installing new combined SAR and GNSS geodetic techniques in one single IGR station

The idea is also to have an absolute anchor system while using GNSS data but the GNSS network in Belgium is old, scarcely distributed, GNSS antennas are not maintained by the regions and some areas are now emptied with no GNSS antenna available. At the same time, many ground deformation areas are in regions devoid of GNSS data and antennas. The GSB in close collaboration with the TuDelft has decided to launch and install new IGR stations at different locations in Belgium. The patent to build those IGR stations have been transferred to X. Devleeschouwer. The IGR station has a cost of almost 19-20 000 EUR but it includes two inverted metallic corner reflector to be aligned for ascending and descending radar satellites, a GNSS receiver/station with a 4G router SIM card installed on a concrete basement.

The need of having an electricity access makes the location very difficult as each IGR station is expected to stay at least 8-10 years on the ground.

The first one was installed in Doel area in a facility area (Figure 113) maintained by the federal nuclear control agency (AFCN). This area is the core of a land subsidence bowl studied in the PhD thesis of Atefe Choopani in the Antwerp

area. All the information related to that station are now implemented in the official international network and available through this website. The data are public and open access meaning that they will be transmitted to the EPOS-portal related to the GNSS station network as well: <https://w3id.org/moid/station.64b7f391b1f58be93303b347>. The valorization of this GNSS station is two-fold as it is close from the nuclear centre of Doel and located in an area a bit outside of the land subsidence bowl of Antwerpen meaning that it is a perfect anchor point to look at the natural subsidence and compaction of the sediments close to the Schelde Area. The first Doel IGR has been also introduced inside the EPOS repository and database (The DOI for the dataset of your DOEL station has been created and inserted in M3G: DOEL00BEL: <https://doi.org/10.24414/ROB-GNSS-DOEL00BEL>).

IGR station – Doel – workload on the field with NGI

The screenshot displays the M3G Metadata Management and Distribution System interface. On the left, an aerial satellite image shows the station location near a river. On the right, the metadata for station DOEL00BEL is listed:

Field	Value
9-CHAR IDENTIFICATION	DOEL00BEL
IRIS DOPUS NUMBER	13170961
SITE LOCATION, COUNTRY	Doel, Belgium (BEL)
STATION OWNER	National Geographic Institute of Belgium
POINT OF CONTACT	ngi(AT)ingi.be, National Geographic Institute of Belgium
INSTALLATION DATE	2022-07-22
STATION STATUS	ACTIVE
LAST ANTENNA	SOPHOCLE_B366
LAST RECEIVER	LEIF POLARODE
LAST TRACKED SATELLITE SYSTEMS	GPS+GLONASS
DOI, DOI PREFIX	View
CHANGE LOG	View
SITE PICTURES	GeodesyNL, IGS site log, EPOS Joan
DOWNLOAD METADATA FORMAT(S)	View
LAST UPDATE OF SITE LOG	2023-06-09
METADATA MAINTENANCE	ngi(AT)ingi.be, National Geographic Institute of Belgium
DOI DAILY RINEX DATA	CC-BY-4.0
DATA LICENSE DAILY RINEX DATA	no embargo period
EMBARGO PERIOD DAILY RINEX DATA	ADD
NETWORK(S)	ADD
PROJECT(S)	ADD

Below the metadata is a map showing the station location in Doel, Belgium.

Figure 113. Details of the Doel IGR station location and Metadata Management information in the M³G portal.



Figure 114. Manual fieldwork done in successive visits on the field in Doel allowing a sequence to fully install the antenna, to connect the electricity and install the modem with the SIM card and to install and correctly oriented the IGR antenna.

The IGR station (Figure 114) is installed inside the alluvial valley of the Scheldt and directly lies on the Formatie van Vlaanderen (composed by coarse tidal channel sands, fine wadden sands and tidal flat clays with peat horizons building

finally up to 2m above MSL). The concrete base was quite thick (50 cm) for this first antenna due to the very windy location.

The second IGR station was installed in January to March 2024 at Houthaelen (Figure 115) inside the military base and the same procedures as for Doel were used during three successive visits to install the antenna. The concrete base was reduced to 25 cm in thickness (Figure 116). This IGR station is not yet implemented in the M³G Metadata repository but will soon be added. We needed to wait more than 6 months to start validating the SAR data and the IGR to collect a sufficient time series analysis to proceed. The same methodological approach will be used as the one already done for Doel (next chapter point) and the processing will soon start. Both approaches, methodology and techniques will be detailed in a future peer-reviewed paper explaining the validation of the SAR vs GPS data.



Figure 115. Location of the second IGR station installed inside the Belgian military base close to Houthaelen.



Figure 116. Pictures taken on the field during the successive phases to dig the trenches (allowing to bring the electricity cables to cabinet of the IGR station) and the square base dug for the creating the concrete basement. The cabinet containing the modem and the recorder is shown also.

The IGR station lies directly on the Quaternary Formatie van Gent composed of eolian sands covered by waste filling materials and a loose conglomeratic level. No clay layers from Neogene nor from the Quaternary are present directly

underneath the IGR station.

Six IGR stations were bought with a full professional GPS antenna/receiver and the RBINS/ GSB is tightly working with a team of the NGI installing GPS antennas in Belgium. This consortium has decided to join their forces in developing and installing these new IGR stations in several case study area where there is a need either because of no more GPS/GNSS antenna and/or associated to ongoing land subsidence or ground deformation features revealed by the detailed SAR analyses of the GSB SAR team. The third one will be installed on the Nimy site of Vivaqua, where groundwater extraction are processed onsite for the company. The first visit out of the three is planned on the 16-01-2025. The fourth one should be installed in a pumping station located close to the Veurne city in an area where there is no GNSS station anymore so there is a need to bring an IGR there for various reason but also because we are located close to the DAS land subsidence bowl already discussed previously. The two remaining ones are on discussions as the Saint-Vaast area or Binche might be good targets but not easy to install because of the electricity issues. The last possibility might be the military base in Marche-en-Famenne where potentially the local conditions are able to satisfy the safety, and the electricity access.

1.5. Validation of the IGR station in Doel

1.5.1. Introduction

The integration of multiple geodetic observation techniques has become increasingly essential for precise and accurate monitoring of the Earth's surface deformation. One innovative approach in this domain is the use of Integrated Geodetic Reference Stations (IGRS), which combine various measurement technologies including Global Navigation Satellite Systems (GNSS), Interferometric Synthetic Aperture Radar (InSAR), leveling, and others.

This chapter focuses on assessing the performance of corner reflectors within the IGRS framework installed at Doel. The need for IGRS becomes particularly evident when addressing the challenges encountered in previous chapters regarding the selection of a stable reference point for PS-InSAR processing. As discussed, comparing data from different satellite missions (e.g., ERS, Envisat, Sentinel-1) introduces significant uncertainties and potential bias due to differences in reference points. These biases can lead to misinterpretations of subsidence or uplift trends across missions. An IGRS provides a consistent, stable reference to minimize these uncertainties, significantly reduce bias, and ensure more reliable comparisons across satellite datasets. Moreover, the implementation of IGRS is not only crucial for current satellite missions but also for future missions that may come online. As new satellites with varying orbital parameters, sensor technologies, and resolutions are launched, the IGRS will serve as a standardized reference point, enabling integration and comparison of InSAR data from different sources. This will enhance the long-term monitoring of deformation and ensure continuity in data quality, making the IGRS an indispensable tool for future geodetic research. Evaluating these corner reflectors is critical for enhancing the accuracy and reliability of geodetic measurements, thereby contributing to a more accurate measuring of land surface deformation.

Artificial radar reflectors, such as corner reflectors, play a significant role in geodetic applications, particularly in enhancing the precision of InSAR measurements. Their primary purpose is to provide a stable, well-defined reference point for detecting motion in the context of surface deformation studies. These reflectors are used to tie the InSAR data to a known position, which can be continuously monitored using GNSS. The integration of GNSS measurements ensures that any motion of the corner reflector reference point is accurately tracked over time, providing a precise and stable basis for assessing land surface deformation. Additionally, they serve in InSAR datum connection and geodetic integration. Initially, SAR observations are positioned in a 2D radar datum (azimuth and range), which can be transformed into a Cartesian geocentric terrestrial reference frame using the range-Doppler equations and an external elevation model.

The IGRS concept addresses the challenge of integrating multiple geodetic techniques by providing co-located reference points. This ensures that observations from different methods represent the same physical processes. GNSS, for example, provides 3D spatial positioning through satellite signals, while InSAR monitors deformation by analyzing differences in radar signal phases between two images. By integrating these methods, IGRS facilitates the translation of InSAR measurements into a consistent geodetic datum (Kamphuis 2019).

The main goal of IGRS is to integrate GNSS and InSAR data to ensure that time series represent consistent deformation characteristics. This integration is crucial for accurately interpreting measurements from various sensors and monitoring methodologies. The known location of the IGRS in a global coordinate reference system allows for calibrated deformation time series and improved geolocation estimates for InSAR scatterers.

In the following chapter, it aims to develop and evaluate the performance of IGRS corner reflectors installed in Doel, Belgium. The objectives include establishing a standard procedure for analyzing the SAR time series of artificial radar reflectors to estimate their Radar Cross Section (RCS), Signal-to-Clutter Ratio (SCR), and time series of range and azimuth movements. The goal is to implement this procedure using an efficient, open-source toolbox called GECORIS.

1.5.2. Theoretical Background

The performance of corner reflectors is crucial for accurate SAR positioning. Unlike transponders, passive corner reflectors are simpler to manufacture due to the absence of electronic components. However, their design and installation require careful consideration of various factors such as application requirements, weather conditions, materials used, background noise at the installation site, and the satellite's signal wavelength and orbit geometry. For a corner reflector to be effective, its reflected signal must be distinguishable in the SAR image, meaning the backscattered signal must be stronger than the surrounding background noise, known as clutter. The SCR quantifies this relationship. High SCR values are essential as they directly impact the accuracy of LOS measurements. For instance, a high SCR ensures that the phase variations caused by nearby scatterers do not significantly affect the measured phase of the dominant scatterer, thus reducing errors in point target measurements.

Extensive research and development efforts have focused on optimizing corner reflector designs for geodetic applications. Various types, including triangular and square trihedral reflectors, have been tested for their backscattering performance and robustness under different weather conditions. These tests aim to identify the most effective and durable designs.

These reflectors have been tested in diverse field conditions and orientations to ensure their effectiveness. For instance, corner reflectors have been evaluated for their performance in both ascending and descending satellite tracks. Following successful testing, these reflectors have been permanently installed at strategic locations to enhance geodetic measurements. The choice of reflector design, including the use of thicker aluminum plates and protective covers, ensures consistent performance in various environmental conditions.

The integration of these theoretical and practical considerations into the design and deployment of corner reflectors directly influences the accuracy of SAR positioning. To further understand and optimize this process, it is essential to delve into the mathematical formulations that govern SAR measurements, SCR, and RCS.

SAR measurements can be represented by the Impulse Response Function (IRF), which is crucial in determining the resolution cell on the Earth's surface. This IRF is typically modeled as a 2D sinc-like function in both azimuth and range directions. For a corner reflector, the signal observed in the SAR image is a combination of its dominant point scattering and the contributions from surrounding scatterers, or clutter. The power of the signal y captured by SAR can be expressed as:

$$y = A \exp(i\psi) \quad (40)$$

where A represents the amplitude, and ψ is the phase. The power P or intensity I of this signal is then:

$$P = A^2 = \Re(y)^2 + \Im(y)^2 \quad (41)$$

where $\Re(y)$ and $\Im(y)$ are the real part and imaginary part of the complex signal y .

For distributed scatterers, the radar brightness β_0 is a useful measure. It provides a normalized value that accounts for the strength of the radar signal as a function of the resolution cell area particularly in the slant-range direction. Radar brightness is derived from the pixel values (Digital Numbers, DN) recorded in the SAR image and is given by:

$$\beta_0 = DN^2 KDN^2 K \quad (42)$$

This expression includes both a pixel scaling factor KDN and calibration constant K . These factors are used to properly scale the digital number DN values and convert them into a standardized radiometric measure.

For idealized point scatterers like corner reflectors, RCS is a critical parameter. It measures how much power is reflected to the radar from a target and is expressed in square meters. The RCS can be estimated using two primary methods: the integral estimation method and the peak estimation method. In the *integral* estimation method:

$$RCS \approx IPKPA CF \quad (43)$$

In this equation, IP is the integrated power within the main lobe of the radar signal response, PA is the pixel area in the SAR image, and CF is accounting for the relative power in the sidelobes. In the *Peak* estimation method:

$$RCS \approx \beta_0 \Delta az \Delta r \quad (44)$$

In this equation, Δaz and Δr are the azimuth and range resolution respectively.

SCR is another key parameter, which is determined by the ratio of the reflector's signal power to the power of the surrounding clutter within the resolution cell. Mathematically, it is expressed as:

$$SCR = \frac{ICR_{peak} \bar{I}_{clutter}}{RCS \beta_0 \bar{I}_{clutter} \Delta az \Delta r} \quad (45)$$

In this equation, ICR_{peak} is the highest intensity of reflector, corrected for the clutter, $\bar{I}_{clutter}$ the expected intensity of the clutter, and $\beta_0 \bar{I}_{clutter}$ multiplied by the resolution cell area is the expected radar brightness of the clutter. The SCR directly impacts the accuracy of the LOS measurements, as it influences the phase variance $\sigma\phi$ which in turn affects the standard deviation of the LOS displacement $\sigma dLOS$. The phase variance can be approximated by:

$$\sigma\phi \approx \sqrt{22SCR} - \sqrt{3\pi} \quad (46)$$

and the corresponding standard deviation of LOS displacement is given by:

$$\sigma dLOS = \lambda 4\pi \sigma\phi \quad (47)$$

where λ is the wavelength of the radar signal (Czikhardt et al. 2021).

The careful consideration of corner reflector design is essential for achieving high SCR and RCS values, which directly

influence the accuracy and reliability of InSAR measurements. As noted, the RCS depends heavily on the physical characteristics of the corner reflector, including its size, shape, and material. For instance, the theoretical RCS for a square trihedral reflector with an inner leg length of 0.7 meters is approximately 34.7 dBm², whereas a triangular trihedral reflector of the same size typically achieves a lower RCS of around 25.1 dBm² (Figure 117). These values, however, can vary in practice due to factors such as orientation errors and environmental conditions. The impact of RCS on SAR positioning is visually evident in Figure 117, which shows how RCS varies with the inner leg size of different types of corner reflectors. This figure underscores the importance of selecting a reflector with an optimal design to maximize the reflected signal's strength and improve measurement accuracy.

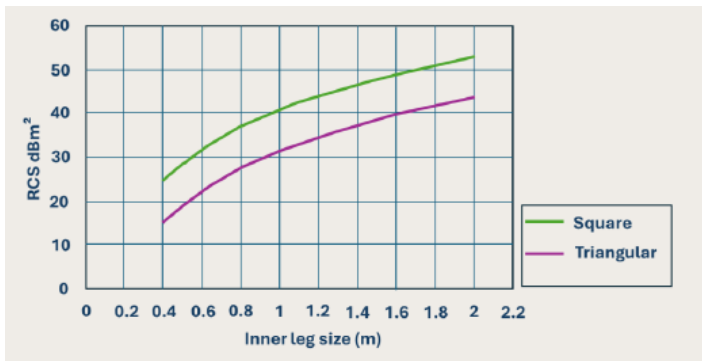


Figure 117. Relationship between Radar Cross Section (RCS) and inner leg length for C-band (Sentinel-1) trihedral corner reflectors, comparing triangular and square designs. The inset illustrates the geometric shapes of the reflectors. Adapted from (Garthwaite et al. 2015).

The design and installation process of corner reflectors also involves selecting appropriate materials and ensuring that the reflectors are oriented correctly relative to the satellite's line of sight. For example, using thicker aluminum plates and protective covers can help maintain consistent performance, even in adverse weather conditions.

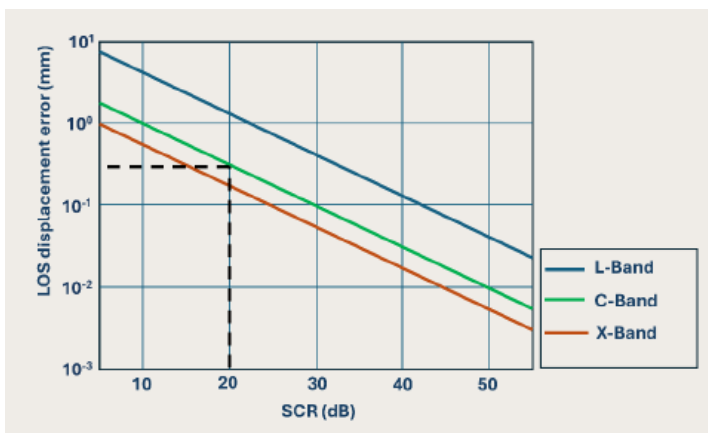


Figure 118. LOS displacement error as a function of Signal-to-Clutter Ratio (SCR) for L/C/X-Band InSAR data. Adapted from (Garthwaite 2017).

As discussed, the relationship between SCR and LOS measurement precision is critical. As illustrated in Figure 118, an SCR of 20 dB can lead to a LOS displacement error as small as 0.5 mm in C-band InSAR measurements. This precision is essential for high-accuracy geodetic applications.

These considerations highlight the necessity of optimizing both the design and deployment of corner reflectors to enhance the accuracy of geodetic measurements. The inclusion of Figures 117 and 118 not only provides a visual representation of these critical relationships but also reinforces the importance of SCR and RCS in achieving precise SAR positioning, thus making them indispensable tools for understanding and improving corner reflector performance in practical applications.

1.5.3. The Doel station validation analysis

Key factors considered during the installation included sky visibility, accessibility, and the specific application requirements for geodetic infrastructure monitoring. Ensuring unobstructed visibility toward the satellites was crucial for maximizing the effectiveness of the corner reflectors. The orientation of the reflectors was calculated based on the

azimuth and elevation angles relative to the known satellite orbits, such as those of Sentinel-1. This precise alignment was necessary to ensure that the reflectors would capture and return the satellite signals without obstruction, thereby providing accurate data for InSAR analysis.

In addition to these technical considerations, the installation process also considered the potential for signal interference and clutter. A thorough SCR analysis was performed before installation to identify the best possible location for the reflectors within the site. This analysis ensured that the chosen location would minimize background noise and maximize the accuracy of the radar signal measurements. The SCR analysis at Doel was particularly important given the potential for interference from nearby structures or vegetation, which could affect the accuracy of the InSAR data. On 22 July 2022, the first IGRS in Belgium was installed at the Doel site. This marked the beginning of the station's capability to support high-precision InSAR measurements. After the initial installation, further refinements were made to optimize the reflector's performance. On 15 May 2023, the reflector was adjusted to achieve an optimal inclination, ensuring it was correctly aligned to receive the maximum Radar Cross Section (RCS). This adjustment was crucial for enhancing the accuracy and reliability of the reflected signals, thereby improving the overall effectiveness of the InSAR measurements conducted at the site.

The GNSS station DOEL00BEL at Doel, Belgium, is a well-established site managed by the National Geographic Institute of Belgium. The IGRS in Doel is approximately located at 51.3218°N latitude and 4.2500°E longitude with an elevation of 45 meters. The station is built on a concrete slab foundation with a depth of 1.3 meters, a thickness of 55 cm, and approximate dimensions of 1 m² (with minor variations). Approximately 5 cm of the concrete slab is visible above the grass level. It features a SEPT POLARX5E receiver supporting GPS, GLONASS, and Galileo satellite systems. The single vertical pole monument stands 2.4 meters tall, anchored on a concrete foundation. The concrete slab rests directly on Quaternary sediments without deeper vertical steel poles; instead, four horizontal steel rods were embedded near the base of the slab, extending 30 cm into the surrounding Quaternary sediments and 30 cm into the concrete. This was done to stabilize and lightly anchor the foundation. The station uses a SEPCHOKE_B3E6 antenna with an SPKE radome, connected by a 30-meter coaxial cable and aligned 10 degrees from the true north. The foundation sits on a combination of sand, clay, and peat layers, which are on sedimentary bedrock. on sedimentary bedrock within the Eurasian tectonic plate, ensuring stable and precise geodetic measurements for regional monitoring. (For further details about the DOEL00BEL GNSS station, including technical specifications and comprehensive site information, readers can visit the official GNSS metadata website).

To complement the installation at the Doel site, ongoing maintenance and monitoring procedures were established. Regular checks are conducted to ensure that the reflectors remain properly aligned and free from obstructions, such as debris or vegetation growth, which could degrade the quality of the reflected signals. This proactive approach helps to maintain the high SCR and RCS values necessary for precise InSAR measurements, ensuring that the Doel IGRS continues to provide valuable data for geodetic and environmental monitoring.

1.5.4. Results

The processing of this chapter was done using the GECORIS open-source Python toolbox. In this analysis, SAR data from tracks ascending 88 and 161 and descending 37 and 110 were used to assess the positioning accuracy of corner reflectors under varying correction factors. Table 23 summarizes the RCS values, acquisition periods, and characteristics of used data for each track:

Track	Geometry	Average RCS before CR installation (dBm ²)	Average RCS after CR installation (dBm ²)	Acquisition period	Acquisition time
110	Descending	9.84	28.8	04/01/2022-28/07/2024	05:58:57-05:59:12
37	Descending	5.21	28.6	11/01/2022-23/07/2024	05:50:47-05:51:03
161	Ascending	5.93	28.8	07/01/2022-25/06/2024	17:33:26-17:33:41
88	Ascending	14.16	28.4	02/01/2022-26/07/2024	17:25:16-17:25:32

Table 23. Summary of RCS values, acquisition time, and periods for different SAR tracks, covering both pre- and post-installation periods.

The Absolute Positioning Errors (APE) in both range and azimuth are calculated as the difference between the detected subpixel peak positions and the expected radar coordinates, considering various timing biases. These biases include contributions from the ITRF position, solid earth tides (SET), tropospheric (tropo) and ionospheric (iono) delays, bistatic correction, Doppler effects, and FM-rate mismatches. For the Doel IGRS corner reflector, calculations were performed

on a triangular corner reflector. The impact of individual SAR positioning corrections was analyzed for ascending and descending tracks, as represented in Figure 118. Each scatter point in Figures 119a-d corresponds to a single Sentinel-1 acquisition, with each graph representing data from a different track (ascending 88, ascending 161, descending 37, and descending 110). These points illustrate how the application of various SAR positioning corrections progressively refines the accuracy, as shown by the clustering of points closer to the origin.

The analysis of range and azimuth errors across four Sentinel-1 tracks reveals distinct patterns in positioning accuracy. Ascending tracks (88, 161) show more initial scatter than descending tracks (37, 110).

However, all tracks benefit from corrections, with descending tracks generally showing tighter clustering after corrections. Across all tracks, FM-rate and Doppler corrections show the most substantial improvement in clustering, particularly in range.

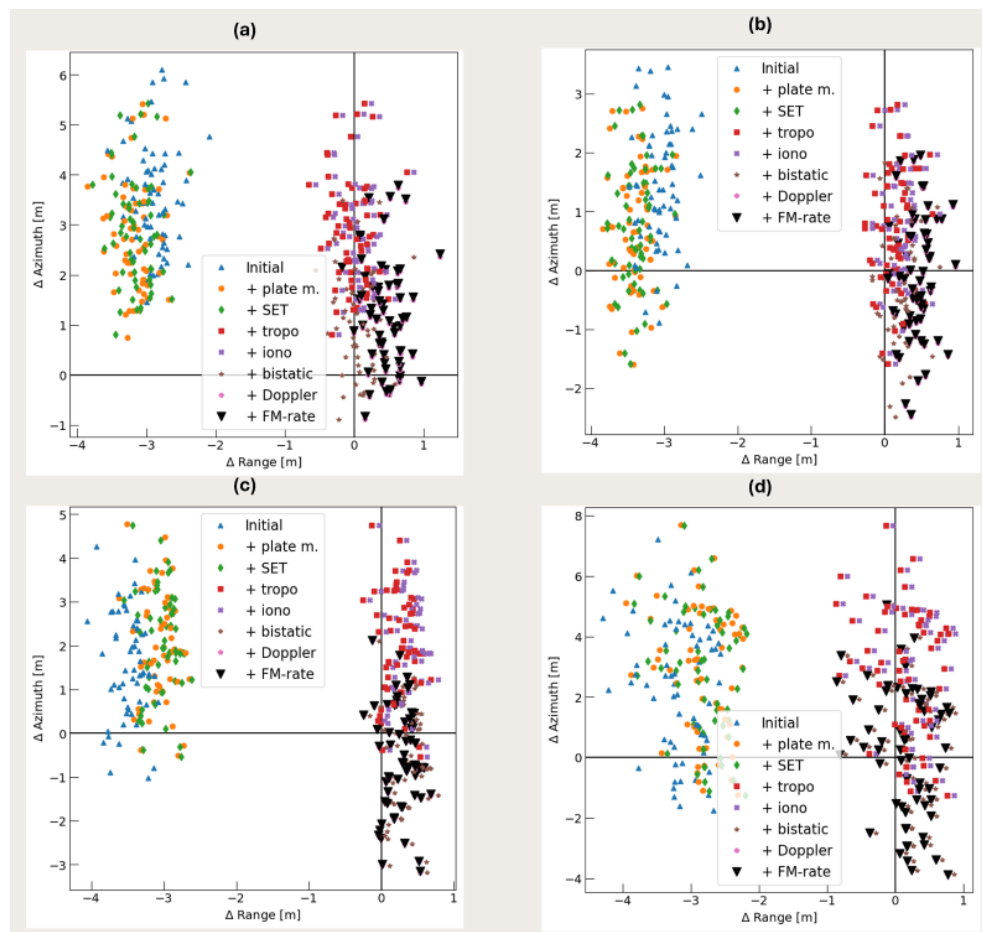


Figure 119. Impact of Individual SAR Positioning Corrections on Absolute Positioning Errors (APE) in Range and Azimuth for the Doel IGRS Corner Reflector. Stack of data from a Track 110 (Descending), b Track 37 (Descending), c Track 161 (Ascending), and d Track 88 (Ascending). Each scatter point represents a single Sentinel-1 acquisition, with different colors and markers indicating the various corrections applied, such as plate motion, SET, tropo, iono, bistatic, Doppler, and FM-rate.

The time series graphs in Figure 120 illustrate the range and azimuth errors for the four SAR tracks over time, with each colored marker representing a different track: blue triangles for ascending 88, green diamonds for ascending 161, orange circles for descending 37, and red squares for descending 110. The horizontal lines in each plot indicate the mean error for the corresponding dataset, serving as a baseline for comparison and highlighting each track's overall positioning accuracy. In the range plot, most tracks fluctuate around their mean lines, but ascending track 88 shows more variability, with some points below the mean, suggesting occasional deviations in range accuracy. Additionally, ascending track 88 shows the highest variability in azimuth positioning, indicated by the largest standard deviation (2.13 m) among the others. Descending track 37 demonstrates the most stability with minimal variation in both range and azimuth (0.19 and 1.01 m respectively).

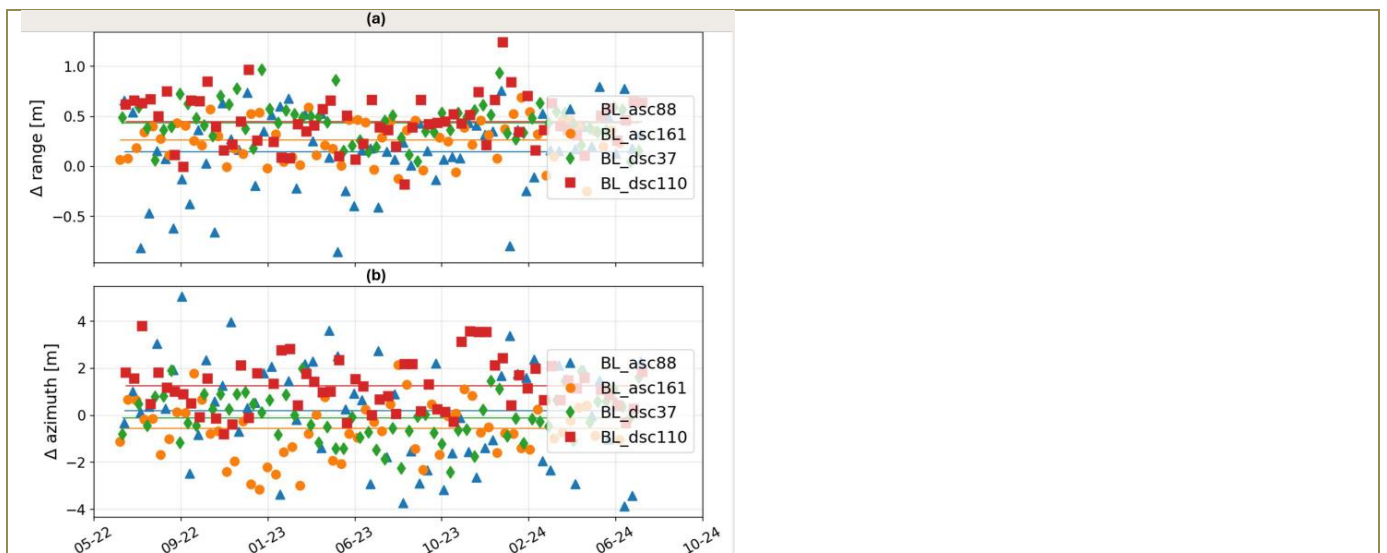


Figure 120. Time series of positioning errors for comparison of a range errors b azimuth errors, across different tracks.

Figure 121 shows the RCS time series for the Doel IGRS corner reflector apparent for four different Sentinel tracks. The SCR of each is calculated and written on the graph. These parameters are key factors that illustrate the performance of corner reflectors. The plotted data reveals how the reflectivity of corner reflectors varies over time. The dashed vertical line indicates the installation and alignment date of the reflector. Before the installation of the corner reflector, the observed RCS was dominated by clutter, as seen in the lower apparent RCS values. After installation, the RCS significantly increased, indicating the impact of the corner reflector on signal strength. The horizontal lines show the average RCS for each track before and after installation.

The SCR values in Figure 121 indicate that the descending tracks (Tracks 37 and 110) generally have higher SCRs—19.7 dB and 19.1 dB, respectively—compared to the ascending tracks (Tracks 88 and 161), which have SCRs of 16.5 dB and 16.1 dB. This suggests that the descending tracks experience less background noise, allowing for clearer detection of the corner reflector signal.

Conversely, the clutter RCS is higher for ascending tracks, indicating that these tracks encounter more background reflections, which could be due to their specific geometric configuration or environmental conditions. This higher clutter RCS may contribute to the lower SCR in the ascending tracks, making the signal less distinct against the background.

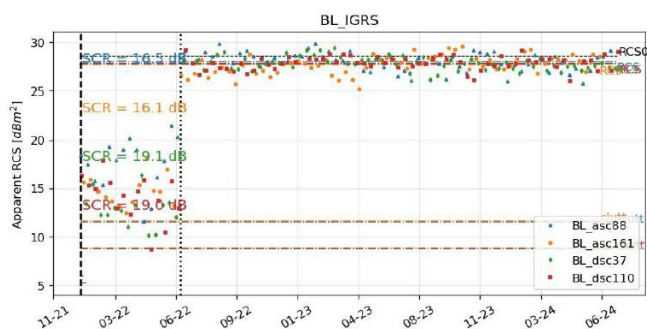


Figure 121. Apparent RCS time series of the Doel IGRS corner reflector for four different Sentinel-1 track

For the Doel IGRS corner reflector, the radar brightness (Beta0) before and after installation was evaluated for all four tracks. Figure 122 shows two examples, one from ascending track 161 (Figure 122a) and the other one from descending track 37 (Figure 122b). These are the result of smoothed data and the oversampling of the radar brightness, which is conducted with a factor of 32.

Figure 122 reflects the radar brightness before and after the installation of the corner reflector on the specified dates (07/01/2022 for track 161 and 11/1/2022 for track 37 for before installation, and 07/06/2023 for track 161 and 29/07/2023 for track 37 for after installation).

Beta0, or radar brightness, is typically calculated for each SAR acquisition. It represents the radar reflectivity of the surface for a specific acquisition, reflecting the power of the radar signal returned to the satellite after interacting with the ground. By analyzing Beta0 across multiple acquisitions, changes in reflectivity over time could be assessed, which can be useful for monitoring surface changes or selecting a master image for interferometric analysis based on the

highest Beta0 values, ensuring the best signal quality for further processing.

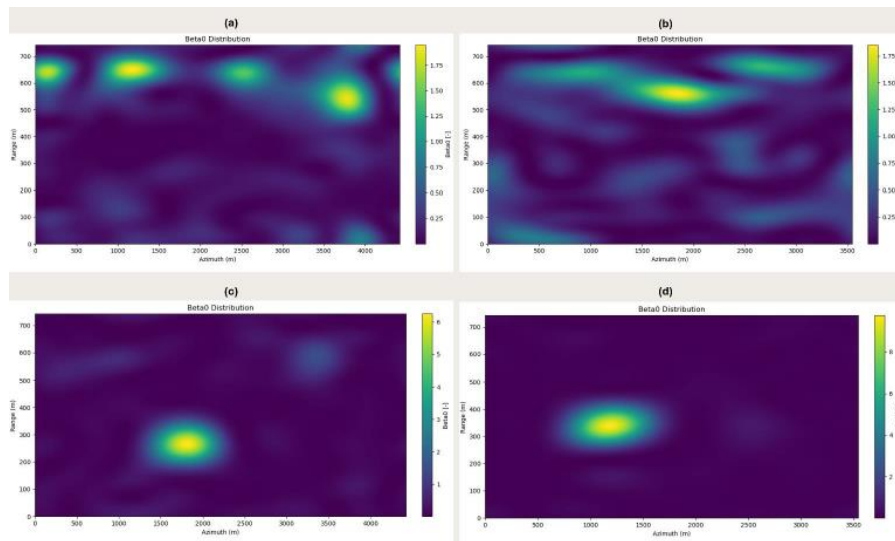


Figure 122. Radar brightness in azimuth and range geometry for (a) before installation for descending track 37 (11/01/2022), (b) before installation for ascending track 161 (07/01/2022), (c) after installation for descending track 37 (29/07/2023) and (d) after installation for ascending track 161 (07/06/2023).

Figure 123 presents cross-sectional views of the radar brightness (Beta0) at its peak value before and after the installation of the corner reflector. The cross-sections were taken along both azimuth and range directions for descending track 37 and ascending track 161, corresponding to Figure 122 specifically.

Figure 123a shows the azimuth and range cross-section for track 37 before the installation of the corner reflector, while Figure 123b presents the same cross-section for track 161 before installation. Figure 5.8c illustrates the azimuth and range cross-section for track 37 after installation, and Figure 5.8d displays the cross-section for track 161 after installation.

Before the installation of the corner reflector, the radar brightness (Beta0) profiles in both azimuth and range directions lacked a distinct peak, meaning the reflected signal was weak and dispersed. This makes it challenging to accurately pinpoint the position of the reflector, which is crucial for precise geolocation and positioning tasks.

After installation, the reflector creates a strong, sharp peak in the Beta0 profile, significantly improving the clarity and accuracy of the reflected signal. This sharp peak is essential for reliable positioning, as it ensures the reflector's location is easily identifiable in the radar data. Additionally, the relationship between SCR and phase noise is investigated. Table 24 summarizes values of SCR, standard deviation of phase, and displacement precision for four different tracks.

Path	SCR (dB)	Standard deviation of phase (degrees)	Displacement precision (mm)
Ascending 88	16.5	6.1	0.5
Ascending 161	16.1	6.4	0.5
Descending 37	19.1	4.5	0.3
Descending 110	19.0	4.5	0.4

Table 24. Values of SCR, standard deviation of phase, and displacement precision for four different satellite paths

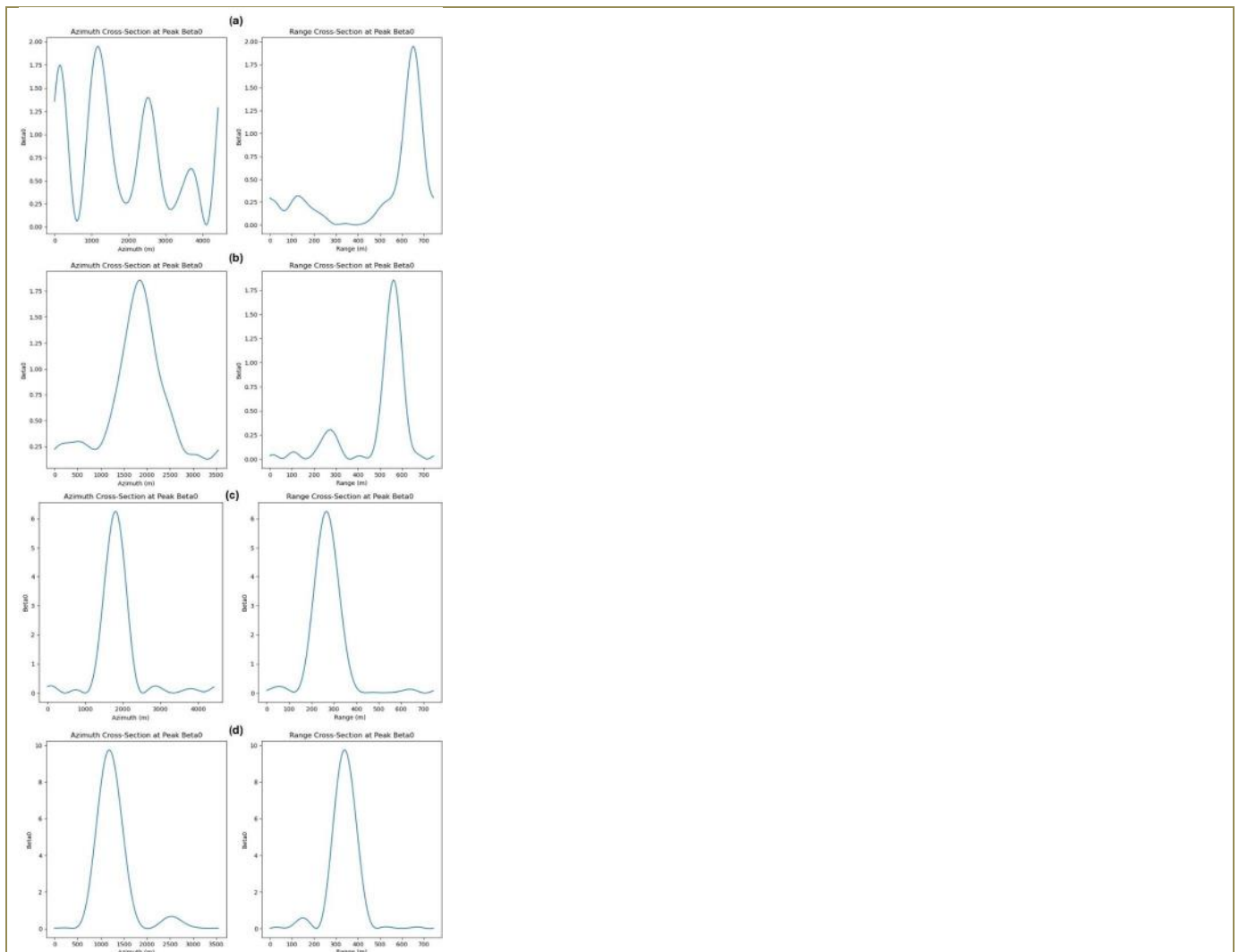


Figure 123. Azimuth and range cross-sections of Beta0 for (a) track 37 before installation of CR, (b) track 161 before installation of CR, (c) track 37 after installation of CR, and (d) track 161 after installation of CR.

The results demonstrate a clear relationship between SCR, phase noise, and displacement precision across the different SAR paths analyzed. As expected, paths with higher SCR values exhibit lower phase noise, leading to improved displacement precision. For example, the descending path 37, with the highest SCR of 19.1 dB, shows a phase standard deviation of only 4.5 degrees, resulting in a displacement precision of 0.349 mm. In contrast, the ascending path 161, which has a lower SCR of 16.1 dB, exhibits a higher phase standard deviation of 6.4 degrees and a corresponding reduction in displacement precision to 0.496 mm. This inverse relationship highlights how stronger SCR ratios lead to more reliable and accurate surface displacement estimates, as phase noise diminishes with increased SCR.

1.5.5. Discussions

The chapter presented a comprehensive analysis of the integration and performance evaluation of IGRS in Doel, focusing on the use of corner reflectors for InSAR applications. The key objective was to assess how corner reflectors enhance the accuracy of surface deformation monitoring through improved radar signal reflectivity, as indicated by RCS and SCR.

The results demonstrate the effectiveness of the corner reflectors in improving the quality of SAR data. The analysis of the RCS time series before and after the installation revealed a significant increase in signal strength, reflecting the impact of the corner reflectors on the radar measurements. This enhancement is crucial for precise geodetic measurements, as the corner reflectors provide a consistent, strong return signal, which is essential for accurate InSAR analysis.

The Beta0 analysis before and after the installation provided further insights into the reflectivity changes induced by the corner reflectors. The radar brightness maps illustrate the substantial increase in radar brightness after the installation, confirming the improved signal quality. This increase is particularly evident in the all track's data, which showed a

notable rise in both RCS and Beta0 values, indicating a more robust and reliable signal post-installation. The discussion also highlighted the role of SCR in performance evaluation. The higher SCR values observed in descending tracks compared to ascending ones suggest that these tracks experience less background noise, leading to clearer and more accurate detection of the corner reflector signal. This finding highlights the importance of considering track geometry and environmental factors when deploying corner reflectors for geodetic purposes.

The results clearly show that higher SCR values lead to reduced phase noise, which in turn improves displacement precision. This finding highlights the potential benefits of having an IGRS available in areas such as Antwerp and Saint-Vaast. If an IGRS had been available from the beginning of periods of different satellite missions in the Antwerp and Sint-Vaast cases, it could have provided a stable, high-SCR reference point, reducing the uncertainty associated with phase noise and enhancing the overall precision of displacement measurements.

Additionally, by anchoring the relative InSAR measurements to a consistent, well-defined geodetic reference frame, the integration of GNSS data would have provided independent verification of reference point stability. In both case studies, the lack of a stable, known reference point meant that displacement measurements could be biased due to reference point motion. Using IGRS would have minimized the potential bias in displacement measurements due to reference point motion.

Overall, the study emphasizes the role of corner reflectors in enhancing the accuracy of InSAR measurements within the IGRS framework. The significant improvements in RCS, Beta0, and SCR post-installation reflect the successful integration of these reflectors into the geodetic monitoring system, providing valuable data for precise surface deformation analysis.

This is a crucial step for the future integration and comparison of time series of LOS measurements, converted to vertical and horizontal displacements, with data from GNSS, ensuring comprehensive and accurate monitoring.

SAR references for all the previous chapters can be found in the two following PhD thesis:

Pierre-Yves Declercq - A study of long term and slow ground movements in Belgium using Multi-Temporal InSAR satellite data. 2020. Thèse de doctorat de L'Univeristé de Liège.

Atefe Chooani - Estimating Surface Displacements Using SAR Data and Hydro-Geomechanical Models and IGRS Performance Assessment. 2024. Thèse de doctorat de L'Univeristé de Liège.

1.6. Thorough statistical analyses of time series:

GNSS velocity field reconstruction

In the previous report, we presented individual estimates of vertical land motions at GNSS stations in and around Belgium. These estimates were obtained thanks to a semi-automatic analysis of the daily vertical position time series of 278 GNSS stations processed and distributed by the Nevada Geodetic Laboratory at the University of Nevada Reno (citation). Since then, the velocity estimates have been controlled by a visual inspection of the trajectory model adjusted to each time series. This verification step led to the removal of 17 unreliable velocity estimates, leaving 261 reliable ones for further analysis (Figure 124).

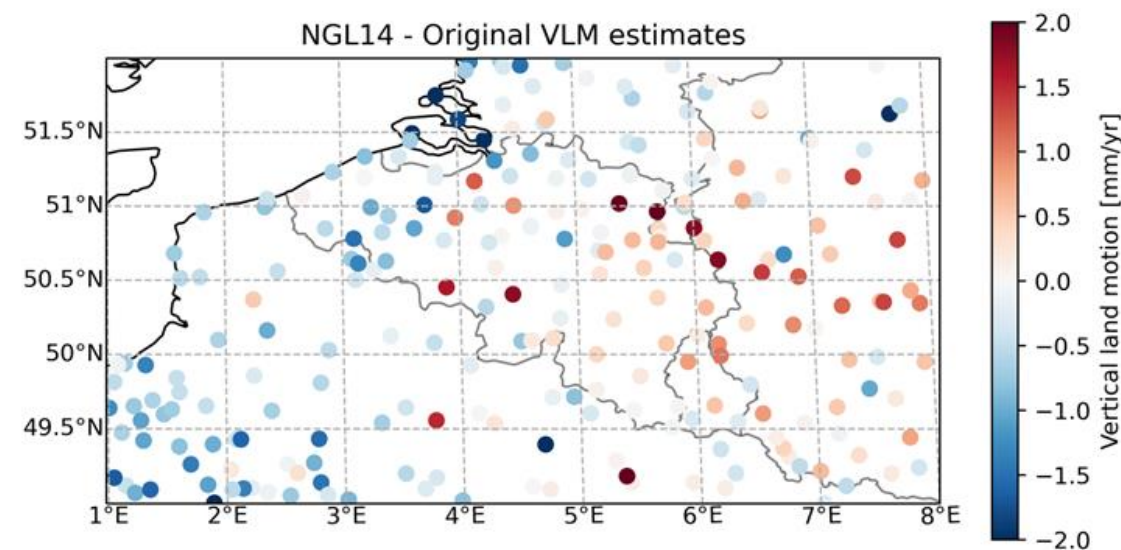


Figure 124. Vertical land motions estimated at GNSS stations in, and around, Belgium.

Because of local effects, the displacements estimated at one GNSS station may not always reflect regional ground motions. Thus, it is necessary to post-process the estimated velocities to extract spatially coherent deformation patterns. To do so, we used a re-weighted version of the robust network imaging method proposed by Kreemer et al. (2020). The re-weighting of the method allowed us to account for the presence of time-correlated noise in GNSS position time series. The estimated deformation resulting from this robust network imaging is presented in Figure 125.

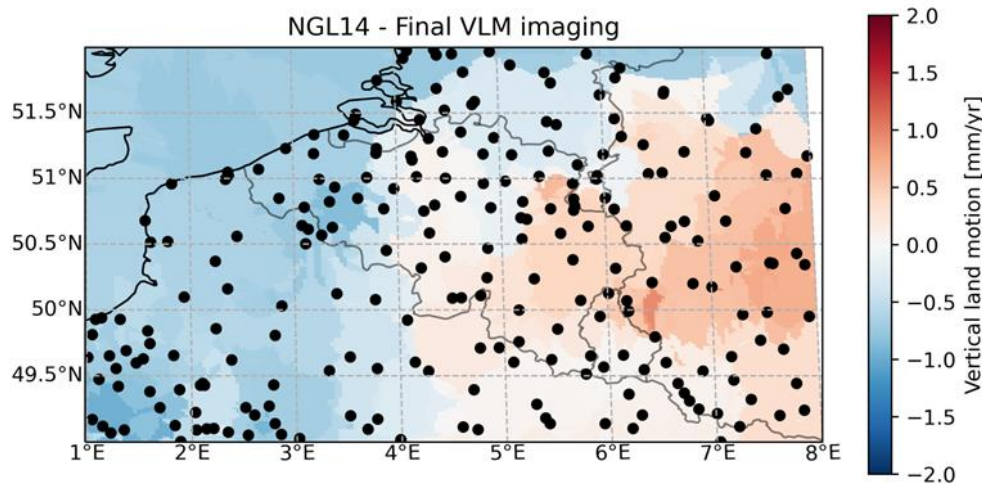


Figure 125. Robust network imaging of vertical land motions observed by GNSS stations in, and around, Belgium.

Because the robust network imaging method involves Delaunay triangulation-based interpolations, the method tends to retrieve artificial velocity transitions at a few kilometres scale. Since the density of stations is not high enough to resolve such short-scale deformations (such as subsidence around Jülich or uplift around the former coalmines in Belgian Limburg), we smoothed the velocity field using a median filter with a 12.5 km radius. Figure 4 presents the smoothed vertical velocities. This figure mainly reveals subsidence in Flanders, and an uplift pattern in the Liege and Luxembourg provinces, and western Germany.

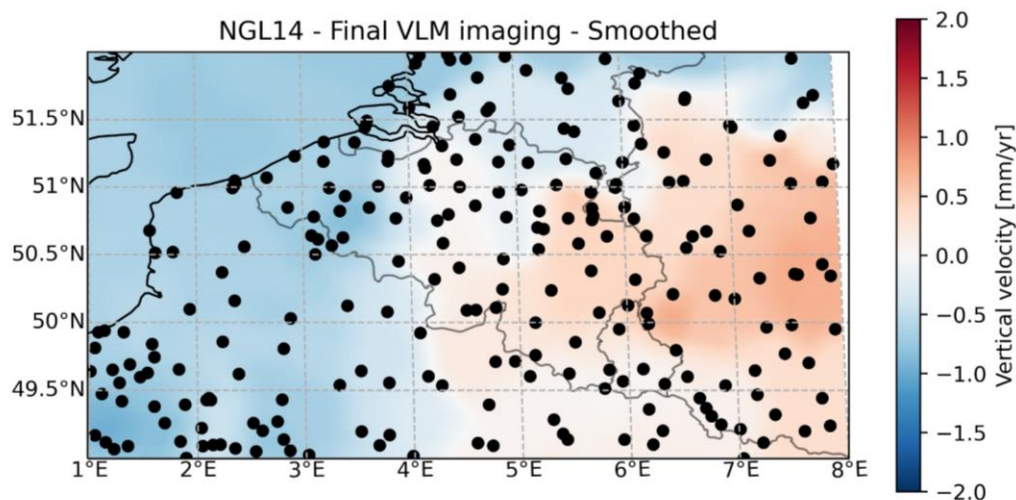


Figure 126. Final smoothed map of vertical land motions observed by GNSS stations in, and around, Belgium.

The subsidence pattern at the coast is observed beyond Belgium and partly explained by the post-glacial isostatic adjustment. On the other hand, the uplift pattern is consistent with the hypothesis of an uplift caused by the buoyant mantle plume below the Eifel region proposed by Kreemer et al. (2020).

1.7. Calibration and comparison of PSI data with GNSS and absolute gravimetry on long and short-term intervals:

Preprocessing of PSInSAR deformation time series

The raw line-of-sight deformation time series estimated at individual permanent scatterers may not always reflect actual

ground motion due to possible processing errors or local effects. To reveal spatially consistent patterns from each deformation time series datasets, we applied a local median filter with a 250 m radius for each epoch. Using such a median filtering approach guaranteed a robustness to spatial outliers and resulted in a noise reduction of about 80% (see Figure 127).

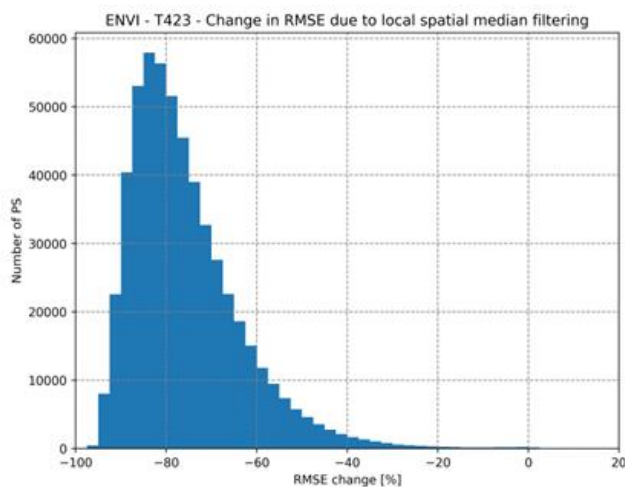


Figure 127. Histogram of the change in RMSE caused by the local spatial median filtering.

After this pre-processing step, we noticed inter-track inconsistencies in the form of nonlinear large-scale deformation errors, a possible signature of orbital ramps. These were especially visible in track T423 of the ENVISAT mission (see the middle track in Figure 128). Considering that large-scale deformation patterns are unlikely to be caused by geophysical causes, we removed deformation patterns with a spatial scale above 25 km by applying a median filter with a radius of 12.5 km.

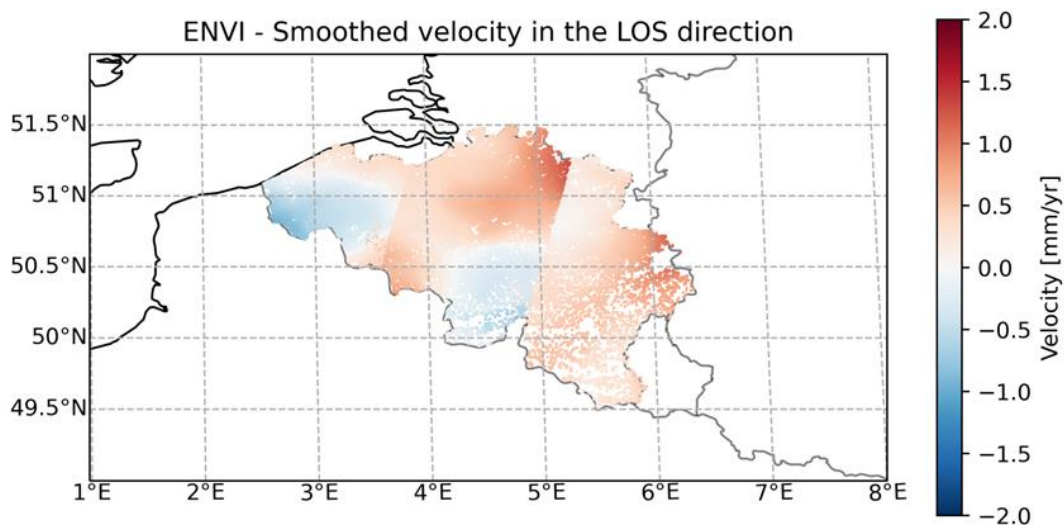


Figure 128. Average LOS velocities of the large-scale signal in the ENVISAT dataset. The North-East/South-West discontinuities represent the transition between the different tracks.

Thanks to these two pre-processing steps, we could better identify long-term deformation patterns and more easily search for possible local changes in deformation triggered by groundwater extraction events occurring during the satellite observation periods.

As a first-order approximation, it is frequent to assume geophysical processes or past anthropogenic activities to produce linear line-of-sight (LOS) deformations. However, when considering groundwater extraction activities occurring within the satellite monitoring era, one can also expect abrupt changes in ground dynamics triggered by pumping events. Thus, searching for velocity changes in LOS deformation time series can be a strategy to automatically detect and quantify groundwater extraction activities over large areas.

To assess the potential of PS-InSAR for the detection of recent groundwater extraction activities we carried out a systematic detection of velocity changes in the LOS deformation time series. In practice, there exist many ways to detect changes in geodetic time series. Based on our previous experience with GNSS position time series, in this project, we employed a detection method based on hypothesis testing in linear models.

We used the so-called Generalised Likelihood Ratio Test (GLRT) (Teunissen, 2006). This method tests the gain in likelihood obtained when adding a discontinuity at a given time. In practice, the GLRT boils down to analysing a positive real-valued statistic "T". The larger this T-statistic gets, the more likely a discontinuity will be present in the time series. In this study, we considered three types of discontinuities: offsets (change in mean), velocity changes, and outliers. By evaluating the T-statistic associated with velocity changes at all epochs, and retaining the maximum values for each PS, one can identify areas subject to nonlinear deformations (see Figure 129).

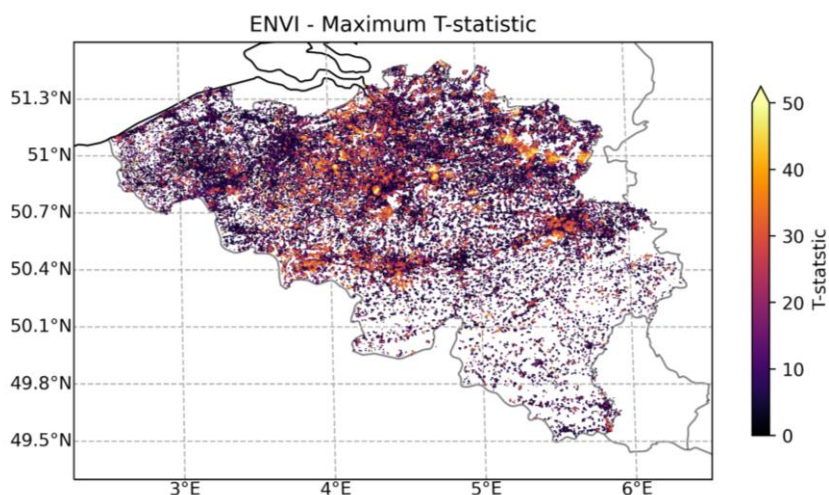


Figure 129. Maximum T-statistic associated with velocity changes for all epochs of the ENVISAT satellite mission.

The bright yellow spots visible in Figure 129 highlight areas in Belgium where adding at least one change in velocity to the trajectory model would be most beneficial. Hence, these areas are likely to be affected by pumping activities, and worth investigating further. Explaining all the nonlinear deformations in Belgium is beyond the scope of this work. However, within the LASUGEO project, we can nonetheless focus on specific examples.

One notable example is the detection of a nonlinear deformation pattern in the south-west of Brussels (Forest-Vorst), only visible on the ENVISAT mission dataset. A further analysis revealed that the local increase in the T-statistic was caused by a subsidence bowl reaching over 4 mm/yr that started in the middle of 2007 (Figure 130). Discussions with Brussels Environment revealed that this large subsidence bowl was related to the construction of a new building within an industrial facility in the centre of this area.

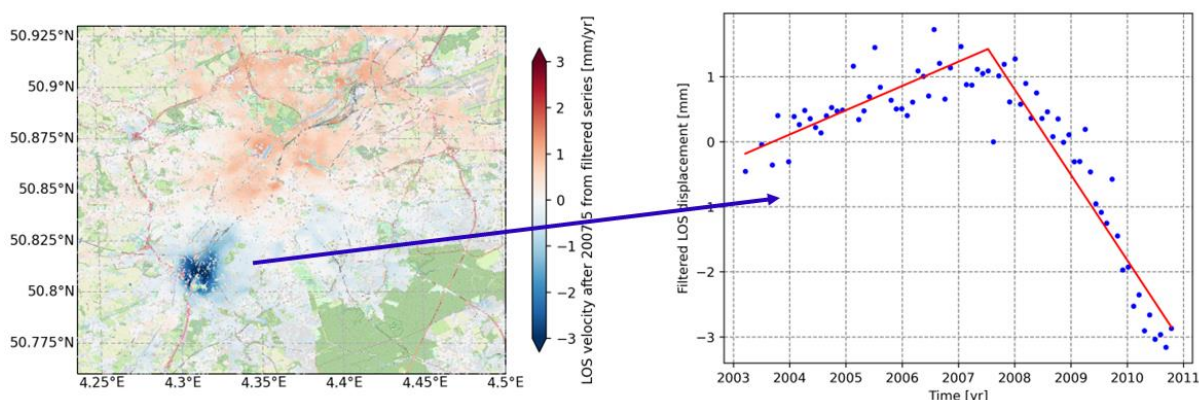


Figure 130. LOS velocities after 2007.5 around Brussels (left); and filtered LOS time series within the subsidence bowl (right).

AUTOMATIC MODELLING OF DISCONTINUITIES IN THE PSINSAR SERIES

Considering the number of PS over the whole country, manually investigating all areas subject to nonlinear deformation to quantify their deformation would be a very tedious task. To avoid such a burden, we developed an algorithm for the automatic modelling of PS-InSAR deformation time series.

This algorithm consists in an iterative analysis of the T-statistic. It is composed of six main steps:
Adjust a-priori linear trajectory model to each time series.
Screen all the time series for outliers, offsets, and velocity changes using the T-statistic.
Select all the time series presenting a T-statistic above a given threshold.
Identify the most likely discontinuity type and date for each time series selected in step C.
Update these series' existing trajectory model(s) to account for the newly identified discontinuity type and date.
Repeat steps B-E until no more T-statistic exceeds the given threshold.
The main products of this algorithm are the trajectory models adjusted to each permanent scatterer. These models can then be used to extract deformation parameters for local and country scale investigations.
An article about the potential of searching for velocity changes in PS-InSAR time series for groundwater monitoring is in preparation.

TIME-VARIABLE VELOCITY FIELDS

Based on the estimated change in velocities at the individual permanent scatterers, we can extract the LOS velocities at different dates to evidence velocity changes over Belgium. The Figure 41 and Figure 42 present instantaneous LOS velocities estimated in 2004 and 2010. As expected, differences between the two velocity fields (Figure 131) are observed where the T-statistics was high in Figure 7.

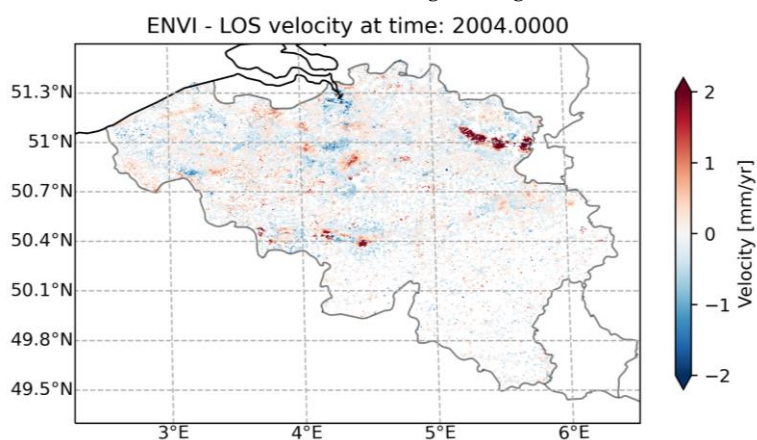


Figure 131. LOS velocities in 2004.0 estimated from the ENVISAT dataset.

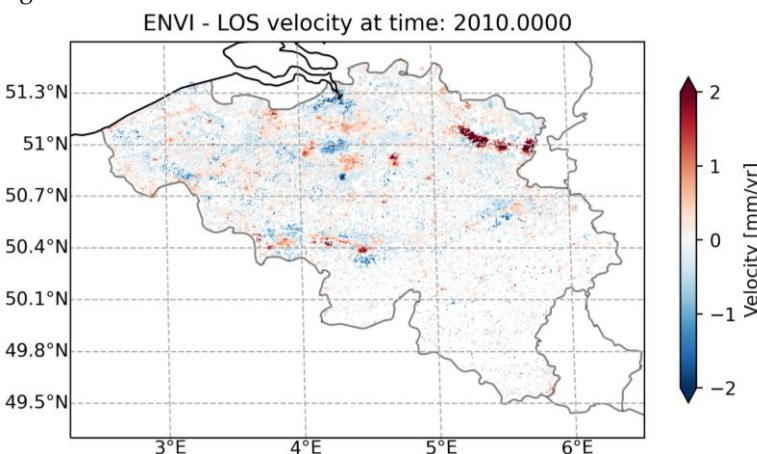


Figure 132. LOS velocities in 2010.0 estimated from the ENVISAT dataset.

ENVI - LOS velocity difference between 2010.0 and 2004.0

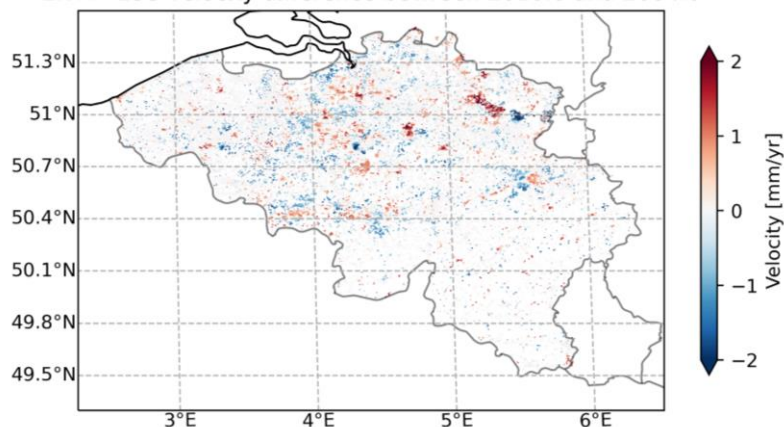


Figure 133. Difference between the 2010.0 and 2004.0 LOS velocities estimated from the ENVISAT dataset.

In the future, these time-variable velocity fields will be used to confront geophysical modelling in areas of interest. A systematic analysis of the estimated changes velocities would certainly be useful to document the influence of anthropogenic activities on ground deformation in Belgium and identify possible deformation related hazards.

ABSOLUTE GRAVITY MEASUREMENTS ANALYSIS

The last types of geodetic measurements used in the LASUGEO project are absolute gravity measurements. The advantage of this technique is that it does not depend on any reference frame. A disadvantage is the sensitivity to possible local effects caused by mass changes. Repeated absolute gravity measurements have been carried out by the Royal Observatory of Belgium (Van Camp et al., 2011) since about three decades in 11 locations: Oostende, Saint-Amand-les-Eaux (FR), Sohier, Werpın, Manhay, Sprımont, Membach, Eifel (DE), Monschau (DE), Jülich (DE), and Bensberg (DE).

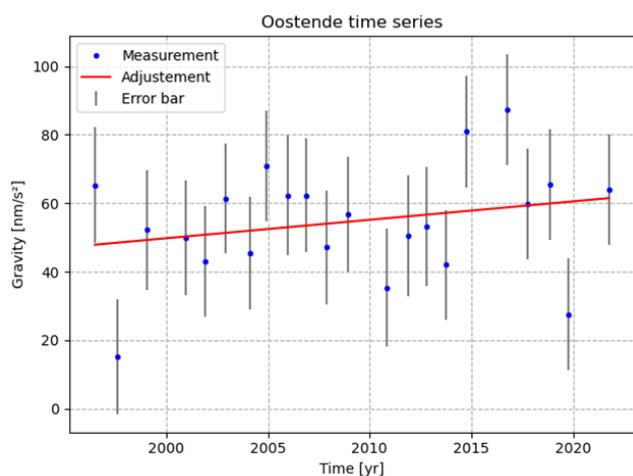


Figure 134. Gravity time series measured in Oostende.

From these repeated measurements, we constructed, for each city, a time series of the change of gravity over the years (Figure 134). Assuming there is no trend in the change of mass near the measurements point, the rate of change of the gravity in nm/s^2 was converted into vertical velocities in mm/yr using a $-2.0 \text{ nm/s}^2/\text{mm}$ conversion factor (Van Camp et al., 2011). Figure 135 presents the estimated gravity-based vertical land motions.

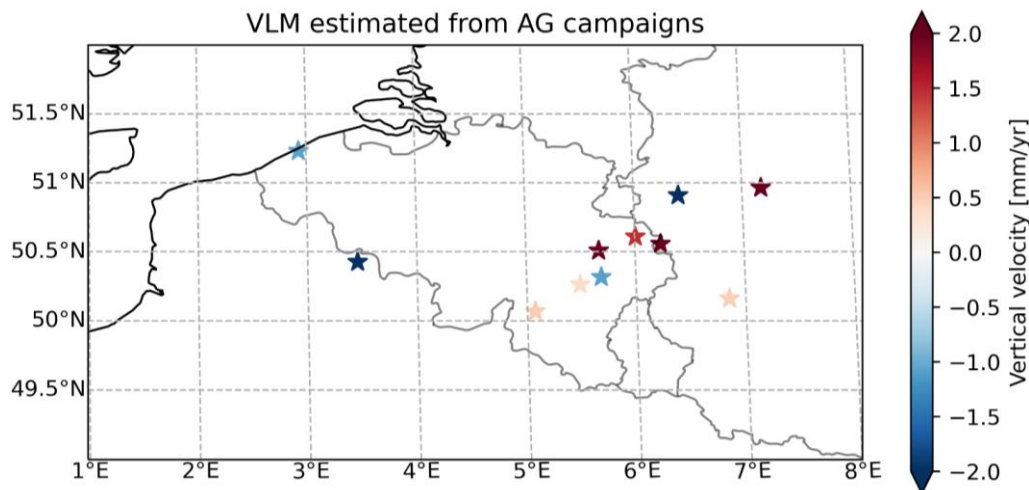


Figure 135. Vertical velocities inferred from the repeated absolute gravity measurements.

Figure 135 shows a relatively good agreement between absolute gravity derived velocities and GNSS velocities (Figure 126). The agreement is however not perfect, certainly due to the small number of data points and the fact that gravity measurements are very sensitive to local effects. In particular, the strong man-induced subsidence of about 1 cm/yr causes a strong increase in gravity of 37 nm/s²/yr (see next Figure 46). We do not have GNSS data at that place, but this is well observed by PSInSAR (<https://egms.land.copernicus.eu/>) or repeated levelling (Van Camp et al., 2011).

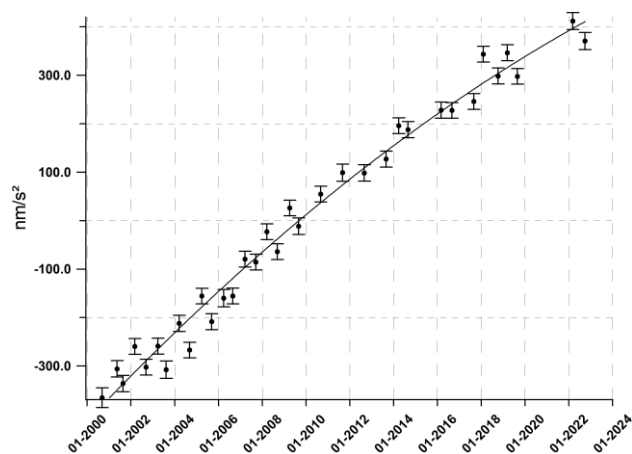


Figure 136. Absolute gravity values in Jülich.

1.6. Analysis and comparison of PSInSAR data vs the other techniques and associated to the six study cases (cfr D.4.4.1/D.4.4.2./D4.4.3./D4.4.4./D4.4.5./D.4.4.6. associated to each ROI i.e. D.2.1.1. to D.2.1.6. presented before)

This task has been integrated in the discussion, models and results for each ROI presented here un this project (i.e. Flanders DAS, TAS, Leuven, Antwerp, Saint-Vaast and Brussels). PSInSAR data will be compared to other techniques and models allowing to further convince that ground deformations observations from EO solutions are controlled, constrained, and confirmed by other geodetic and non-geodetic techniques. The main issues observed during the project are related to the accessibility and to the availability of data to work on the development of models using other techniques (i.e. hydrogeological, or geomechanical deformation, on the reliability of some information in the area under study). Several areas have clearly a lack of data and there is a need to start a monitoring approach using other techniques while the SAR data and imagery can be used and will be used in the future. Some issues have been highlighted as well, the lack of SAR data before 1991 to return in the past, the reliability of the PS data points as related to the reference points and/or anchor point (absolute reference point, partly solved with GNSS station and the new IGR stations). The most important aspect of each case study is also what the PSInSAR data represent in terms of information as it depends a lot on the nature of the anthropic points used as a PS, on the understanding of the subsurface information related to the infrastructures and the foundations associated to them. Moreover, the PS data points give information on a ground deformation visible at the surface that is the sum of deep and shallow geological phenomenon. Deciphering the causes of those deep vs shallow geological features changes that can have an impact by adding or subtracting their behaviors

to give the final intensity of the deformation (i.e. the velocity in mm/yr), is a real challenging aspect as again it requires a lot of geological data on the subsurface and the more we work, the more we have difficulties to find convincing geological explanations as it requires subsurface data that should be acquired by different field geophysical, airborne, drilling, CPT campaigns.

WP5 Future land subsidence vs groundwater exploitation: models and scenario – Deliverables (D.5.1.(see chapters 1.3/1.4 before)/D.5.2.)

This task has been dropped out due to the time frame constraint related to the retirement of Marc Van Camp and the absolute necessity to end up the PhD thesis of Atefe Choopani in due time although it was coincident also with the end of the activities of the Prof Kristine Walraevens and Prof Alain Dassargues before their retirement. This appealing approach cannot be set up immediately due to inconsistent and opposite answers/results depending on the case studies presented here before while some were quite aligned, and others were totally inconclusive meaning that we need to discuss deeply and in details to discriminate potential deep vs shallow causes that are always difficult either to separate either to estimate from the surface observations. SAR observations have shown and illustrated the evolution of long-term phenomenon that can change from land subsidence to uplifting conditions while decreasing in time and returning progressively to an equilibrium state before returning to land subsidence (i.e. like the alluvial plains in the Brussels area that were following these very long-term trend on > 30 yrs).

3. FINAL RESULTS

WP1

The results and publications issued from the project are disseminated throughout the personal and institutional accounts on social media and scientific websites.

WP2

Six sites were studied during the project and were studied from the hydrogeological aspects for 5 of them with the objectives to produce hydrogeological models based on the available data like the pumping wells activity, the piezometric data, the hydrogeological parameters and geological models when available to bring them inside the GIS projects. Hydrogeological models are progressively developed and delimited geographically to include the SAR velocities values representing surface deformation areas observed and obtained from the SAR processing's. The regular updates on SAR data allowed the different teams to have important discussions on the origin of the ground deformations but the estimation of the importance of the deep vs shallow deformation behaviors remain a critical aspect and need further investigation in some areas. Archive's data are missing for most of the areas to have an overview on a longer term. It is important to determine the hydrogeological conditions also in the past and probably well before the time of the identification of the land subsidence or the ground deformation processes. Geological, hydrogeological, geotechnical data were collected and used to help in the developments in the different models that are expected. Other target sites were inserted and were not foreseen at the beginning and concerns two areas where land deformation were observed: 1° - regional uplift along the Senne valley and localized land subsidence in the alluvial plains of the Brussels Region; and 2° - regional land subsidence in the district of Saint-Vaast were also analyzed with the piezometric data collected by the ISSSeP services. Further monitoring are essential to maintain and achieve in the future as those ground deformations are clearly visible and identified on a long-term time interval.

WP3

Field campaigns blocked during the covid crisis and the follow-up actions foreseen were totally stopped in relation with the departure from ROB of both Dr Kevin Gobron in August 2022 and Dr Michel Van Camp in March 2023.

WP4

SAR images across Belgium are collected from the different EO hubs and regarding the different satellites and orbits. All these data are progressively implemented on a strong 48To LaCie 6big server with a RAID5 system allowing to properly store, manage and back-up both the SAR images and the results acquired resulting from the SAR processings. This server has been blocked and not available for 6 months (March to September 2023) due to the crash disk and failure of one disk. The RBINS IT department has not been able to find a quick solution. After 6 months, a new disk arrived from the IT and following a procedure to include the new disk in the RAID-5 system, all the data were still there and preserved. This is the best way to protect and store the SAR images on the long term. The Sentinel images are collected and progressively added in this storage server to store and retrieve all the SAR images that are useful for further developments using this technique.

Ground control points combining two geodetic techniques (corner reflectors and GPS stations) called IGR stations were bought, two were installed and the second one installed in May 2024 has now reached a sufficient long time interval to collect a sufficient number of SAR images from Sentine-1A to validate the data collected from the SAR approach and to compare with the GNSS values acquired as well since the installation. Thos IGR are part of the belgian GNSS network and will be assigned and recognized on the EPOS and European platform. A third one is foreseen on the Vivaqua site in Nimy and should be installed in the next months with a potential working frame around March-April 2025. Three other stations are still under discussion to determine the best potential sites considering the requirements in electricity access for the GPS station and the need of safety and security of the installation on a specific site. Those criteria and the need for an open and large open area without building and trees inhibited several sites that were prospected on the field without having all the requirements or the electricity access. The idea of using solar panels was also discussed between NGI and GSB teams but this solution is not optimal during the winter period and brings us back to the same aspect, find and guarantee electricity access. Three spots are still searched, one in Veurne along a groundwater pump station in an area where GNSS data are missing so this area is of prime importance and should be re-discussed with the company, but the main issue is that the owner of the land is another company that has never given positive feedback till now. A future work is thus necessary to secure this place to install the IGR before the summer 2025. The two last IGR should find another potential area potentially through military bases where NGI can more easily secure the access, guarantee the safety and obtain the electricity access (Marche-en-Famenne and Arlon were cited as promising places for installing GNSS stations). Another potential site could be the Lavoir of Peronnes Binche where a federal building hosting federal collections is present but the discussion between the "Régie des Bâtiments" and the company that is the owner of the site were difficult essentially because the IGR could only be installed very far from the main building along the

parking slot at the entrance meaning a very long trench to dig (125 m) to bring the electricity cables till there. The expectations are to take decisions and install the last two before the end of 2025.

WP5

The developments of the different models are necessary before launching this phase. They are already inserted in the different chapters associated to each target sites description of the ongoing results produced for the different case study sites, but the opposite and very different scenarios and unclear geological causes have not created the best atmosphere to move forward. The successive retirements of several partners and the step out of the second PhD thesis launched on the Leuven area have created a gap in the scientific requirements to achieve those goals thought initially as feasible with a full dedicated partner consortium.

4. CONCLUSIONS AND RECOMMENDATIONS

Conclusions

This work and associated project presents an extensive investigation into land subsidence deformation areas (i.e. DAS and TAS aquifers, Antwerpen, Leuven all located in Flanders and Saint-Vaast) observed and monitored through long historical and recent SAR imagery data on more than 30 years of European satellite SAR imagery acquisitions. One case study deal with the Brussels Region and more specifically to a smaller area where geothermal use and drillings were done. In that area, an uplift was visible from the SAR imagery acquisitions and follow-up during more than 30 years as well.

Using advanced monitoring techniques, including Persistent Scatterer Interferometric Synthetic Aperture Radar (PS-InSAR), piezometric well monitoring, and numerical modeling, the research explores the dynamics of ground deformation in these areas and highlights the importance of integrated approaches to hazard assessment and risk mitigation.

Deep aquifer system under the western part of Flanders (DAS)

The intensive exploitation of the Landenian, Cretaceous, and Paleozoic aquifers since the 1960s has led to significant declines in piezometric levels, exceeding 100 meters in some areas, driven by the economic boom of that era. This overextraction caused extensive regional depression cones and aquifer compaction, resulting in widespread land subsidence. Compaction of the Ypresian aquitard due to pumping from the Landenian aquifer has been particularly impactful, with subsidence continuing even after groundwater levels began to recover, especially in layers with low vertical hydraulic conductivity.

InSAR data for 1992–2001 and 2003–2010 revealed consistent spatial patterns of subsidence, with the highest rates observed in a NW-SE zone in SW Flanders. While high subsidence rates in the NW correlate well with intense Landenian aquifer exploitation, rates in the SE are less clearly linked, possibly due to unaccounted factors or underestimated depression cone extents.

The groundwater flow model for the DAS did not fully capture the piezometric depression cone in the Cretaceous aquifer, likely due to incomplete pumping data. Additionally, the limited spatial correlation with piezometric trends in the Paleozoic aquifer suggests that the rigid basement rocks exhibit low elasticity and minimal compaction.

The Tertiary Aquifer System (TAS) under the central part of Flanders (i.e. the Merchtem area)

The MODFLOW SUBSIDENCE (SUB) module was integrated into the flow model to calculate layer compaction and surface subsidence. The model predicts a compaction of approximately 0.2 mm in the Ypresian Aquifer and 0.5 mm in the Ledo-Paniselian Aquifer after 10 years of pumping, resulting in cumulative land subsidence of less than 1 mm at the surface.

However, InSAR data for the region around Merchtem show localized subsidence rates of 1 mm/year to 4 mm/year, which significantly exceed the model's prediction of under 1 mm over a decade. This discrepancy suggests that groundwater extraction alone is unlikely to be the primary driver of the observed surface subsidence.

The model indicates drawdowns of approximately 3 m and 2 m in the Ypresian and Ledo-Paniselian Aquifers, respectively, after ten years of pumping, with total subsidence predicted to remain below 1 mm. In contrast, satellite-derived InSAR data reveal higher rates of subsidence, indicating the involvement of additional factors beyond groundwater extraction in driving land subsidence in the region.

Leuven area

In the region of Leuven, two zones of land subsidence have been identified by PS-InSAR in the North of the city. In this area, the land subsidence could be linked to the presence of many historical and ongoing pumping wells. A 3D regional groundwater flow model coupled with a 1D geomechanical model (SUB model) was developed to understand the local consolidation processes and verify the assumptions.

The compaction computed using the SUB model overestimates the land subsidence values observed using the PS-InSAR measurements. This might be due to uncertainties related to the parameterization, conceptualization and calibration of the 3D groundwater flow and 1D geomechanical models. This can also be due to the difficulty of comparing PS-InSAR measurements revealing surface deformations with the results of subsurface models.

Antwerp: Land Subsidence

The study in Antwerp employed a combination of PS-InSAR analysis and numerical modeling to examine land subsidence over three decades. High-resolution TerraSAR-X data (2019–2022) and historical SAR datasets (1992–2023) revealed persistent subsidence trends, with the highest rates observed in the harbor area. A detailed analysis of a site outside the backfill zone allowed the isolation of groundwater-driven deformation, excluding the effects of

load changes from backfill materials. Numerical models simulated aquifer-specific swelling and compaction due to changes in water pressures. For instance:

- Declines in water heads in the Ruisbroek-Berg and Lower Oligocene Aquifers led to substantial compaction.
- Rising water heads in the Wommel-Lede Aquifer caused swelling, partially offsetting overall subsidence.

The study validated its numerical models by comparing deformation rates with those derived from PS-InSAR data, noting strong consistency across datasets. However, some discrepancies emerged, primarily due to limitations in subsurface parameter estimation and temporal gaps in data. The findings underscore the need for continuous high-quality data collection and integrated monitoring systems to improve the understanding of subsidence drivers in complex settings.

Saint-Vaast: Hydrogeological Hazards

In Saint-Vaast, the research focused on natural hazards in a post-mining environment, where historical drainage galleries and groundwater dynamics influenced subsurface stability. Analysis of three decades of SAR data (1992–2023) and piezometric well measurements (2009–2023) identified patterns of uplift and subsidence linked to hydrogeological disturbances and sediment transport.

Significant incidents in 2009 and 2018 were investigated in detail. Rising groundwater pressures led to clogging, pressure buildup, and eventual ruptures, triggering mudflow outbursts and substantial sediment transport. For instance:

- The 2009 clog rupture was followed by a phase of significant subsidence due to sediment outflow.
- A similar event in 2018 resulted in rapid subsidence, correlating with rising water heads and subsequent sediment discharge into the Haine River.

The study demonstrated the predictive value of PS-InSAR and piezometric monitoring for identifying critical breakpoints in displacement patterns, which can forecast future events. It highlighted the need for proactive risk management, given the vulnerability of the region to groundwater-induced hazards.

Brussels area

The industrialization of Brussels during the 19th and early 20th centuries, particularly in areas like the Tour & Taxis site near the canal and railway facilities, caused significant overexploitation of confined aquifers. This led to a substantial drop in piezometric heads, which influenced water pressures in the overlying loose sediments. With the gradual relocation of industries out of the city during the 20th century, groundwater pumping rates decreased, resulting in a steady rise in piezometric heads since the 1960s. These changes have stabilized in recent years, transitioning the city from experiencing land subsidence to an elastic rebound of approximately 1 mm/year.

Using a 1D hydro-geomechanical model, the study successfully simulated the long-term trends of land subsidence and subsequent uplift at the Tour & Taxis site. A comparison with InSAR-derived time-displacement curves and velocities from 1992 to 2019 demonstrated strong agreement, validating the model's calibration of compressibility and permeability properties for the key compressible layers.

To achieve more accurate simulations of hydrogeological and geomechanical processes, the development of a 3D groundwater flow model coupled with multiple 1D hydro-geomechanical models is recommended. This approach would allow for a more comprehensive representation of spatial variability in hydrogeological conditions. However, this ambitious goal requires:

1. A detailed dataset on the spatially distributed properties of geological layers, such as compressibility and permeability.
2. Reliable historical and current records of groundwater pumping.

Such advancements would improve our understanding of complex subsurface dynamics and support better-informed decision-making for urban development and hazard mitigation in Brussels and similar settings.

Conclusions and Implications

The findings from both areas emphasize the critical role of integrated geodetic and hydrogeological monitoring in understanding land deformation and managing associated risks. The project highlights:

1. The significant influence of aquifer water dynamics on land subsidence and deformation patterns.
2. The necessity of continuous, high-resolution data collection to address challenges related to data scarcity and improve model reliability.
3. The value of combining satellite-based observations with in-situ measurements for comprehensive hazard assessment as shown by the good estimations and comparisons between the SAR observations and the hydrogeological and geomechanical models established for three areas. However, at present state of research, two other cases were not able to confirm that the groundwater overexploitation in the past and

the active groundwater extractions were the main causes of the land subsidence deformations observed with the long interval of time of SAR monitoring (i.e. > 30 years).

This research contributes to bring valuable insights into subsurface dynamics in several case study areas for which ongoing peer-reviewed publications are under review and foreseen from the different partners of the consortium. The work done is also offering a framework for future studies and the development of effective mitigation strategies in regions facing similar geohazards (i.e. land subsidence and or ground deformations associated to the groundwater uses throughout Belgium).

Recommendations for further use of the PSInSAR data vs other techniques

1. Challenges in Installing IGR

Finding suitable locations for IGR installation is a complex task due to the need for wide, open areas free of buildings and trees, as well as requirements for safety and security fencing or protected area permissions. Additional challenges include administrative hurdles with landowners and ensuring affordable electricity access. These logistical and administrative steps were underestimated at the project's inception. Despite these obstacles, our teams (RBINS/GSB and NGI) have taken the lead in ensuring their practical functionality, requiring multiple site visits. The next phase involves validating the IGR as permanent corner reflectors and GNSS stations. These considerations must be addressed from the start of similar projects to expedite implementation. A positive aspect is the long-term utility of these installations (8–10 years), which guarantees their use for national and international initiatives, including the EPOS Belgium GNSS database and future research projects.

2. Increased Sentinel-1 SAR Image Availability

The growing volume of Sentinel-1 SAR images for nationwide processing poses significant challenges in terms of storage and computational requirements, as more than 6 TB of data must be managed. The recent launch of Sentinel-1C on December 5, 2024, enhances the Sentinel-1 constellation alongside Sentinel-1A, restoring a six-day interval between acquisitions. While this improves data availability, it further emphasizes the need for stronger professional workstations to handle the increasing computational demand efficiently.

3. Limitations of C-Band Sentinel-1 SAR Images

The ± 20 m resolution of Sentinel-1 SAR images limits their effectiveness for localized studies. High-resolution SAR images (1–3 m), such as those from TerraSAR-X (TSX) or CosmoSkyMed, are essential for precise geodetic analyses. During the project, two historical TSX datasets covering Antwerp and Brussels were processed but not yet fully integrated into the research. Unfortunately, recent TSX images (the last 18 months) must be purchased, and their high cost poses a significant barrier for studies in Belgium, where observed ground deformations are slow and subtle. These deformations, influenced by natural hazards and human activities under changing climatic conditions, necessitate affordable access to high-resolution datasets for effective subsurface management.

4. Future Challenges in PSI Data Utilization

One critical challenge with PSI datasets is identifying and categorizing the specific nature of each Persistent Scatterer (PS) point. This information is essential for understanding how ground deformations interact with anthropogenic structures and their subsurface foundations. Accurate characterization requires integrating additional databases on human and engineering infrastructures within study areas, demanding significant effort and resources.

5. Need for Comprehensive Data for Modeling

Many case study areas in the project suffered from insufficient and sparsely distributed data, hindering the development of detailed models. Subsurface geology lacks adequate monitoring through diverse equipment, techniques, and tools. This deficiency complicates the differentiation of shallow and deep geological processes contributing to observed surface deformations. PSI data, while revealing surface movements, require complementary geological, hydrogeological, and geomechanical data to model the interactions effectively.

6. Laboratory and Field Experiments

To distinguish shallow from deep geological causes of surface deformations (i.e. like land subsidence), applied laboratory and field experiments on-site using varied equipment (IGR, drillings, extensometers, geophysical campaigns, CPT, etc.) are essential. Understanding these localized processes is a prerequisite for scaling up mechanisms and applying advanced methods, such as artificial intelligence. Ground control points, including IGR stations, corner reflectors, and GPS antennas, will play a critical role in these efforts.

7. Producing thrusted SAR observations at national scale

The combination of SAR data at a national scale, integrating processing results from various satellite footprints, has faced challenges due to artifacts along the borders of contiguous datasets. These artifacts have been partially mitigated through detailed statistical analyses of the time series produced by individual SAR datasets (ERS1/2, ENVISAT, Sentinel-1A, and Sentinel-1B). However, further refinement requires additional control points, such

as those provided by GNSS stations, to enhance the calibration of the processing framework. The increasing number of Persistent Scatterer (PS) points generated by SAR acquisitions and processing intensifies the need for a dense network of GNSS stations distributed across Belgium. Unfortunately, funding issues have led to the removal or insufficient maintenance of some GNSS stations, resulting in gaps within the network. To address this, it is critical to prioritize the expansion and maintenance of the GNSS network by replacing removed stations, filling existing gaps, and installing new models such as Integrated Geodetic Reference (IGR) stations. These IGR stations, which combine two geodetic techniques in one location, enhance the GNSS network and provide reliable absolute anchors for PS-InSAR observations, improving the accuracy and reliability of national-scale SAR data.

5. VALORISATION ACTIVITIES

5.1 PUBLICATIONS

Publications in peer-reviewed journals (with Impact Factor)

- Choopani, A., Orban P., Declercq, PY., Devleeschouwer X., Dassargues A. (2025, under review). *Challenges in comparing land subsidence measurements by PS-InSAR with simulations from coupled hydro-geomechanical modeling: a case study in Antwerp harbor. Hydrogeology Journal.*
- Choopani, A., Declercq, PY., Ronchi, B., Devleeschouwer X. (2024). Assessing hydrogeological hazards in the post-mining region in Saint-Vaast, Belgium: insights from three decades of SAR data and piezometric analysis. *Natural Hazards* (2024). <https://doi-org.ezproxy.ulb.ac.be/10.1007/s11069-024-07056-4>
- Declercq P.-Y.; Duser M.; Pirard E.; Verbeurt J.; Choopani A.; Devleeschouwer X. (2023). Post Mining Ground Deformations Transition Related to Coal Mines Closure in the Campine Coal Basin, Belgium, Evidenced by Three Decades of MT-InSAR Data. *Remote Sensing*, 15, 725. <https://doi.org/10.3390/rs15030725>
- Gobron, K., Rebischung, P., de Viron, O., Demoulin, A., Van Camp, M., *Impact of offsets on assessing the low-frequency stochastic properties of geodetic time series, Journal of Geodesy vol. 96 (2022). DOI: 10.1007/s00190-022-01634-9*
- Gobron, K., Rebischung, P., Van Camp, M., Demoulin, A., de Viron, O., *Influence of aperiodic non-tidal atmospheric and oceanic loading deformations on the stochastic properties of global GNSS vertical land motion time series, J. Geophys. Res.: Solid Earth vol. 126 (2021). <https://doi.org/10.1029/2021JB022370>*
- Choopani A., Declercq P.-Y., Dassargues A., Devleeschouwer X. (2021). Land subsidence observed in the Merchtem Area (Flanders) – 30 years of SAR data associated to groundwater withdrawal? International Geoscience and Remote Sensing Symposium – IGARSS 2021 Brussels, Belgium, 12-16 July 2021, conference paper.
- Declercq P.-Y., Choopani A., Dassargues A., Devleeschouwer X. (2021). Areas prone to land subsidence and their evolutions in Belgium during the last 30 years. International Geoscience and Remote Sensing Symposium – IGARSS 2021 Brussels, Belgium, 12-16 July 2021, conference paper.
- Declercq P.-Y., Gérard P., Pirard E., Walstra J., Devleeschouwer, X., (2021). Long-Term Subsidence Monitoring of the Alluvial Plain of the Scheldt River in Antwerp (Belgium) Using Radar Interferometry. *Remote Sensing* 13/6: 1160. <https://doi.org/10.3390/rs13061160>, (open access).

5.2 PARTICIPATION/ORGANISATION OF SEMINARS (NATIONAL/INTERNATIONAL)

Oral presentation, poster... and/or organisation of workshops, symposia etc.

Scientific communications in congress

- Declercq, P.-Y., Choopani, A., Verbeurt, J., Devleeschouwer, X. (2023). Post Mining Ground Deformations from Land Subsidence to Rebound: An Overview of the Campine (Limburg, Belgium) Coal Mining District. In the International Geoscience and Remote Sensing Symposium, Pasadena, USA, July 2023.
- Choopani, A., Orban, P., Declercq P.-Y., Devleeschouwer, X., Dassargues A. (2023, July). Application of a Multidisciplinary Approach to Assess Consolidation in Different Geological Layers at a Local Scale in Antwerp. In the International Geoscience and Remote Sensing Symposium, Pasadena, USA.
- Moreau A., Choopani A., Declercq P.-Y., Orban P., Devleeschouwer X., & Dassargues A. (2023a, April 19). A Summary Review Based on Case Studies of the Challenges Related to the Comparison of Displacements Measured by PS-InSAR and Simulated by Geomechanical Coupled to Groundwater Models. The Tenth International Symposium On Land Subsidence. <https://orbi.uliege.be/handle/2268/302365>
- Moreau A., Choopani A., Declercq P.-Y., Orban P., Devleeschouwer X., & Dassargues A. (2023b, April 26). Difficulties arising when PS-InSAR displacement measurements are compared to results from geomechanical and groundwater flow computations. EGU General Assembly 2023. <https://doi.org/10.5194/egusphere-egu23-16384>
- Choopani A., Declercq P. Y., Verbeurt J., De Doncker F., Orban P., Dassargues A., & Devleeschouwer X. (2023). A step towards accurate integrated monitoring of the sinking zones in the coastal area of Antwerp

due to possible hydrogeological and geomechanical processes. In 10th International Symposium on Land Subsidence (TISOLS 2023). Copernicus Publications, Göttingen, Germany. <https://hdl.handle.net/2268/303659>

- Declercq P. Y., Choopani A., Verbeurgt J., Devleeschouwer X. (2023). Post mining ground deformations from land subsidence to rebound: an overview of the Campine (Limburg, Belgium) coal mining district. In IGARSS 2023
- Choopani A., Orban P., Declercq P. Y., Devleeschouwer X. & Dassargues A. (2023). Application of a multidisciplinary approach to assess consolidation in different geological layers at a local scale in Antwerp. In IGARSS 2023.
- Choopani A., Declercq P. Y., Verbeurgt J., De Doncker F., Orban P., Devleeschouwer X. & Dassargues A. (2023). Subsidence Evolution of Antwerp Region, Belgium over 77 Years, Using Historical Levelling and GNSS Data and Recent Persistent Scatterers Interferometry Observations. In EGU General Assembly 2023.
- Choopani A., Ronchi B., Declercq P.-Y., Devleeschouwer X. (2022). Ground Deformations Related to an Old Drainage Adit in The Abandoned Coal Concession Around Saint-Vaast (Wallonia, Belgium) Analysed Using PS-InSAR and Piezometric Wells Time Series IMWA 2022, Christchurch, New Zealand, 6-11 November 2022. Conference Paper submitted mid-August 2022, 6 pages.
- Devleeschouwer X., Choopani A., Declercq P.Y. (2022). Ground Deformations Observed for Three Decades (1992-2022) above Old and Deep Coal Mines Reused for Deep Gas Storage Sites (Wallonia, Belgium) using PS-InSAR Time-series. IMWA 2022, Christchurch, New Zealand, 6-11 November 2022, accepted, oral presentation.
- Devleeschouwer, X., Choopani, A., Moreau, A., Walvarens, K., Van Camp, M., Van Camp, M., Gobron, K., Dassargues, A., Orban, P., Declercq, P., The LASUGEO project: monitoring LAnd SUBsidence caused by Groundwater exploitation through gEODetic measurements, (2021). 7th International Geologica Belgica Meeting 2021.
- Gobron, K., Rebischung, P., de Viron, O., Van Camp, M., Demoulin, A., Influence of non-tidal atmospheric and oceanic loading deformation on the stochastic properties of over 10,000 GNSS vertical land motion time series, (2021). Invited talk presented at EGU 2021 meeting on 2021-04-27 (virtual).
- Gobron, K., Declercq, P., Devleeschouwer, X., Van Camp, M., Statistical imaging of the deformation over Belgium using multiple geodetic techniques, (2021). Talk presented at the 7th International Geologica Belgica Meeting 2021.
- Gobron, K., Rebischung, P., de Viron, O., Demoulin, A., Van Camp, M., Impact of Offsets on Assessing the Low-Frequency Stochastic Properties of Geodetic Time Series, (2022). Talk presented at EGU, May 2021, Vienna.
- Choopani A., Declercq P.-Y., Dassargues A., Devleeschouwer X., (2021). Land subsidence observed in the Merchtem area (Flanders) - 30 years of SAR data associated to groundwater withdrawal? IGARSS 2021, Brussels, July 12-14 2021 (conference paper, accepted)
- Declercq P.-Y., Choopani A., Dassargues A., Devleeschouwer X., (2021). Areas prone to land subsidence and their evolutions in Belgium during the last 30 years. IGARSS 2021, Brussels, July 12-14 2021 (conference paper, accepted)
- Choopani A., Declercq P.-Y., Orban P., Devleeschouwer X., Dassargues A. (2021). Land subsidence as revealed by PS-InSAR observations in the Antwerp area (Belgium): first steps towards the understanding and modeling. 48th IAH Congress, September 6th – 10th, 2021, Brussels (accepted).
- Moreau A., Declercq P.-Y., Orban P., Devleeschouwer X., Dassargues A. (2021) Modelling land subsidence caused by groundwater exploitation and revealed by geodetic InSAR measurements in the Leuven area. 48th IAH Congress, September 6th – 10th, 2021, Brussels (accepted).

5.3 SUPPORT TO DECISION MAKING (IF APPLICABLE)

For the authorities' decision making, it is very important to be informed about the causes of land subsidence that are related to surface deformation observations and monitoring throughout a long interval. The natural hazards influencing the surface deformation observations were related to groundwater withdrawal (from shallow or deep aquifers), climatic drought, rock removal and/or dewatering in mining areas, or other causes.

Scientific Approach to Advocate for Informing Public Authorities about Geohazards issued from groundwater exploitations and the case study discussed here inside and during the project.

Geohazards such as groundwater withdrawal and intensive groundwater exploitation pose significant risks to

infrastructure, ecosystems, and public safety. A structured, scientific approach can effectively convey the necessity of informing public authorities and implementing appropriate measures. Here's an outline:

Groundwater withdrawal reduces pore pressure in aquifers, leading to land subsidence, reduced aquifer capacity, and changes in groundwater flow patterns. The consequences are (i) Land subsidence: causes damage to infrastructure such as buildings, roads, and pipelines. (ii) Aquifer Depletion: limits water availability for future use, impacting agriculture, industry, and drinking water supplies. (iii) Environmental degradation that impacts surface water bodies and ecosystems dependent on groundwater and, (iv) increased flooding: land subsidence can exacerbate flooding in urban and coastal areas.

Risk assessment and prediction should use scientific models: hydrological models simulate groundwater recharge and withdrawal rates. Geomechanical models predict land subsidence. Data Collection with groundwater levels monitored via piezometers, satellite-based remote sensing (e.g., InSAR) for detecting subsidence. Risk Mapping identifies areas at high risk, helping to prioritize interventions.

Economic Costs due to repair and maintenance of damaged infrastructure implies a loss of agricultural productivity due to reduced irrigation capacity and an increased disaster recovery costs following floods or subsidence events. The social consequences are water scarcity leading to conflicts or migration and public health issues from contamination of groundwater (e.g., intrusion of seawater or pollutants).

Policy and governance implications should use (i) early warning systems as authorities need real-time data to issue warnings and mitigate risks. (ii) zoning regulations restricting intensive groundwater withdrawal in vulnerable areas and (iii) resource management to put in place sustainable extraction limits to balance recharge and withdrawal.

Communication and advocacy by engaging stakeholders as public authorities, scientists, engineers, and communities must collaborate, simplifying complex concepts using visual tools like maps, graphs, and animations to illustrate risks and potential solutions, and framing the argument highlighting long-term economic savings and risk reduction from proactive measures.

The recommendations for public authorities were to (i) invest in monitoring by installing equipments in regions with the necessary tools to track groundwater levels and land movement, (ii) promote sustainable practices, (iii) encourage water conservation and alternative water sources and (iv) develop contingency plans preparing for emergencies arising from subsidence or water shortages.

Groundwater-related geohazards are complex, but their risks can be significantly reduced with informed policy decisions. Public authorities equipped with scientific data can implement proactive measures to safeguard resources, infrastructure, and communities. Informing them is not just a recommendation but a necessity for sustainable development and resilience in the face of environmental challenges.

How Climate change-driven environmental challenges create Geohazards

Climate change exacerbates geohazards by altering environmental and geological systems, intensifying risks associated with droughts and intense precipitation. These climatic changes influence hydrological cycles, land stability, and ecosystem dynamics, leading to new or worsened geohazards associated with the use of the aquifers. Droughts are prolonged periods of low precipitation, causing water scarcity and affecting geological systems. Key impacts include (i) groundwater depletion and/or increased reliance on groundwater during droughts leads to excessive withdrawal, reducing pore pressure in aquifers with associated land subsidence, aquifer compaction, and reduced storage capacity for future water use. (ii) Soil desiccation and cracking with dehydration of soils reduces cohesion and structural integrity, especially in clay-rich areas giving an increased vulnerability to landslides and ground collapse. (iii) Moreover, drought-induced vegetation dieback weakens root structures that stabilize slopes and accelerate soil erosion and slope failures.

Intense rainfall events, increasingly frequent due to climate change, rapidly alter the water balance in geological systems. Key impacts include (i) Soil saturation and erosion as excess water increases soil weight and reduces shear strength creating landslides and mudflows. (ii) Flooding due to high-intensity precipitation can cause river overflows, flash floods, and urban flooding leading to Scouring and undercutting of riverbanks, destabilization of infrastructure, and erosion of natural levees. (iii) Rapid infiltration of water in soluble rock regions (e.g., limestone) can dissolve underlying materials implies karstic collapses and the formation of sinkholes. (iv) Permafrost thawing (induced by precipitation combined with heat) induced by rain on snow or ice accelerates thawing in permafrost regions, which has almost no effects on the Belgian territory.

The combined impacts of droughts and intense precipitation by alternating cycles of drought and intense rainfall create compounded risks as (i) soil compaction and rehydration cycles destabilize soil creating rapid erosion and slope failures. (ii) aquifer recharge and overpressure of depleted aquifers can lead to hydraulic fracturing or seismic activity with earthquakes induced by rapid groundwater movement. The glacial retreat with melting glaciers destabilizes mountain slopes, exposing bedrock to erosion and increasing risks of rockfalls and landslides. The sea-level rise influences the coastal areas facing intensified erosion and salinization of groundwater, destabilizing foundations and aquifers but also sustain an increased storm intensity while stronger storms result in higher rainfall rates and prolonged flooding with widespread destruction of landscapes and infrastructure.

Strategies for mitigating those geohazards from the ongoing climate change implies (i) early warning systems to monitor climatic variables and geological responses to predict risks. (ii) sustainable ground-water management to avoid over-extraction of groundwater and promote aquifer recharge. (iii) the work on infrastructure design to build resilient structures capable of withstanding variable climatic and geological conditions. (iv) to start reforestation and soil conservation measures to stabilize slopes and reduce erosion through vegetation cover.

Conclusion

Climate change exacerbates geohazards by altering the delicate balance of geological and hydrological systems. Addressing these challenges requires integrating climate models with geohazard risk assessments to enhance resilience and preparedness. Proactive measures can significantly reduce societal, environmental, and economic vulnerabilities. Part of the ongoing work of the Lasugeo was to study land subsidence areas having a clear impact on urbanized and densely populated areas where the ground deformations observed at the surface are weak, slight and long-term processes due to human-induced causes with potential important consequences that can be slightly or strongly impacted by some of the climatic changes affecting specific areas (like Antwerpen harbour and the Scheldt river and estuary including the Doel power plant facilities or other areas like the brewery sites that are using aquifers for economic industry and developments where there is a need of strong and long-term stability of the aquifers through time).

6. ENCOUNTERED PROBLEMS AND SOLUTIONS

The scientific activities are still ongoing, publications in IF peer-reviewed journals are planned in the different teams, cross-comparisons in between the teams are expected for the third annual report. NGI even not associated at the origin of the LASUGEO project is now a full partner associated with the GSB in the development of the new IGR stations and in the willingness to develop, build, submit new projects associated to the wish of developing and installing a new Belgian network composed of IGR stations. Three projects have been submitted so far in different calls and were selected but not funded.

Regarding the **WP2** case studies, those linked to the DAS in Western Flanders area and the Tertiary central aquifer system have continued and are nearing completion. The Leuven ROI case has been stopped and the PhD as well. The last ROI in Antwerp is still part of the ongoing PhD thesis. Another (fifth) area has been started (Saint-Vaast) in the WP2 and will be included in the PhD thesis.

For the work on the **WP3** (gravimetry and time series analyses), the ROB partners have almost stopped all the activities as explained before.

For the SAR processing aspects (**WP4**), the hybrid mode of homeworking three days and office activities for two days a week are regularly implemented. The SAR team has the computer chains, the processing steps, and the possibilities to control remotely the different steps. The work has been focused in finding suitable sites to install IGR but the rebuttal aspect is the need of a real large open field for the GPS antenna to allow interacting with all the GPS satellites. The need of electricity for having the GPS station running is also another aspect partly not considered into site-decision. In some cases, for instance, several months were lost in 2023 trying to install an IGR in the site De Blankaart from the WaterGroep but even after two visits and discussion on potential location to install the IGR, the only spot was not that good because of trees and the company asked to make a renting contract to pay the electricity fee but at an amount of a bit more than 1000 EUR a year, which is too much for us. Considering the long term of the IGR, ten years, the cost of the electricity, which is very limited to run the SIM-card of the antenna. The decision was taken to not continue there. For some remote areas that are better located in an open-field area, the installation of solar panels with a buried battery could be a solution but we fear that it can drastically be reduced in wintertime.

A difficulty to create a national SAR ground deformation map for Belgium has encountered similar issues as observed in other countries. In a way or in another, the data need to be adjusted and smoothed statistically. A solution has been found with the help of the SkyGeo team. A ground deformation map based on Sentinel-1A processing's and covering the Netherlands, the Grand-Duchy of Luxembourg and Belgium is now fully accessible online at:

<https://bodemdalingskaart.portal.skygeo.com/portal/bodemdalingskaart/u2/viewers/basic/>